UNIVERSIDAD POLITÉCNICA DE MADRID

Escuela Técnica Superior de Ingenieros Industriales

Optimization of polypropylene surface texturing with ultrafast lasers. A semi-empirical and computational methodology for wettability control

TESIS DOCTORAL

Presentada para optar al título de Doctor por:

Julen Molinuevo López

Ingeniero industrial por la Escuela de Ingenieros de Bilbao

Madrid, 2024

Living without and aim

is like sailing without a compass.

John Ruskin

UNIVERSIDAD POLITÉCNICA DE MADRID
Escuela Técnica Superior de Ingenieros Industriales

Doctorado en Ingeniería Mecánica

Optimization of polypropylene surface texturing with ultrafast lasers. A semi-empirical and computational methodology for wettability control

TESIS DOCTORAL

Presentada para optar al título de Doctor por:

Julen Molinuevo López
Ingeniero industrial por la Escuela de Ingenieros de Bilbao

Bajo la dirección de:
Dr. Carlos Molpeceres Álvarez
Dra. Eva Rodríguez Vidal

Madrid, 2024

Título: Optimization of polypropylene surface texturing with ultrafast lasers. A semi-empirical and computational methodology for wettability control

Autor: Julen Molinuevo López

Programa de Doctorado: Doctorado en Ingeniería Mecánica

Dirección de tesis:

Carlos Molpeceres Álvarez, Catedrático, Universidad Politécnica de Madrid

Eva Rodríguez Vidal, Tekniker

Revisores externos:

Tribunal de tesis:

Fecha de defensa:

Agradecimientos

Después de varios años realizando esta tesis, dentro de las cuales es necesario incluir una difícil etapa como ha sido la pandemia del coronavirus, me gustaría mencionar en estos agradecimientos a todas aquellas personas que me han empujado en todo momento para terminar este trabajo.

Lo primero, agradecer a mis directores de tesis, Eva Rodríguez (Tekniker) y Carlos Molpeceres (UPM), quienes se han comprometido a guiarme, asesorarme y ayudarme durante estos cuatro años de tesis. Muchas gracias por enseñarme a terminar este arduo trabajo. Gracias por estar ahí las veces que me he sentido bloqueado y no he sabido seguir.

Agradecer a la UPM y al equipo del Centro Láser por permitirme ser parte del alumnado de la Universidad y también por permitirme visitar sus instalaciones, donde he podido trabajar durante una temporada corta. A Miguel Morales, por ayudarme con la parte de simulación, y por permitirme manejar su programa de COMSOL desde Euskadi. Y a su equipo, en general, con el que me he sentido muy a gusto y donde me he sentido como uno más durante mis breves estancias en Madrid.

Agradecer a Tekniker, por confiar en mí, dejarme entrar en sus instalaciones y dejarme a mi disposición de todo lo que necesitaba para realizar la tesis, y en particular a Iban, Vanesa y Jon, entre otros, por ayudarme y por el trabajo en equipo que me habéis demostrado tener. No solo he aprendido a llevar a cabo mi tesis, sino también a trabajar en un ambiente profesional y a llevar unas pautas de trabajo competentes que me han ayudado y ayudarán a sobrellevar cualquier problema o escenario, y mucho más. Por supuesto, no pueden faltar aquellos que más me han aguantado durante esta etapa, siendo estos mis compañeros (y excompañeros) de trabajo más cercanos y de coche: Gonzalo, Patricia, Ángela, Javi, Iñigo o Sergio, entre otros, con los que he compartido no solo cafés en Tekniker, sino también muy buenos momentos fuera del ambiente de la oficina. Habéis sido un soporte que me ha ayudado durante muchas horas a terminar este proyecto.

Fuera del ámbito laboral, me gustaría comenzar dándole las gracias a mi pareja, María, la cual me ha ofrecido su ayuda en todo momento. Ella ha sido quien, en los momentos en los que las cosas no salían como quería, me apoyaba y me hacía ver que era capaz de todo. Sin dudarlo ningún instante, ha sido mi pilar central y la que me ha aguantado durante varios años. Y, por supuesto, el otro pilar fundamental es el de mi familia: mi ama, mi aita, mi hermano, mi hermana y mis cuñadas (e incluso mi pequeña sobrina, que su sola presencia ha ayudado muchísimo esta última etapa), a quienes más o menos, todos y todas han puesto su granito de arena en este proyecto que he ido realizando. Todo lo que se me ha "chinchado" ha valido la pena. También agradecer al aita y ama de mi pareja, los cuales han tenido la misma implicación en preocuparse e interesarse por mis avances en la tesis, así

como también agradezco a mis mejores amigos y amigas, tanto de Bilbao como de Poza, con especial mención a Martín, Borja, Gabriel, Noa, Lucía, Bea, Ainara, Jon y Cristina, entre otros (me gustaría nombrar a muchos más, pero no quiero que esto sea más largo de lo que ya es), quienes me habéis ayudado mucho más de lo que creéis.

En general, gracias a todos y a todas por todo el apoyo mostrado, sin el cual no hubiera crecido ni una décima parte en ámbitos generales, y me veo más seguro y capaz de afrontar nuevos escenarios.

¡GRACIAS!

ABSTRACT

Over the last decades, the study of surface functionalization regarding the concept of wettability has been on the rise. The number of papers published on the modification of a surface's natural ability to retain or repel a droplet has grown exponentially from the 1980s to the present day. Through purely superficial changes in inherent material properties such as wettability, laser surface texturing has emerged as one of the most interesting technologies for applications related to the generation of superhydrophobic surfaces that promote easy cleaning or reduce the adhesion of water in liquid and/or solid state. However, the process of achieving surfaces with specific wettability properties, i.e. with a desired minimum contact angle, can consist of a large number of trial-and-error steps including:

i. Parametrization of the laser micromachining process
ii. Characterization of the introduced surface modification: topography and morphology
iii. Functional characterization of the surface.

This process must be repeated for each manufactured texture, which leads to an increase in manufacturing time, with its associated economic cost. For this reason, wettability prediction models for surfaces undergoing both physical and chemical modifications have been proposed over the last decades to reduce this cost.

In this thesis, the main objective is to provide a guide for future materials and feature geometries, showing the steps to follow to study the effect of different topographical parameters that define a texture on the contact angle, as well as introducing a simulation modelling tool to predict which type of texture and/or dimensions offer the best results. This is intended to reduce the window of dimensions to be considered and, consequently, to reduce the experimentation time. Thus, the process of selecting textures to achieve specific wettability objectives would be streamlined not only at the laboratory level but also at more relevant environments (at a more industrial levels), which could lead to throughput improvements in terms of surface functionalization.

In order to achieve the objective described above, this thesis proposes the elaboration of a Design of Experiments in which a number of textures are fabricated by means of ultrashort pulse laser technology in a polymeric material with a relatively high use in the industry such as polypropylene. Beforehand, a complete study is performed regarding the comparison between two pulse emission modes (Single Pulse and Pulse Train or Burst Mode). The main advantages and disadvantages of both operation modes have been evaluated and those parameters that allow an optimal quality/throughput ratio for the considered application have been identified. Once selected the

optimal parameters, the corresponding textures have been developed. The Design of Experiments focuses on the evaluation of the probabilities of each factor in the modification of the contact angle, and a simplified prediction model obtained by regression is proposed.

The experimental results for the Design of Experiments serve as validation parameters for the simulation of wettability at different textures, performed with COMSOL Multiphysics. A finite element model is proposed with the CFD (Computer Fluidic Dynamics) module, which makes use of the union of two physics such as the kinetics of the fluid (Laminar Flow) and the identification of two different phases in a medium, divided by an interface (Two Phase Flow, Phase Field). In this case, the effect of different simulation parameters on the results is studied and the optimal mesh size is established to provide results (in terms of contact angle) similar to the experimental ones. The results allow understanding the effect of each topographical factor defining a texture on the final surface wettability and provide a map of results similar to those observed experimentally.

RESUMEN

Durante las últimas décadas, el estudio de la funcionalización de superficies en lo que respecta al concepto de mojabilidad ha ido *in crescendo*. El número de artículos publicados en relación a la modificación de la capacidad natural de una superficie a retener o repeler una gota ha crecido de forma exponencial desde los años 80 hasta hoy en día. A través de cambios exclusivamente superficiales de propiedades inherentes del material como es la mojabilidad, se ha demostrado que el texturizado por láser de una superficie es una de las tecnologías con mayor interés en aplicaciones relacionadas con la generación de superficies superhidrófobas que fomentan la fácil limpieza o que logran reducir la adherencia del agua en estado líquido y/o sólido. Sin embargo, el proceso para lograr superficies con propiedades de mojabilidad específicas, es decir, con un ángulo de contacto mínimo deseado, puede consistir en un gran número de pasos de prueba y error que incluyen:

i. Parametrización del proceso de micro fabricación por láser
ii. Caracterización de la modificación superficial introducida: topografía y morfología
iii. Caracterización funcional de la superficie.

Este proceso se tiene que repetir para cada textura fabricada, lo cual conlleva un aumento del tiempo de fabricación, con su coste económico asociado. Por esta razón, durante las últimas décadas se han propuesto modelos de predicción de mojabilidad en superficies sometidas a modificaciones tanto físicas como químicas para reducir este costo.

En esta tesis, el objetivo principal es proporcionar una guía para futuros materiales y geometrías, en la que se muestre los pasos a seguir para estudiar el efecto de diferentes parámetros que definen una textura en el ángulo de contacto, además de introducir una herramienta de modelado por simulación para predecir qué tipo de textura y/o dimensiones ofrecen mejores resultados. Con esto se pretende reducir la ventana de dimensiones a considerar y, por consiguiente, reducir el tiempo de experimentación. De este modo, el proceso de selección de texturas para lograr objetivos específicos de mojabilidad se vería agilizado no solo a nivel de laboratorio sino también enfocándolo a niveles más industriales, con el que se podría lograr mejoras en la productividad en términos de funcionalización de superficies.

A fin de lograr el objetivo descrito anteriormente, en la presente tesis se propone la elaboración de un Diseño de Experimentos en el que se fabrican un número de texturas mediante tecnología láser de pulso ultracorto en un material polimérico con un uso relativamente alto en la industria como es el polipropileno. Previamente, se realiza un completo estudio comparativo entre dos modos de emisión de pulsos (pulso único y tren de pulsos o modo ráfaga). Se han evaluado las principales

ventajas e inconvenientes de ambos modos de operación y se han identificado aquellos parámetros que permiten una óptima relación calidad/rendimiento para la aplicación considerada. Una vez seleccionados los parámetros óptimos, se han desarrollado las texturas correspondientes. El Diseño de Experimentos se centra en la evaluación de las probabilidades de cada factor en la modificación del ángulo de contacto, y se propone un modelo de predicción simplificado obtenido por regresión.

Los resultados experimentales para el Diseño de Experimentos sirven como parámetros de validación para la simulación de la mojabilidad en diferentes texturas, realizada con COMSOL Multiphysics. Se propone un modelo de elementos finitos con el módulo de CFD (del inglés, Computer Fluidic Dynamics), en el cual se hace uso de la unión de dos físicas como son la cinética del fluido (Laminar Flow) y la identificación de dos fases diferentes en un medio, dividido por una intercara (Two Phase Flow, Phase Field). En este caso, se estudia el efecto de diferentes parámetros de simulación en los resultados y se establece el tamaño de mallado óptimo que permite proporcionar resultados (en lo que respecta al ángulo de contacto) similares a los experimentales. Los resultados permiten entender el efecto de cada factor que define una textura en la mojabilidad final y proporciona un mapa de resultados similares a los observados experimentalmente.

Table of contents

List of Figures

Chapter 2

Chapter 3

Chapter 4

Chapter 5

Chapter 7

Annex II

Annex III

Annex IV

List of Tables

Chapter 2

Chapter 3

Chapter 5

Annex AIV

List of Acronyms and Symbols

P_{avg}: Average laser power (W)

P_{peak}: Peak laser power (W)

I: Pulse irradiance (W/cm^2)

λ: Wavelength (nm)

v_s: Scan speed (mm/s)

E_p: Pulse energy (μJ)

I: Irradiance (W/cm^2)

F: Laser fluence (J/cm^2)

E_{th}: Ablation pulse energy threshold (μJ)

SP: Single Pulse mode

BM: Burst Mode

f_{SP}: Pulse repetition rate (KHz)

f_n: Burst repetition rate (KHz)

n, ppb: number of pulses inside a burst

N: number of scan layer or overscan

D_S, ω_0: Beam spot radius (μm)

D_C: crater diameter (μm)

d_C, d_g, d_s: Crater/groove/cavity depth (μm)

h_r: recast material height (μm)

w: groove width (μm)

HAZ: Heat Affected Zone

SRR: Specific Removal Rate, or efficiency (μm/ μJ)

RR: Removal Rate, or throughput (mm^3/s)

V_n: Removed volume (mm^3)

U_d: pulse or burst overlap (%)

f_{qp}: trade-off factor between quality and throughput (-)

CA, θ: Contact Angle (º)

CA_0, θ_0: Intrinsic or Reference Contact Angle (º)

CAH: Contact Angle Hysteresis (º)

A: Roll-off Angle (º)

θ_Y: Young contact angle (º)

θw: Wenzel contact angle (º)

θ_{CB}: Cassie-Baxter contact angle (º)

f_w: Wetting state parameter

r_f: Topographic factor (-)

f_{SL}: solid to liquid surface fraction (%)

DoE: Design of Experiments

a: pillar width (μm)

b: cavity width (μm)

h: pillar height (μm)

h_{2D}: double pillar height for the 2D simulation cases (μm)

σ: surface tension (N/m)

CFD: Computer Fluid Dynamics

FEM: Finite Element Method

γ: mobility parameter ($m^3 \cdot s/kg$)

χ, Mob: mobility tuning parameter ($m \cdot s/kg$)

ε : interface width (μm)

LS: Level Set method

PF: Phase Field method

VOF: Volume Of Fluid method

MM: Moving Mesh method

Chapter 1

GENERAL INTRODUCTION

1. 1. Motivation

Throughout the last decades, the modification of the surface wetting capability has become one of the most interesting topics in several industries [1, 2, 3, 4, 5]. The wettability control via topography modification of a surface is an experimental procedure that involves: a pre-selection of the type of features to be developed and their dimension range, the selection of proper laser parameters for each texture design, and the surface characterization. A typical surface structuring procedure while searching for the most appropriate texture to ensure a specific contact angle requires the development of a number of textures with different dimension (in the range of micro and nanometers) and/or different geometries, the topographic and morphologic characterization of each one of them, and the wetting measurement in every case. From the results, the most appropriate textures are selected, if any. Moreover, this procedure must be carried out for each studied material. Thus, the main drawback of the wettability control study via topographic modification is the time-consuming procedure followed to obtain and assess reliable results. Therefore, accelerating the pre-selection of the texture, based on a previous knowledge regarding the behaviour of the contact angle with the topography modification, is desired, either by providing a prediction model for a specific material or by the generation of a computational modelling that can help the researcher beforehand. This way, a cost reduction in terms of the use of the equipment and the working hours from the researcher may be achieved.

In this thesis, the wettability modification of a polypropylene surface is performed with an ultrashort pulse laser. A complete comparative procedure is performed between the Single Pulse operation and the relatively new Burst Mode available in ultrafast laser systems. Polypropylene is one of the most used polymers in several industrial applications (packaging, textile or automotive industries, among others) due to its excellent properties such as its high resistance to fatigue, natural hydrophobicity, non-toxicity, chemically inert, etc. To the author's best knowledge, little research has been reported during the last decades regarding the interaction between ultrashort laser pulses (in the range of femtoseconds) and this polymer, especially in terms of processing with burst of pulses instead of the traditional single pulses. Additionally, a lot of work have been put on the understanding and prediction of the wettability of a surface with the topography (and/or chemical) modification throughout the last decades, and in this thesis a full methodology is proposed in order to provide a step-up on this wettability prediction that may help enhancing the surface texturing in industrial environments.

1. 2. Objectives

Based on the motivation of the present work, the **main objective** of this PhD thesis is the development of a procedure that accelerates the preselection of one or more textures to ensure a specific wetting condition. By combining the experimental and numerical simulation modelling, the aim is to assess its reliability as a guiding tool for future works on the effect of topography on the wetting of a texture. Furthermore, it is desired to provide potential tools for understanding the effect of each of the dimensional parameters that can define a texture on the contact angle and for predicting this value. Therefore, the goal is to take a step forward in speeding up the process of selecting and manufacturing textures to industry-typical production levels.

The **secondary objectives** of this work can be divided into several categories.

1. Laser ablation of polypropylene
    - Assessment of the advantages and disadvantages of considering the Burst mode provided by the laser system over the Single Pulse mode on the trade-off between the quality and throughput, and on the efficiency of the ablation process.
    - Provide insights regarding the ablation mechanism and the pulse interaction due to high repetition rates on the laser-polymer interaction.
2. Wettability modification of polymeric surface through textures developed by laser micro structuring.
    - Evaluation of solely the topographic effects on the contact angle variation of the polypropylene and the establishment of a procedure to assess the effect of each topographic parameter on this modification.
    - Obtention of a semi-empirical predictive model for the considered polymer and the definition of the steps needed for the same purpose on a new polymeric material.
3. Computationally assisted modelling of the topographic effect on the contact angle variation
    - Understanding of the procedure followed by the solver in COMOSL Multiphysics to provide the different outputs, based on a previously defined inputs by the user.
    - Obtention of the different parameters in the software to validate the outputs with the experimental results.
    - Assessment of the topographic factor effects on the obtained contact angle and comparison with the experimental results.

- As a secondary objective, the establishment of a generic step-by-step procedure for the simulation under different inputs and conditions.

1. 3. Structure of the thesis

This section aims to facilitate the lecture of the present doctoral thesis, which is composed by a total of 7 chapters and four annexes. A further division into three different parts can be made in the Chapter 5, i.e., Part I, Part II and Part III.

- Chapter 1: General Introduction

This chapter introduces the main motivation of this doctoral thesis, and summarizes each chapter included in it. Additionally, the scope and objectives are summarized.

- Chapter 2: Background research

In this chapter, a thorough review of the previous works regarding the main topics of this thesis is carried out. First, a brief introduction to the importance of the polymeric is given, highlighting the main reasons for the choice of the polypropylene as the material used in this thesis (properties, relevance to the industrial applications, and the lack of reports on the ultrashort pulse ablation of this specific material, etc.). The second part presents a detailed review of the main fundamentals of the laser ablation process, centred on the mechanisms that govern the ultrashort pulse interaction with the polymeric material. Moreover, the key laser parameters that can be adapted in order to perform an efficient ablation process are summarized, alongside the definition of the burst operation mode available in the laser system used in this work. The third section focuses on the Laser Surface Functionalization as an emerging approach of the laser ablation mechanism in order to enhance various surface properties without modifying its bulk properties. The main applications in which this concept is used are also listed and reviewed. Then, in the fourth section, the main concept this thesis work with is introduced, i.e., the phenomenon of wettability, defined by the Contact Angle, along the advances reported by previous authors regarding the predictability of this parameter. Finally, a detailed review of the computational modelling of this phenomenon is presented, listing, and briefly describing the different approaches and tools available.

- Chapter 3: Methodology and instrumental techniques

This chapter introduces the main methodology proposed and followed throughout the thesis, providing a detailed description of each step followed, from the definition of the design of the

experiments to the assessment of the results obtained from experimentation and the simulation. The main experimental equipment used in this work are introduced.

- Chapter 4: Computational modelling

A detailed description of the selected modelling approach is provided, in terms of physical model, the solver configuration and the meshing of the domains, among others.

- Chapter 5: Results and discussion

In this chapter, the main experimental results are presented and discussed. As previously stated, the present thesis can be split into three main blocks, and hence this chapter is divided in their three corresponding parts.

  - Part I: Laser parameter optimization for the ablation of polypropylene

The first part of this chapter covers the observation throughout the experimental results of the laser parameters that provide the best results regarding the optimum trade-off between quality and throughput. First, crater-like structures are developed (i.e., the most basic structure obtainable in pulsed lasers) and the main ablation mechanisms is identified. The topography, removed volume, efficiency, throughput and quality of these features are assessed while considering two different pulse emitting modes (Single Pulse Mode and Burst Mode), and the advantages and disadvantages of both modes are discussed. These results are gathered in the author's first publication in JCR Journals. Afterwards, the effect of additional parameters that are not taken into consideration in crater-like structures are assessed by developing grooves and square cavities.

  - Part II: Laser surface texturing for the wettability control of polypropylene

After the first parameter window that ensures the trade-off between quality and throughput, a Design of Experiments is proposed, in which several different textures are developed and their contribution to the contact angle variation is assessed. The effect of each factor defining the texture topography is assessed through a regression model, from which a simplified model is obtained. Moreover, a relationship between the topography and the contact angle variation is identified.

  - Part III: Computational modelling of the wetting behaviour of a water droplet on laser textured surfaces on polypropylene

The third part of this chapter focuses on the computational modelling of the wetting process of a droplet on top of a surface. The potentiality of this model is assessed regarding its capability to provide results with a similar behaviour than in the Part II. The main objective is to observe if, by

maintaining the input parameters, solely changing the topography of the surface provokes contact angle modification that correspond with the experimental results. A complete step by step procedure is presented in which both the initial and boundary conditions are indicated, and the estimation of the non-physical parameters related to the model is detailed. The same sensibility procedure is followed with the meshing of the domains. The advantages and disadvantages of using a 2D or 3D system are assessed, focusing on the simulation time, due to the desired acceleration in the pre-texture selection step.

- Chapter 6: Conclusions

This chapter contains the most remarkable conclusions obtained from the present doctorate thesis, divided into several subsections corresponding to each part defined in the chapter 5, alongside an overall conclusion.

- Chapter 7: Future work

This chapter shows the potential applications regarding the proposed computational model in new systems and under different conditions that are not considered in this thesis. It also includes different questions that arose during the execution of the present work, which do not affect the fundamental scope of the work.

- Annex I: Scientific output

The first annex lists the different contributions of the author directly related with this work in the form of publications and contributions to conferences.

- Annex II: Additional experimental instrumentation

The second annex briefly describes the experimental equipment used in the work, introduced in the chapter 3.

- Annex III: Simulation results

The third annex provide additional material of the complete simulation results.

- Annex IV: Extrapolation to other laser systems

Lastly, the fourth annex resumes the findings obtained during the author's stay in the Laser Centre from the UPM, in which the ability to extrapolate the results from this work to other laser systems was assessed.

Chapter 2

RESEARCH BACKGROUND

2.1. Introduction

The control of the wetting performance of a surface can be accomplished through techniques and technologies that involve the modification of the surface energy of the material. The most important approaches to achieve this can be classified as follows:

- Bulk material modifications

The modification of a material's bulk properties involves the design and synthetization of chemical structures in the intrinsic chemical structure of the material [6]. This is generally interesting to modify and improve the main limitations from polymeric materials, which can be relatively easily achieved through the incorporation of functional groups or through copolymerization with other polymers [7]. However, when the functionalization that is desired to implement is primarily localized in the surface (erosion resistance, wettability, anti-icing, etc.), instead of modifying the entire bulk material, surface treatments are usually applied.

- Surface functionalization
    - Chemical modification of the surface

Chemical modifications involve the use of chemical agents to alter the properties of the surface [8], such as oxidation, reaction, or the application of a coating of a different material on top of the original surface. The main technologies regarding this category are the Chemical Vapor Deposition (CVD), Atomic Layer Deposition (ALD), laser surface texturing (when the laser-material interaction promote a chemical modification of the surface, such as the oxidation of a metal, etc.), wet chemical treatments, etc.

    - Physical modification of the surface

Surface modification by physical routes is an ecofriendly, relatively simple, and scalable alternative to the chemical functionalization. The physical methods also provide an additional robustness that is required for industrial applications [9]. They involve the roughness and topography modification by the induction of micro and nanofeatures on the surface, which are usually centred on the tuning of the inherent wettability. The main technologies in this category are Physical Vapor Deposition (PVD), laser surface texturing, mechanical grinding, etc. Other techniques that change the surface of a surface are the microinjection, hot-embossing, roll to roll, extrusion, etc. However, in cases like the microinjection or the hot embossing, the micro and nanostructures must be previously done into the metallic mold and transferred afterwards into the polymer.

The increased use of these technologies has led to an exponential increase of the number of research publications regarding the surface wettability topic, as it can be seen in Fig. 2. 1. It can be observed how the number increased from 400 (between the years 2000 and 2002) to more than 9000 between 2020 and 2023. Among the listed approaches, the physical and chemical modifications have been widely studied. More specifically, among the physical techniques, the modification of the topography of the texture has proven to successfully modify the inherent properties of a surface, which involves a change in its overall rugosity [2]. Laser surface texturing is one of the most competitive technologies to achieve controllable high-quality micro and nanostructures involved in the topography alteration (which can be seen translated into an increase in the number of publications regarding the use of this technology in the wettability modification field in Fig. 2. 1). Several industries have been working on this specific surface functionalization to enhance the inherent properties of a material, such as the controlled water adhesion for antibacterial surfaces in the packaging industries [10, 11], the anti-icing surfaces for the aeronautic industries [12], the reduced friction to cut the fuel consumption in the naval industries [13], or the controlled drug delivery in microfluidic chips in the biomedical field [14], among others.

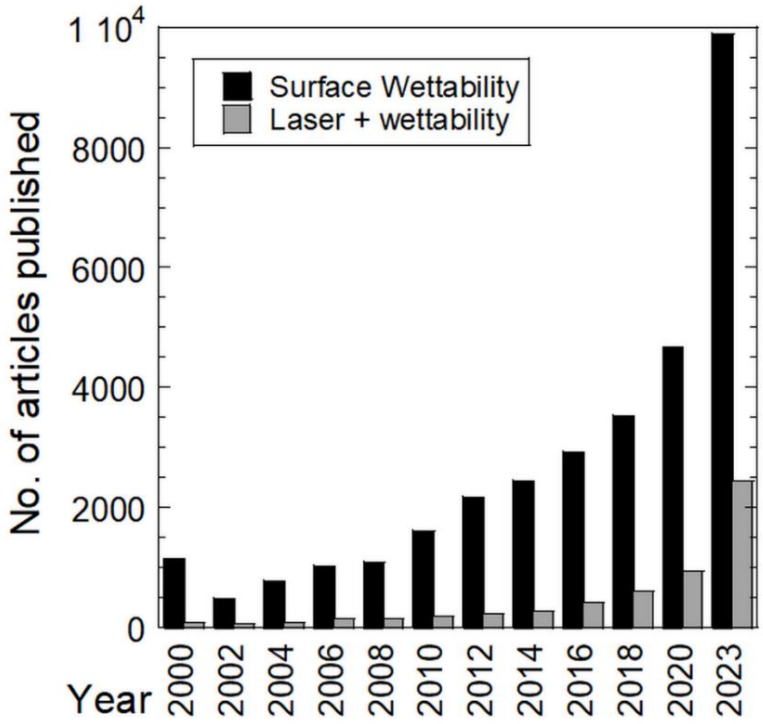

Fig. 2. 1 Evolution of the publications regarding the wettability and those specific to the laser technology, based on the results from Scopus [15].

Compared to other lasers sources, the ultrafast laser ablation technologies has prompted the researchers to focus lately on improving laser performance and maximizing its capabilities in order to improve this disadvantage, i.e., increasing the pulse repetition rate to GHz or THz (promoted by the use of pulse bursts) [16], developing polygonal scanners [17], or studying the laser parameters that optimize the efficiency of the ablation process and/or the volume removal rate (which ca be related to each other) [18]. However, it is because of the main advantages that the laser technology has gained attraction over other similar technologies (CW and short pulse lasers, photolithography [19], coating [20], microinjection of textured moulds [21, 22], etc.), which involve: the capability of developing structures in the micrometer [23] and nanometer [24] scales with a relatively high quality within a controllable environment, fast processing time, no need of vacuum, no contact between the processing tool and the sample, high control of the shape and size of the micro and nanostructures, clean to environment, among others. This technology has been widely used in application fields such as the aeronautic and aerospace [25, 26], the tribology and surface engineering [27, 28], or the automotive [29, 30], among others.

In this thesis, the focus is aimed at the laser technology processing of a relatively widely used (in industrial applications) polymeric material such as polypropylene.

2.2. Polymeric materials

While metallic materials have always been considered as the first option in industrial applications, over the last decades the polymeric materials have experienced an increased relevance and interest that have pushed them to be one of the first options to consider. In fact, one of the main reasons of this increase is that the polymers (which include plastics, elastomers, thermoplastics, biopolymers, high-performance polymers, etc.) can be used in a wide range of applications that include the automotive, aeronautic, packaging or electronics among many others.

The overall properties of the polymers, such as the overall lightweight, high chemical and/or corrosion resistance, low production and manufacturing cost (compared to the metallic materials), etc., makes them the first option to choose in many applications [31]. Additionally, the polymers are constantly changing. The inherent properties of the polymers can be tuned to adapt their performance under specific circumstances, depending on the application, thus new polymers can also be developed, further increasing the interest and importance of these materials nowadays, to the point where they are even replacing metallic components [31]. For example, the properties of

polyolefins (polyethylene, polypropylene, etc.) have been changed in order to modify their response to light or temperature, among others [32].

In addition, the use of natural biopolymers has increased over the last decade as a result of increased environmental concerns in recent years to reduce environmental impact and dependence on fossil fuels [33]. Their relatively ease of recycling and low toxicity to human health has made them one of the most interesting materials to work with [33].

Among the many options available to the industry, polypropylene has stood out and has been used in a wide range of applications.

Polypropylene (PP) was first discovered in Milan, in 1954, by Giulio Natta [34]. However, it was not until 1957 that it began its commercial production by Montecanini [35].

The easy availability of the monomer used for this polymer, i.e., the propylene, increased exponentially the global production of the PP to higher levels than other polymers (including the PVC) between the 2000 and 2010 decades. More specifically, the production levels were 10 times higher in 2012 than it was in 1982 [36, 37] (see. Fig. 2. 2). Nowadays, the production levels of this polymer have surpassed the 60 million tons per year [38].

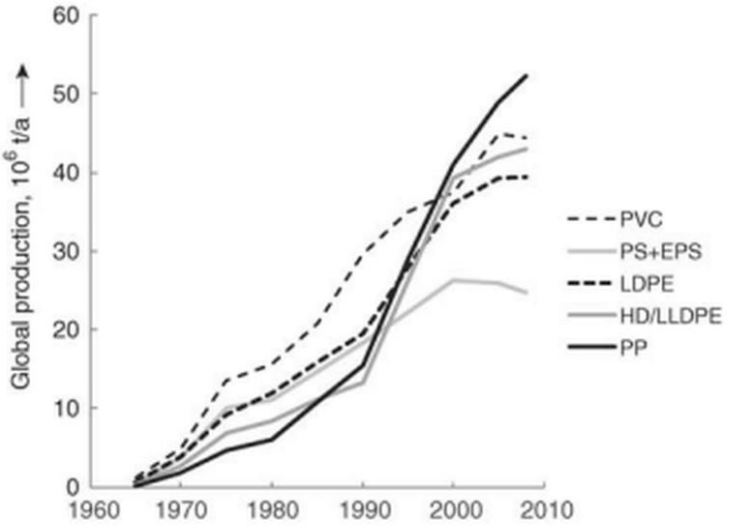

Fig. 2. 2 Evolution of the production of standard thermoplastics (figure from [36])

The main applications of this polymer cover the package production (bottle, container and canister production) and food industries due to the non-toxic, chemically resistant and recyclability properties, the pharmaceutical and chemical industries (production of pipelines and conduits, syringes, etc.), the textile industry (carpets, rugs, synthetic fibers, tools, etc.), the furniture and

construction industry (insulation, gas installations, cables, furniture, etc.) and automotive industry (body parts, bumpers, etc.), among others [39] (Fig. 2. 3).

Fig. 2. 3 Main PP applications (References ordered from left to right [40, 41, 42])

2.3. Laser ablation process

2.3.1. Laser-material interaction

2.3.1.1. Fundamentals of the laser-material interaction

Laser ablation consists of the removal of material from a solid surface by the absorption of the incoming energy from the laser source. The interaction between the laser and the surface can be defined by several mechanisms such as the absorption, transmission, and reflection of the incoming energy, which may be accompanied by additional diffuse effects, i.e., the process where the unidirectional light is deflected into multiple directions (scattering).

When the laser beam reaches the surface, part of its energy is either absorbed by the material, transmitted through the material and/or reflected to the surroundings. However, depending on the type of material, the specific mechanisms by which the absorption takes place are different [43]. Therefore, the nature of the material in terms of response to the incident light (wavelength, irradiance, etc.) play a key role in understanding the laser-material interaction mechanisms that govern the ablation process. In general, physics regarding the laser interaction with a material involve the coupling of the photons into the available vibrational or electronic states, depending on the photon energy. The excitation of the electrons promoted by their absorption of the photons from the laser results in the generation of heat, followed by the Beer Lambert law [44], defined in section 2.3.1.2. This law states that the amount of light absorbed by the material depends on the absorption coefficient (α), the scattering coefficient, the material thickness (e), and the irradiance of the laser source [43] (see Fig. 2. 4). Therefore, the absorptance (A) is the ability of a material to absorb part of the incoming laser light through different mechanisms. The laser radiation not

absorbed or scattered by the material can either propagate through the material and exit the sample from the opposite face (which defines the transmittance, T) or back through the incident face (defining the reflection, R). Both T and R have a direct (T_G and R_G) and diffuse (T_D and R_D) component, the latter derived from the scattering effects.

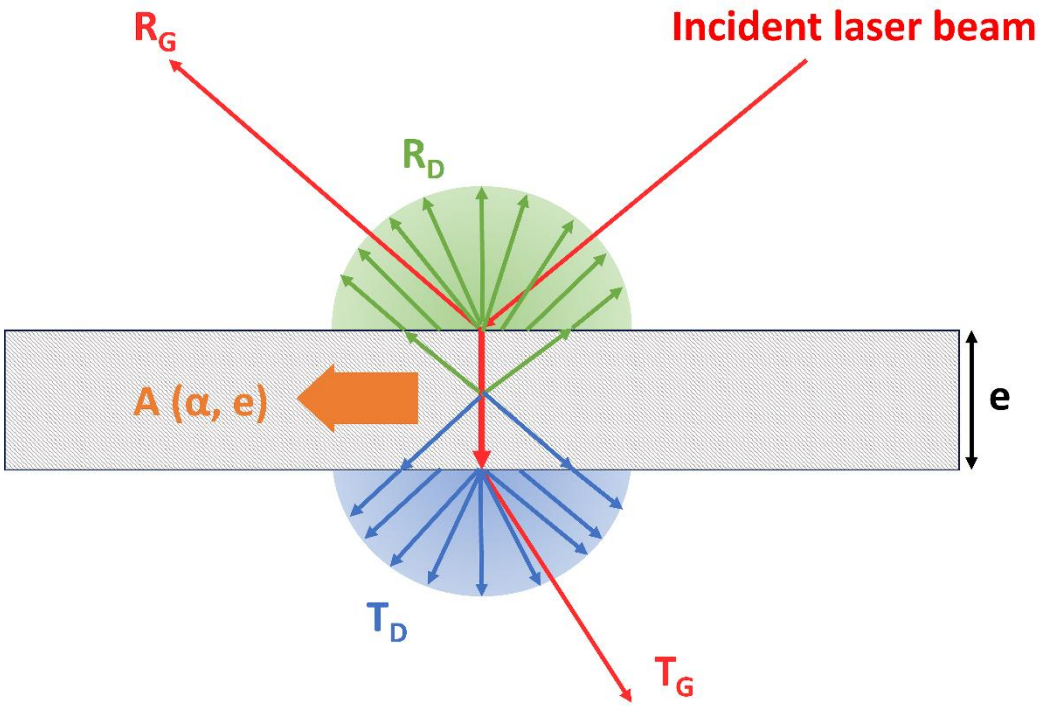

Fig. 2. 4 Schematic representation of the fundamental mechanisms occurring during laser-material interaction

The absorbed energy induces the heating of the material, which drastically increases the surface temperature on a small area directly related with the laser spot, which ranges from few microns to hundreds of microns over a relatively small time defined by the pulse duration (τ). The heating effects lead to a melting or vaporization of the material, and hence the ablation occurs. During the transition from solid to gas state of the material, a plasma plume is formed [44]. The ablated volume is related with the penetration depth and the laser spot radius (ω_0). The penetration depth can be determined by both the optical (l_α) and thermal penetration (l_{th}). The dominance of one of them over the other is determined by the nature of the ablation mechanism. The material is ablated through melt expulsion, vapor pressure and the recoil of light pressure, followed by a quick dissipation of the heat that occurs in the bulk material, which form a recast material zone around the ablated area. The drawbacks concerning the heat dissipation (i.e. the fast increase of the thermal effect on the bulk material) strengthens the need for using ultrafast laser pulses to ensure high quality micro structuring without thermally damaging the surface.

Depending on the irradiance (among other parameters, as it is going to be discussed in section 2.3.1.2), the laser is capable of inducing damage onto the surface. The irradiance value from which the ablation is visible is called the *threshold* [45] or *ablation threshold* [46] and material is thereby removed from the surface.

2.3.1.2. Ultrafast laser systems: focus on the ablation of polymers

Among the pulsed lasers, the ultrashort pulse laser systems are those which emit pulses with τ values below the nanosecond range, and they are currently available with pulse widths from a few to several ps [47]. These particular systems have attracted the attention to the researchers due to several characteristics such as the capability to ablate difficult materials, such as the ones that are transparent to certain wavelengths, and the promotion of the cold ablation, i.e., the capability of ablating material with reduced heat affected zones by the direct transformation of the solid into plasma [48], among others. Several publications have shown that CW and short pulses, contrary to the ultrashort pulses, could not process certain material that were transparent to the wavelength of the corresponding lasers system [49, 50, 51]. This happened due to the ablation mechanisms that governed the laser-material interaction for the corresponding pulse duration and/or pulse irradiances.

The ablation mechanisms of a surface can be identified as linear and non-linear mechanisms, more commonly known by the photon absorption capability of a medium (linear and nonlinear photon absorption). These mechanisms are independent of the pulse duration, but their respective significance is stronger depending on this pulse characteristic, the material, the pulse energy, and the wavelength [52], especially the former and the latter.

- Linear mechanisms

As it was previously introduced, the linear absorption is a process governed by the Beer-Lambert law, which relates the depth of the absorbed radiation, z, by the eq. (1).

$$I(z) = I_0 e^{-\alpha z} \tag{1}$$

Where I(z) is the laser irradiance at depth z, I_0 is the incident laser irradiance, and α is the photon absorption coefficient. Additionally, the ablation depth, d, which defines the precision in the

structure depth when subjected to purely linear mechanisms, can be calculated by the eq. (2) [52].

$$d = \frac{1}{\alpha} ln\,(\frac{I}{I_0})$$

(2)

The material absorbs the laser radiation linearly. The linear ablation mechanisms are related to the single-photon excitation of the electronic (in the UV and visible (VIS) wavelengths) or vibrational transitions (IR) [53]. As the ions of the lattice subsystem commonly do not absorb the laser energy in this regime, it is usually absorbed by the free electrons. In fact, when the free electrons get hit with the photons from the laser beam, the energy is absorbed and transferred to the lattice by collision through inverse bremsstrahlung process, which breaks the chemical bonds [54]. This excitation induces heat with longer pulse durations, following the Beer-Lambert law from eq. (1), with a consequent raise of the temperature and melt of the surface [44]. Therefore, it can be said that the linear regime involves a photothermal process due to the heating of the surface. This ablation mechanism is typical in the short pulse and longer laser interactions with the surface (pulse durations longer than 10 ps). In fact, in these pulse durations, considering the processing of a polymeric material, in order to promote the linear ablation, the photon energy should be larger than the energy bandgap associated to the material, which in these cases, they are restricted to wavelengths in the UV range [55].

- Non-linear mechanisms

As it has been explained, the linear ablation involves the absorption of photons. However, this regime mainly depends on the nature of the material, the wavelength of the incoming laser light and its irradiance, among others. Some materials, depending on the pulse duration, show relatively low absorption capabilities to certain wavelengths (i.e., the transparent materials to the NIR wavelengths, for example), which is translated into a null effect of the photothermal processes on the ablation of the material. Therefore, laser systems with short or longer pulse durations (from ns to CW) are usually not capable of processing these specific materials at certain wavelengths. On the other hand, laser systems with pulse durations in the ultrashort ranges (lower than 10 ps) have demonstrated their capability to ablate these materials due to a second ablation mechanism that occur during the interaction in such a small span of time. Other than the photothermal absorption, a photochemical effect occurs (both processes combined are known as photophysical process), specially at higher irradiances [56]. Unlike the photothermal process, in the photochemical there is (almost) no temperature change, but a direct and very quick material transition from liquid to vapor states

occurs. The duration of the pulse is shorter than the relaxation time (electron-to-ion propagation time, among others) and also there is no heat diffusion phenomenon occurring during the interaction time between the laser and the surface [57]. Therefore, the heat diffusion and the residual heat accumulated (which is furtherly explained in section 2.3.2) on the material is reduced and the quantity of the remolten material is reduced, as well as the **Heat Affected Zone** (**HAZ**, defined as the zones of the material that has not melted but the microstructure and base mechanical properties has changed due to the laser interaction [58]) is relatively decreased. This thermal effect mitigation is the reason the ultrashort laser ablation is also known as "cold ablation". Within the nonlinear mechanisms, several types of ablations can be observed. The typical high peak power of the ultrashort pulses focused on a relatively small volume promotes **multiphoton ablation processes** [56, 59]. It produces seed electrons which can multiply due to the avalanche ionization, which may promote the plasma formation [60], specially at higher irradiances. In fact, avalanche ionization, which can generate high electron densities, make highly transparent materials strongly absorbing, inducing an *optical breakdown*, alongside the previously mentioned plasma formation [53]. As explained by Vogel et. al. [61], the nonlinear propagation effects are more pronounced the shorter the pulse duration and the higher the irradiance of the laser, producing a more important optical breakdown on the material.

Rahaman et. al. [62, 63] observed the optical properties modification of a PP sample after the incidence of femtosecond laser pulses. They stablished different ablation regions depending on the pulse energy based on the transmittance variation. At lower pulse energies, denoted as the Region I, the absorptance, reflectance and transmittance values were constant with the fluence, which corresponded to a linear ablation region that did not damage the PP. As the pulse energy increased, these mechanisms started to change (the reflectance and transmittance decreased while the absorptance increased) within the Region II, in which the nonlinear absorption was observable. In fact, in [64] they observed that, the higher the pulse energy, the lower the transmittance and reflectivity, and hence the absorptivity of the PP sample increased from 30% to almost 90%. At the highest pulse energies (Region III), the absorptance suffered a sudden decrease, probably due to anomalous mechanisms that created new phases that changed the reflectance and transmittance values.

In short, while the short pulses, due to the pulse duration being within the range of the relaxation time, promote the linear ablation mechanism known as the photothermal process, the ultrashort pulses promote the photophysical ablation (photothermal and photochemical). The former usually leads to higher HAZ, transmits the heat through thermal conduction and generates more recast

material and accumulated debris on the surface, whereas the latter promotes the cold ablation that represents the absence of HAZ and provides better quality structures with lesser accumulated material and debris (see Fig. 2. 5).

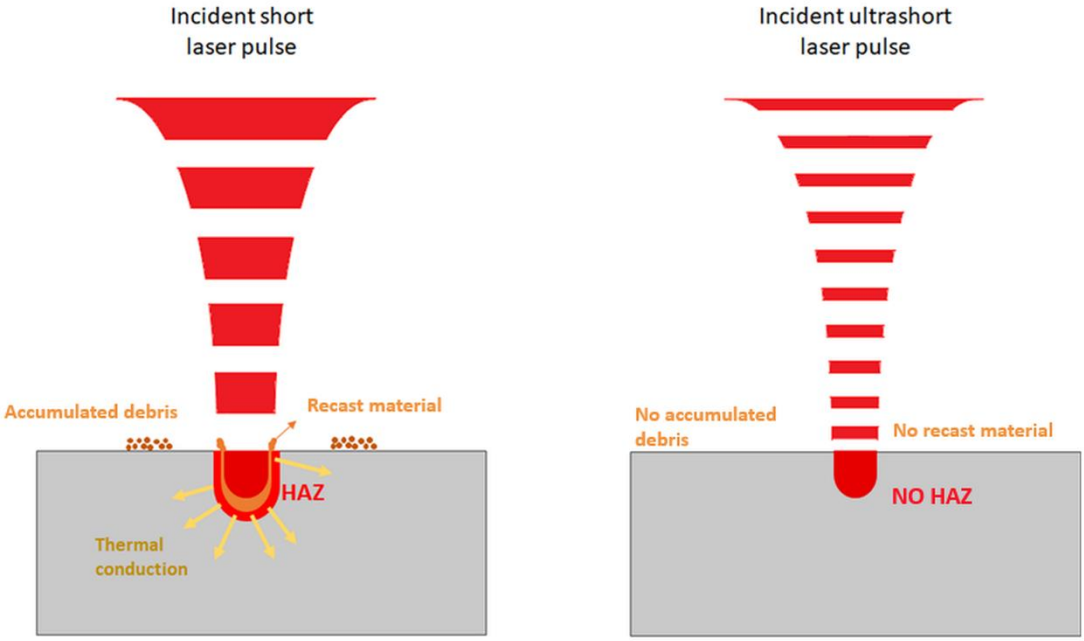

Fig. 2. 5 Schematic representation of the most basic ablation phenomena that occurs with short (left) and ultrashort (right) laser pulses.

Another aspect that affects the ablation mechanism during the ultrashort (and longer) pulse interaction with the material is the rugosity of the surface. In several studies [65, 66, 67] it was demonstrated that these features are capable of modifying the absorption capability of the material and reducing the energy required to trespass the corresponding ablation threshold subtype and damage the sample. This reduction, occurring mainly due to the rugosity, morphologic and optical effect is called the incubation effect. This effect occurs typically when several pulses reach the sample at the same affected area. The first pulses may produce a change in the surface, which enhances the incubation effects and thereby the next pulses produce a bigger impact on the ablation process. Therefore, for the laser ablation process, the incubation may be defined as the thermal influence of the previous laser pulses onto the ablation process of the following pulses [68].

2.3.2. Key parameters for the laser ablation process

When referring to the ablation process, the laser-material interaction is different for each type of laser source and nature of the material. Hence, the user must tune the different laser parameters accordingly to these considerations in order to obtain the desired results.

The **wavelength** (λ) is provided by the laser source, and in many commercial Diode Pumped Solid State (DPSS) and fibre lasers, it can be switched between the fundamental value and its corresponding higher order harmonics. Depending on the wavelength, the absorption capability of the material may change (and thus the ablation process). In pulsed laser system, different parameters concerning the rate at which the energy exits the source can be tuned. The main magnitudes that the users can select and control are the **average power** (P_{av}), one the most important parameters that can be used to calculate several laser parameters such as the **peak power** (P_{peak}, see eq. (3)), or the **pulse energy** (E_p from now on, see eq. (4)), both of which are furtherly used to determine other values.

$$P_{peak} = \frac{P_{av}}{\tau \, f_{SP}} \tag{3}$$

$$E_p = \frac{P_{av}}{f_{SP}} \tag{4}$$

In the previous equations, f_{SP} is one of the laser parameters that are exclusively related to the pulsed lasers, known as the **pulse repetition rate**, i.e., the frequency at which the pulses are emitted, which is also one of the most important laser parameters to consider. It is also the inverse of the temporal spacing between the pulses. According to the eq. (3) and (4), for a fixed average power, the higher the repetition rate, the lower the E_p.

Aside from the E_p, the **fluence** (F) is usually used as an important parameter to determine the different ablation regimes. For a Gaussian profile, it can be calculated with the E_p and the **spot radius** (ω_0, obtained at a distance of $1/e^2$ from the maximum irradiance [68], which rarely coincides with the diameter of the ablated crater, D_c) by the equation (5):

$$F = \frac{E_p}{\pi \omega_0^2} \tag{5}$$

As indicated before, this equation is a particular example for a pulse with a Gaussian profile (Fig. 2. 6 a). This profile is defined by a Gaussian irradiance curve (I(r)), whose value depends on the location from the center of the beam (where the peak irradiance is located). As the location gets further away from this center, the irradiance decreases. However, there exist other types of beam shapes. The top-hat shape (Fig. 2. 6 b), for example, differs from the Gaussian in the irradiance profile, which in this case remains approximately constant both at the center and at the extremes. Lastly, some authors [69, 70, 71] have worked on the obtention of different beam shapes by multibeam interference, or by amplitude and wave front shaping in order to modify the irradiance profile inside the pulse and thereby generating customized shaped structures. Ackermann et. al. used the latter [72] to generate irradiance profiles with a shape of snowflakes and performed a complete study regarding the quality of the ablated structures (in terms of roughness, homogeneity or shape accuracy). Therefore, a more general fluence calculation would be expressed by the eq. (6).

$$F = \frac{E_p}{A_s} \tag{6}$$

Where A_s is the area of the spot, regardless of the shape and irradiance profiles.

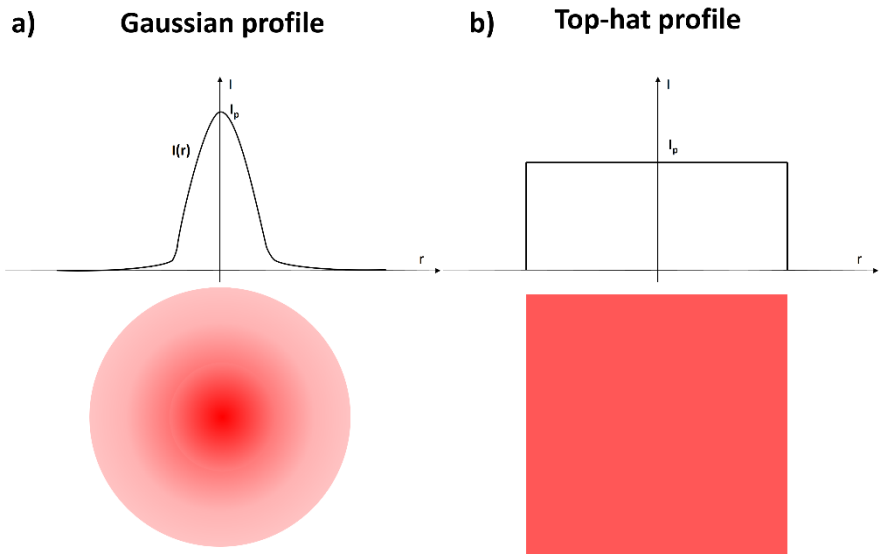

Fig. 2. 6 Beam shaping of a) Gaussian profile and b) Top-hat profile with a squared shape.

Regardless of the shape of the beam, several ablation regimes can be observed depending on the fluence (or on the E_p as well, as it is directly proportional to the former), as explained in the previous

section. In this work, due to the nature of the pulse emitting modes used, instead of the fluence, the E_p ablation threshold is going to be used.

When the ablation process involves the overlapping of pulses, the **scanning speed** of the scanning system (v_s) has to be considered, which determines the position of the next pulse by the equation (7), which corresponds to the **distance between pulses**, d_{pp}, or pitch:

$$d_{pp} = \frac{v_s}{f_{SP}} \tag{7}$$

The higher the overlap value, the lower the d_{pp}, and the more pulses accumulated over a certain area. Hence, the higher the overlap, the stronger the incubation effect, the ablation rate may increase but the processing time increases accordingly. Therefore, as previously stated, a fair trade-off should be established in order to optimize the process in terms of removed volume and processing time.

As it was mentioned before, after the incidence of a laser pulse onto a surface, the sample suffers a temperature raise that is transferred to the bulk material through heat conduction and after a period of time, the surface cools down again. However, if a second pulse is emitted onto the same spot within a time span lower than the time needed for the surface to cool down, the heat gets accumulated into the surface and the temperature of the material raises to higher values [73, 74] This mechanism is called **heat accumulation**, and it is dependent on the laser repetition rate and pulse overlap (heat accumulation by subsequent pulses, HAP), and also on the number of scan levels (heat accumulation by subsequent scans, HAS). This mechanism leads to and overall decrease of the processing quality [75, 76, 77] due to the excessive temperature increase to values higher than the melting point of the material (see Fig. 2. 7), which leads to undesirable thermal effects on the sample such as changes in the properties of the material, thermal stresses or the melting and solidification of the material. Therefore, in order to avoid these defects (depending on the application, i.e., if maximizing quality or throughput is desired), the laser parameters should be carefully selected.

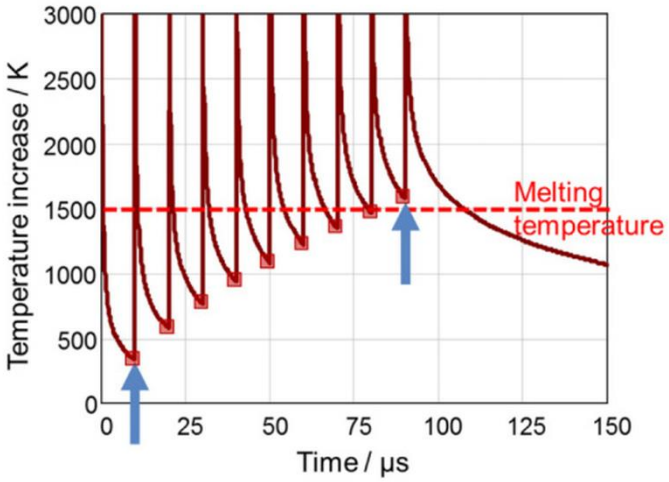

Fig. 2. 7 Example of the temperature increase due to the heat accumulation after the incidence of several pulses (figure obtained from [74])

The **residual heat** is referred to as the remaining heat accumulated by the surface after the incidence of a pulse. The absorbed energy by the sample produces a heat increase that stays on the surface and leads to the heat accumulation [75]. Therefore, the residual heat is the main phenomenon that enhances the heat accumulation of the material.

As it was stated before, PP is an interesting polymer due to its relatively high melting point (for homopolymers, 160 ºC approximately [78]), which is low compared to a conventional steel sample (1500 ºC, approximately [79]) and even aluminum (around 660 ºC [79]). Therefore, to avoid or inhibit the reach of the melting point, several strategies can be selected, i.e., working with lower repetition rates to provide the surface with more time to cool down, which affect negatively on the throughput, or working with a different pulse emitting mode from the conventional Single Pulse mode.

2.3.3. Laser ablation with the burst mode

The laser pulse emitting mode denoted as **Burst Mode (BM)** is in fact a train of pulses spaced temporally in a low amount if compared with the individual reference pulses, specified by the emission of the amplifier, and usually known in laser operation as **Single Pulse mode (SP)**. The BM operating mode provided in several laser systems selects a number of pulses, n, from the seed source with a pulse picker, which form a group denoted as Burst (Fig. 2. 8). The seed generates

pulses separated by a period (T_{seeder}) defined by the repetition rate of the oscillator (eq. (8)). In the SP mode, the individually amplified pulses are separated by the amplifier repetition rate (f_{SP}), whereas in the BM, the amplifier emits the bursts separated by the **burst repetition rate** (f_b).

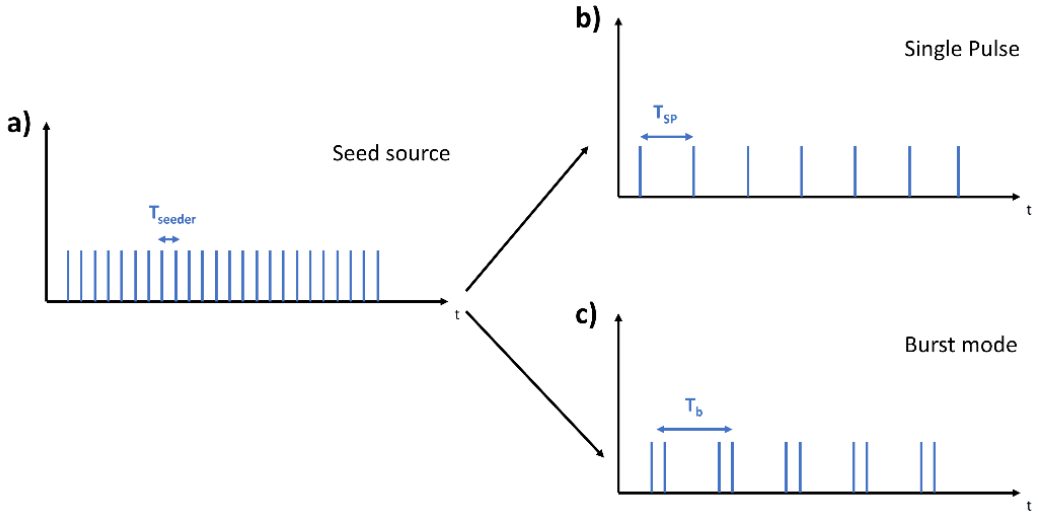

Fig. 2. 8 a) Seeder pulse emission, b) SP mode and BM mode

$$T_{seeder} = \frac{1}{f_{seeder}} \tag{8}$$

The difference in the pulse-to-pulse temporal distance between both pulse emitting modes may provoke a high impact on the outcomes and effects on the ablation of a sample. Over the past 20 years, different studies regarding the ultrafast laser processing of different materials with pulse bursts have been reported [80, 81, 82, 83, 84, 85, 86, 87, 88, 89, 90, 91, 92, 93, 94, 95], most of them focusing on the laser ablation of metals or semiconductors.

Neuenschwander et. al. has reported an extensive study in this field [84, 85, 86, 87, 88, 89, 94]. In general, they have studied the effect of using SP or BM on the ablation of cavity-like structures on different metals and semiconductors. In some works [86, 87, 88], they have assessed the influence of each pulse mode in the ablation efficiency (defined as the removed volume per unit of energy, as it is going to be explained later in this thesis) in order to identify the peak fluence value at which the maximum throughput is achieved. In [87], they performed several experiments on copper and silicon with ultrashort pulses (in the range of picoseconds) at wavelength values of 1064 nm and 532 nm. They developed squared cavities with SP and BM ensuring that each pulse has the same energy. Therefore, while keeping the repetition rate fixed, they adapted the number of scan levels

(or number of machined layers) so that the number of total pulses that reached the sample was the same in every case (the number of scan levels of the SP was n times higher than in the case of the BM with n pulses inside the burst). They thereby observed that at 1064 nm in silicon, the overall efficiency increased with n (up to 8) and identified a fluence value at which the efficiency reached its peak (from which further fluence increase would lead to a throughput reduction). On the other hand, in copper at 532 nm, they concluded that the BM (with up to 3 pulses) was not more efficient than the SP. In [86], they assessed the influence of other parameters on the efficiency of the ablation process of steel, copper, silver and gold at wavelengths of 1064 nm. Other than the effect of varying the number of pulses inside a burst, the **pulse-to-pulse temporal distance** (Δt) was also varied and determined that, depending on the material and the number of pulses inside a burst, decreasing this distance could have advantageous or disadvantageous outcomes, e.g., 3-pulsed bursts with lower Δt values were more efficient in copper, but with 2 pulses per burst, higher Δt showed better performance. Aside from the obtention of maximum efficiencies, they also assessed the influence of heat accumulation of the target sample in the ablation process with bursts of femtosecond pulses [88], and also measured the residual heat and observed its impact on the results [87]. In [88], they provided useful insights regarding the high impact of the heat accumulation in the BM processing of carbon coated surfaces. In fact, they underlined the key role of the heat accumulation on the increased efficiency of the ablation process with the BM when compared to the SP.

The use of bursts has gained an increased attention due to how it affects the heat accumulation and hence the overall quality and efficiency of the ablation process when compared to the SP mode. Bonamis et. al. [96] recently proposed a two-way ablation mechanism regarding the ablation process with burst pulses in the range of GHz. They specified that the first stage involved the heating of the material to a liquid state by accumulation effects, followed by a second stage in which the ablation process was effective on the hot surface. Neuenschwander et. al. [84] reported a surface quality reduction (for a steel surface) when an increased number of pulses inside a burst was considered, as the heat accumulation was higher than with the SP mode. More specifically, they observed that the fluence window at which a good quality surface is obtained was narrower (and lower) as the number of pulses inside the burst increased. Recently, Le et. al. [97] reported a complete comparison between the SP and BM (in the latter with Δt values corresponding to MHz repetition rates) on the ablation efficiency of copper and stainless steel, and the heat accumulation and residual heat effects on the throughput. They demonstrated the potential of the BM on fulfilling

the industrial requirements and observed better overall results with BM and lower overlap values (30% in copper and 60% in steel).

Metzner et. al. developed crater-like structures on CoCrMo alloys [81] and squared-like structures on silicon and cemented tungsten carbide [82] and pointed out the advantages of using the BM. They concluded that the structure depth obtained with an 8-pulsed burst was 20 times higher with the same processing time than considering the SP mode. Recently, Gaudiuso et. al. [95] studied the SRR of single pulses and THz burst pulses on silicon using 200 fs-pulses, supported by theoretical analysis (Two-Temperature Model, TTM). They stablished a parameter window where the BM was more efficient than the SP mode, more specifically, when applying 2 and 4 pulses per burst with 2 THz intra-burst frequency.

Despite the increased publications regarding the ultrafast ablation of metals and semiconductors with pulse bursts, few reports have studied the femtosecond pulse burst influence on the ablation of polymeric materials [98] and, more specifically and to the author's best knowledge, none focused on PP samples.

2.4. Surface functionalization via Laser Surface Texturing

The laser technology has witnessed a significant increase in terms of use and applicability in a growing number of different fields that englobe the health (ophthalmology, surgery, etc.), engineering, and security/defence (weaponry, guidance, etc.) sciences [99]. The laser technology proved to be a useful tool for its capability to modify the topography or chemical nature, and thereby the superficial properties without modifying the bulk properties of a material. This technique is known as **surface functionalization** and has proven to be an effective and simple way of providing or enhancing different properties of a material. More precisely, the ultrashort pulses could be considered to be a better option among other laser sources due to the highly focused interaction with the material into a relatively small volume and hence has a minimal impact on the bulk properties of the material.

The surface functionalization via laser structuring (more commonly referred as **Laser Surface Texturing**, LST) covers a wide range of applications [100]:

- Advance wettability control:

Surface wettability is an intrinsic property of a material, and a fundamental property that governs the interaction between a liquid and a solid. It revolves around the modification of the surface energy both physically and chemically to repel o attract a liquid droplet more easily [2]. Nowadays, understanding the changes in the wettability due to topographical modification of the surface remains an important topic to develop advance materials that combine good inherent properties with enhanced wetting capabilities, which vary depending on the application.

The wettability is going to be the focus of this thesis, and it is going to be explained in more detail in section 2.5. The wettability (or more specifically, the surface energy, as it is going to be explained in section 2.5) can be used as a basis for several applications, two of which are explained below:

- Icephobic surfaces

The ice formation on airplanes during the flight under specific atmospheric conditions has encouraged researchers to develop surfaces that either inhibit the formation of ice or facilitates its elimination through surface modification. The formation of ice in the wings, especially in the leading edge, is considered one of the most hazardous scenarios during the airplane flights, due to the modification of the surface topography and morphology, which leads to a consequent loss of the aerodynamic properties of its geometry (the flow around it would become turbulent, and the boundary layer could be broken) and a consequent loss of energetic efficiency. Other than in aerodynamic applications, in air conditioners and refrigerators the ice formation leads to an unwanted increase of the power consumption [101]. Vercillo et. al. [102] proposed design rules that a metallic laser textured surface should fulfil to prevent the ice accumulation on the surface. For example, they established that the dimensional range of the peak-to-peak width between structures should be at least one order of magnitude lower than the mean diameter value of the ice particles in the atmosphere (see Fig. 2. 9 b). Furthermore, it cannot be much smaller, as the particle-surface contact area would not be small enough to reduce the adhesion forces (see Fig. 2. 9 a). This way, by a combination of micro and nanostructures, it can be ensured that the particles cannot fully enter the gaps of the microstructures and get trapped, and an air layer is formed between the particle and the surface, reducing the adhesion forces.

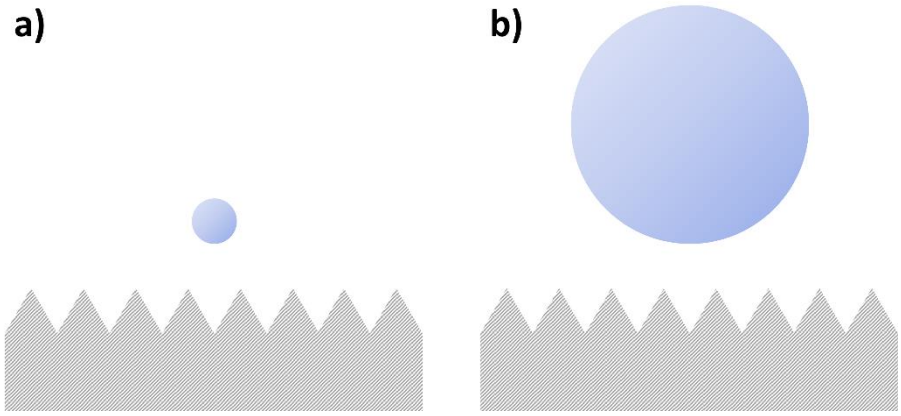

Fig. 2. 9 a) Peak-to-peak distance similar to the particle diameter and b) peak-to-peak distance of an order of magnitude lower than the diameter

Milles et. al. [25] studied a more active method for the accumulated ice elimination on a laser textured surface through an electromagnetic shaker inside a wind tunnel. They performed these tests on aluminium samples with several LST methods that included Direct Laser Writing (DLW), Direct Laser Interference Patterning (DLIP, which involves the interference of several partial beams that were previously split from the source beam, and were overlapped and focused on the same spot, generating customized beam shapes [103, 104, 105], and observed that the best results were obtainable with DLIP structures with periodic structures with a periodicity of an order lower than the mean particle diameter. Additionally, other authors observed that, in general terms, LST provided an improvement to the anti-icing capability of aluminium surfaces with DLW with femtosecond lasers. Volpe et. al. [106] observed that the water (ice) accumulation on pillar-like structures was reduced for samples stored at -20ºC. Prime et. al. [107] showed promising results regarding the ice adhesion reduction of aluminium surfaces with parallel groove-like structures. However, the icephobic surfaces of purely laser structured surfaces (without any coating) is still being studied to date.

- Antibacterial applications

The deposition of undesirable substances on the surface is called surface fouling and may affect the functionalization of the surface negatively [108]. The biofouling, more specifically, is referred to as the bacterial deposition on the surface (and its consequent spreading by multiplication), which contribute into the health degradation of several key elements of vehicles, or into their operating throughput [109]. More specifically, in the packaging industry, in which PP is considered to be one of the most used polymers, the accumulation of this microorganisms may lead to the contamination

of several elements such as food or oil. Therefore, in order to reduce or eliminate the biofouling, with the LST a reduction and control of the bacterial adhesion onto the surface is desired.

Some publications regarding this topic are centered on the LST of surfaces to prevent the bacteria retention by reducing the adhesion [109, 110]. Rajab et. al. [109] managed to reduce the number of bacteria retained in the surface of a Ti-6Al-4V metal by the generation of surface structures in both micro and nanometer range, with the addition of chemistry modifications during laser ablation. Lutey et. al. [110] assessed the bacterial retention capabilities of different topographies on stainless steel samples. More specifically, they compared the retention of two types of bacteria (i.e., *E. coli* and *S. aureus*) on unstructured surfaces and textures based on both micro and nanometric features. They observed that, depending on the type of bacteria, some patterns were better than the others, but the overall efficiency of the nanostructures were better.

Another type of antibacterial surfaces revolves around the elimination of this microorganism through the puncturing of their membrane [111]. Based on the nanostructures found in cicadas or dragonfly's wings, some authors [112] have tried to model the geometry and dimensions in order to provoke the bacterial membrane to rupture and thus killing it as soon as it reaches the surface. However, the membrane thickness of each bacterium is different, and thus the selected topographical parameters may not work in every case. This approach also depends on the adhesion forces of the bacterium onto the surface.

- Tribological applications

The friction reduction between the contact of two surfaces has shown an especial interest due to the highly impactful damage it generates on automotive or hydraulic elements, etc. The tribological performance enhancement has been shown to not only protect key elements of automobiles, but also reduce the energy consumption [113]. Several authors have studied the tribological enhancement of surfaces on which crater-like structures have been developed with LST. Ezhilmaran et. al. [114] studied the effect of the microstructure density on the coefficient of friction, performed by a femtosecond laser in a piston ring. They observed that the higher the density of the craters, the lower the coefficient and, therefore, the better performance. However, they also concluded that further increasing the density could result in an adverse effect on the friction reduction. They stablished a density of 16% as the optimum value, as the maximum friction reduction was achieved (the coefficient of friction went from 0.13 in a non-textured surface to 0.05). Li et. al. [115] investigated the lubrication behaviours of room temperature gallium-based liquid

metals for different loads between steel-steel plates. They also assessed the LST effect on the lubricant performance based on the measured friction coefficient. More specifically, the developed crater-like textures with different crater densities (textured area ratios of 5%, 15% and 35%) and observed that the LST improved the lubricant performance, especially with 15% densities. Therefore, LST has shown great enhancements regarding the tribological performance, especially regarding the friction coefficient reduction.

- Aerodynamic/hydrodynamic applications

Nature is a wide source of information regarding the enhancement of surface properties. For example, the sharks are capable of swimming at relatively high speed thanks to their skin. In fact, their skin is filled with well-designed micropatterns that have proven to improve the hydrodynamics inside the water [116]. Fig. 2. 10 shows an image of the microstructures of a great white shark skin [117].

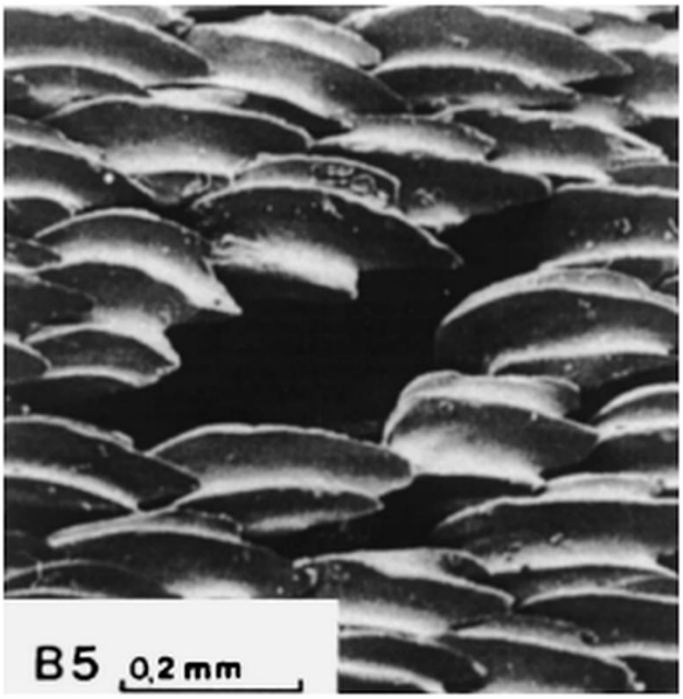

Fig. 2. 10 Great white shark skin microstructure (image obtained from [117])

Some authors have tried to replicate these surfaces onto several elements such as the ship's hull [117]. These surfaces have attracted both the aircraft and marine transportation interest, due to the relatively high weights they carry during the transport. The capability of reducing the drag forces can lead to important fuel savings and hence the enhancement of a more sustainable operation due to the reduced emissions and environmental impact. Therefore, during the last decades, several

works have been published regarding this topic [118, 119, 120, 121]. Rong et. al. 122] developed laser textured surfaces containing bioinspired micro and nanostructures and observed that the drag reduction ratio (in %) was reduced with the increase of the fluid velocity for a flat aluminium-magnesium alloy surface, and also concluded that the patterned surfaces were able to reduce even further that value. Bixler et. al. [123] developed shark-skin inspired riblets of different geometries and dimensions and provided of a deep insight into the effect of the riblets on the pressure drop. They also studied the effect of the riblet height, the aspect ratio and surface roughness on the drag reduction, and also assessed the flow type provided by each riblet (laminar or turbulent). More specifically, they stablished that the considered riblets were able to pin the turbulent vortices and reduce the shear stress from this turbulent flow.

- Aesthetic applications

Other applications involve the use of LST to modify the aesthetic of a surface, for example. By changing the roughness of a metallic surface, it is possible to change the colouring of the surface for optical applications [124]. Therefore, the overall objective is to modify the surface roughness to produce a visual impact.

2.5. Surface wettability

The physics regarding the wetting of a liquid droplet on a solid has attracted the attention of many researchers over the past decades [125, 126, 127]. The wetting phenomenon is the capability of a droplet to spread onto a surface as soon as they contact with each other. Considering a water droplet, depending on the nature of the solid surface, it can be more hydrophilic (the droplet trends to spread on the surface more easily) or hydrophobic (the surface prevents the droplet from spreading). This property is defined by a parameter known as **Contact Angle** (CA), which is the angle that a liquid forms with a solid (Fig. 2. 12) or another liquid surface during the spreading (advancing) or recoiling (receding) process, or after reaching an equilibrium state. The concept of the CA was proposed by Young [128], and it was defined as a relationship between the interfacial tension (γ) of the solid (S), liquid (L) and vapor (V) phases (see eq. (9), where θ_Y is the Young CA, γ_{SV}, γ_{SL}, and γ_{LV} are the solid-vapor, solid-liquid and liquid-vapor interfacial tensions, respectively). Young proposed this equation for smooth, homogeneous surfaces.

$$cos(\theta_Y) = \frac{\gamma_{SV} - \gamma_{SL}}{\gamma_{LV}} \quad (9)$$

A surface is **hydrophobic** if the CA is higher than 90º, and **hydrophilic** if is lower than 90º. Moreover, inside the hydrophobic surfaces, a more specific type of surface of overall great interest can be identified. These are known as **superhydrophobic surfaces**, which are widely known by their ability to self-clean and stay dry [129]. They present very low surface energies and provide CA values higher than 150º. However, this value alone could not be enough to ensure that the surface is superhydrophobic. A second parameter should be taken into consideration, known as CA Hysteresis, as it is going to be explained later in this section.

The CA a droplet forms with the surface is directly related to the **surface energy**, i.e., the combination of attractive and repulsive forces that pull or rejects the liquid from the surface. Another definition would be the work necessary to increase the solid-liquid contact area [130]. The higher the surface energy, the higher the attractive forces and the lower the CA, whereas, on the other hand, the lower surface energy, the higher the CA [131]. The surface energy can be expressed by two components, i.e., the dispersive and the polar components, and the wettability of a surface depends on the combination of these components both in the sample and in the liquid. Surfaces with high dispersive components tend to attract liquids with dispersive molecules and repel the polar liquids, and vice versa with high polar surfaces (see Fig. 2. 11). Therefore, the CA modification revolves around the change of the polarities of the molecules from the surface (i.e., modifying the polar and dispersive component) by either altering the chemistry of the surface or by changing the contact area by providing the sample with topographical changes via LST, lithography, etc.

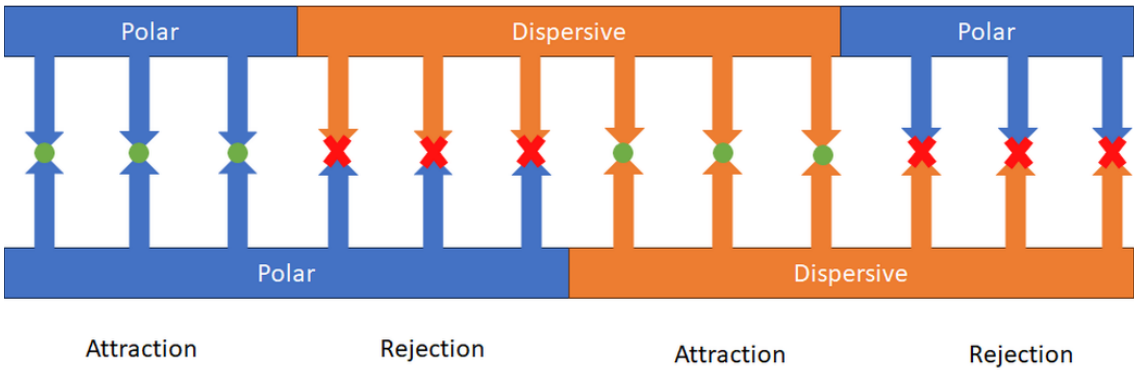

Fig. 2. 11 Interaction between the polar and dispersive components between the solid and the liquid

Another important factor that affects the wettability of a liquid on a solid surface is the **surface tension** (**σ**), which is defined as the tendency of the liquid to reach the equilibrium state at the minimum contact area possible. Another definition is the energy necessary to apply into a liquid to break its resistance to maintain the minimum contact area. This property varies for every liquid, and the wettability revolve around a complex combination of these energies and other factors (topography, chemistry, etc.).

The ability to control the wettability of a certain material can provide of numerous applications such as self-cleaning surfaces [127], water-oil separation [132], etc. Chemical modification involves the surface energy alteration with the use of a more hydrophobic or hydrophilic material on top of a surface [2]. Physical modification by the change of surface topography and morphology can also control surface energy and thus surface wettability. In the latter approach, the use of micrometric and/or nanometric structures by laser texturing has proved the feasibility of this method to successfully control the surface wettability [133, 134, 135]. Several studies have been reported for the past decades [136, 137, 138, 139] regarding the enhancement of the hydrophobicity over a wide range of materials with solely the topographic and morphologic modification of their surfaces. Moreover, not only the dimension value has proved to be able to change the wettability, but also the geometrical shape of the structures resulted in CA variations. In fact, some shapes showed an enhanced CA increase when compared to others, as shown by Qiao et. al. [140]. They showed that grid-like patterns gave CA values higher than groove and dimple-like structures.

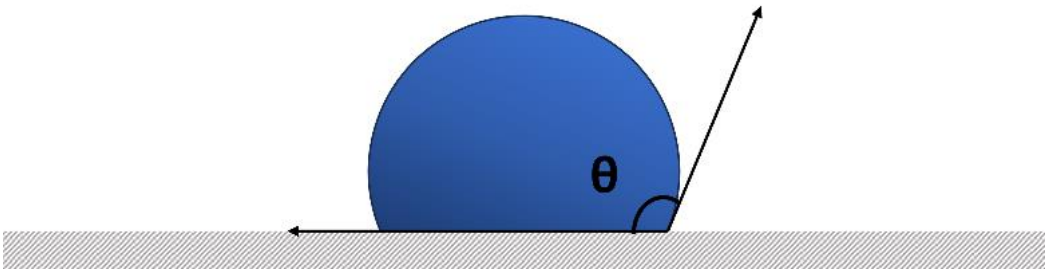

Fig. 2. 12 Definition of the Contact Angle (CA)

Another important parameter that characterizes the wettability of a surface is the **Contact Angle Hysteresis** (CAH), which is defined as the difference between the advancing (maximum, θ_a) and receding (minimum, θ_r) contact angle of a moving droplet on a surface (see the eq. (10) and Fig. 2. 13). This parameter can measure the energy dissipation during the motion of a droplet and appears when inhomogeneities are present in the surface, such as roughness, deformation, contamination, etc. [141].

$$cos(CAH) = cos\ (\theta_a) - cos\ (\theta_r)$$

(10)

The lower the CAH, the more similar the advancing and receding values. This value alone, however, is not enough to describe the wetting behaviour of a surface but must be accompanied by the CA measurement. If the CA is high enough (>90º), lower CAH would imply that both advancing and receding CA are high, and hence, the surface is more hydrophobic. On the other hand, if it is low enough, lower CAH would imply that the surface is more hydrophilic. This parameter helps the CA to ensure that a surface is superhydrophobic. More specifically, the criterion to meet the requirements for this type of surfaces are that the CA must be higher than 150º and the CAH lower than 10º.

Finally, a third CA parameter can be introduced, which also helps determining the superhydrophobic nature of a surface. The **Roll-off Angle** (α) is the minimum angle of inclination needed by a sample for a deposited droplet to start sliding-off the surface (see Fig. 2. 13). In this case, a surface is superhydrophobic if the CA is higher than 150º and α is lower than 5º.

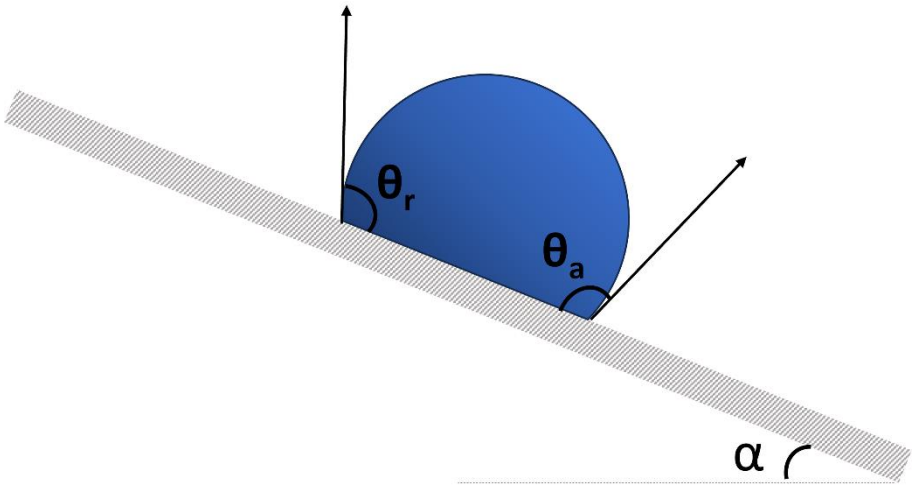

Fig. 2. 13 Schematic view of the advancing and receding contact angles, and the roll-off angle

Due to the difficulty of the physics behind the CAH, most of the studies regarding the understanding and prediction of the wetting phenomena has been centered on the static CA (referred in this work simply as Contact Angle, CA). Several studies [142, 143, 144] used the Wenzel and Cassie Baxter (CB) models to help understanding the CA results. Wenzel et. al. [145] considered the impact of the surface roughness on the apparent contact angle (θ_W), whereas Cassie et. al. [146] considered the situation where the droplet does not fully cover the textures and it floats

on top of air pockets (θ_{CB}). Therefore, these approaches rely on solely the topographical changes on the CA, i.e., the topographic or Wenzel factor (r_f) and the solid/air fractional area, (f_{SL}), both defined later in the section 3.4. Both are related to the Wenzel and CB equations with the eq. (11) and (12) respectively. However, the applicability of these equations is limited to whether the liquid fully penetrates the texture cavities (Wenzel state, see Fig. 2. 14 a), or it sits on top of the pillars with an air pocket below the droplet (CB state, see Fig. 2. 14 b), but they do not consider any possible wetting states in which the wetting is not homogeneous along the contact area.

$$cos(\theta_W) = r_f cos\,(\theta_Y) \tag{11}$$

$$cos(\theta_{CB}) = f_{SL}\, cos(\theta_Y) - (1 - f_{SL}) \tag{12}$$

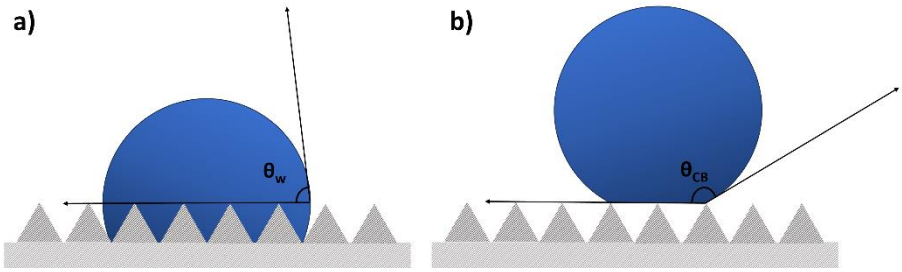

Fig. 2. 14 Droplet on a) a Wenzel state and b) a Cassie Baxter state

Cheng et. al. [147] proposed a CA prediction model based on the minimization of the surface energy reached at the equilibrium state, in which several intermediate wetting states between Wenzel and CB were considered. They reported a numerical method to predict the CAH but also provided an equilibrium contact angle (θ_E) expression for a partially wetted textured surface (see eq. (13)) in which they included a factor (f_w) that defined each of the possible wetting states by adopting a value between 0 (CB state) and 1 (Wenzel state).

$$cos(\theta_E) = [r_f f_w + f_{SL}(1 - f_W)]\, cos(\theta_Y) - (1 - f_{SL})(1 - f_w) \tag{13}$$

Montes et. al. [148] used the modified CB equation to take into account the roughness of the surface as in Wenzel equation (see eq. (14)).

$$cos(\theta_{CB}) = r_f\, f_{SL}\, cos(\theta_Y) - (1 - f_{SL}) \tag{14}$$

A different approach was followed by other authors who published studies regarding the effect of the different topographical modifications on the wettability. Fernández et. al. [149] observed a CA reduction with the increase of the f_{SL} in squared-like textures. Yin et. al. [150]concluded that, based on the simulations regarding the droplet wetting of several pillared surfaces, the pillar/grove height was the most impactful dimension, while the pillar width had little effect on the CA. The author of this thesis [151] observed that the pillar height was in fact the most important magnitude affecting the CA of direct laser textured ABS, and he stablished a relationship between the topographic factor, r_f, and the CA.

Aside from the micrometer structures, many authors assessed the influence of the effect of the nanostructures and/or the combination of both micro and nanofeatures (known as **hierarchical structures**) on the CA. These structures are known for having multiple roughness levels, and also for their overall ability to provide high CA values [152] (see Fig. 2. 15). This can be accomplished by promoting the CB state, due to the low solid-liquid contact area achieved by the formation of an air layer between the droplet and the surface. The introduction of lower scale structures inside higher scale features can enhance this phenomenon by further decreasing the surface energy [153]. However, these textures generally show low robustness and poor wear resistances [129].

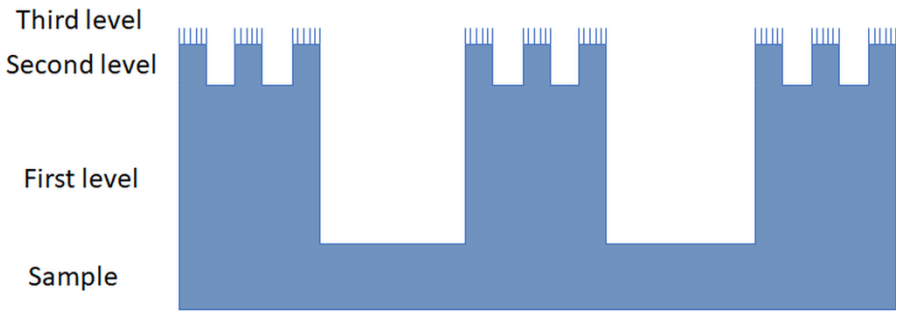

Fig. 2. 15 Schematic representation of the different structure levels inside a hierarchical texture

The wetting states in these textures include the lotus effect and the rose effect [100]. In this case, depending on the presence or absence of water inside the microstructure and/or nanostructure, the wetting states are defined as resumed in the Table 2. 1.

Table 2. 1 Wetting states of the hierarchical structures.

Wetting state	Air inside microstructure	Water inside microstructure
Air inside nanostructures	Lotus effect	Rose effect
Water inside nanostructure	Cassie Baxter state	Wenzel state

An example of hierarchical structures developed by LST are the **Laser Induced Periodic Surface Structures (LIPSS)** [154]. The LIPSS are periodic nanostructures that appear on solids after the incidence of a laser beam onto the surface and is highly dependent on the laser wavelength and polarization [155] (see Fig. 2. 16). By correctly setting up the E_p or the laser fluence, alongside the effective number of pulses per area, the obtention of these nanostructures may be possible. They appear with pulse durations from continuous wave (CW) [156] to a few femtoseconds [157, 158] on metallic [159], semiconductor [160], dielectric [161] and polymeric [162] surfaces. Among the different theories regarding the formation of these nanostructures (plasmon polaritons [162, 163], hydrodynamics [162, 164], etc.), the most accepted theory is based on the interference occurred during the laser ablation between the incident laser beam and the electromagnetic waves scattered on the surface roughness [165].

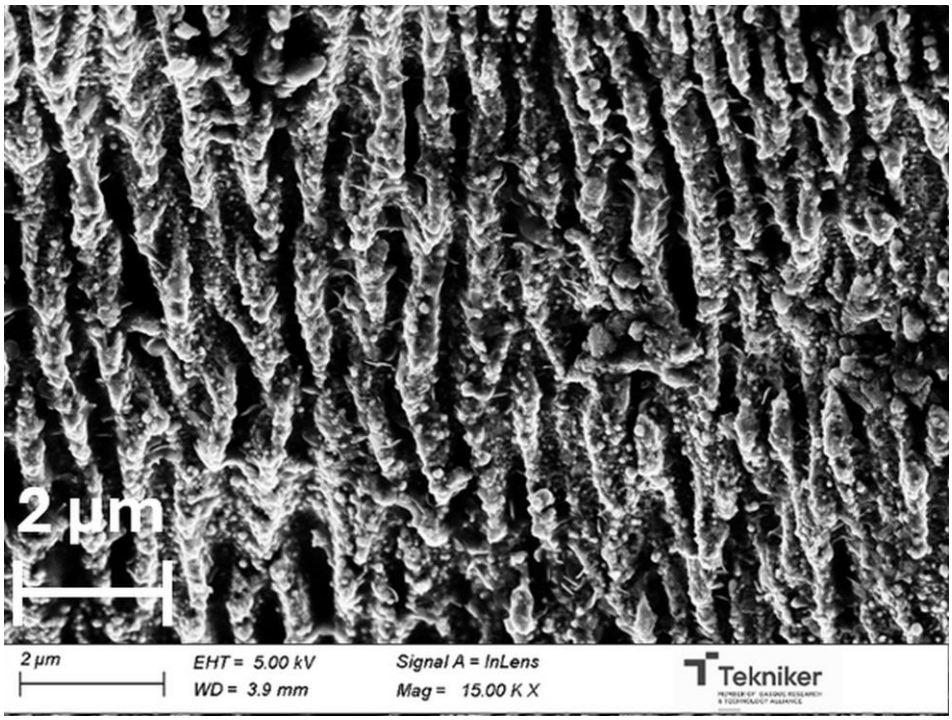

Fig. 2. 16 LIPSS structures on metallic surfaces by fs-laser processing

Several LIPSS types can be identified, depending on the fluence and the effective number of pulses [166], as it can be observed in Fig. 2. 17. However, the two main types are the Low Spatial Frequency LIPSS (LSFL) and the High Spatial Frequency LIPSS (HSFL), which are differenced by the periodic distance between the structures and the direction of these structures. In the former, the periodicity equals a value between half the wavelength and the wavelength itself, and the direction is usually perpendicular to the beam polarization. In the latter, on the other hand, the periodicity is smaller than half the wavelength and the direction is usually parallel to the beam polarization. Even though the nature of the formation of these nanostructures is still under debate, they can be somewhat controllable, which can be highly useful for several applications, as it is going to be explained later.

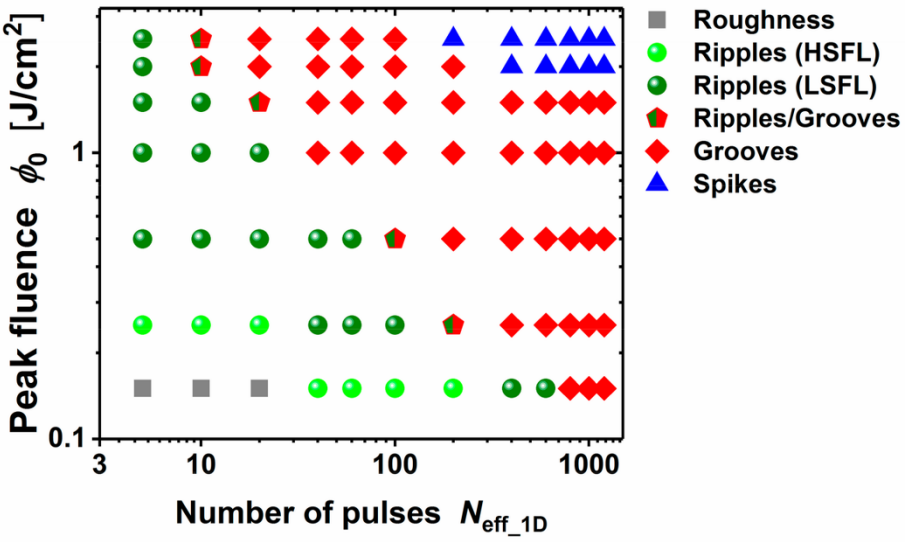

Fig. 2. 17 LIPSS morphological map formed on 100Cr6 steel upon fs-pulsed laser, depending on the fluence and effective number of pulses (image from [166]).

Lastly, the nature of the material plays a key role in the CA variation in time. The main differences may be observed between the metallic and the polymeric materials. In the former, during the laser interaction with the metallic surface the plasma affects the chemical properties of the surface, as observed by Wan et. al. [167], who treated the surface with air plasma on an untextured aluminium surface with no morphological changes and observed a drastic CA decrease from 93° to 30°, in concordance to other similar studies [168, 169]. The addition of micro-dimples further decreased the CA to 20°. The main transition mechanisms revolve around the removal of the carbonaceous contaminants and the attachment of oxide groups, which contribute to the polar component of the surface, decreases the CA of a water droplet; afterwards, depending on the environment in which the sample was stored, the polar groups start absorbing organic molecules, which on the other hand

contribute to the disperse component and increase the CA [170]. Hence, the organic compounds from the atmosphere are vital for the CA transition to occur [171]. This transition may take place from hours to days, depending on the storage conditions, the material or the laser treatment, among others. Nevertheless, in the latter, the CA transition is much less pronounced due to the less formation of microstructural changes in the surface, as little or no polar components appear (such as oxides).

The importance of the wettability is observable in many cases in which this concept is used as a basis for a specific functionalization of the surface. Within the previously stated application examples, the results are somewhat related to the adhesion modification (i.e., the increment of the CA). Therefore, the increased CA from the surfaces have been used as a guiding tool for the obtention of surfaces with promising results regarding lower ice adhesion, antibacterial properties, or reduced friction between surfaces, among others.

2.6. Wettability modelling by computer assisted simulations

In addition to analytical and empirical approaches, over the past years many studies have been published regarding the simulation of the wettability of a liquid droplet on a flat or structured surface via computational methods [172, 173, 174, 175]. Several different simulation methods can be selected in order to reproduce the wettability of a droplet over a surface, depending on the focus of the modelling.

Molecular Dynamic simulations (MD) provide a more in-depth insight of the physics of the contact line mobility of a liquid droplet on a solid surface, as it takes into consideration the interaction between the particles from both surfaces in a nanoscale system defined by the Lennard-Jones potential [176]. Several publications regarding the MD simulation of droplets have been reported throughout the past years [177, 178, 179, 180, 181] in which they analysed the viability of their results on the capability to estimate the wettability of rough surfaces. Wang. et. al. [180] reported how several fluid or physical variables such as the nanoparticle volume fraction affected the spreading of the droplet in the MD simulation, and hence the CA, on a textured surface. Khan et. al. [181] studied the effect of several texture parameters on the wetting transition between the Wenzel and Cassie Baxter states, concluding that these wetting states were strongly dependent on the surface fraction and pillar heights. Another type of simulation that revolve around the properties of particles is the **Monte-Carlo method**. Both methods are used in order to understand the fluid

organization near the surface [182]. This method proposes the use of random moves of particles to estimate the different outcomes of an event and give a probability value of the occurrence of that event being acceptable or rejectable [183].

On the other hand, **Computational Fluid Dynamics (CFD)** is capable of simulating different physical effects within a macroscale range and solving the moving interface problem of two or more fluids within a defined region [184, 185, 186, 187, 188]. CFD use numerical methods and discretize and solve the governing equations of the fluid flow [189]. The **Two-Phase Flow** is a particular example of the multiphase flow, which includes the **Volume of Fluid** (VOF), **Lattice-Boltzmann Method** (LBM) [185], **Moving Mesh** (MM), **Level Set** (LS) and **Phase Field** (PF) methods for the modelling of free surfaces and interface tracking. Malgarinos et. al. [186] analysed the VOF simulation results of the spreading of a water droplet onto several flat hydrophilic and hydrophobic solid surfaces comparing with both experimental and numerical results from other publications. They assessed the modelling of the force adhesion for low and medium Weber number impact. Also, they introduced the dynamic CA not as a boundary condition on the wall, but as a derived results from the wetting forces acting on the droplet. They observed similar results when compared to simulation and experimental results reported in other publications. Moreover, the CFD numerical results can also be of great utility to understand the effect of different topographic factors on the surface wettability, as shown by Zhang et. al. [187] in a 3-dimensional environment. More specifically, they established a critical pillar height and CA values that must be surpassed in order to observe a transition between the Wenzel and CB states. Lastly, the phase interface tracking methods (i.e., MM, PF and LS) have been widely used throughout the last decades. In these cases, their objective revolves around the identification of the different phases coexisting in the system and separate them by an interface. In the Two-Phase flow modelling, they are mainly used to accurately define the interface position between two immiscible fluids throughout the simulation time. These three methods are defined as follows:

- **Moving Mesh (MM)**

The MM was proposed by Li et. al. [190, 191] and treats the free surface as a geometrical surface that separates two defined domains [192]. This method is particularly good with dynamic interfaces and accurately reproduces the interface movement when compared to PF and LS methods. In fact, in this method, the mesh moves alongside any moving object within the system, whereas in the other two the mesh remained as stationary. This is achieved through the mesh adaptation to the geometry of the moving bodies, which makes it a relatively computationally expensive option. However, it cannot resolve situations where the domain splits into several bodies (i.e., it cannot

handle topology changes) and it is the most expensive between the three as well, regarding the computational cost [192]. Moreover, in the MM models, when geometrical structures are considered, the contact line is subject to several reconfigurations and the resolution of complex equations are required. Lastly, unlike the LS and PF, the MM is not capable of working with turbulent flows and must only be used in laminar flow simulations [193]. Despite its drawbacks, the MM is considered one of the best options to work with in terms of ease of use, but the possible topological changes that can be observed under certain conditions (i.e., high-speed falling droplets, among others), this method has not been considered in this work.

- **Level Set (LS)**

Contrary to the MM, the LS (and the PF) tracks the interface through an auxiliary function (defined later in this thesis) within a fixed mesh. This method calculates the position of the interface through an additional transport equation, alongside the Navier-Stokes' (NS) and continuity equations. The interface is defined as a region where the auxiliary function adopts a value of 0.5. Moreover, this parameter varies from 0 to 1 across the interface, depending on the phase located on the considered region. In this method, a reinitialization parameter has to be considered due to how the LS function can be a signed distance function (it represents the distance of a point from the interface), which requires this parameter after each time step in order to ensure the accuracy of the LS [194]. The LS is numerically more robust than the PF, as it depends more in the mathematical equations and lesser in the physics. However, it is more computationally expensive than the PF and it does not provide an accurate solution when the surface tension is taken into consideration [192].

- **Phase Field (PF)**

Similarly to the LS, the PF depends on an auxiliary function, and it calculates two additional transport functions, besides the NS and continuity equations. However, in this case, the PF provides a diffuse representation of the interface (it has a finite width between the two phases) and captures more accurately the interface morphology [195]. In this case, due to the nature of the diffuse interface, the PF is more numerically expensive than the LS, but it can solve more accurately advanced physics such as the fluid-structure interaction. Also, the non-zero thickness interface may enhance the mass loss of the droplet. However, the mass conservation from this method is better than in the LS which in numerous times a mass conservation procedure has been necessary to be implemented in order to achieve a mass balance between phases [196], although COMSOL provide a conservation enhancement with the "Conservative form" option available, which restricts the mass diffusion along the boundary domains. However, this can cause numerical errors, especially in

models where the fluid moves along the symmetry axis, as it is a singular point of the domain. Amiri et. al. [197] observed that the profile deformation of a bubble simulated by the PF was smoother than in the LS, due to the energy minimization-based equations, as it is going to be explained later. Also, they determined that the shrinkage that the droplet experience during the simulation (due to conservation problems, related to the mobility) was greater in the LS, i.e., the PF was able to maintain the bubble volume more efficiently. Zhu et. al. [188] performed a comparison between the LS and PF, concluding that, in the case of a rinsing bubble, the PF was able to capture the bubble changes more accurately and with less computational time than its counterpart. Recently, Provenzano et. al. [198] performed a detailed PF set up with COMSOL to observe the simulation results regarding the wettability of different surfaces in which both the topography and the intrinsic CA were varied. They observed that the simulation results were faithful to the experimentally obtained results. Therefore, the PF is the better choice when the objective revolves around the knowledge of the exact position of the interface and when its shape is of upmost importance, taking into consideration the more extensive applicability than the MM. A more detailed description of the PF equations is going to be provided in section 4. 2.

Based on the advantages and disadvantages resumed before, due to the nature of the work behind this thesis, the PF was selected as the Two-Phase flow method. The PF is included in the CFD module of COMSOL Multiphysics (COMSOL AB, Stockholm, Sweden) [199], which is an easy-to-use simulation software that present an in-built module that couples the Laminar Flow and Phase Field branches. Both are coupled together through a Multiphysics branch, as it is going to be detailed in section 4. 1.

To date, to the best of the author's knowledge, little research has been published regarding the effect of a textured surface (i.e., the effect of the surface topography modification effect) on the wettability of a water droplet via CFD Phase Field simulations with COMSOL Multiphysics [174, 200], and its potential utility as a tool for reducing the dimensional parameters needed to study to ensure a specific CA.

Chapter 3

METHODOLOGY AND INSTRUMENTAL TECHNIQUES

3.1. Introduction

The strategy proposed in this thesis to study the effect of the laser surface texturing on the change of the intrinsic wettability revolves around two different approaches based on a numerical simulation and a semi empirical regression model. The methodology followed in the present thesis is summarized in the graphical abstract from Fig. 3. 1. After selecting the material, the first step is to define the Desing of Experiments (see section 3.4), obtaining the total number of textures needed to establish a relationship between the topography and the measured CA.

In order to develop these textures, a complete study of the laser-material interaction is performed, in which the laser parameters that provide the optimal ablation process are identified. This study is divided into several steps that involve the in-depth assessment of different inputs for crater-like, groove-like and cavity-like structures before the final selection when developing a texture. In the case of the craters, the importance of the pulse interaction when working with different pulse emitting modes is addressed, focused on the effect of the E_p on the crater topography and morphology, the removed volume, and the efficiency of the ablation process. For this purpose, the results attributed to each pulse was evaluated, thus observing the possible interactions between two consecutive pulses. Afterwards, for the selected pulse mode and energies, the overlap between the pulses was introduced as a new parameter, and the value that provided an optimum trade-off between productivity and quality was identified. Due to this overlap, the effect of the E_p on this trade-off and quality was assessed again in cavity-like structures, which would be used afterwards to generate the final textures. Lastly, based on the quality objective desired in this work, a finer evaluation of the Ep effect on the quality of the textures was performed, alongside the number of overscans needed to reach the previously defined texture depths.

With these optimized parameters, the calculated number of textures from the design of experiments were developed, the topography and morphology were characterized, and the CA was measured in each case. The results from these experimental results were used as an input for the validation procedure of the computational model, which was focused on the development of a simulation model that could provide similar results as those observed experimentally. This simulation was divided into three main topics, beginning with a mesh convergence study, followed by the input parameter estimation (revolved around the mobility of the system) and finished by assessing the outputs (i.e., the CA measurement) and comparing them with the experimental results.

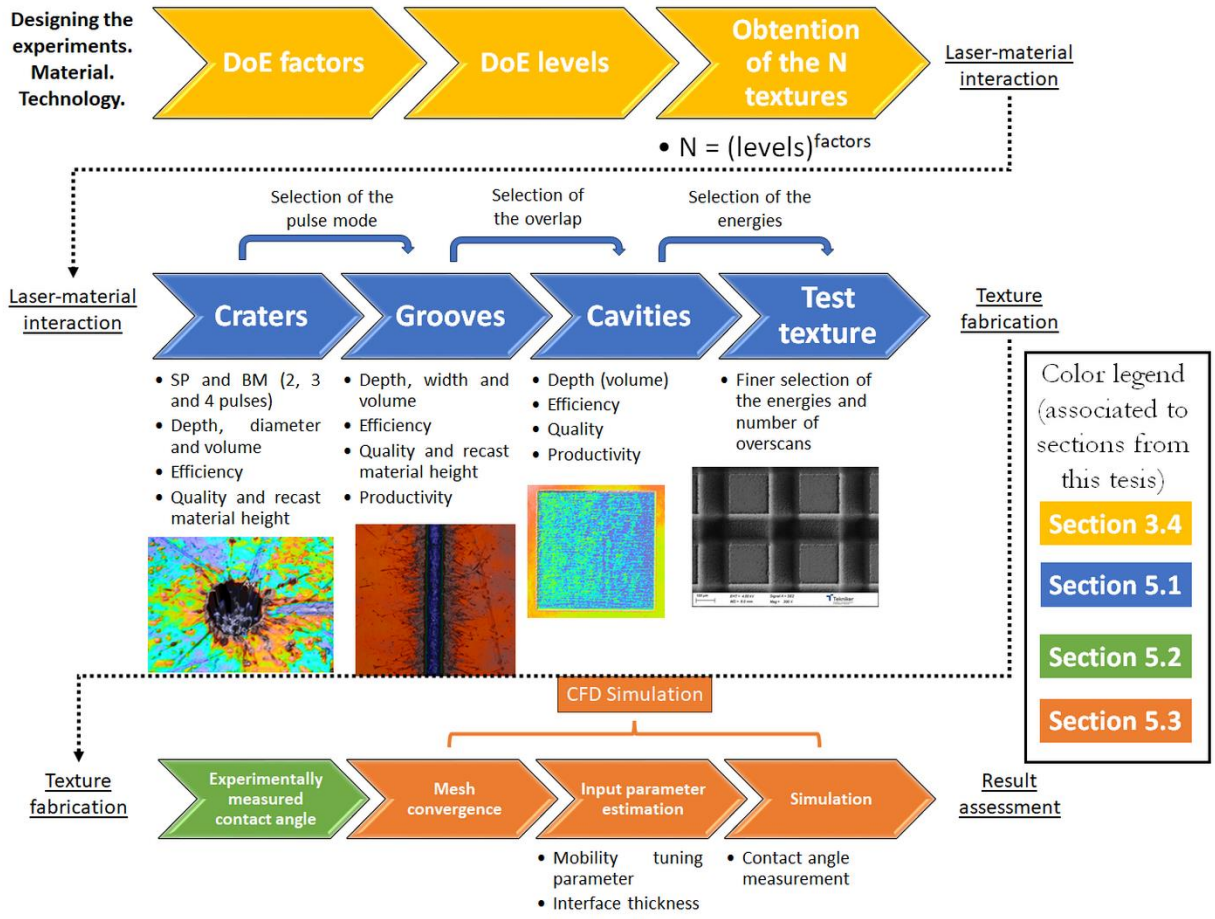

Fig. 3. 1 Graphical abstract of the methodology followed in the present work (the colour legend shows to which section from the thesis corresponds each shown step)

Before detailing the methodology followed in the present work, the material and laser system used are going to be introduced in the sections 3.2 and 3.3, respectively. The sections 3.4, 3.5 and 3.6 detail the methodology followed in this work.

3.2. Polypropylene

First of all, the material was chosen, which in this work was Polypropylene. As it was previously introduced, the easy availability of the monomer of the PP has boosted its use in a relatively high number of applications. **Propylene** (Fig. 3. 2), also known as **propene**, is a petrochemical monomer derived from crude oil via through a process called cracking, which involves the breaking down of large hydrocarbons into smaller ones, and from natural gas or coal [201]. Afterwards, these

monomers are bond together through polymerization to form large chains known as Polypropylene (Fig. 3. 3). The main syntheses to produce the PP are the Ziegler-Natta polymerization (ZN catalyst) [202] and the metallocene catalysis polymerization [203]. PP is a thermoplastic polymer produced by the polymerization of these monomers into structures that provides the material with remarkable properties. Since the propylene monomer is asymmetric, different configurations can be achieved, i.e., isotactic (iPP), which are arranged on one side of the carbon chain, syndiotactic (sPP), which are arranged alternatively, and atactic (aPP), which are irregularly arranged (see Fig. 3. 3). The iPP is the most used form in industry, as it can be used to form high-crystalline PP (which increases the tensile properties and strength [204]), but also because the sPP is more elastic and less resistant than the iPP. The aPP, due to the random ordering of the methyl groups, is commonly found as a byproduct in iPP samples [205].

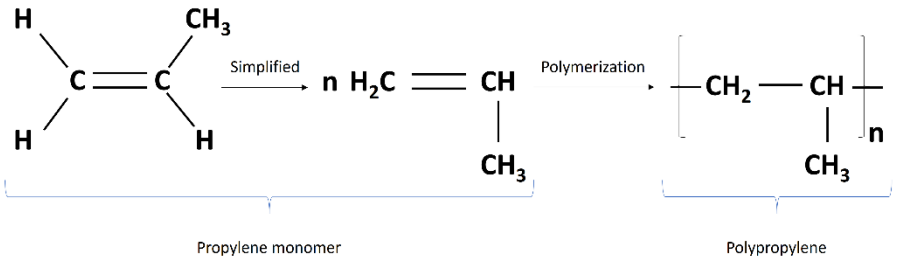

Fig. 3. 2 Chemical structure of the propylene monomer and the polypropylene after the polymerization

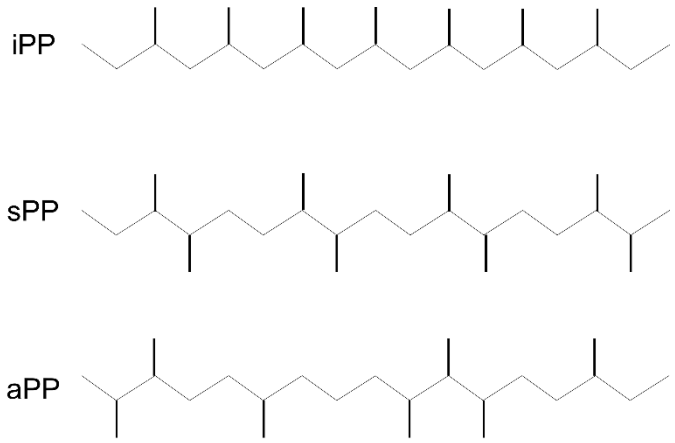

Fig. 3. 3 Basic chain structures of the PP

PP is a widely used cheap, non-toxic, highly resistant to fatigue, hydrophobic and chemically inert thermoplastic that has become one of the most globally used polymeric materials for many different industrial applications [36]. It can be found in a wide variety of applications due to its strength,

toughness, low density, and high melting point, alongside its excellent processability [206 , 207]. Moreover, contrary to alternative polymers such as Polyethylene, Polystyrene or Polyvinylchloride, PP has shown great recyclability (inert product) and, alongside the Polyethylene, can reduce the carbon footprint due to the lower environmental impact of the production technology [208].

Nevertheless, by the addition of several additives during or after the polymerization process, improved properties can be provided to the bulk PP, depending on the application. In fact, there are different PP resin, each with different properties (such as rigidity, heat resistance, transparency, etc.) that are used in different applications. Based on the chemical and physical properties, PP can be divided into three types: homopolymer (HPP), random copolymer (RCP) and impact copolymer (ICP) [209]. The former is the PP that only contains the propylene monomer, and it is the most common PP in the manufacturing industries. The others contain ethylene as a co-monomer in the PP in different grades.

PP sheets were supplied by GoodFellow [210] (PP303150). More specifically, a PP homopolymer were used, which is the most commonly used PP due to its excellent resistance/weight ratio, easy welding, easy machining and its higher rigidity than the copolymer. The samples' colour was natural, as no colouring additives were employed during nor after the polymerization process. The samples dimensions were 150x150x1.4 mm. Surface roughness (Ra), measured by a profilometer (Dektak 8, Veeco) at both PP faces, was 147 $\pm$ 27 nm and 129 $\pm$ 16 nm. The optical characterization of the PP was performed on an UV/VIS/NIR Perkin Elmer Lambda 950 spectrophotometer equipped with an integrating sphere (150 mm Int. Sphere) [211]. Optical properties analysis was carried out by measuring the percentages of the transmitted (T) and reflected I light over the spectral range 400 to 1500 nm with a resolution of 5 nm. The absorption (A) was afterwards calculated by the equation (15). At wavelengths of 517 nm, the percentage of the absorbed light was around 0.09% (see Fig. 3. 4), which shows the high transparency of this material in the considered wavelength

$$A\,[\%] = 100 - T - R \qquad (15)$$

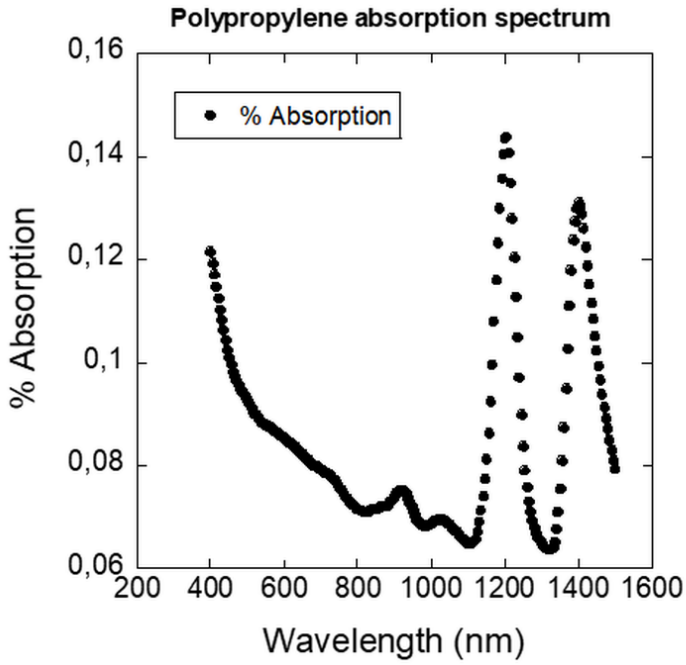

Fig. 3. 4 Absorption spectrum of the Polypropylene.

3.3. Laser system

For surface modification of the PP samples, a Coherent MONACO femtosecond-picosecond laser system was used, emitting in the second harmonic (517 nm), integrated in a micromachining workstation from 3D-Micromac. The sample positions can be selected with lateral resolution in the micrometer range. The laser was guided by a 2D galvanometric scanner with focusing lens of 100 mm focal length, providing a spot diameter of 20 μm at the focal plane (Fig. 3. 5), a depth of focus of 552 μm for the second harmonic and a work area of 40x40mm^2 at the work plane.

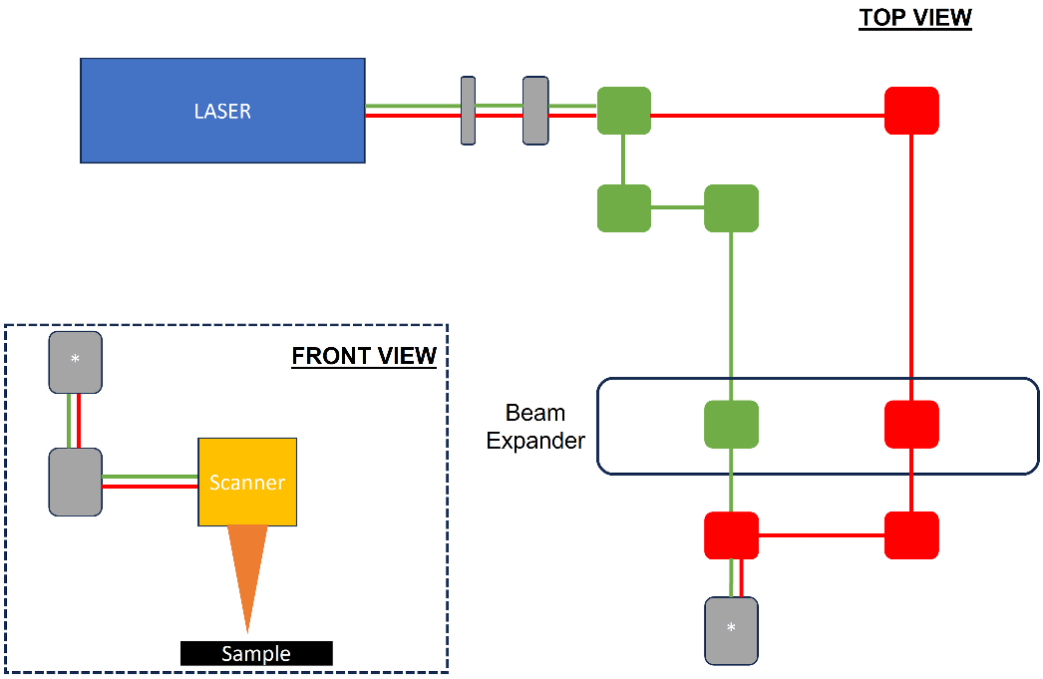

Fig. 3. 5 Top-view and front-view schematic representation of the laser system (in green and red, the 517 and 1030 nm optical guiding, respectively).

The technical specifications of the laser system used in the present thesis are resumed in Table 3. 1. It must be clarified that several parameters, such as the output power, are values measured at the exit of the laser system and is always higher than the laser power reached at the workstation, mainly due to the absorption or scattering effects that occur during the beam guiding through the optical components to the work sample (see Fig. 3. 5). Hence, the laser power (and thereby the E_p) measured at the sample location is always going to be lower than the source, as it is going to be seen later in this work.

Table 3. 1 General specifications of the MONACO laser system for the 517nm wavelength

Technical characteristics (wavelength of 517 nm)	
Output power	30 W (at 750 KHz)
Energy	40 µJ (at 750 KHz)
Pulse width (FWHM)	300 fs – 10 ps
Seed repetition rate	50 MHz
Pulse repetition rate (output)	1 – 750 KHz – 50 MHz

Laser beam characteristics	
Spatial Mode	TEM_{00}
Beam quality	$M^2<1.2$
Beam divergence	<1 mrad
Beam Diameter	2.7 ± 0.3 (mm, at output)
Beam circularity	>85 %
Polarization ratio	>100:1
Polarization direction	Vertical ± 3º

The Monaco laser system is provided by a laser seed that emits pulses at high repetition rate of 50 MHz (i.e., the temporal separation between two consecutive pulses in the seeder is T_{seeder} = 20 ns) for the following pulse picking and amplification [212]. The seed Acoustic-Optic Modulator (seed AOM) on the seed laser allows the pulse train to be divided onto lower repetition rates. Afterwards, these pulses are amplified by a high-gain Amplifier and an output AOM allows the adjustment of several laser operating parameters such as the power tuning or the pulse selection options. The MONACO can work with two different pulse emitting modes, i.e., SP and BM. In the latter, the number of **pulses per burst (ppb or n)** can be selected, from 2 to 4 ppb. When switching between the modes, the laser system changes the repetition rate to ensure that each pulse inside the burst has the same E_p, by satisfying the eq. (16):

$$f_{SP} = n\, f_n \qquad (16)$$

Where f_{SP} is the repetition rate of the SP operation and f_n is the repetition rate of the selected BM, associated to the number of pulses inside the burst, n. Fig. 3. 6 gathers a schematic view of the main parameters that drive the energy per pulse onto the sample for each emitting mode. The temporal separation of two consecutive bursts is determined by the burst period T_n (see eq. (17)) and it is n times higher than the temporal separation of two consecutive pulses in SP (see eq. (18)), according to eq. (16).

$$T_{SP} = \frac{1}{f_{SP}} \qquad (17)$$

$$T_n = \frac{1}{f_n} \tag{18}$$

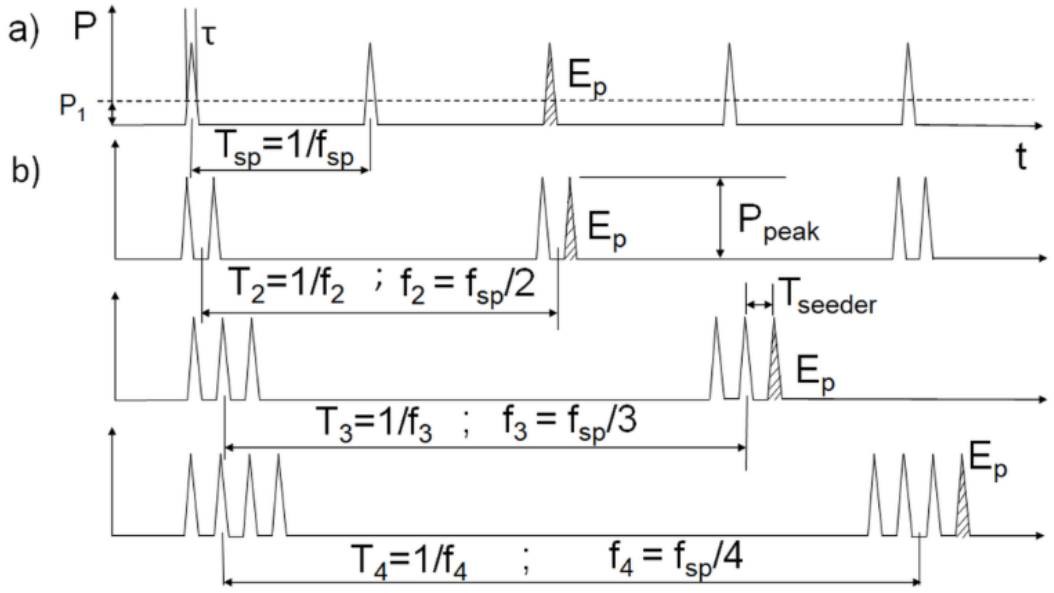

Fig. 3. 6 Schematic view of the MONACO a) SP mode; b) BM with 2, 3 and 4 ppb

As it can be observed in Table 3. 1, the nominal repetition rate is set at 750 KHz, while it can be reduced by a divider. This frequency divider can reduce the output repetition rate by an integer value, while maintaining the output E_p. On the other hand, the repetition rate can be manually set to values higher than 750 KHz, but the E_p is thereby reduced, as it can be observed in Fig. 3. 7.

In the present work, the nominal repetition rates were used (750 KHz for the SP, and the corresponding repetition rates for the BM, as defined by the eq. (16)) which offered the maximum obtainable E_p as well. The ablation mechanism of the PP with pulses with a duration of τ = 300 fs was assessed.

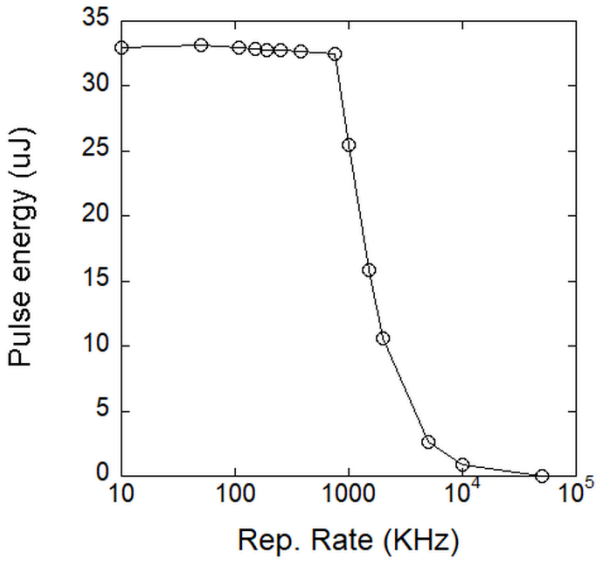

Fig. 3. 7 Laser output E_p variation with the repetition rate (at λ = 517 nm).

By varying the attenuation of the power, the output E_p follows a non-linear trend, as observed in Fig. 3. 8.

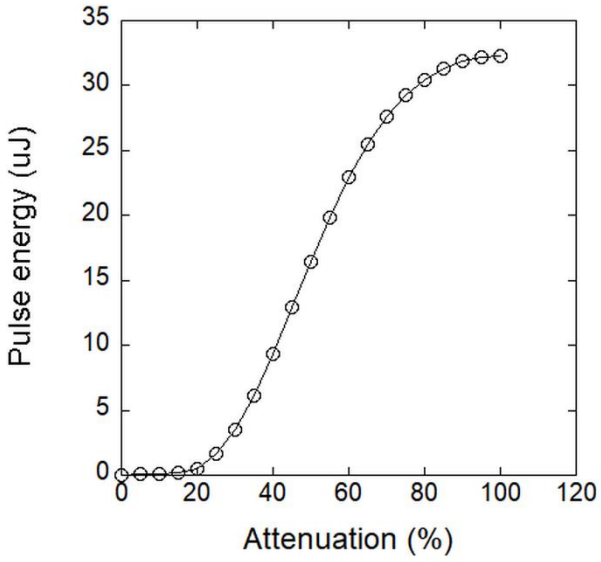

Fig. 3. 8 Laser output E_p variation with the power attenuation (at λ = 517 nm).

3.4. Definition of the Design of Experiments

This strategy started with the definition of the **Design of Experiments (DoE,** from now on) [213], a statistical and systematic approach to process optimization widely used in a large variety of industries [214]. It revolves around the definition of some factors and levels. A *factor* is a controllable variable of interest, i.e., the dimensional parameters that define a texture (in this work), and the *levels* are different values assigned to the factors within the range of interest. The DoE models the output behaviour centered solely on the factors and the interactions between each other. Therefore, it provides a full understanding on how each factor affect the response and minimizes data quantity [215]. This tool has demonstrated its capability of successfully working with data clouds and it was considered as the best option to work with based on the nature of the present work, in which obtaining a semi empirical model that helped predicting the topographic effects on the output (in this work, the CA) was desired.

The total amount of combinations possible with the factors and levels provide the total number of textures needed to develop by LST (obtained with eq. (19)) to observe, assess, and understand the effects and impact of each factor on the experimentally observed CA (i.e., the impact of solely the topographical modification of the surface).

$$Number\ of\ textures = levels^{factors} \tag{19}$$

The geometry of the texture and the levels of the factors were chosen based on previous experience, laser system limitations and on other works and research publications. In this work, the shape and geometry of the structures were selected based on an author's previous work [151] performed in a different polymeric material, i.e., ABS. These textures consisted of square pillars (see Fig. 3. 9 and Fig. 3. 10), used by previous works to modify the CA [216, 217, 218].

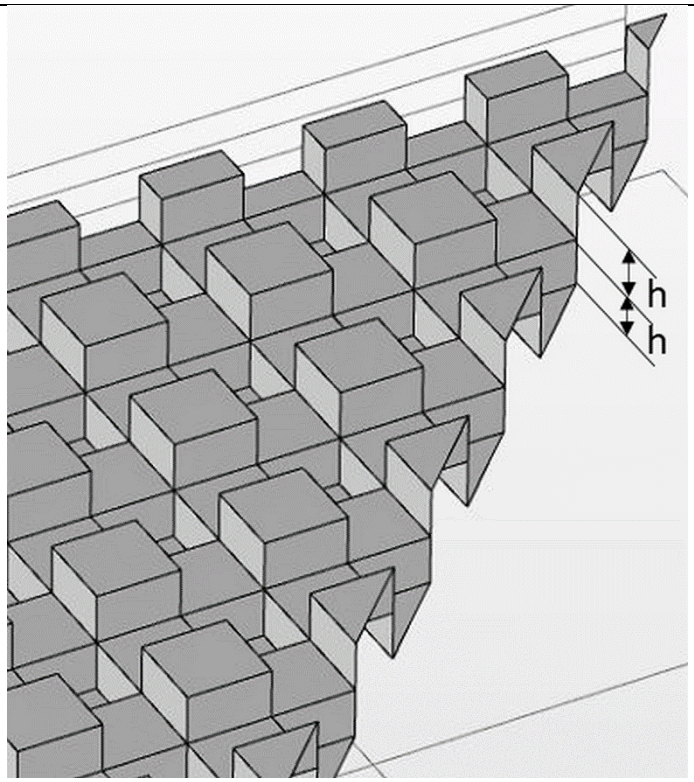

Fig. 3. 9 An example of a 3D texture, in which both texture depths (h) can be observed.

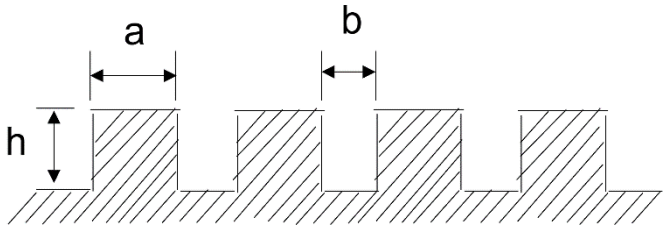

Fig. 3. 10 Schematic view of square pillar patterned micro-texture profile definition.

In Fig. 3. 9, it can be observed that a double depth was included. This is because the micro-textures generated by direct laser ablation followed a texturing strategy that involved the combination of horizontal parallel lines, followed by perpendicular vertical lines, which generated several spots where the laser interacted with the sample twice (see Fig. 3. 11), in which the depth was measured to be approximately two times h. However, when talking about pillar heights in this work, it is going to be referred to the first depth, except in the case of the computational modelling, as it is going to be explained later.

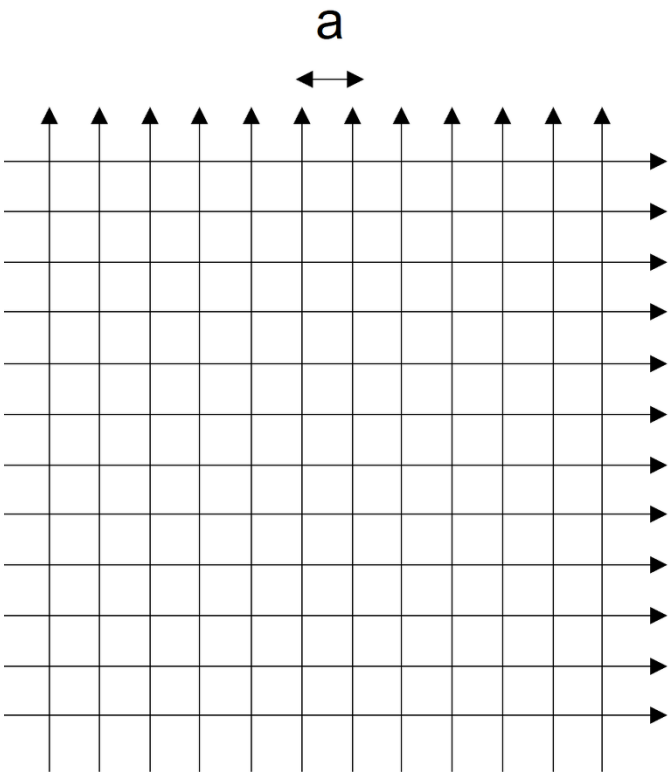

Fig. 3. 11 Schematic representation of the laser grooves produced to develop the square pillar structures (a is the pillar width, whereas b is determined by the laser spot and E_p).

In this work, the DoE employed a 3^3 full factorial design due to its capability to capture complex interactions between multiple variables, and their contribution to the desired outcome can be evaluated as well. This design takes into consideration 3 factors and 3 levels per factor. The topographical definition of each texture was selected as the potential contributors to the variation of the contact angle obtained from the experiments. In the case of the selected geometry, the factors and their respective levels were defined as:

- Pillar width, a: it is the width of the square-shaped pillars, and three levels were considered (low, medium, and high), based on previous works [151]: 75 μm, 150 μm and 225 μm.
- Cavity width, b: it is the spacing between two consecutive pillars, and the same three levels as the defined in the previous factor were considered: 75 μm, 150 μm and 225 μm.
- Pillar height, h: it is the pillar height from the first depth observed in Fig. 3. 9, and three levels were considered as well, but with different values than the other two: 10 μm, 40 μm and 70 μm.

Table 3. 2 summarizes the DoE factors and levels considered in the present work.

Table 3. 2 Factors and levels defined in the DoE.

Factors	Level 1	Level 2	Level 3
Pillar width (a) (μm)	75	150	225
Cavity width (b) (μm)	75	150	225
Pillar height (h) (μm)	10	40	70

Based on the defined topographical parameters, each micro-texture has associated a corresponding **topographical factor** (also known as **Wenzel factor**) $\mathbf{r_f}$ [219], which defines the increase of the projected contact area when compared to the flat surface (eq. (20)). Its value equals 1 when the surface is flat (without any micro-texture), and it is greater than 1 when the surface is textured:

$$r_f = 1 + \frac{4ah + 4bh}{(a+b)^2} = 1 + \frac{4h}{a+b} \quad (20)$$

This factor groups all three topographical parameters, and may provide of useful information regarding the effect of each case on the CA. However, it is not capable of showing the effect of each parameter on the CA variation. The DoE may help overcome this situation and understand more thoroughly the contribution of each parameter on the output.

Another topographic parameter that may be interesting to observe is the **surface fraction**, $\mathbf{f_{SL}}$, i.e., the solid/air ratio on which a droplet rests if it was in a Cassie Baxter state (see eq. (21)).

$$f_{SL} = \frac{a^2}{(a+b)^2} \quad (21)$$

The analysis of results of the DoE can provide of a better understanding of the topography effects on the CA measurements and trends. Moreover, the contribution of each factor on the result can be assessed with a backward regression analysis, in order to determine the factors that best explained the variation in the dependant variables (in this case, the CA). The backward regression analysis consists in a series of iterative steps, in which the least significant factors on the variation of the output were identified and then removed from the definitive Regression Model. The least significant variables were the ones that did not meet a significance level criterion, which is usually set at

probability values of p=0.05 [220]. Significance levels higher than this value were referred as variables that presented a relatively low impact on the output, whereas variables with lower p values showed a significant impact on the outcome. Hence, the final Regression Model resulted from the backwards regression analysis only accounted for the variables with the lesser p value, which is lower than 0.05.

In order to facilitate the interpretation of the results, the different factors were normalized by modifying the variable as defined in eqs. (22), (23), and (24):

$$X_1 = \frac{\mathrm{a} - 150}{75} \tag{22}$$

$$X_2 = \frac{\mathrm{b} - 150}{75} \tag{23}$$

$$X_3 = \frac{\mathrm{h} - 40}{30} \tag{24}$$

3.5. Laser material interaction and texture development

The next step involved an optimization process of the laser parameters that started with the development of crater-like structures with the ultrashort laser system. The **surface topographical characterization** involved the acquisition of 2D, and 3D images of the different topographic structures performed by laser by means of a confocal microscopy (SNEOX, Sensofar) [221]. A schematic view and a brief description of the equipment can be seen in section AII. 1, from the Annex II: EXPERIMENTAL INSTRUMENTATION. From the obtained images, several key aspects of the developed structures were taken into consideration when performing the measurements.

During the experimentation regarding the crater-like structures, the influence of the temporal separation between the pulses in SP and BM on the crater diameter, crater depth and ablated volume was established. In order to achieve this, a direct comparison between craters developed by n SP

pulses overlapped at the same position (denoted in the present thesis by layer) was compared to one BM of n ppb (see eq. (*25*)).

$$n\,E_{SP} = E_n \tag{25}$$

Where E_{SP} is the pulse energy of each SP, and E_n is the summation of the energy of each pulse inside the burst (in BM). Therefore, in this thesis, the pulse energy is denoted as E_P (for the pulses of both SP and BM).

From the craters, three dimensional parameters were considered (crater diameter, D_c, crater depth, d_c, and the height from the recast material accumulated on the edges, r_h), which were measured as depicted in Fig. 3. 13 a). For the specific cases of the craters, due to its relative geometrical simplicity, the removed volume was determined by a postprocessing software, known as Mountainmaps® (Digital Surf [222]). This software allows the user to further analyze the topography by providing of additional features such as peak and valley distance and volume obtention, among others. In this thesis, the ablated crater volume was obtained by manually defining the crater diameter profile from the confocal image, and based on the relative position (in the depth direction) of a measured point from the original surface, the software could identify it as a valley or a peak (see Fig. 3. 14, in which it can be observed that, inside the diameter profile definition, both the crater and the top surface areas were identified). The measurement of the total removed volume allows the estimation of the removed volume for each pulse, both in SP and BM, according to the study of Metzner et. al. [223] and eqs. (*26*) and (*27*): the volume removed by the n^{th} pulse can be obtained by removing the total volume of the $(n-1)^{th}$ pulse ($V_{tot(n-1)}$) to the total volume of the n^{th} pulse (V_{totn}). Fig. 3. 12 shows the volume removed by each pulse (V_1 is not represented due to the swelling effect, as it is going to be explained later in this chapter).

$$V_n = V_{tot_n} - V_{tot_{n-1}} \tag{26}$$

$$V_{tot_n} = \sum_{1}^{n} V_n \tag{27}$$

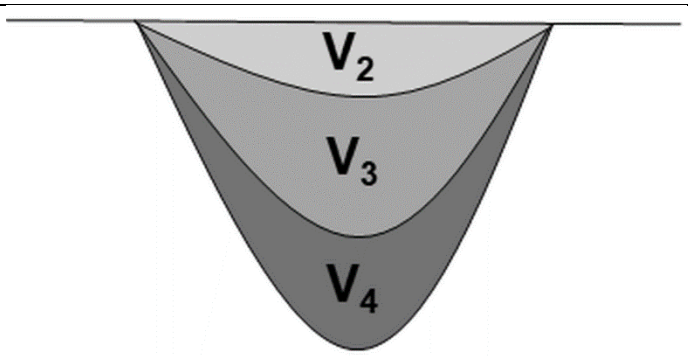

Fig. 3. 12 Schematic representation of the volume measurements. V2, V3 and V4 refers to the volume removed by the 2nd, 3rd and 4th pulses in the SP or BM. V1 is not represented due to the swelling effect.

The volume was a key measurement in this work, as it was used for the evaluation of the laser processing efficiency and throughput. The **ablation efficiency**, or **Specific Removal Rate**, **SRR** (in $\mu m^3/\mu J$), is referred in this thesis as the energy needed to ablate a specific volume, as defined by Kramer et. al. [86]. It describes how effectively is the E_p transferred into the surface, and the corresponding effect in material ablation, and it can be calculated by the volume removed by each pulse divided by the E_p, according to eq. (28).

$$SRR\ (crater) = \frac{V_n}{E_p} \qquad (28)$$

The throughput, or Removal Rate, RR (in $\mu m^3/s$), represents the total volume removed during the ablation process of the structure. In the case of craters, the removal rate is determined by dividing the corresponding total volume after n pulses divided by the temporal duration of this process. In this case, only the temporal separation between two consecutive pulses (t_{pp}) is taken into consideration, as the pulse duration can be neglected. In the SP mode, the t_{pp} is determined by the repetition rate (in KHz) and in the BM, on the other hand, by the seed oscillator repetition rate (in MHz), as determined in eq. (*29*).

$$RR\ (crater) = \frac{V_{tot_n}}{t_{pp}(n-1)} \qquad (29)$$

Lastly, the quality of the microstructures was assessed by means of the r_h, and the surface morphology characterization with a Scanning Electron Microscopy (SEM, ZEISS GeminiSEM 500) [224]. In the section AII. 2, a brief description of the SEM is provided. The nature of the sample

can greatly affect the imaging process of the SEM microscope. While a metallic surface is usually highly conductive, which facilitates the image processing with electrons, the polymeric materials are usually less conductive. This insulating property means that the electron may be trapped on the surface and its accumulation provokes an overcharge of the image (Fig. 3. 15 a). Therefore, in this work, in order to obtain a relatively good quality image, a very thin metallic coating (in this work, gold) was sputtered onto the surface in order to improve the image quality and avoid the overcharging of the sample (Fig. 3. 15 b).

Based on the three parameters necessary in this work to be considered to be optimal, i.e., efficiency, throughput and quality, the laser parameters that provide the best results were identified and selected before continuing with the grooves.

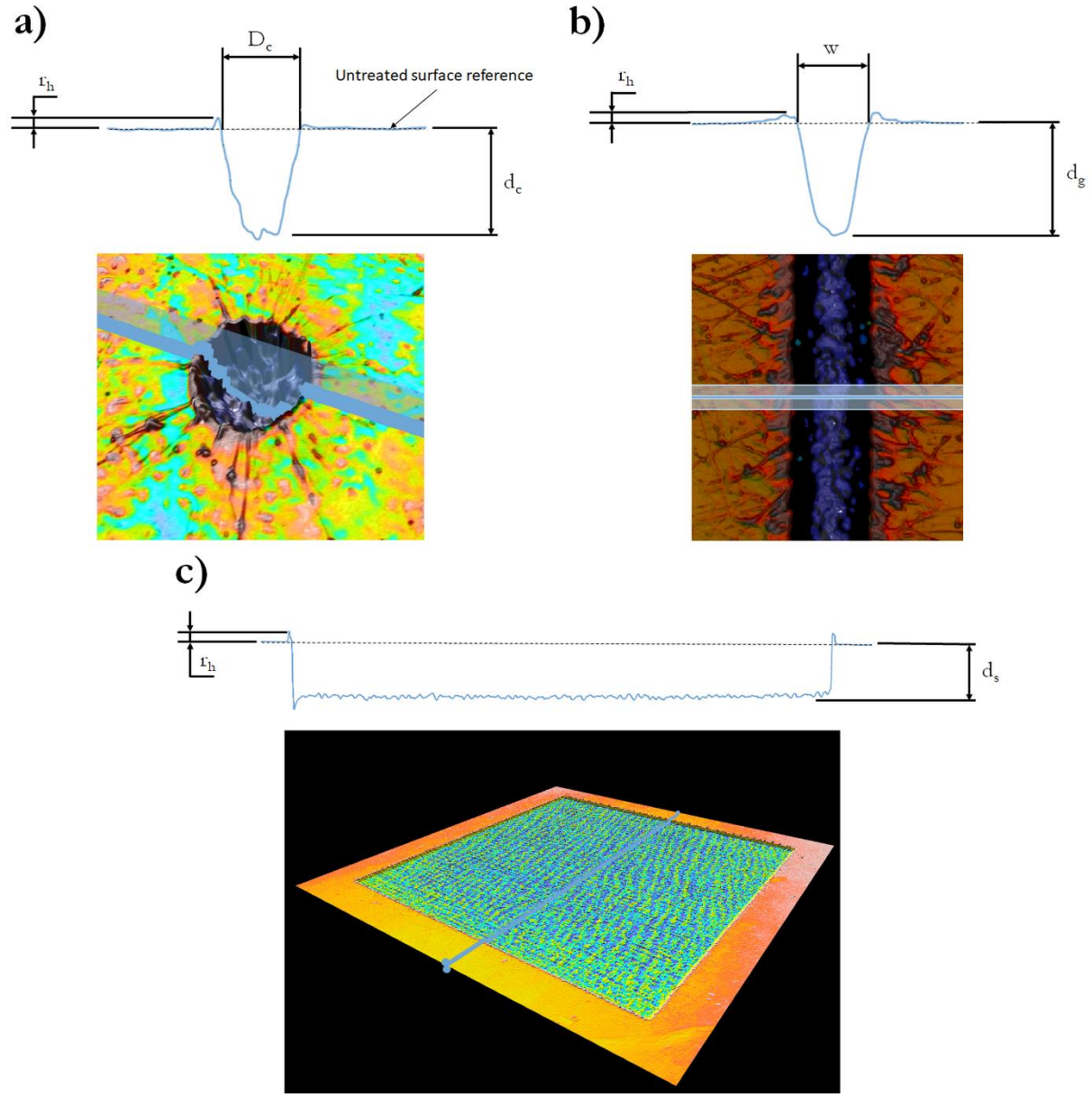

Fig. 3. 13 Dimensional parameter characterization procedure for a) a crater, b) groove and c) cavity

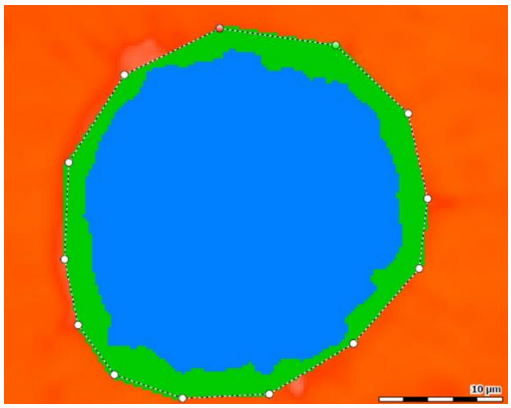

Fig. 3. 14 Top view crater volume obtention with Mountainmaps (in blue the crater hole is depicted, which is used to calculate the corresponding removed volume, and in green the surface is represented).

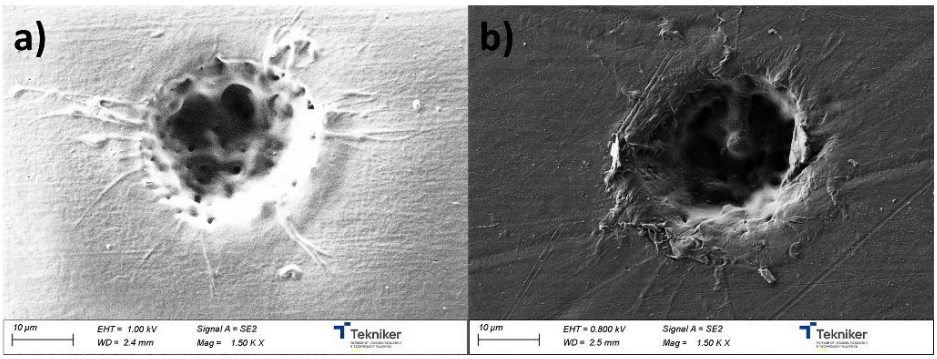

Fig. 3. 15 a) Overcharged PP sample with no coating, b) uncharged coated PP sample (with gold)

In the case of the grooves, the throughput grew in importance, as key factors such as repetition rate between the bursts (f_b) and the scanning speed (v_s) from the galvanometric scanner were introduced. Hence, the burst **overlap** (U_d) effect on the quality, SRR and RR were assessed, as this parameter included both the f_b and v_s, following the eq. (30) [56]:

$$U_d = \left(1 - \left(\frac{v_s}{f_b\, D_s}\right)\right) * 100 \qquad (30)$$

Where D_S is the diameter of laser spot (twice the spot radius, ω_0).

In this case, grooves of 2 mm length were developed, and the total removed volume was determined by multiplying the length by the mean value of the width (w) and depth (d_g) of the groove, measured on several different locations. The topography characterization performed can be observed in Fig. 3. 13 b). Contrary to the study with the craters, in this case and onwards the SRR is going to be calculated based on the total energy deposited on the area and the total removed volume, V_{tot_groove}, which can be calculated with the total number of pulses needed to produce it, E_{tot_groove}, as determined by the eq. (31).

$$SRR\ (groove, cavity) = \frac{V_{tot_{groove}}}{E_{tot_{groove}}} = \frac{V_{tot_{cavity}}}{E_{tot_{cavity}}} \qquad (31)$$

The removal rate, or throughput, was calculated as the ratio of V_{tot_groove} and the processing time measured during the experiments, t_{groove}, following the eq. (32).

$$RR\ (groove, cavity) = \frac{V_{tot_{groove}}}{t_{groove}} = \frac{V_{tot_{cavity}}}{t_{cavity}}$$

(32)

To identify the optimum U_d, a mathematical parameter that provides the optimal trade-off between throughput, efficiency, and quality (by means of r_h) was defined. In this work, it was identified as the **trade-off factor** (**TOF**), which related the three output values from before. Considering that, in general terms, maximizing the removal rate could lead to bad quality outputs, or maximizing the quality could lead to relatively low throughputs, the optimal scenario would depend on the application, there are some cases where the quality, efficiency or throughput should be sacrificed in order to achieve the desired objective. During this methodology step, the laser parameters that provided the highest SRR and RR and the lowest r_h were selected, by means of an expression that represents this objective (see eq. (33)). Therefore, this factor was used as a guiding step, as the obtained parameter could be adapted based on the application.

$$TOF\ = \frac{SRR\ \ RR}{r_h}$$

(33)

Before developing the textures, with the selected overlap value, the E_p effect was assessed again, but in this last case, the groove overlapping effect was established, in order to develop square cavities. Squared cavities of 2 x 2 mm^2 were developed by performing parallel lines as depicted in Fig. 3. 16. The distance between the lines in the vertical direction, also known as **hatching** (d_{bb}) in this work, was manually matched to the spatial distance between bursts, as determined by eq. (34). This way, the same number of bursts reached the sample in the horizontal and vertical directions (see Fig. 3. 16). All the cavities were developed with a single **scan level** (or **overscan**), i.e., the number of times the same laser pattern was repeated.

$$d_{bb}\ = \frac{v_s}{f_b}$$

(34)

The same methodology as described for the grooves was followed. In this case, as the width of the cavities was constant in every case, only the depth of the groove d_s and the r_h were measured (see Fig. 3. 13 c). The SRR, RR and TOF were calculated with the eqs. (31), (32) and (33), respectively.

Similarly to the grooves, the E_p that provided the highest TOF was selected for the texture development.

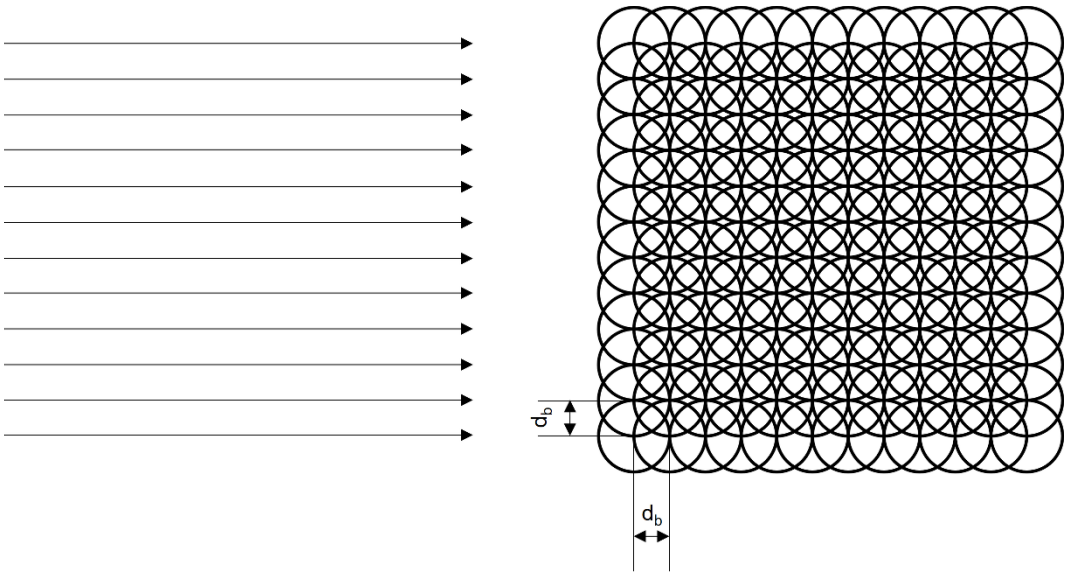

Fig. 3. 16 Cavity strategy (left) and burst location on each parallel line, separated by d_{bb} (right)

3.6. Texture effect on the intrinsic wettability: experimentation and simulation

With the previously selected parameters, texture examples were performed, by following the strategy defined in Fig. 3. 11. In this work, the objective was obtaining texture profiles as close as possible to the theoretical profile (Fig. 3. 9), hence, minimizing the r_h was desired. The E_p and number of scan levels were adapted to ensure this objective.

After developing all the textures of 15 x 15 mm^2, the topography and morphological characterization was performed, as defined in Fig. 3. 17. Afterwards, the CA was measured three times in each case to ensure the repeatability of the effect of the topography on the wettability by means of a goniometer, Surftens Universal goniometer (OEG) [225] (defined in detail in section AII. 3, from the Annex II: EXPERIMENTAL INSTRUMENTATION).

The experimentally obtained results were used as a validation tool for the simulations performed in COMSOL Multiphysics. The detailed methodology for this computational modelling can be found in the next chapter, COMPUTATIONAL MODELLING. The output from the simulation (the CA) was measured by a postprocessing tool known as ImageJ [226].

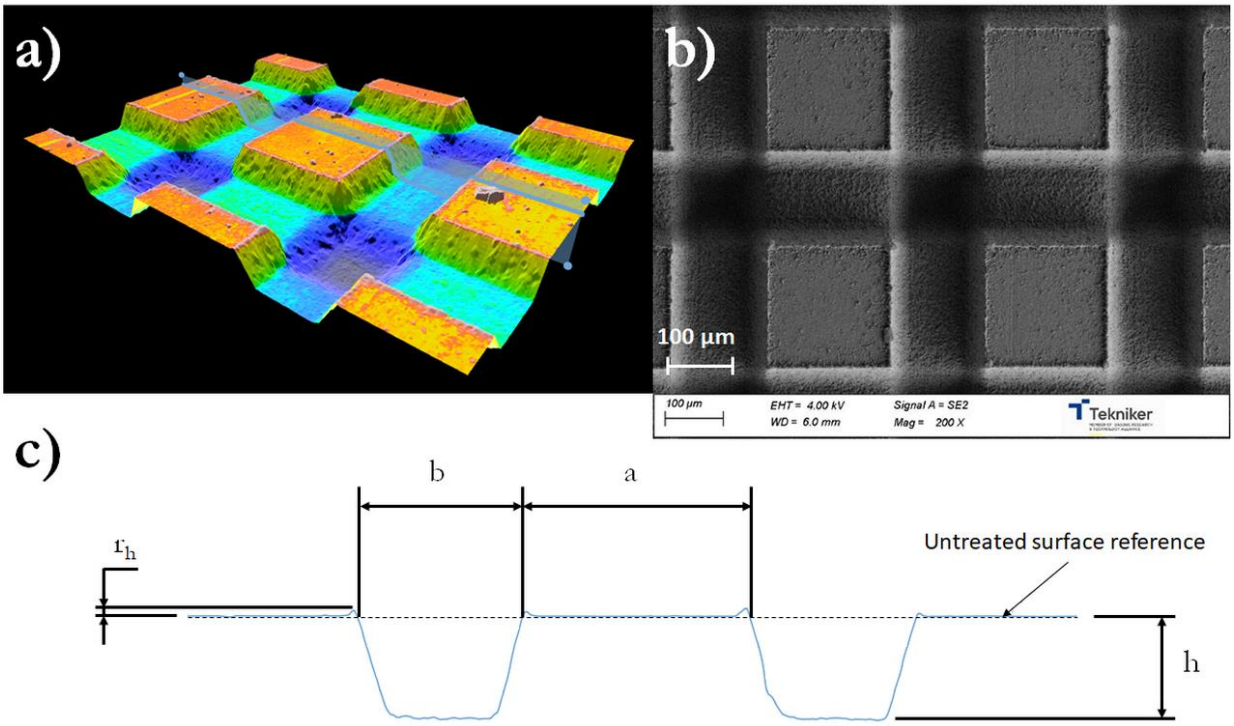

Fig. 3. 17 a) Texture topography image by confocal microscopy, b) morphology by SEM and c) topographical measurements performed in the cut plane from a)

Chapter 4

COMPUTATIONAL MODELLING

4. 1. Computational modelling

In this work, in order to approximately reproduce the goniometer setup with the computational simulations, the next scenario is considered: the droplet is assumed to be completely spherical (in a 3D environment) or completely circular (in a 2D environment), and it is released closely from the surface with an initial velocity of zero m/s. The main objective is to simulate a droplet carefully deposited on the surface, as it is done with the goniometer.

For the simulation of a water droplet impingement onto a surface, a **Finite Elements Method Computational Fluid Dynamics (FEM CFD)** model was developed in COMSOL Multiphysics® 5.4a [199]. The physic laws that describe a time dependent problem can be expressed through one or more partial differential equations. However, in the majority of problems they cannot be solved through analytical approaches. To obtain a solution, the FEM divides (or discretises) a domain into small elements or cells that are part of a mesh that can be approximated to the original domain shape, thus these differential equations can be approached with numerical model equations, which can be solved with numerical methods [227]. The FEM reaches the solution by minimizing the error derived from the solution to the numerical equations. The iterative process in which this minimization is achieved, and a stable and accurate solution is obtained is called **convergence**. The convergence does not only mean accuracy, but also consistency and stability in the solution process. In non-linear problems, which are strongly influenced by boundary conditions, the stability and convergence can be difficult to demonstrate, hence it is usually required an iterative process in which the grid or mesh element size is successively refined, also known as mesh convergence [228], as it is going to be explained and applied in section 5. 3. 2. 1

This software is capable of using both two and three-dimensional environments. The main advantage of using a 3D system is the possibility of developing any type of texture with relatively low restrictions. Moreover, it is also capable of simulating the influence of several aspects that cannot be included in a 2D environment, such as the double depth effect of the texture on the contact line movement along the structures, or the influence of the interface movement on a direction onto the spreading over a different direction. However, the main drawback of these systems revolves around the relatively high computational cost, due to the high number of mesh elements required to define the geometry. A 2D environment, on the other hand, will not be able to fully capture the realistic phenomenon of the droplet wetting, especially on more complex textures like the ones used in the present study, but, in general terms, the number of elements required to define the entire geometry is lower than in the case of a three-dimensional system.

The computational modelling proposed in this work required of a complete study regarding several parameters that may affect the results. This study included several parametric simulations with which the simulation results could be assessed and compared to those obtained experimentally. Therefore, a simple reference model is proposed at first with a **2D symmetric** system, in which a symmetry line was defined, so that the problem could be even more simplified, and the simulation cost was sharply reduced. In this case, the hypothesis that the droplet falls on the middle of a pillar is considered, due to the symmetric nature of the system. This model would be used to identify the simulation inputs and parameters that would fit more accordingly to the experimental data.

In this thesis, for the 2D symmetric model, due to the impossibility of including both texture depths depicted in Fig. 3. 9, an equivalent bi-dimensional profile was considered. Due to the difficulty of selecting the appropriate equivalent topography profile that could represent more accurately the wetting modification of a texture, in this thesis a 2D texture in which only the effect of the double depth was considered (see Fig. 3. 10, where the double depth can be seen as two times h, denoted as h_{2D}, that satisfies the eq. (35)).

$$h_{2D} = 2h \tag{35}$$

Therefore, the extreme condition where the depth was maximum was considered. Additionally, based on the experimental results that are going to be presented in section 5. 2. 2, this value corresponds to a 2D topographical factor (r_{f2D}, as seen in eq. (36)) that is equivalent to the experimentally obtained r_f ($r_{f2D} = r_f$).

$$r_{f_{2D}} = 1 + \frac{2h_{2D}}{a + b} \tag{36}$$

4. 2. Laminar Flow and Phase Field equations

COMSOL can solve multiphase flow problems with several methods that can be divided into disperse or interface tracking methods. The former takes into account the volume fraction between the phases throughout the domains (i.e., the different geometrical areas or locations defined in the computational model), whereas the latter include physics like velocity and pressure in exchange of higher computational costs. Among the latter, the different options were previously defined in section 2.6. In terms of fluid flow, however, COMSOL can work under Laminar and Turbulent

environments, which appearance can be predicted with the Reynolds number (R_e), which relates the ratio between the inertial and the viscous forces [229]:

$$R_e = \frac{\rho U L}{\mu}$$

(37)

Where ρ is the fluid density (kg/m^3), U is the fluid velocity field (m/s), L is the characteristic length, which in the case of a FEM can be considered as half the mesh element size ($h_{mesh}/2$) and μ is the fluid viscosity (Pa·s). If R_e is higher than a critical value, the inertial forces predominate over the viscous and the fluid moves in a chaotic state known as the turbulent regime. Due to the nature of the droplet deposition simulated in this work (as in observed in the goniometer), relatively low velocities are expected and thus, a laminar flow is more likely to occur during the simulations. Therefore, a laminar flow hypothesis is first considered.

In this work, the interface tracking method denoted as **Phase Field** (**PF**) and the **Laminar Flow** interfaces were considered to simulate the falling and spreading of a droplet onto a surface. The PF allows to track the interface performance between the droplet and the micro-structured surface. As it was previously explained, this interface defines the diffuse interface between two (or even three) different phases. In this study, two phases were considered, namely, gas and liquid phases, separated by an interface that defines the profile of the liquid droplet. The PF interface defines an auxiliary parameter, known as the **interface tracking parameter,** or Phase Field parameter (ϕ), that equals -1 when the domain is filled with liquid and 1 when it is filled with gas, identifying the droplet diffuse interface centred at $\phi = 0$.

In the Laminar Flow interface, incompressible fluids were considered, which follows the **Navier-Stokes (NS)** equations, namely the continuity and momentum equations, as seen in eqs. (38) and (39)(41), respectively, in which the gravity effect was included:

$$\frac{\partial \rho}{\partial t} + \nabla \cdot (\rho \boldsymbol{u}) = 0$$

(38)

$$\rho \frac{\partial \boldsymbol{u}}{\partial t} + \rho(\boldsymbol{u} \cdot \nabla)\boldsymbol{u} = \nabla \cdot [-p\boldsymbol{I} + \tau_{visc}] + \boldsymbol{F}$$

(39)

where $\boldsymbol{I}$ is the identity matrix, p is the pressure (Pa), τ_{visc} is the viscous stress tensor (Pa) and $\boldsymbol{F}$ is the sum of all volume force vectors (N/m^3).

Assuming the incompressibility of the fluid flow during the droplet wetting of a surface, and taking into consideration the surface tension and gravity effects during this process, the NS equations can be rewritten as follows:

$$\frac{\partial \rho}{\partial t} + \rho \cdot \nabla \boldsymbol{u} = 0 \tag{40}$$

$$\rho(\boldsymbol{u} \cdot \nabla)\boldsymbol{u} = \nabla \cdot [-p\boldsymbol{I} + \mu(\nabla \boldsymbol{u} + (\nabla \boldsymbol{u})^t)] + \boldsymbol{F_{ST}} + \rho \boldsymbol{g} \tag{41}$$

where $\boldsymbol{g}$ is the gravity field and $\boldsymbol{F_{ST}}$ is the surface tension, which can be expressed in the PF as:

$$\boldsymbol{F_{ST}} = G\nabla\phi \tag{42}$$

where G is the chemical potential:

$$G = \left(\frac{\lambda\psi}{\varepsilon^2} - \frac{\partial f}{\partial \phi}\right) \tag{43}$$

where $\partial f / \partial \phi$ is a user-defined source of free energy, which in this study was set to zero to isolate the system from any other source of energy and to reduce the complexity of the model. In eq. (43), λ is the mixing energy density and ε is a capillary width that represents the **thickness of the interface**. The latter is an important parameter that must be properly set up [230], as too big values may lose accuracy of the shape of the free surface, and too small values may provide numerical errors if the corresponding mesh resolution is incorrectly selected. ψ is a PF help variable determined by the interface thickness and the interface tracking parameter, as defined in eq. (44):

$$\psi = -\nabla \cdot \varepsilon^2 \nabla\phi + (\phi^2 - 1)\phi \tag{44}$$

The PF considers the following equations to track the interface, based on the Cahn-Hilliard diffusion method, which involves the energy minimization through the chemical potential, G:

$$\frac{\partial \phi}{\partial t} + \boldsymbol{u} \cdot \nabla\phi = \nabla \cdot \gamma \nabla G \tag{45}$$

Which can be rewritten by using the eq. (43) into:

$$\frac{\partial \phi}{\partial t} + \boldsymbol{u} \cdot \nabla \phi = \nabla \cdot \frac{\gamma \lambda}{\varepsilon^2} \nabla \psi$$

(46)

where γ is the **mobility**, which determines the kinetics of the Cahn-Hilliard equation [231]. Both γ and σ (**surface tension coefficient**) are related to λ and ε via the equations:

$$\lambda = \frac{3\varepsilon\sigma}{\sqrt{8}}$$

(47)

$$\gamma = \chi \varepsilon^2$$

(48)

In eq. (48) χ is the **mobility tuning parameter**, which determines the diffusivity of the phase field, i.e., defines the relaxation time of the interface. The proper value of this parameter must be introduced, as it cannot be too large (to avoid instabilities) yet must be small enough to provide a sharp interface. As it was explained before, ε is a parameter that control the thickness of the region where ϕ changes from -1 to 1. Again, to fully capture the droplet movement alongside the textured wall, a ε value should be small enough to be compared to the experimental sharp interface, however it should be big enough to avoid computationally expensive simulations and to keep the interface thickness constant. In section 5. 3. 2, the procedure followed to obtain the mesh size, ε and χ values that provide a converging result and the most fitting outputs when compared to those from the experimental ones is reported.

The PF monitors the interface location at a given time with the use of the auxiliary parameter, ϕ, and provides the properties of the fluid in terms of density and viscosity following the equations:

$$\rho = \rho_1 V_{f,1} + \rho_2 V_{f,2} = \rho_1 + (\rho_2 - \rho_1) V_{f,2}$$

(49)

$$\mu = \mu_1 V_{f,1} + \mu_2 V_{f,2} = \mu_1 + (\mu_2 - \mu_1) V_{f,2}$$

(50)

where V_f is the volume fraction of the fluid, which determines the volume of each fluid in a certain point of the domain, and is identified by a value between 0 and 1, following the equations:

$$V_{f,1} = \frac{1-\phi}{2} \tag{51}$$

$$V_{f,2} = \frac{1+\phi}{2} \tag{52}$$

$$V_{f,1} + V_{f,2} = 1 \tag{53}$$

Therefore, when the domain is filled by a liquid (ϕ = -1), $V_{f,1}$ equals 1 and $V_{f,2}$ equals 0, and vice versa when the domain is filled with gas. On the interface region, where both fluids coexist in a mixed state, ϕ = 0 and V_f equals 0.5 in both cases, resulting in a density and viscosity values equalling the sum of half the corresponding to the liquid and gas states.

4. 3. Brief comparison of the Phase Field with the Level Set method

Contrary to the PF, which uses both a PF variable (ϕ) and a help variable (ψ), the LS only tracks the interface evolution through an equivalent LS variable, also denoted as ϕ. In this method, ϕ varies from 0 to 1, being 0.5 the middle value of the diffuse interface. The LS calculates the density and viscosity of each fluid by the eqs. (54) and (55) and the interface position through the eq. (56).

$$\rho = \rho_1 + (\rho_2 - \rho_1)\phi \tag{54}$$

$$\mu = \mu_1 + (\mu_2 - \mu_1)\phi \tag{55}$$

$$\frac{\partial \phi}{\partial t} + \boldsymbol{u} \cdot \nabla\phi = \gamma \nabla \cdot \left(\varepsilon \nabla\phi - \phi(1-\phi)\frac{\nabla\phi}{|\nabla\phi|} \right) \tag{56}$$

However, in this case, γ is not the mobility, but the reinitialization parameter previously defined in section 2.6, which controls the interface's behaviour according to eq. (56). This parameter ensures

that the variation in ϕ occurs within the interface thickness defined by ε. Similarly to the PF method, this reinitialization parameter needed a tuning for the LS to correctly perform the simulations. Therefore, too low γ values could cause variations inside the fluids (outside the interface diffuse), which could lead to the creation of new fluid-fluid interfaces in incorrect locations. Too large values, on the other hand, could cause small time steps and high computation times. The ε is also needed to be tuned, as explained in the previous section.

Therefore, both LS and PF are similar methods with different approaches to control the phase variable ϕ. The latter is usually preferred when the surface tension has a large impact on the simulation. This occurs in the case studied in this thesis, the droplet impingement on a surface, due to the big differences in the densities of the water and air, which strengthens the selection of the PF as the most suitable method for the simulation in this thesis.

4. 4. Computational domain definition

Fig. 4. 1 shows the considered 2D symmetric system, under the simplification that the droplet falls on top of the middle of a pillar, for a given texture. The coexisting domains and the boundary conditions are represented. The domain defined by the subindex 1 (in equations like (51), (52), (54) or (55)) is considered to be the water (ϕ = 1), whereas the domains filled with air have the subindex 2 (ϕ = -1). The water droplet (and the air domain) is cut by half by the leftmost vertical line. In this section, a description to each defined conditions and boundaries is provided. Additionally, it is important to notice that, due to the nature of the problem, there is no fluid inputs nor outputs, defining a system where no air flow is present, preventing the deformation of the droplet due to kinetics forces provoked by this addition.

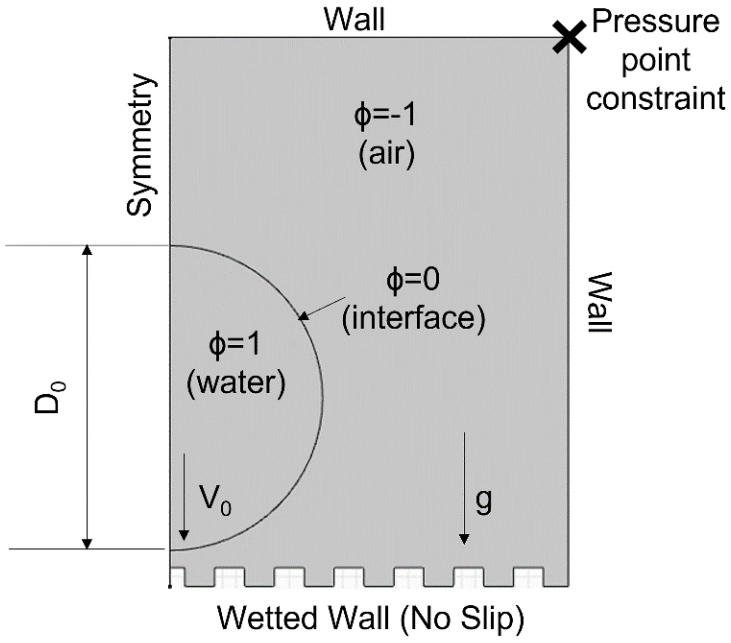

Fig. 4. 1 A schematic representation of the simulation domain and boundary conditions.

4. 5. Axial symmetry

As previously introduced, in order to save computational work a 2D symmetric condition is considered. Due to the lack of axial symmetry of the textures, an axisymmetric condition cannot be applied. Thereby, a symmetry condition is applied in the leftmost line from Fig. 4. 1, which applies not only to the geometry but also to the loads and physics. The symmetry condition prevents the penetration through the selected boundary and eliminates the gradients in the same direction (see eqs. (57) and (58), for an incompressible fluid). In these equations, **n** is the vector perpendicular to the interface.

$$\boldsymbol{u} \cdot \boldsymbol{n} = 0 \tag{57}$$

$$[-p\boldsymbol{I} + \mu(\nabla \boldsymbol{u} + (\nabla \boldsymbol{u})^t)]\boldsymbol{n} = 0 \tag{58}$$

4. 6. Wetted Wall

To simulate the fluid interaction with the surface, a wetted wall feature is added, in which the CA is introduced as an input. This feature prevents the liquid penetration into the surface (the mass flow is zero).

$$\boldsymbol{n} \cdot \varepsilon^2 \nabla \phi = \varepsilon^2 \cos(\theta_{WW}) |\nabla \phi| \quad (59)$$

$$\boldsymbol{n} \cdot \frac{\gamma \lambda}{\varepsilon^2} \nabla \psi = 0 \quad (60)$$

Where θ_{ww} is the contact angle introduced as an input in the Wetted Wall boundary. Eq. (59) impose the CA in the selected wall, which in this work was chosen as the **Intrinsic Contact Angle** of a flat, CA_0, set at $\mathbf{CA_0 = 111 \pm 5^o}$, as measured experimentally in a flat untreated PP surface with the goniometer.

Lastly, a No-Slip boundary was set in this WW surfaces. As its name suggests, this condition prevents the slipping of the interface while in contact with the solid structure and sets the tangential component of the velocity at zero (additionally to the already null value of the normal component). In other words, with the No-Slip condition, the fluid moves with zero velocity relative to the surface boundary. This No-Slip condition was imposed over the Slip Boundary because the latter greatly increases the computational cost due to the introduction of new complex equations, such as the length scale of the slip wall, which would increase the degrees of freedom by one [198]. Additionally, if a No-Slip condition is imposed, if the interface is defined as a sharp boundary, it could lead to singularities that can be overcome by considering it as a diffuse, as it happens in PF and LS methods [232].

4. 7. Other conditions

In the Laminar Flow module, the effect of the **gravity** was included, a droplet diameter (D_0) of 2.3 mm was used (corresponding to a volume of 5 μL), and an initial droplet velocity (V_0) of 0 m/s was set (situated at a very close position from the surface) in order to reproduce the carefully deposited

droplet with the goniometer setup. Therefore, the droplet moves downwards due exclusively to the gravity effect.

For the NS equations to be properly solved, a **Pressure Point Constraint** of 0 Pa was included on the top vertex of the system. This way, a known pressure value is provided to the solver, and thereby the obtention of infinite possible pressure values is prevented, thus eliminating the consequent divergence of the simulation. The pressure in the Laminar Flow interface is calculated as an absolute value, resulting from the summation of a reference pressure (set at the atmospheric pressure of 1 atm) and the relative pressure value provided as an input (i.e., the 0 Pa included in the Pressure Point Constraint indicate that the pressure at that point is the atmospheric pressure), and follows the equation:

$$p = \mathrm{p}_0 + p_{ref} \tag{61}$$

Where p_0 is the input pressure and p_{ref} is the reference pressure.

Lastly, the interface is manually indicated as the droplet boundary, so that the software knows that at that boundary, ϕ =0.

4. 8. Meshing of the domains

After defining the different domain and boundary conditions, the meshing of the different domains must be done to fully define the model. As it was previously introduced, the FEM revolves around the division of a domain into smaller elements, which can be done with the meshing process. **Meshing** is, therefore, referred to the transformation of a continuous geometric shape into elements of different shapes (i.e., into a geometry composed by finite elements, as seen in Fig. 4. 2). These elements can be of 1D, 2D or 3D, depending on the system:

- 1D: the elements are lines (either straight or curved).
- 2D: the elements can be triangles or quadrilaterals.
- 3D: the elements can be tetrahedral, pyramidal, triangular prisms or hexahedral.

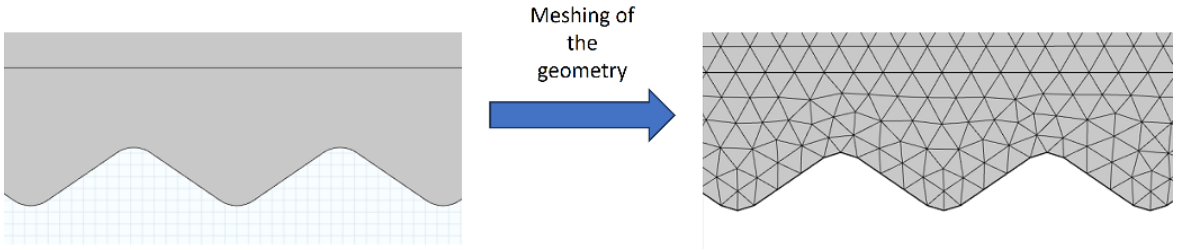

Fig. 4. 2 Meshing of a geometrically structured surface

The size of each mesh element can be varied manually. The smaller (the finer) the elements, the geometry is shaped with a higher number of cells and the mesh reproduces the geometry more accurately. Hence, the simulations can be more accurate in their results. However, the computational cost greatly increases, as the simulation has to calculate the equations in a higher number of cells. On the other hand, increasing the size reduces the computational cost, but the geometry is mora abrupt, and the results are less reliable. Therefore, the meshing of the domains needs to fulfil a trade-off between the quality and accuracy of the results, and the computational cost. The size of the mesh can be manually controlled by modifying the next parameters:

- Maximum element size: as its name suggests, a maximum size value can be set. This value could be used to ensure the quality of the geometrical shape at certain critical locations.
- Minimum element size: the minimum value can be useful to prevent the introduction of too many elements in locations such as corners or fillets.
- Maximum element growth rate: it defines the difference between the cell size in zones where a transition between smaller and bigger elements occurs.
- Curvature factor: it determines how big an element can be alongside a curved boundary. This value could be of interest in zones where rounded edges (fillets) or where the droplet exists.
- Resolution of narrow regions: this value controls the number of layers of mesh elements in narrow regions. This parameter could be of interest in the domains near the textured surface.

The mesh size should be carefully defined in order to fulfil the accuracy-computational cost trade-off. As it is going to be explained later in this thesis, the mesh size is highly dependent on parameters such as the surface texture and ε. In fact, in the case of the former, due to the importance of the texture effect on the CA, the cell size should be small enough to properly define the geometry of the textures and, in the latter case, it should be smaller than ε to avoid numerical instabilities. Moreover, the accuracy of the simulation results and the convergence highly depends on the mesh

quality. This is determined with the skewness, which is the default quality measure, and penalizes those elements whose angles are too large or too small when compared to those of an ideal element. The absolute value of the skewness is always between 0 and 1, being 0 when the mesh element is degenerate, and 1 when its shape equals the ideal one. In fact, a bad meshing process could generate inverted cells (which corresponds to the skewness values closer to 0), which may be responsible of the divergences of the solution.

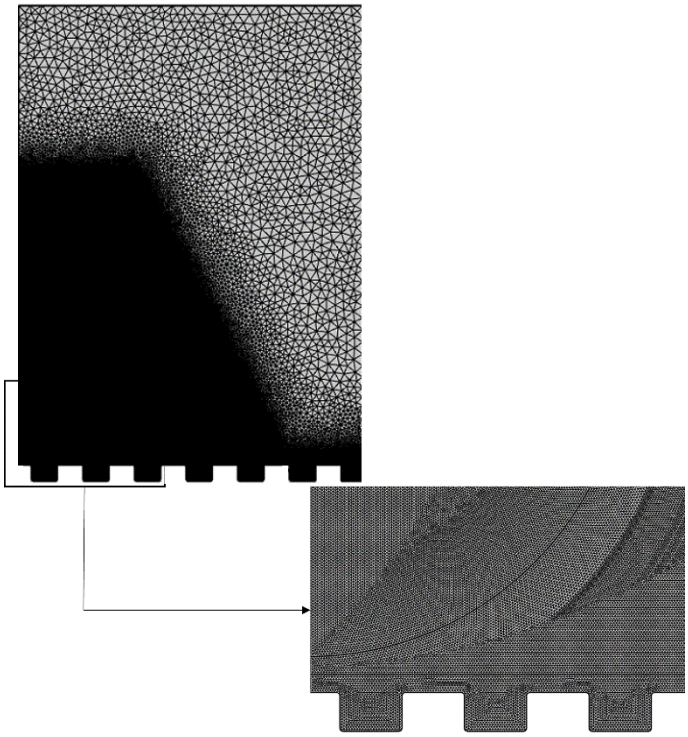

Fig. 4. 3 Meshing example of the different domains conforming the simulation setup for a given texture. The finer mesh locations correspond to the result of a mesh improvement process. Due to the very small element sizes from the near texture zones, a zoomed image of this location is provided

Fig. 4. 3 shows a meshing example of one of the considered 2D texture, in which the cell size difference between the different domains can be observed. This difference occurs due to the mesh improvement process needed to be performed in the mesh locations where a change in the shape has been observed (i.e., the locations from which the droplet interface moves during the simulation). In order to evaluate the meshing process, COMSOL can provide a statistical summary of the overall mesh of the system (see Fig. 4. 4). This table give information regarding the average and the minimum mesh quality of every cell, including a histogram, and is a helpful tool to correctly assess the viability of the constructed mesh for the simulation.

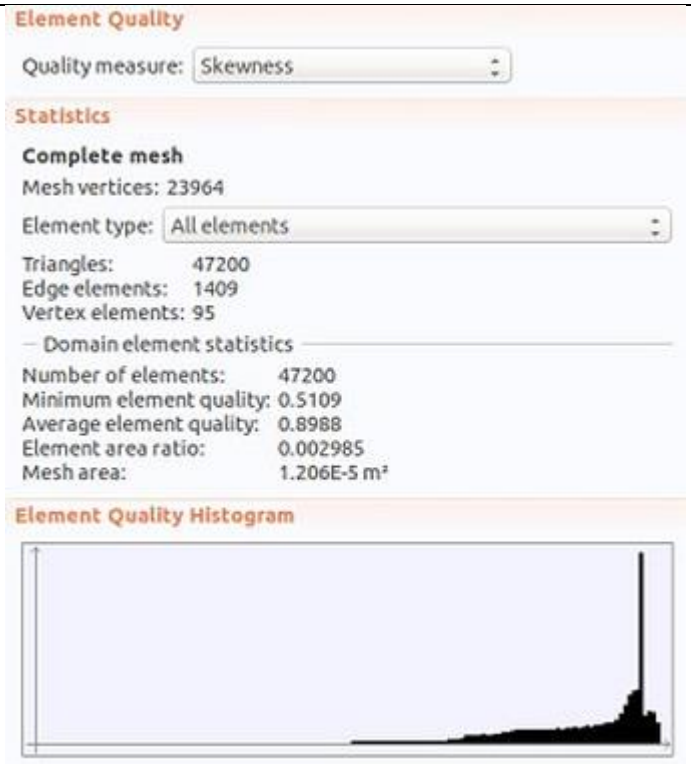

Fig. 4. 4 Example of a mesh statistic summary

In the Annex III (SIMULATION RESULTS), the different configurations available in the solver are described.

4. 9. Transition to 3D domains

After setting up the 2D setup, a 3D domain is considered. In this case, the double depth of the experimentally developed textures can be considered, as observed in Fig. 4. 5. To reduce the number of elements in the meshing of the 3D system, due to the symmetric nature of the selected structures (i.e., square-like pillars), two symmetry planes are considered. The symmetric planes divide the system into eight sections, and one of them is selected to be modelled. The geometric texture is constructed using the included CAD constructor from COMSOL, then two work planes are defined delimiting the desired section (both planes form an angle of 45 degrees), which are lastly used to plot the complete 3D results by including a "mirror + rotate" operation. This result can be observed in section 5. 3. 4.

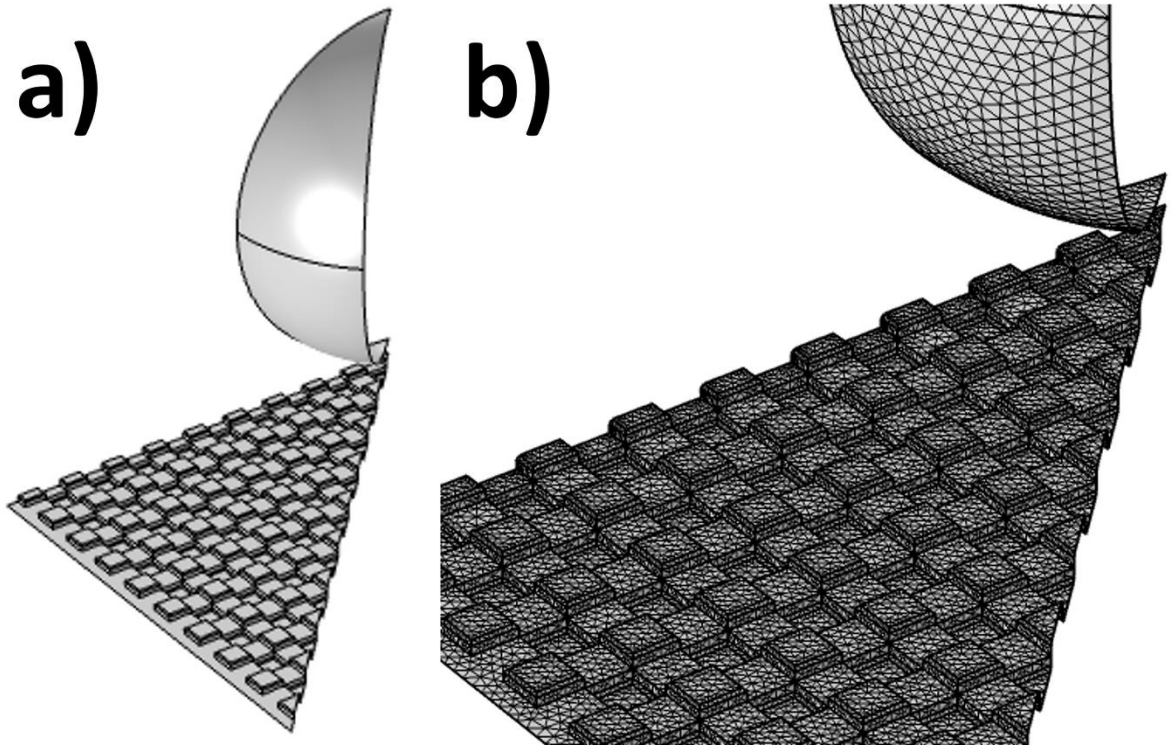

Fig. 4. 5 Definition of the a) 3D geometry, with two plane cuts where the symmetry planes are located, and b) 3D meshing, on a close-up image where the double depth can be observed.

Contrary to the 2D simulations, the main objective of the 3D simulation revolves around the observation of the effect of the double depth and the several spreading directions on the final shape of the droplet and the air entrapment inside the cavities for different selected textures. The main reason is the relatively high computational cost required to simulate a three-dimensional physic, as the number of elements in this case drastically increases when compared to the analogous 2D case.

Chapter 5

RESULTS AND DISCUSSION

Part I

Laser parameter optimization for the ablation of polypropylene

5. 1. 1. Introduction

The objective of the first part of the results chapter is to perform a laser parameter optimization procedure capable of providing an optimal trade-off between the structure quality and the throughput for the considered material. In this part, a complete comparative study is done between the two available pulse emitting options (SP and BM). The main focus of this section is to identify the advantages and/or disadvantages that the BM offers when compared to the more traditional SP mode.

This part is divided into two sub-sections, i.e., a fundamental study of the influence of the laser parameters on the laser-material interaction, and the results observed by introducing new parameters in order to develop square-like structures. In the former, the ablation mechanism observed on the PP is assessed. In both sub-sections, a comparison between the results obtained with the BM and SP is established, ensuring that the same conditions are applied in both cases.

5. 1. 2. Study of the laser-material interaction

5. 1. 2. 1. Burst Mode and Single Pulse mode influence on topography

A first study of the topographical parameters induced on the PP by each pulse on both SP and BM and a set of laser parameters is introduced in this section. Firstly, a series of experiments were focused on the identification of the **damage pulse energy threshold** (i.e., the E_p from which a morphological change can be induced on the PP surface, but no removal occurred) and the **ablation pulse energy threshold** (the E_p from which not only the morphological change is induced but also material removal can be observed) by the development of craters at wavelengths of 517 nm. Therefore, several craters were developed with increasing E_p from 0 to 22 μJ (for pulses of 300 fs). As observed in Fig. 3. 4, the low absorptance of the PP indicates that the laser-polymer interaction must be nonlinear (or multiphoton absorption) due to the absence of electronic transitions between the valence and the conduction bands with a single-photon energy [49]. Due to the high peak irradiances provided by femtosecond laser systems (10^{12} to 10^{15} W/cm^2 [233]), the PP absorbed the energy through these nonlinear mechanisms.

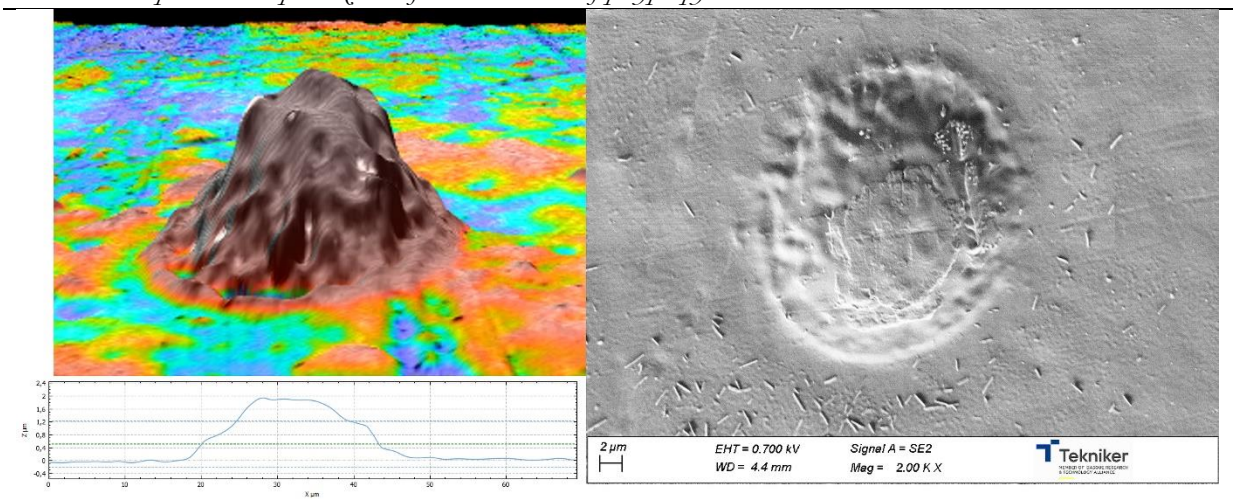

Fig. 5. 1 Confocal (left) and SEM (right) images of a crater produced by an individual SP.

Fig. 5. 1 shows the confocal and SEM images of the resulting craters. It can be observed that after the interaction between the individual SP and the PP, no volume removal occurred, but a hump-like structure was produced, even at the highest E_p available in the laser system. This **swelling** phenomenon observed in Fig. 5. 1 after the incidence of the individual SP could be caused by the formation of inside the PP sample when irradiated with ultrashort pulses in the fs range, as explained by Rahaman et. al. [62] and Ortiz et. al. [234]. These bubble formations inside the surface may push the material through the outer layers; however, due to the very short relaxation time induced by the ultrashort fs pulse, these bubbles cannot collapse in time to cause the formation of the crater. These results were also observed by Belaud et. al. [235] who reported this swelling behaviour with individual SP with fluences up to 3.25 J/cm^2. Therefore, due to this swelling phenomenon, the spot diameter and the ablation E_p threshold cannot be obtained by fitting them to the equation provided by Liu [236] (see eq. (62)), and Pettit et. al. [237] (see eq. (63)).

$$D_c^2 = 2\omega_0^2 \ln\left(E_p/E_{th}\right) \quad (62)$$

$$d = 1/\alpha_{eff} \ln\left(E_p/E_{th}\right) \quad (63)$$

Where E_{th} is the ablation E_p threshold, d is the crater depth and α_{eff} is the effective absorption coefficient (not applicable to multiphoton ablation processes). This swelling phenomenon was the reason why the removed volume of the first pulse was not included in Fig. 5. 2. Therefore, the first

pulse modified the morphology and rugosity of the surface, but it did not create any crater. Furthermore, E_p below 2.5 μJ (corresponding to fluence values of 1.174 J/cm^2) could not produce any observable change in the surface. Therefore, it can be confirmed that this value corresponds to the damage E_p threshold. This value may represent a transition between the linear and nonlinear ablation regimes of the PP, which is similar to the value of 0.94 J/cm^2, reported by Rahaman et. al. [62, 64].

After the incidence of a second, third and fourth pulses (either in SP and BM), the hump like structure defined by the swelling phenomenon was collapsed and a well-defined crater could be observed (see Fig. 5. 2 a), defined by its diameter and depth, unlike before. However, in the case of the second pulse from the BM (Fig. 5. 2 b), the **redeposition** of the removed material inside the structure did not allow to obtain a reliable measurement of the crater depth and removed volume (the diameter was measurable). The redeposition occurred when, due to the relatively small temporal distance between the pulses in the burst, the latter incident pulse interacted with the particle plume, pushing back the material into the crater [238]. Therefore, the depth and volume results of this particular case were not included.

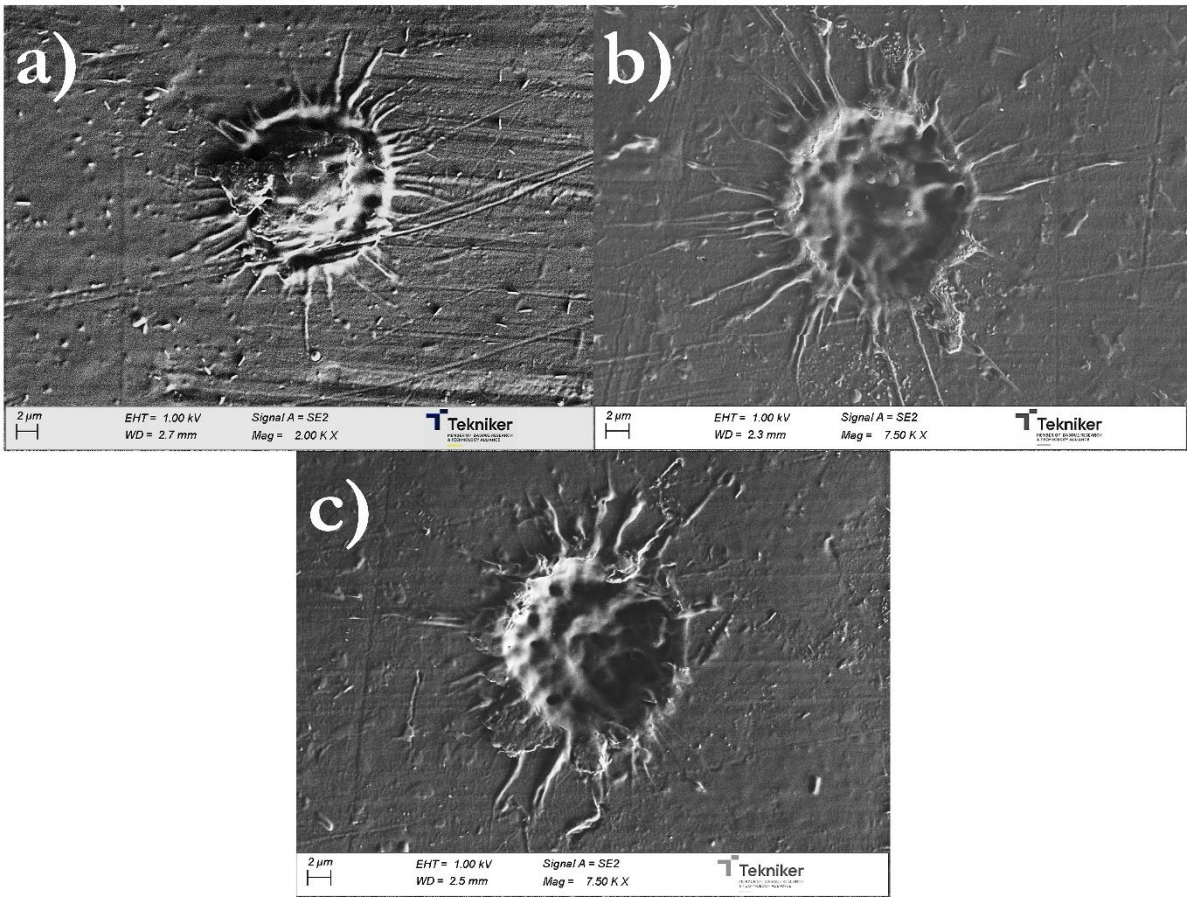

Fig. 5. 2 SEM images of a) one individual 3.5 µJ pulse, b) 2-pulsed burst of 6 µJ per pulse and c) 2 SP of 6 µJ per pulse.

Hence, even though the first pulse was not capable of preventing the formation of the dome-like structure even at E_p values of 22 µJ, the second pulse in both pulse emitting modes overcame this situation, even at low energies. This could be due to the incubation effect, as the rugosity and the optical properties [64] of the surface changed after the incidence of the first pulse, decreasing the ablation E_p threshold of the following incident pulse. Moreover, the high irradiances from the ultrashort pulses at the localized area defined by the spot led to the ionization of the surrounding ambient air and the promotion of the plasma plume when the pulse was capable of eliminating a certain material volume. These phenomena could interact with the incoming pulses depending on the temporal separation between them, and these interactions were indirectly observable in the results. In fact, the plasma and/or particle cloud formation could absorb or reflect part of the incoming energy from the following pulses and, consequently, the energy that reached the surface would be reduced (which is also known as the energy **shielding**) [44, 54, 238].

Fig. 5. 3 and Fig. 5. 4 show the evolution of results in terms of a) D_C, b) d_C and c) V_n when varying the E_p for both the BM and SP, respectively. In this thesis, each individual pulse is denoted as

"pulse" and "layer" for BM and SP modes, respectively. It should be clarified that, unlike the case of the crater diameter and depth, the plotted removed volume corresponded to the contribution of each pulse to the total eliminated volume, as explained in section 3.5 (Fig. 3. 12). On the other hand, in the case of the crater diameter and depth, the total values are included instead. It can be observed that, as explained before, the redeposition of the material in the second pulse in the BM prevented the plotting of the crater depth and V_n, as opposed to the second layer from the SP. Hence, the results for the second "pulse" were not included in the graphics in Fig. 5. 3 b) and c).

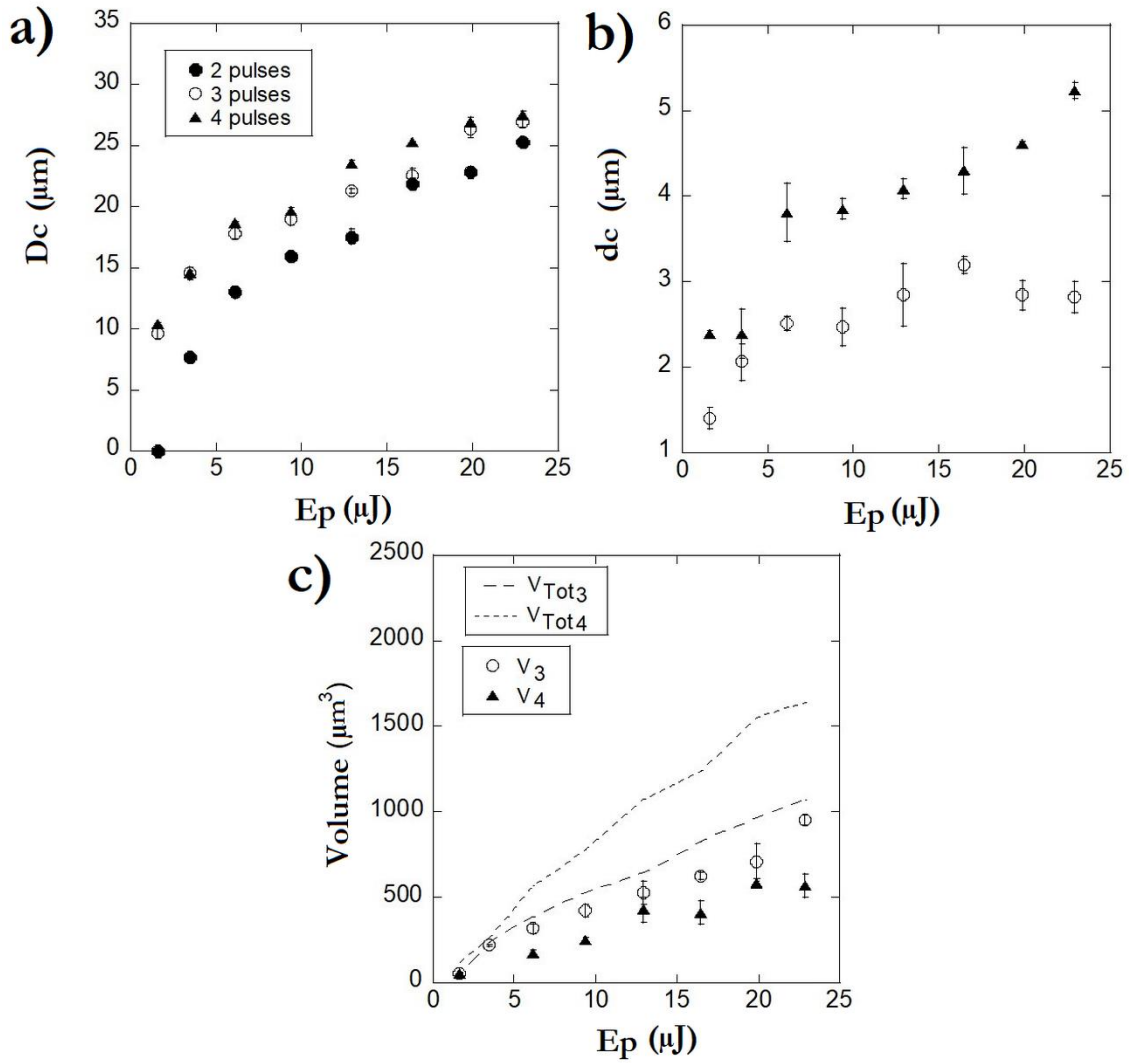

Fig. 5. 3 a) D_c; b) total crater depth, d_c and c) ablated volume per pulse (V_n) and total ablated volume per n pulses (V_{Totn}) in BM as function of the E_p. Data from 2 pulses was not included in depth and volume graphics, the material accumulation inside the crater hindered the depth and volume measurements.

This thesis establishes a possible hypothesis to explain the results observed in Fig. 5. 3 and Fig. 5. 4, based on the interaction between pulses due to the relatively low temporal distance between them. The hypothesis states that the interaction between the pulses has more impact in the BM than in

the SP, which affects the individual performance of each pulse within a larger E_p range. As previously explained, the pulses inside a burst are temporally separated by 20 ns (as determined by the oscillator repetition rate of 50 MHz), whereas in the SP mode, these pulses are separated 1.43 µs (corresponding to the amplified repetition rate of 750 KHz), and hence, the consecutive pulses from the SP mode reach the material 30 times slower than in the BM. This low temporal distance can strengthen the shielding and redeposition effects on the incoming pulses. Therefore, this hypothesis relates the D_C, d_C and V_n with these pulse interactions.

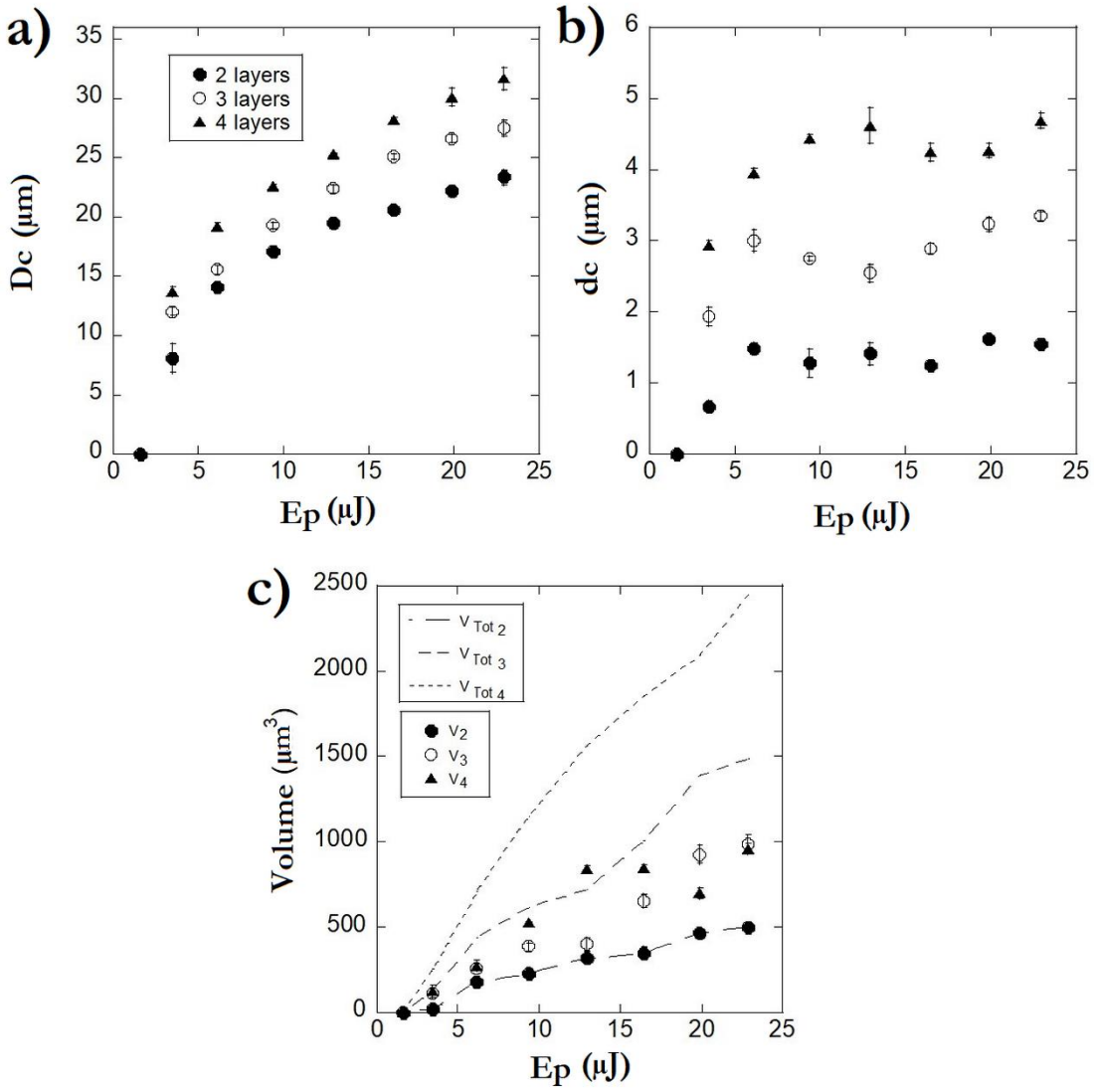

Fig. 5. 4 a) D_c; b) total crater depth, d_c and c) ablated volume per pulse (V_n) and total ablated volume per n layers (V_{Totn}) in SP as function of the E_p. In this case, well-defined craters were obtained with two pulses, and all topographical dimensions were able to be included in the graphics.

The results from Fig. 5. 3 a) and Fig. 5. 4 a) shows a clear increase of the D_C with the E_p in BM and SP, respectively, following a similar trend after the incidence of each pulse or layer. In the specific

case of the BM, the introduction of a third and a fourth pulse with the same energy did not provide of any diameter increase. On the other hand, the same behaviour cannot be observed in the SP mode, as increasing the number of pulses involved a remarkable diameter increase.

These findings could demonstrate how the temporal distribution of the pulses on the material could play a key role in the ablation mechanisms of the PP. Taking into consideration that the pulse irradiances followed a Gaussian profile (see Fig. 5. 5, based on [81]), it can be defined an ablation irradiance threshold, denoted as I_{th}, equivalent to the previously defined ablation E_p threshold, E_{th}. The crater diameter, D_C, is defined by this threshold, as it can be observed in Fig. 5. 5), and its size depends on the E_p, [81]. However, when two pulses with a temporal distance small enough to interacted with each other, the shielding from the plasma and/or particle plume and/or the air ionization resulted in a consequent reduction of the energy reaching the surface. This was translated into higher intensities needed from the consecutive pulse to overcome the shielding and ablate the surface, i.e., the threshold increased to I_s. Therefore, the new crater diameter, corresponding to this new threshold, D_{CS}, did not increase in size and the resulting crater would equal the value of D_C. The findings from Fig. 5. 3 a) and Fig. 5. 4 a) demonstrate that in the BM, the pulse interaction effect was more pronounced than in the SP, and a stronger shielding effect was seen in the former case [44].

On the other hand, if the temporal distance between pulses was high enough, due to the incubation effects promoted by the rugosity modification and the accumulated defects of the surface, the diameter could be increased to D_{Cinc}. This was possible as the incubation effects and the lower interaction between pulses after the incidence of multiple pulses, which may cause the promotion of the optical absorption of the sample due to the shrinkage of the optical bandgap (E_g) and, consequently, decrease the ablation energy threshold [239]. Therefore, this threshold decreased from I_{th} to I_{inc}, resulting in the previously indicated diameter increase, as observed in Fig. 5. 5. This behaviour was more appropriate to the SP ablation results from Fig. 5. 4 a), as depicted by the clear D_c increase with the incoming number of pulses.

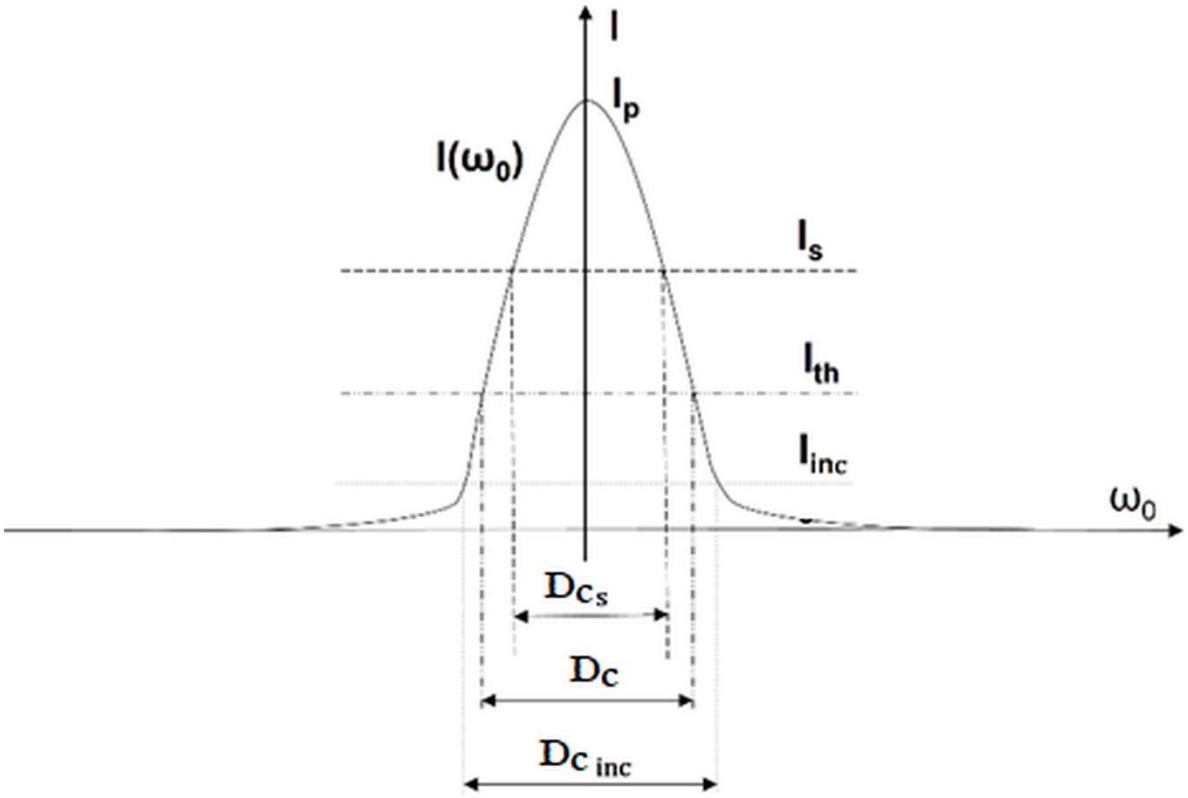

Fig. 5. 5 Gaussian irradiance profile of the laser beam. The ablation irradiance thresholds for each intrinsic, shielded and incubation cases are included, with the corresponding output crater diameter value.

The shielding explanation can also be applied to the rest of the figures. From Fig. 5. 3 b) and Fig. 5. 4 b), it can be observed that, in general terms, increasing the E_p eventually led to a saturation effect, as a further increase in E_p did not lead to an increase in the depth. Apart from the fourth pulse from the BM, this characteristic E_p was identified at values of E_p = 6 μJ. This saturation effect was also observed by Ortiz et. al. [234], who reported a groove saturation depth on Poly-L-lactide (PLLA) polymer when applying SP picosecond pulses, in which the ablation mechanism involved the multiphoton ablation as well, and by Sohn et. al. [59, 240], who reported a similar trend in crater depth saturation on an oriented polypropylene when irradiated by 184 fs SP at 785 nm wavelengths with energies up to 500 μJ. This saturation could be related to the difference in the laser ablation regimes when the E_p was increased, as explained by Chen et. al. [241] who performed a thorough study regarding the different laser ablation regimes on silicon samples. Lastly, the fourth pulse from the BM was the only case in which higher E_p did not lead to a plateau, which could be related to the relatively higher SRR of the third pulse, as it is going to be explained in the section 5. 1. 2. 2.

However, for a better understanding of the evolution of the crater depth with each pulse, the volume removed per pulse should also be considered (see Fig. 5. 3 c) and Fig. 5. 4 c)). In these figures, both the removed volume per pulse, V_n (depicted as dots), as the corresponding total removed volume, V_{totn} (lines), were plotted. Here, it can be observed that in the case of the BM, the third pulse was capable of removing more volume than the following pulse. This could also be related to the pulse interaction mentioned before: the second pulse in the BM removed a negligible volume due to the redeposition of the material back into the crater, which would have created a small plume that may have contained particles of the removed material. Therefore, the third pulse would find little obstacle to reach the surface and consequently, in addition to the incubation effect, the energy efficiency was increased, as it is going to be seen shortly. This high-volume removal led to a greater plasma plume that absorbed and reflected a greater amount of the incoming pulse from the fourth pulse, resulting in less depth removal. Therefore, this pulse volume reduction between the third and fourth pulses could strengthen the possible explanation regarding the pulse interaction, which was also observed by Metzner et. al. [223] on metal alloys. They reported a repetitive V_n reduction as they increased the pulse number inside a burst up to eight. Even though different materials were considered, the observed behaviour could be a particular case of the studies performed by Metzner et. al. on metal.

5. 1. 2. 2. Burst Mode and Single Pulse mode influence on crater quality and efficiency

Among all the different aspects that could be taken into consideration regarding the quality of a structure, the accumulated material (or recast material) on the edges of the features was the most critical parameter (even if it meant a reduction of the throughput of the process), as the objective was to both minimize the possible effect of this debris on the contact line movement (and hence in the measured CA) and to produce surface textures whose profiles are as close as possible to the theoretically defined textures (optimal quality), used in the DoE and in the computational modelling.

Fig. 5. 6 shows the morphological characterization of craters developed at E_p at which the depth saturation identified previously was reached (E_p =6 μJ, and Ep=13 μJ in the exceptional case of 4 pulses in SP) and at maximum E_p (E_p =22 μJ) for the BM (Fig. 5. 6 a) and SP (Fig. 5. 6 b). An illustrative comparison was performed when different number of pulses of identical E_p reached the sample with both pulse emitting modes, in which the crater topography and material redeposition

and/or splashing around the structure was assessed. For both modes, the same number of pulses of the same E_p delivered in the BM produced craters with less splashing than in the SP mode.

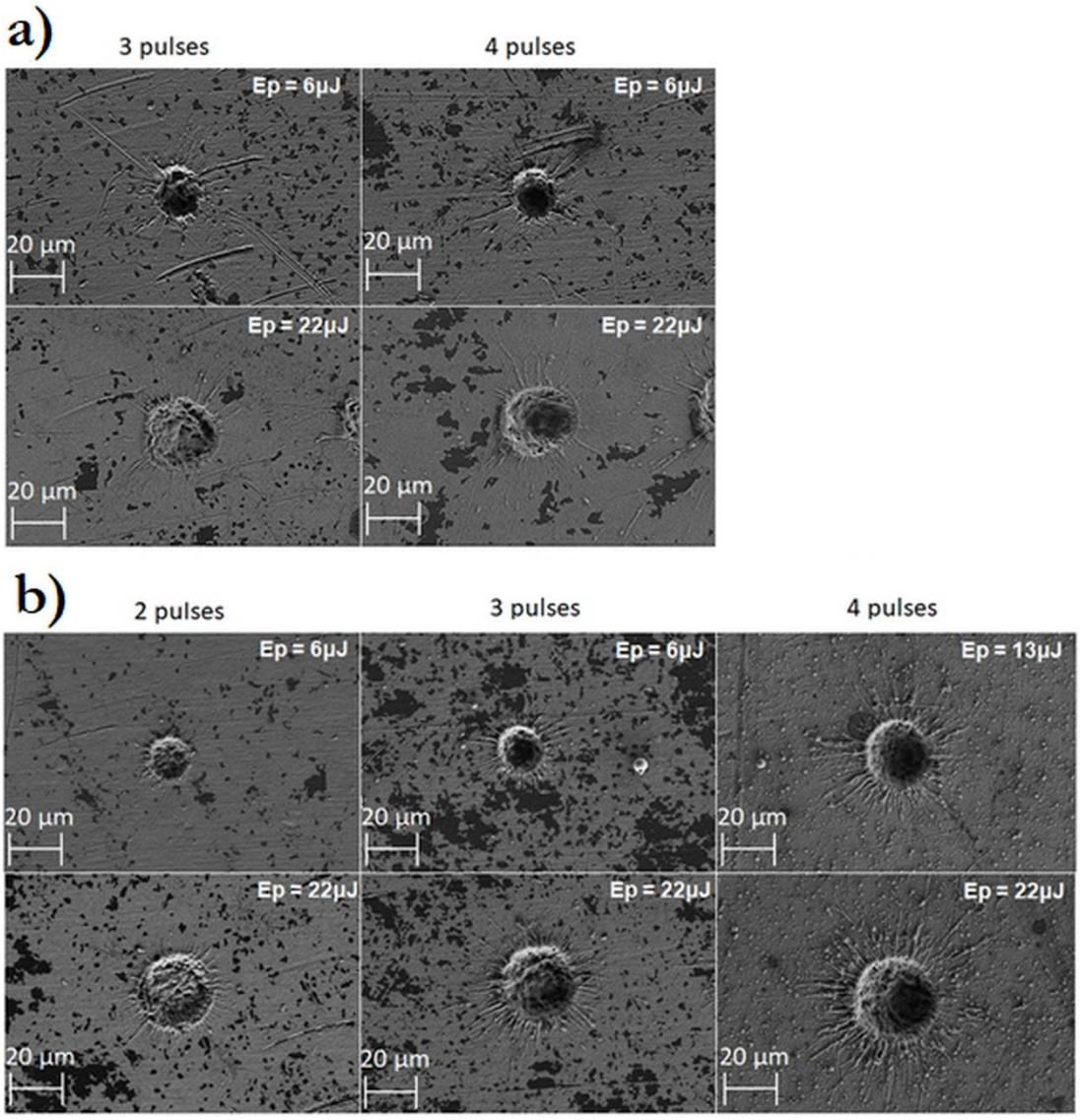

Fig. 5. 6 SEM images of craters developed with a) BM and b) SP mode. The second pulse of the burst was not included, as it did not ablate a well-defined crater in terms of depth.

Considering the crater quality, it can be observed in Fig. 5. 6 and Fig. 5. 7 that the laser ablation of the PP induced pore formation inside the crater, which was observed in other works, in materials such as PMMA [242, 243], PLLA [56, 234] or PS [244]. This could be due to the ablation mechanism described before and it involved the possible formation of gas bubbles inside the deeper layers of the material [56]. Fig. 5. 6 reveals that increasing the E_p resulted in a crater with higher diameters and material remelted around it (or splashing). For both emitting modes, craters developed in BM with the same number of pulses and the same energy delivered less splashing than

SP. However, the total removed volume from the SP was greater than in the BM, which could result in an increased material redeposition and an overall worse quality. Therefore, in terms of crater quality, a fair and reliable comparison should be performed between two craters from which the same V_{totn} was removed. For instance, as observed in Fig. 5. 7, comparing craters made with 3 pulses in both modes that would meet the requirement from before, pulses with E_p values of 20 μJ in the BM and layers with E_p of 16 μJ in the SP mode should be compared. In terms of quality, the SP crater showed more redeposited material and higher splashing and thus, the BM seemed to generate craters with improved quality.

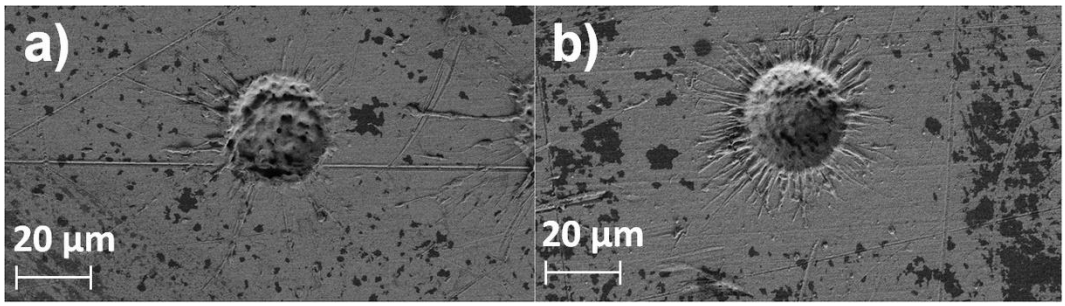

Fig. 5. 7 Craters developed with a) 3-pulsed bursts (BM) of 20uJ per pulse, and b) with 3 SP of 16uJ per pulse.

The efficiency (SRR, as determined by eq. (28)) and the possible interactions between the ablation process of each pulse in both SP and BM were assessed. Fig. 5. 8 present the efficiency of each individual a) pulse and b) layer, by taking into consideration the description provided in section 3.5.

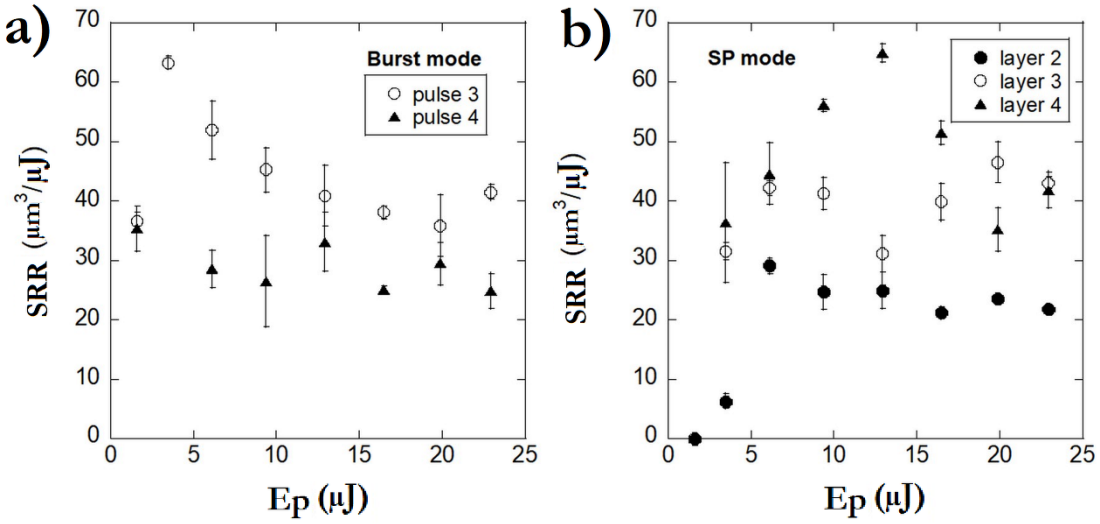

Fig. 5. 8 Specific Removal Rate (SRR) of each pulse with a) BM and b) SP mode as function of the E_p. The second pulse of the BM generated a non-defined crater in terms of volume removal; therefore, the SRR regarding this case is not presented.

The efficiency of each pulse on the ablation of the PP can be used as an easy-to-use approach to understand the pulse interaction. For the BM (see Fig. 5. 8 a), the third pulse showed the highest SRR, more specifically at E_p values of 3.5 μJ for 3 pulses per burst, from which a continued decrease was observed until E_p values of 22 μJ. This could be explained based on the redeposition of the material or by the increased ionization of the air, which led to a higher energy absorption by plasma, more common at higher E_p. The SRR showed the slope variation of the volume when increasing the E_p, which can be seen in Fig. 5. 3 c) and Fig. 5. 4 c), in concordance to the eq. (28). Therefore, working with E_p values closer to the ablation threshold should give a more efficient ablation process. Contrary to the SRR increase with the number of layers that can be observed with the SP (see Fig. 5. 8 b), in the case of the BM, the SRR increased upon emitting the third pulse, followed by an efficiency decrease of the fourth pulse. This SRR behavior between the pulses was included in the review of Förster et. al. [94]. They showed this periodic behavior of the maximum SRR of copper, brass and aluminum when increasing the ppb, as it has been indicated in the present thesis, showing that the shielding and redeposition of material inside the craters may have influenced the ablation process of the PP, which strengthen the possible explanation proposed in this work.

Fig. 5. 9 shows a direct comparison of the SRR variation between the third and fourth pulse in each mode (pulse and layer 3 in Fig. 5. 9 a), and pulse and layer 4 in Fig. 5. 9 b). In general terms, the SRR increases with the E_p from the ablation pulse energy threshold to a value where the efficiency was maximum. This optimal E_p was lower in the BM than in the SP, due to the pulse interaction effects, which permitted the SP to work with higher energies more efficiently. Further E_p increase from this optimal value led to a sudden saturation or decrease of the SRR, indicating that higher energies resulted in lower efficiencies and hence, proves that using lower E_p was appropriate to promote a more efficient ablation process. For the BM, the third pulse showed the highest SRR, while in the SP mode it was the fourth pulse instead, as observed in Fig. 5. 9.

Additionally, it can be seen how the third pulse of the BM removed volume in a more efficient way when the energy per pulse was closer to the ablation threshold, while the SP mode started being more efficient for pulse energies higher than 15 μJ. These results show how high pulse energies induced higher plasma clouds and/or pushed more material in the particle cloud back into the surface, up to a point where the efficiency decreased drastically. The first pulse could not generate a particle cloud due to the swelling effect (even though it could ionize the surrounding air). It was after the second pulse when the material removal occurred and when a particle cloud could appear. However, the low removed volume could imply a weak shielding effect, especially at lower pulse energies, which could explain the increased efficiency (SRR) of the third pulse at these values.

Therefore, the third pulse could have created a plasma and particle plume of stronger shielding effects, which would have led to higher energy absorption and, therefore, a decrease on the ablation efficiency of the fourth pulse, as it can be observed in the case of the BM (see Fig. 5. 8 a).

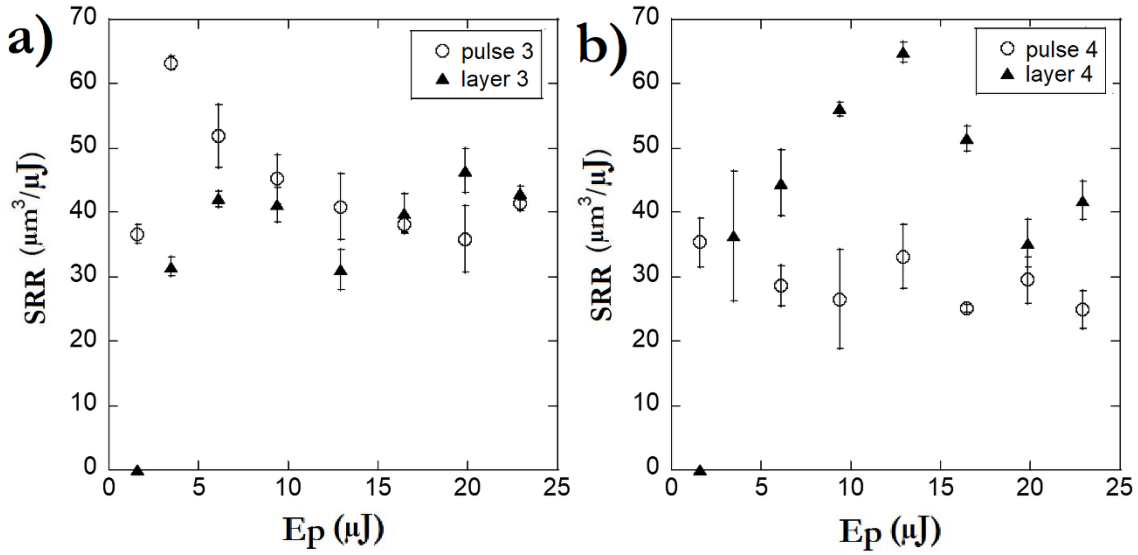

Fig. 5. 9 SRR comparison between both emitting modes for a) the third pulse (BM) and layer (SP) and b) the fourth pulse (BM) and layer (SP).

In the SP mode, on the other hand, due to the bigger temporal separation between pulses, the impact of this shielding effect was not as great as in the other mode, and thus, the fourth pulse was more efficient in this case, which was translated into higher D_C, d_C and V_n (see Fig. 5. 4). Considering 3 pulses emitted in both modes, comparing the craters obtained with an efficiency of 45 $\mu m^3/\mu J$ (9 μJ in BM and 20 μJ in SP mode), the depth and the ablated volume obtained with the SP mode was higher than the obtained with the BM. However, the energy introduced by the burst was half the one corresponding to the SP mode, expecting that the quality of the former was going to be higher, as the pulse energies were closer to the ablation threshold and since the removed volume was 3 times lower. Therefore, higher SRR values meant that the energy was optimally used to ablate more volume (less energy was lost during the entire ablation process), but it did not necessarily involve that it was better in terms of quality.

5. 1. 2. 3. Burst Mode and Single Pulse mode influence on the removal rate

The removal rate (RR) results assessed by eq. (29) can be seen in Fig. 5. 10. When considering the BM, the RR remains constant with 3 and 4 pulses per burst, whereas considering the SP mode, a clear increase with the number of pulses can be identified. Moreover, it can be observed that as the E_p increased, the RR increased as well. The growing trend with the E_p is directly related to V_{totn} showed in Fig. 5. 3 c) and Fig. 5. 4 c), whereas the slope is related to the temporal separation between two consecutive pulses. The latter can be observed by the difference in the y-axis scale of Fig. 5. 10 a) and b). Hence, it can be concluded that the BM is faster since it removed material 45 times faster than in the case of the SP mode. Moreover, considering 4 pulses per burst did not provide any improvement on the RR when compared to the 3-pulsed burst. Working with higher pulse energies provided greater RR, but not only decreased the SRR, but also increased the r_h around the crater edges from 0.632 ± 0.03 μm obtained with 6 μJ (pulse energy that provides the maximum SRR) to values of 0.800 ± 0.18 μm obtained with 22 μJ (corresponding to the maximum removal rate). In addition, the material splashing around the crater increased as well as its overall quality was worse.

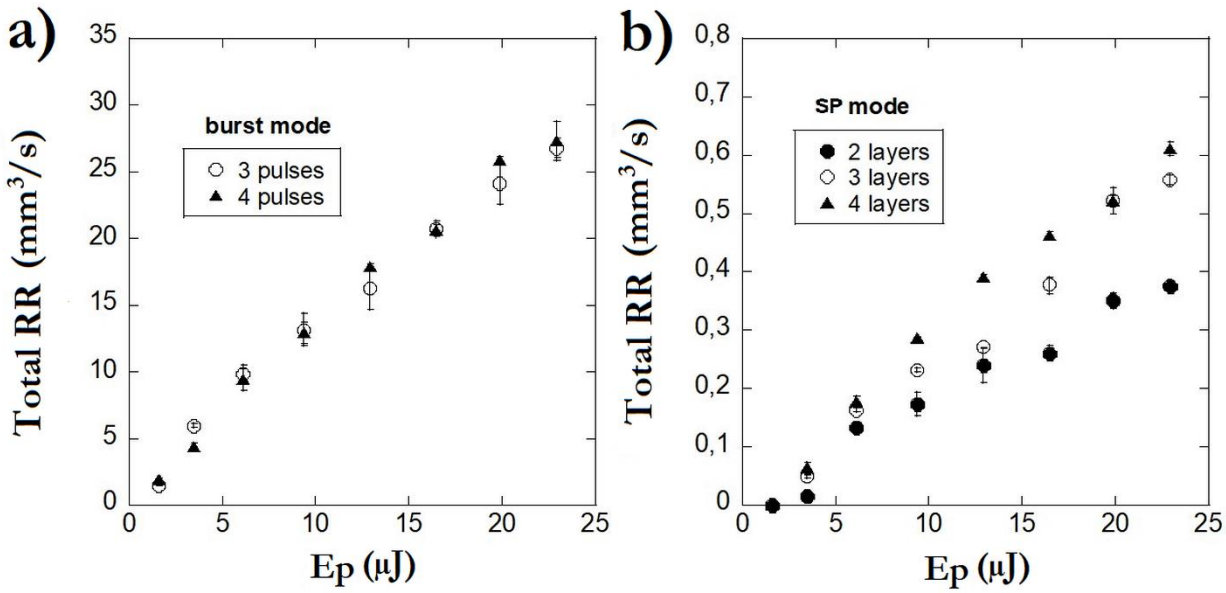

Fig. 5. 10 Total removal rate after 2, 3 and 4 pulses in a) BM; b) SP mode as a function of the pulse energy. The removal rate of the second pulse in the BM was not included due to the redeposition of the material hindering its measurement, Notice the y-axis scale difference.

5. 1. 3. Assessment of the overlap and pulse energy effect on the ablation process

5. 1. 3. 1. Overlap effect on one direction (grooves)

From the results presented in section 5. 1. 2, related to the crater development, the BM with 3 pulses per burst demonstrated to be the most promising laser regimen to meet the requirements contemplated in this work.

Several grooves were developed while varying the pulse overlap, i.e., by changing the v_s, as the f_b was kept constant at the maximum available value of 750 kHz due to throughput reasons. Due to the negligible temporal distance between the pulses inside the burst when compared to the burst repetition rate and the scanning speed (this distance was 667 times lower than the burst repetition rate), it was assumed that the three pulses inside the burst were deposited in the same spot defined by D_C. Several U_d values were considered, from 50% to 90% (following the equation (30), which corresponded to v_s values from 2227 mm/s to 445 mm/s, respectively. All the grooves were performed at a single scan level (or overscan). Fig. 5. 11 shows a) the groove profiles at different U_d values and b) the groove d_g, w and r_h accumulated on the edges. It can be observed that, as U_d increased, not only the grooves were deeper, but also their width was higher. The recast height did not exceed the 1 µm height in any case and in general terms this value was higher as U_d increased.

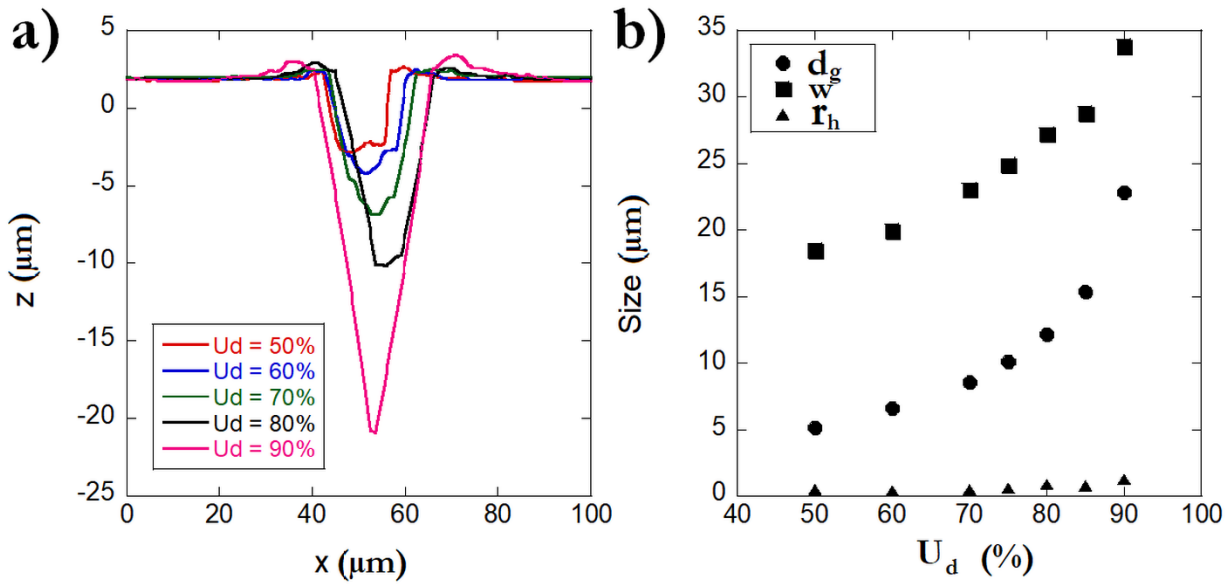

Fig. 5. 11 a) Groove profile, and b) topographical parameters from the groove with different overlap values

Fig. 5. 12 a) shows the SRR and RR of the laser processing of the groove structures for several U_d values. It can be observed that the higher the U_d, the better results in terms of SRR and RR, however the quality of the structures were reduced and produced a higher r_h The most suitable results would be the ones that would offer the highest SRR and RR values, and the lowest recast heights, as explained in section 3.5.

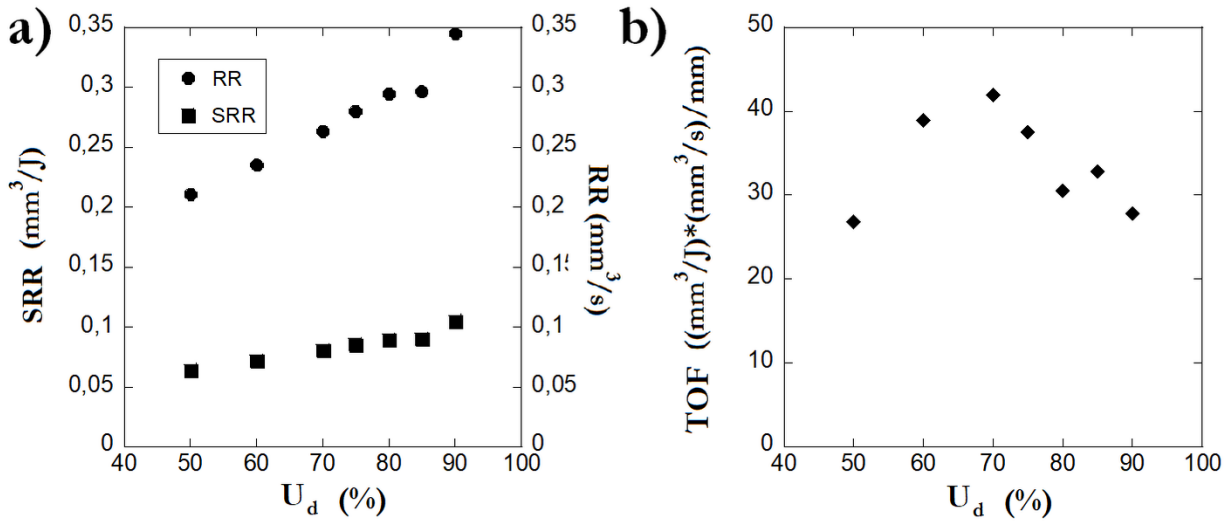

Fig. 5. 12 a) SRR and RR results and b) quality-throughput trade-off factor, for each overlap value

Fig. 5. 12 b), it can be deduced that working with Ud = 70 % provided the results with the highest trade-off and hence it was the selected overlap for the development of the cavities. It can be seen that, even though higher overlaps provided higher removal rates and the energy was more efficiently used to remove a greater volume, the quality was worsened. Le et. al. [97] observed that, in case of copper and steel, it was preferable to work with lower overlap values in BM (60% in steel).

Introducing pulse bursts overlapped to each other with constant pulse energies showed different results from the craters. The higher the overlap, the higher number of pulses that reached the sample. More specifically, considering that each burst had 3 pulses, and that the number of bursts inside the line can be obtained by dividing the total length of the line by d_{bb}, the number of pulses ranged from approximately 1000 (U_d=50 %) to 5000 pulses (U_d=90 %). This would mean that the total energy deposited on the latter line would be 5 times higher than in the former. From Fig. 5. 11, it can be seen that the line depth increased at an exponential rate with the pulse overlap, similar to the width of the line, and the recast material height did not show big differences, even though it was higher as the overlap raised. These minor differences may have occurred due to the possible nonlinear ablation mechanism identified previously at these pulse energies. However, the results

observed from Fig. 5. 12 b) showed that overlaps between 60 % and 75 % were the most optimal to accomplish the defined requirements in terms of TOF.

5. 1. 3. 2. Pulse energy effect on two directions (cavities)

After selecting the optimal overlap value, a new pulse energy study regarding the efficiency, throughput and quality were performed on the BM with 3 pulses per burst, now taking into consideration the repetition rate and the scanning speeds. Moreover, the recast height values could be potentially assessed, due to the overlapping in both perpendicular directions, which could not be considered in craters as deeply as in this case.

Fig. 5. 13 resumes the results observed in the cavities in terms of d_S, r_h, SRR, RR and TOF. As expected, the depth increased with the pulse energy, reaching a maximum height value over 100 μm. This topographic parameter followed a linear trend with the E_p. However, the recast material did not show this linear behavior, as it presented a sharp increase from 6 μJ to 9 μJ, being the latter a value from which the quality decreased drastically. In terms of SRR and RR (Fig. 5. 13 b), they were calculated following the eqs. (31) and (32). Considering the SRR, varying the E_p its maximum value at 2 μJ, followed by a continued reduction as E_p increased. This behaviour was similar to the trend observed in craters, even after the introduction of the new laser parameters (i.e., the f_b and the v_s). The RR increased linearly with the pulse energy, similar to the depth behavior. Finally, following eq. (33), the quality-throughput trade-off factor was plotted, and it can be observed in Fig. 5. 13 c). Again, working with pulse energies of 2 μJ showed the best results regarding this trade-off, and proved that working with values closer to the ablation threshold was the best option regarding this specific criterion.

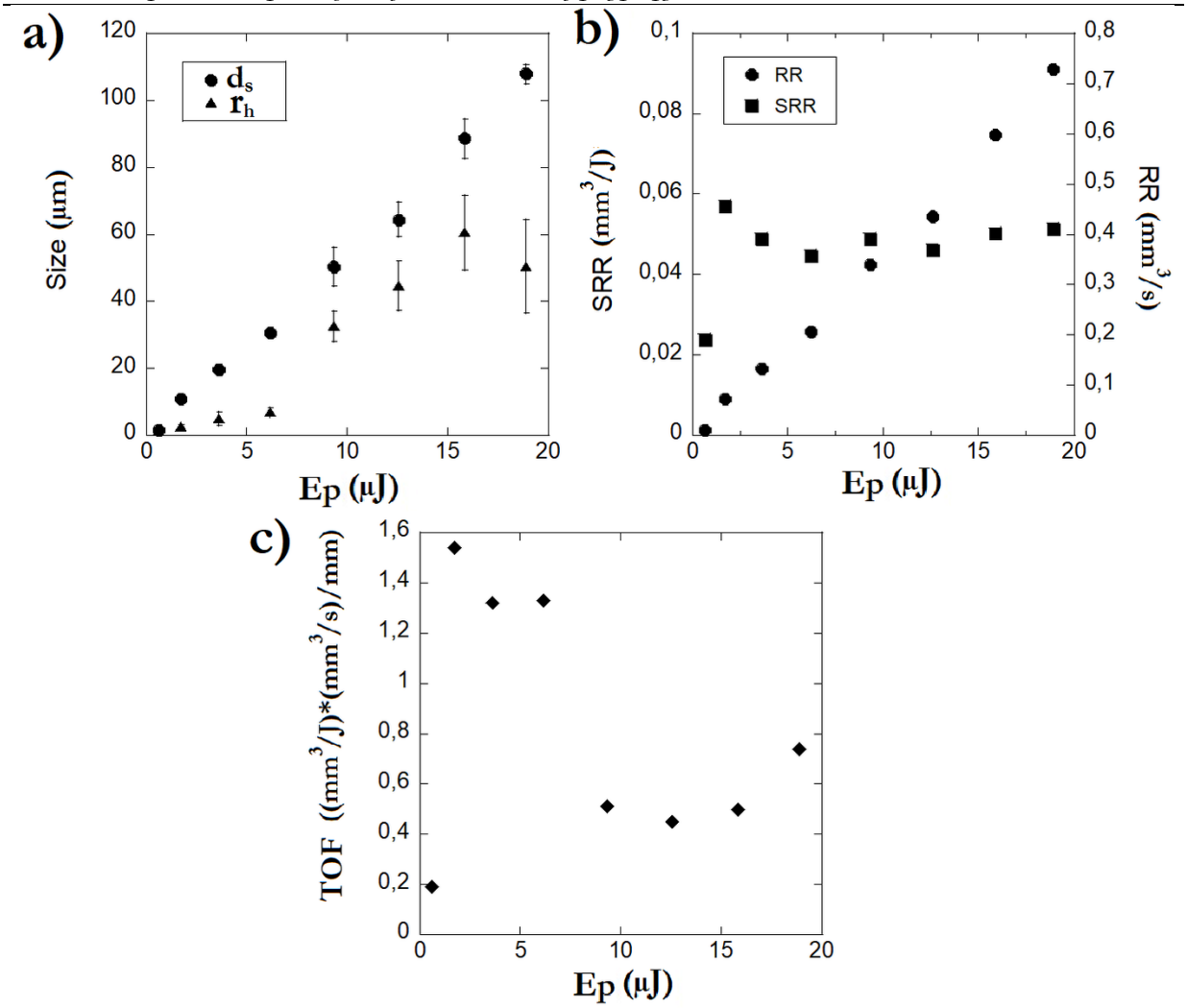

Fig. 5. 13 a) Cavity depth and recast material height, b) SRR and RR and c) trade-off factor of the cavities developed with different values of Ep.

Fig. 5. 14 shows the SEM images of the PP intrinsic flat surface (Fig. 5. 14 a)) and the cavities performed at different pulse energies, more specifically, with 3.5 µJ and 20 µJ. Overall, it can be observed the difference in quality after using higher pulse energies. The higher the E_p, the deeper the structure, and also the smoother it may look the cavity surface inside; however, as the parallel lines were developed, the material was eventually accumulated and deposited on the edge, as observed in Fig. 5. 14 c). Therefore, in terms of quality, cavities developed with lower E_p showed an overall better quality.

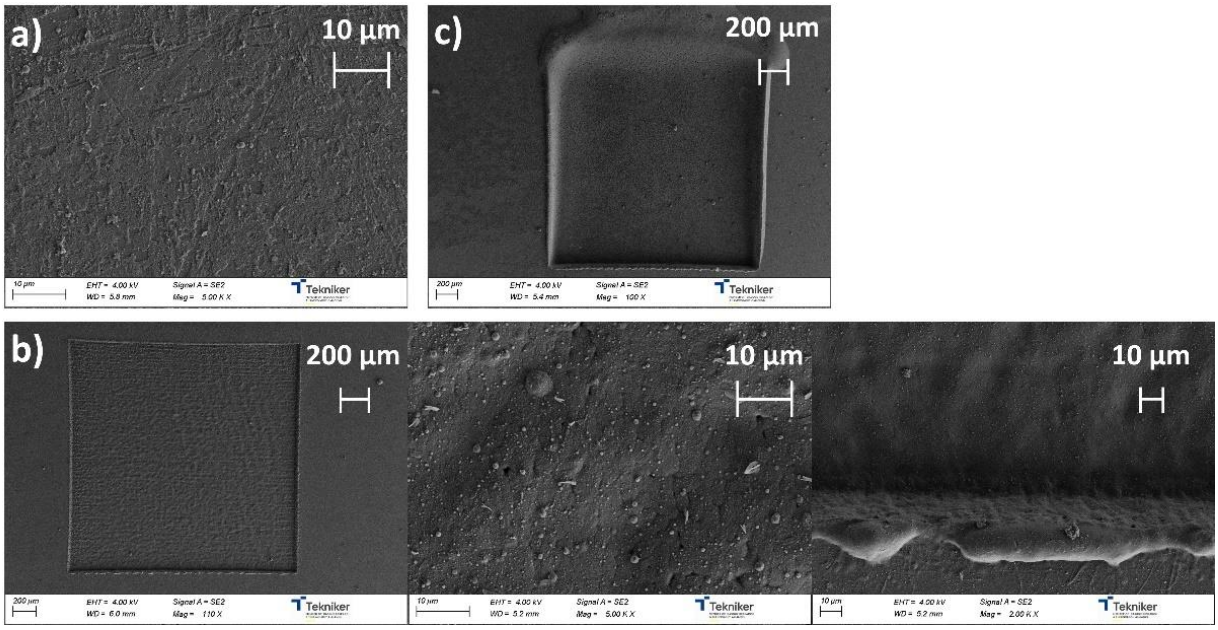

Fig. 5. 14 SEM figures of a) intrinsic flat surface, b) an overall view of a cavity performed with E_p = 3.5 µJ, a detail of the surface morphology and a detail of the edges, and c) a cavity developed with 20 µJ

Observing the results from the cavities, as depicted in Fig. 5. 13, the crater depth did not reach any saturation effect, contrary to the crater-like structures, possibly due to the high temporal distance between the bursts (4 µs, 3 times higher than the temporal distance between SP pulses), which could permit the plasma plume to be weaker or disappear, even at high E_p and, additionally, the incubation effect, led to a clear increase of the depth. However, the high number of pulses of increased pulse energies implied a consequent accumulation of residual heat and a thermal damage that produced a drastic increase of the r_h that greatly decreased the quality of the cavity, as observed in Fig. 5. 14. An increased E_p alongside the high number of pulses in the cavity could have led to an increment of the temperature of the surface to values higher than the melting point, and thereby the thermal effects were dominant. Contrary to the results from the craters, even though the ablation mechanism changed with the pulse energy, the cavity depth did not reach a saturation, possible due to, principally, the introduction of a bigger temporal separation in the form of the burst repetition rate.

From Fig. 5. 13 b), observing the SRR evolution with the pulse energies, it can be concluded that, even though the depth showed a clear increase with E_p, the lower efficiency observed in craters (see Fig. 5. 8 a)) was reproducible in this case, which demonstrated the importance of the pulse interaction inside the bursts even in this case. Hence, the energy distribution played a key role in the SRR and quality of the structures. In the case of the grooves, the total deposited energy was increased with the rising of the overlap between bursts, whereas in the craters and cavities, it was due to the increasing of the E_p. Therefore, it should be obvious that, due to the pulse interactions

between the pulses inside the burst predominated against the interactions between the bursts, increasing the overlap would not affect the SRR negatively, but it did when increasing the pulse energy in the case of the cavities. On the other hand, in terms of RR, the results showed a similar trend than in the other cases, demonstrating that the material ablation in a more thermal regime were still better in terms of throughput. However, when a good trade-off between quality and throughput was searched, as observed before, the more non-lineal ablation, due to the weaker interactions between pulses and the lower recast material produced, should be selected (in this case, pulse energies of 2 μJ).

Part II

Laser surface texturing for the wettability control of polypropylene: a semi-empirical Design of Experiments

5. 2. 1. Introduction

Once the laser parameter window has been optimized, in this second part of the results section the final parameter approximation is performed to develop textured surfaces. In this section, this process optimization will be addressed to minimize the thermal affection and thus, ensure that quality of the microstructures is as close as possible to the modelling features. A Design of Experiments (DoE) is performed in order to provide a semi-empirical model able to predict the CA of a textured surface on a PP sample. Moreover, the effect of each topographic factor on the wettability is identified throughout the implementation of a regression model.

5. 2. 2. Laser texturing process

The laser parameters selected from the previous steps were considered for the development of the 27 textures defined in the DoE (. Table 5. 1. In the following sections, a hypothesis is assumed. The **null hypothesis H_0** is as follows: the CA variation with the physical modification n a polymeric material by LST is mainly due to the topography effects. The non-null hypothesis (H_1) says that the chemical modification of the polymeric properties after the incidence of ultrashort pulses have a greater effect on the CA variation. The numerical results from the simulations in section 5. 3. 3 can provide the most conclusive outputs, due to the possibility of eliminating the chemical effects on the textured surfaces.

Table 5. 1 Laser parameters for the laser texturing

Pulses per burst	λ (nm)	τ (fs)	E_p (μJ)	v (mm/s)	U_d (%)
3	517	300	2	1500	70

First, small textured areas of 5x5 mm^2 were developed following the strategy depicted in Fig. 3. 11. In general terms, as explained in the previous sections, the heat accumulation is an important parameter to take into consideration in the laser ablation of the PP, due to its relatively low melting temperature. In order to ensure comparatively good quality structures, not reaching that temperature value is desired, and thereby, while using the BM with the corresponding repetition rate modification

from eq. (16) may result in an advantageous situation, due to the longer time to cool down the sample, still low E_p are needed in order to ensure that objective. Therefore, in this specific case, taking into consideration the computational simulations that are going to be performed afterwards, quality structures are prioritized (i.e., the absence or minimization of recast material accumulated on the edges of the microstructures), rather than throughput. In this case, the number of **overscan** or **scan levels** (i.e., the number of times the same vector was repeated at the same location, N) were varied to provide the textures with the pillar height defined in the DoE. It was observed that, depending on the pulse energy and the number of N, a recast material can be observed either in the edges inside the texture, or at the top of the pillars (see Fig. 5. 15). to eliminate or reduce the debris of the edges, additional scan levels at pulse energies closer to the ablation threshold were considered. This threshold was identified at E_p values of 1 μJ, which was slightly lower than in [245] due to the incubation and heat accumulation effects added by the pulse overlapping.

Table 5. 2 summarizes the parameters used to develop the different textures, in which the number of scan levels with pulse energies of 2 μJ (N_1) and with pulse energies of 1 μJ (N_2) are indicated. The textures were developed as a combination of these two pulse energies (N_1 + N_2). In Fig. 5. 15 it can be observed how following this strategy the texture quality was increased both in the cavities and on top of the pillars.

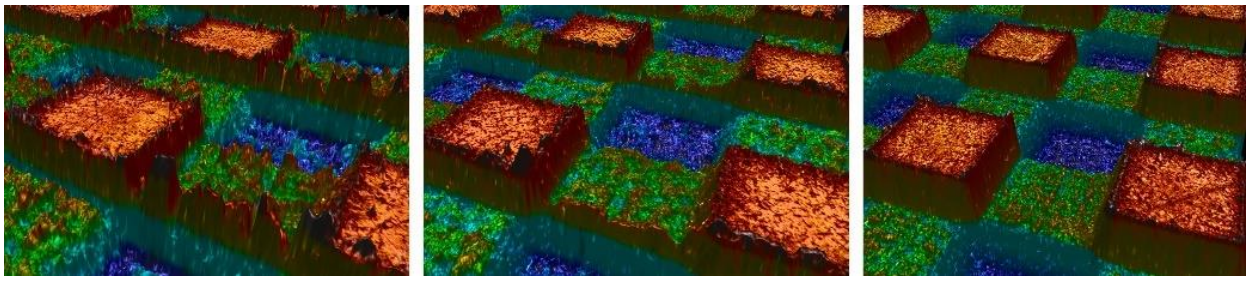

Fig. 5. 15 Recast material accumulated on structures, for the same E_p with one scan level (left), 2 scan levels (middle) and with additional low E_p scan levels (right)

Table 5. 2 Laser parameters adapted to obtain the desired depth. The total depth was obtained as a combination of N_1 + N_2 scan levels.

h (μm)	N_1 (Ep = 2 μJ)	N_2 (Ep = 1 μJ)
10	1	3
40	1	20
70	1	40

Table 5. 3 gathers the topographical dimensions regarding each developed texture, alongside the measured CA.

Table 5. 3 Topographical definition of each texture, and the measured CA

Texture	a (μm)	b (μm)	h (μm)	r_f (-)	f_{SL} (-)	CA (º)
1	75	75	10	1.267	0.250	129 ± 6
2	75	75	40	2.067	0.250	140 ± 2
3	75	75	70	2.867	0.250	140 ± 0
4	75	150	10	1.178	0.111	130 ± 1
5	75	150	40	1.711	0.111	137 ± 5
6	75	150	70	2.244	0.111	139 ± 2
7	75	225	10	1.133	0.063	130 ± 3
8	75	225	40	1.533	0.063	131 ± 1
9	75	225	70	1.933	0.063	136 ± 1
10	150	75	10	1.178	0.444	125 ± 4

11	150	75	40	1.711	0.444	125 ± 7
12	150	75	70	2.244	0.444	140 ± 0
13	150	150	10	1.133	0.250	133 ± 1
14	150	150	40	1.533	0.250	138 ± 2
15	150	150	70	1.933	0.250	135 ± 1
16	150	225	10	1.107	0.160	127 ± 1
17	150	225	40	1.427	0.160	138 ± 1
18	150	225	70	1.747	0.160	132 ± 2
19	225	75	10	1.133	0.563	135 ± 1
20	225	75	40	1.533	0.563	139 ± 2
21	225	75	70	1.933	0.563	138 ± 1
22	225	150	10	1.107	0.360	131 ± 1
23	225	150	40	1.427	0.360	142 ± 1
24	225	150	70	1.747	0.360	144 ± 2
25	225	225	10	1.089	0.250	121 ± 4
26	225	225	40	1.356	0.250	138 ± 3
27	225	225	70	1.622	0.250	137 ± 1

As it can be observed in Fig. 5. 16, in general terms, low recast material heights were obtained and, as the depth was increased, the ratio r_h/h was decreasing (from approximately 0.18 with h=10 μm to 0.05 with h =70 μm), indicating that the recast height did not grow when higher number of N were applied, reaching a possible saturation value of approximately 3.5 μm. This could be related to the different ablation regimes occurring during the texture development, as explained in [246] with

Si wafers, in which the authors observed how the recast layer height increased with the fluence and identified different trends within several fluence ranges. Moreover, as indicated previously in this work, and as explained in [62], [73] and [245], the swelling phenomenon could potentially generate this recast material, alongside the shielding plasma provided by the three-pulsed bursts and the non-evaporated material due to the possible heat-accumulation produced by residual heat accumulated on the surface. Fig. 5. 17 shows the SEM images of the textures labelled by a) 2, b) 12, c) 24, and d) 25. In here, the difference in the rugosity may be observed, and the lower the pillar height, the higher the rugosity. Fig. 5. 18 shows the SEM and confocal images of the textures 2 and 24, corresponding to pillar heights of h = 40 μm and h = 70 μm.

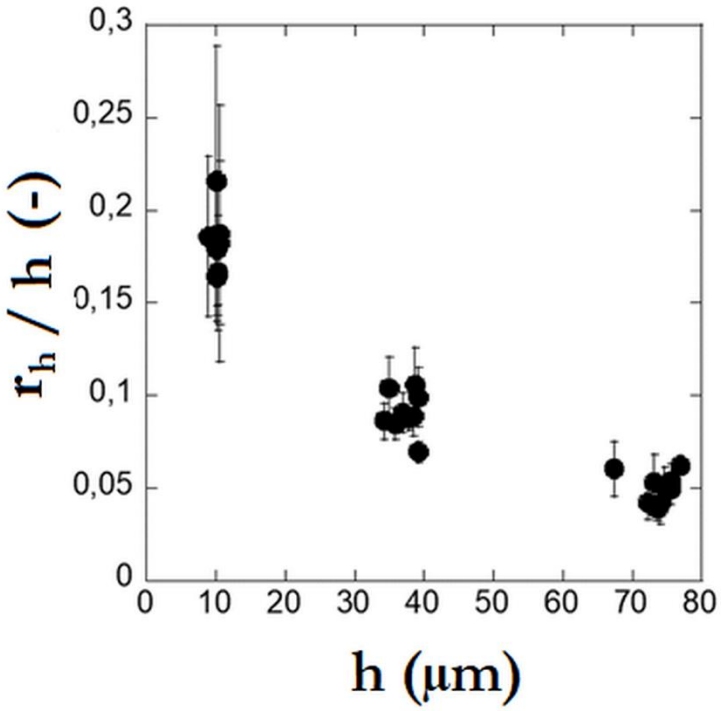

Fig. 5. 16 Recast layer – height aspect ratio for each obtained pillar height.

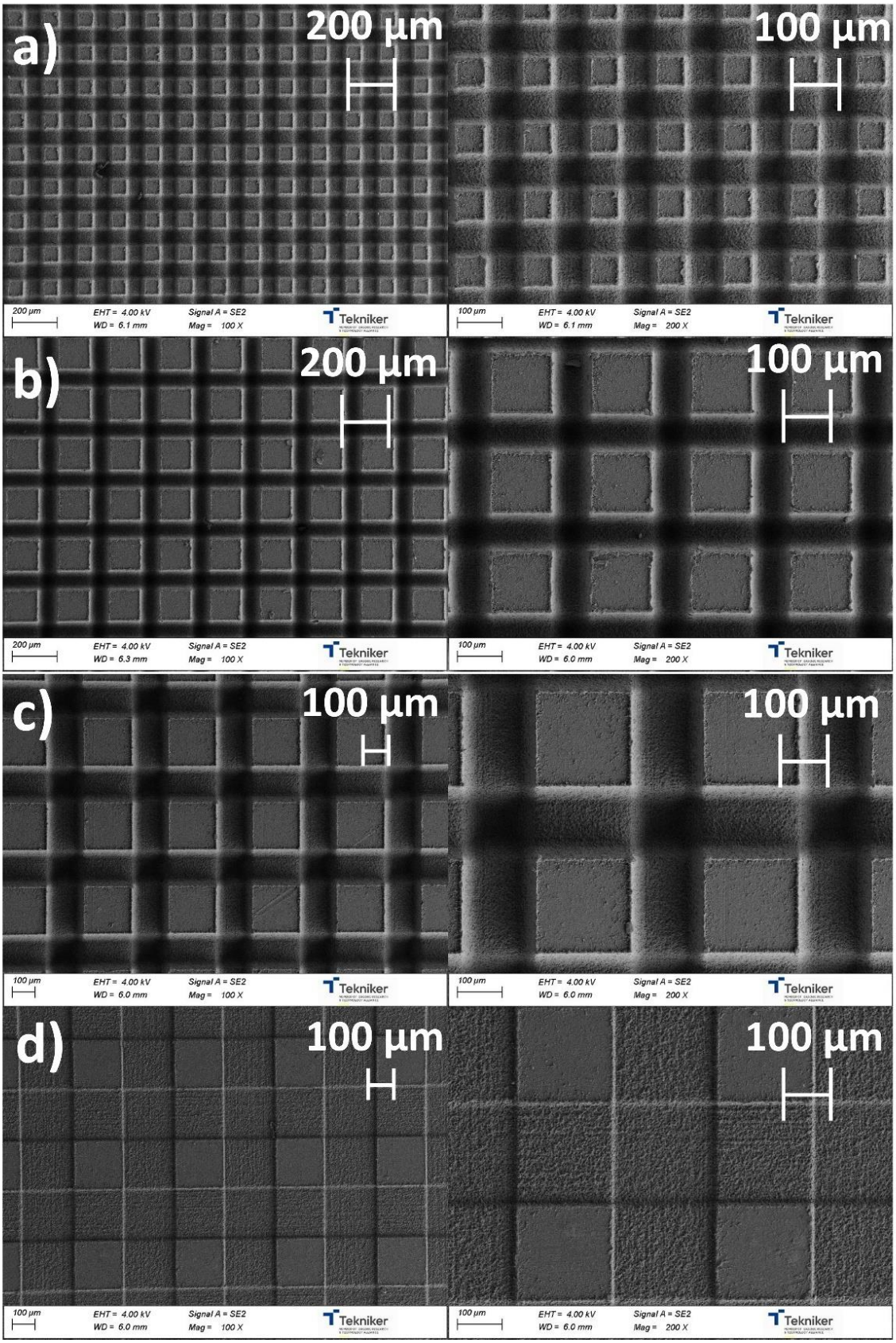

Fig. 5. 17 General (left) and detailed (right) SEM images of the textures labelled as a) 2, b) 12, c) 24, and d) 25

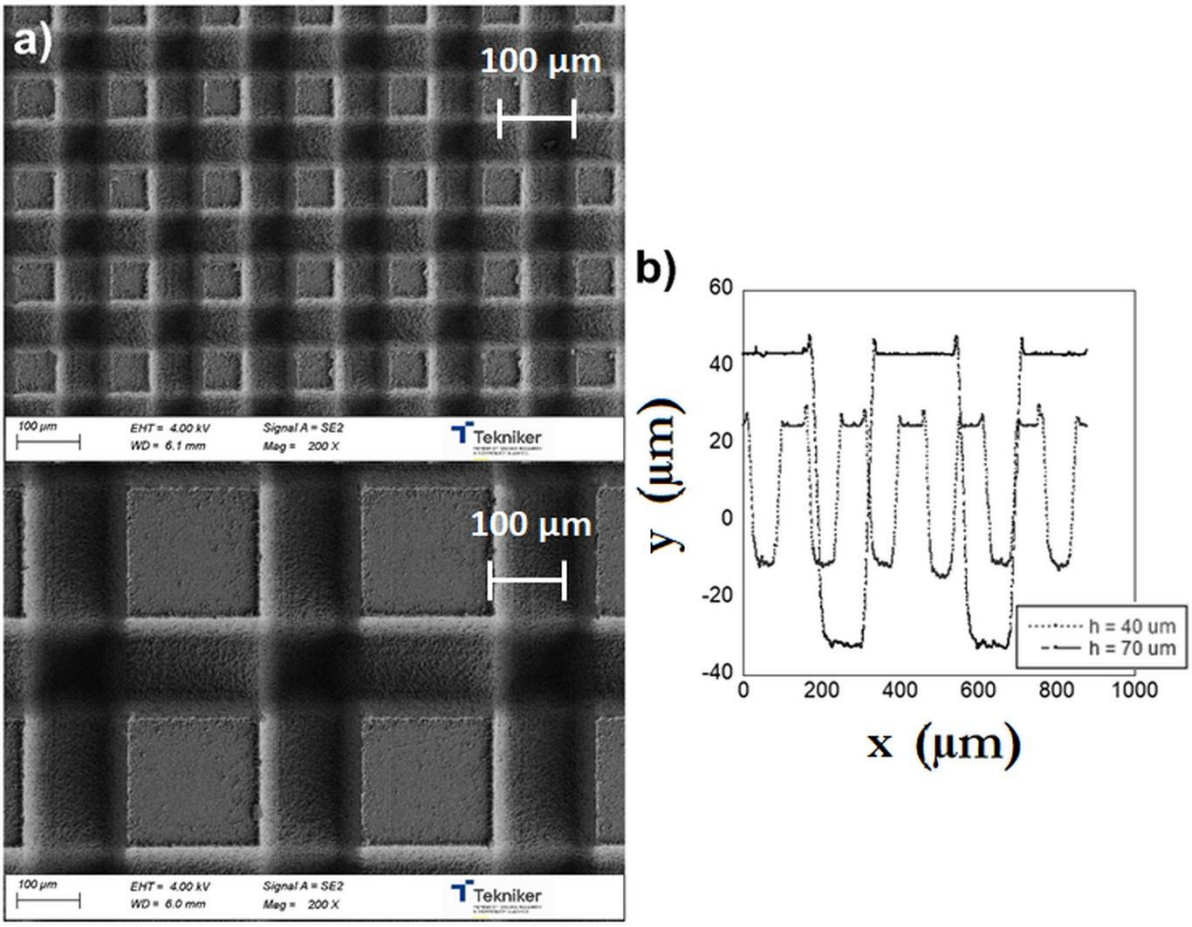

Fig. 5. 18 a) SEM image of textures with h = 40 um (top) and h = 70 um (bottom), and b) the respective texture profile obtained with the confocal microscope.

Fig. 5. 19 a) shows the average CA of the 27 textures as a function of the corresponding r_f (see eq. (20)). It can be observed how, due to the surface patterning provided by the laser technology, the measured CA value raised from 111º (intrinsic value of an untreated surface) to a maximum value of approximately 145º, making the surface more hydrophobic than it was on a flat surface. Fig. 5. 19 b) shows the droplet shape on two textures that provided the maximum and minimum average CA (identified in Fig. 5. 19 a). These specific results corresponded to textures 24 (maximum) and 25 (minimum).

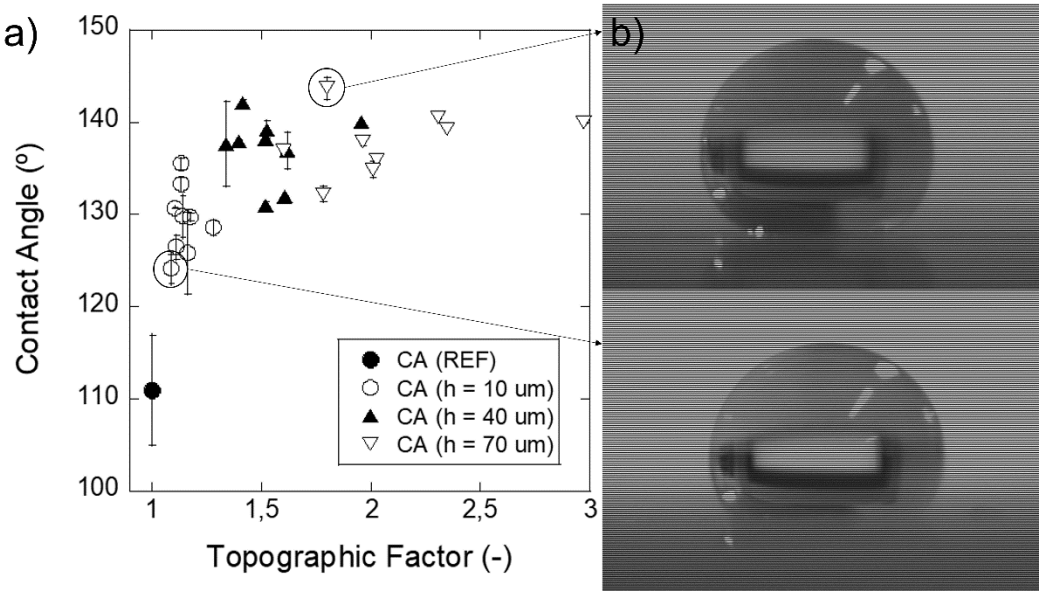

Fig. 5. 19 a) Contact angle variation with the topographic factor, grouped by the three defined h, and b) the image of a droplet placed on the texture that provided the maximum (top) and minimum (bottom) CA

The figure shows three different zones, defined by the pillar heights, h, which reveals the remarkable influence of this topographical parameter on the resulting CA. The results show a sharp increase with r_f values closer to 1, upon reaching a plateau around a r_f of 1.4. Therefore, in general terms, increasing the topography factor leads to higher contact angle values. However, a same r_f value may provide different CA values, due to the different pillar density and height combinations that may result in a same r_f. This behaviour was also observed in injected textured PP samples reported by Romano et. al. [247], in which they developed different geometrical shapes such as pyramids or hexahedral patterns, and they eliminated the chemical effect by performing the laser structuring on a steel mold, and afterwards transferred to the PP. Another report provided by the author of this thesis also observed this behaviour in [151], in which textures based on square pillars with similar r_f (from 1 to 3) values were made on an ABS sample. Therefore, even though different materials were considered, similar trends could be observed, regardless of the potential effect of the recast material on the CA. This trend could demonstrate that solely a topographical modification could only increase the inherent CA of a surface to 145º (in this work), approximately.

Fig. 5. 20 shows the CA variation with the other topographical defining parameter, f_{SL}. It can be observed that, in this case, the CA did not follow any defined trend, contrary to the r_f. These results were in good concordance to the reported figures in a previous work [151] in ABS. The effect of this parameter on the CA can be more easily assessed in the simulation results from the section 5. 3. 3.

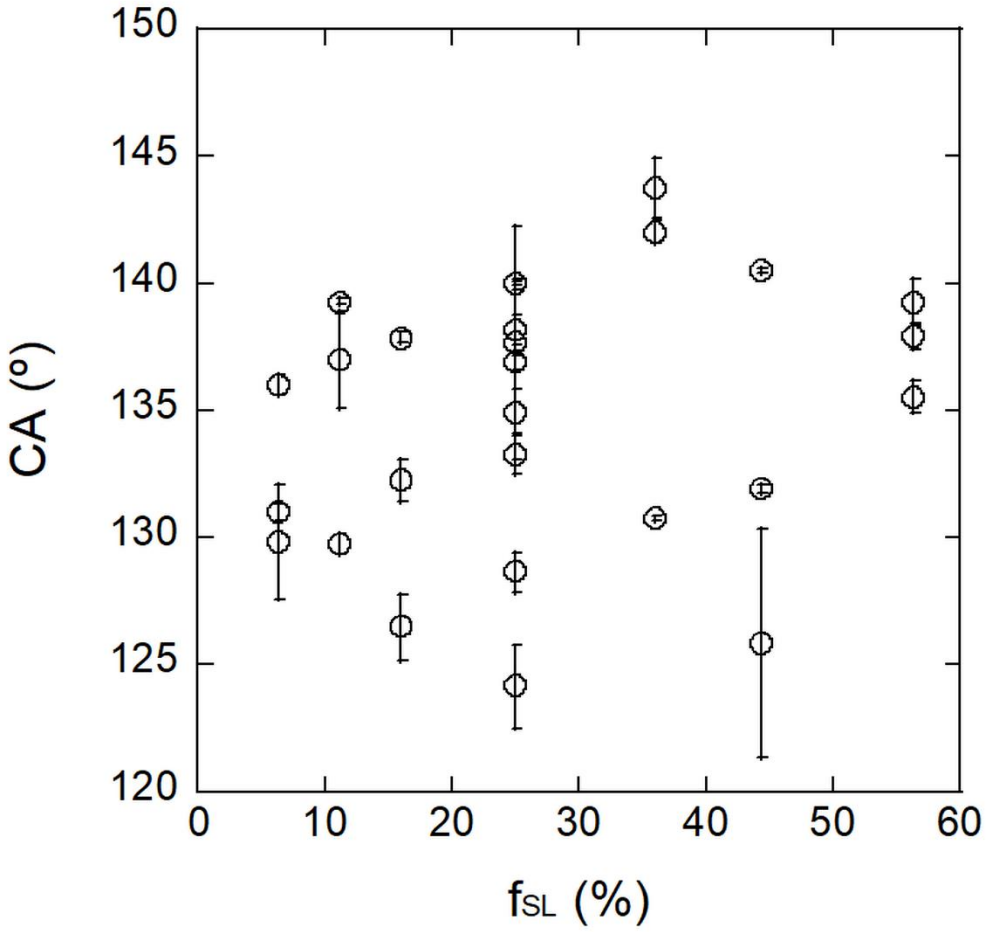

Fig. 5. 20 Solid surface fraction effect on the CA variation

5. 2. 3. Regression model

The topographic factor grouped every dimensional parameter that defined each considered texture. However, the isolated effect of each dimensional parameter could not be fully established only with r_f and f_{SL}. Therefore, a regression model, presented in section 3.4, was developed with a data analysis option available in Excel.

By observing the Fig. 5. 19 and Fig. 5. 20, and assuming the possible complexity of the CA variation with the DoE factors, the equation obtained from the regression would satisfy the following equation:

$$Y = \beta_0 + \beta_1 X_1 + \beta_2 X_2 + \beta_3 X_3 + \beta_{12} X_1 X_2 + \beta_{13} X_1 X_3 + \beta_{23} X_2 X_3 + \beta_{11} X_1^2 + \beta_{22} X_2^2 + \beta_{33} X_3^2$$

(64)

Where Y represented the output of the model, i.e., corresponding to the measured CA, and β represented the model coefficients which would be estimated to represent more accurately the CA variation. In this study, β_0 was the ordinate value at the origin (or intercept), β_i were the lineal coefficients, β_{ii} were the quadratic coefficients, which represented the nonlinearity of the system, and β_{ij} were the interaction coefficients among the factors.

First, a table was drawn, in which the output (Y) and the considered normalized factors (X_1, X_2 and X_3, i.e., the columns referred to the linear coefficients) were included, with their respective levels (as seen in Table 5. 4), following the outline from the Table 5. 3. Afterwards, an additional column was introduced for each quadratic and interaction coefficients observed in eq. (64). Therefore, Table 5. 4 summarizes the initial regression parameters. In this table, the first values that were introduced were the CA values obtained experimentally and the factors, which could adopt a value of -1, 0 or 1, depending on the level (the lowest level, i.e., 75 μm for the X_1 and X_2 and 10 μm for the X_3, equalled -1, whereas the highest level equalled 1). The remaining data was dependant on the values from the linear factors and were calculated with the eqs. (65) and (66):

$$X_{ii} = X_i^2$$

(65)

$$X_{ij} = X_i X_j$$

(66)

Table 5. 4 Factor values from the first regression step

Texture	X_1	X_2	X_3	X_{11}	X_{22}	X_{33}	X_{12}	X_{13}	X_{23}	CA (º)
1	-1	-1	-1	1	1	1	1	1	1	129 ± 6
2	-1	-1	0	1	1	0	1	0	0	140 ± 2
3	-1	-1	1	1	1	1	1	-1	-1	140 ± 0
4	-1	0	-1	1	0	1	0	1	0	130 ± 1
5	-1	0	0	1	0	0	0	0	0	137 ± 5
6	-1	0	1	1	0	1	0	-1	0	139 ± 2
7	-1	1	-1	1	1	1	-1	1	-1	130 ± 3
8	-1	1	0	1	1	0	-1	0	0	131 ± 1
9	-1	1	1	1	1	1	-1	-1	1	136 ± 1
10	0	-1	-1	0	1	1	0	1	1	125 ± 4
11	0	-1	0	0	1	0	0	0	0	125 ± 7
12	0	-1	1	0	1	1	0	-1	-1	140 ± 0
13	0	0	-1	0	0	1	0	1	0	133 ± 1
14	0	0	0	0	0	0	0	0	0	138 ± 2
15	0	0	1	0	0	1	0	-1	0	135 ± 1
16	0	1	-1	0	1	1	0	1	-1	127 ± 1
17	0	1	0	0	1	0	0	0	0	138 ± 1
18	0	1	1	0	1	1	0	-1	1	132 ± 2

19	1	-1	-1	1	1	1	-1	1	1	135 ± 1
20	1	-1	0	1	1	0	-1	0	0	139 ± 2
21	1	-1	1	1	1	1	-1	-1	-1	138 ± 1
22	1	0	-1	1	0	1	0	1	0	131 ± 1
23	1	0	0	1	0	0	0	0	0	142 ± 1
24	1	0	1	1	0	1	0	-1	0	144 ± 2
25	1	1	-1	1	1	1	1	1	-1	121 ± 4
26	1	1	0	1	1	0	1	0	0	138 ± 3
27	1	1	1	1	1	1	1	-1	1	137 ± 1

By introducing the data from this table as an input to the data analysis from Excel, the resulting output provided with the values of each coefficient, alongside their respective probabilities, and the coefficient of determination, R^2, among others. These results help understanding how impactful each factor is on the output (based on the probabilities) and how well the obtained model fits and predicts the output (based on the R^2). Table 5. 5 summarize the most significant results from this first regression model step output.

Table 5. 5 First regression step results for a significance level of 5%

	Coefficients	Probability
Intercept	137.78	0
X_1	0.73	0.39
X_2	-1.7	0.06
X_3	4.48	4.82e-5
X_{11}	-0.46	0.21
X_{22}	0.36	0.07
X_{33}	-0.04	0.02
X_{12}	1.87	0.66
X_{13}	-2.73	0.73
X_{23}	-3.73	0.97

As explained in section 3.4, a backward regression was performed in order to simplify the model and to assess the effect of each factor on the CA. The backward regression was an iterative process in which the next procedure was followed in each step: 1) after the obtention of the previous table, the factor with the highest probability was identified (in the case showed in Table 5. 5, this factor would be the interaction between the cavity width and the pillar height, X_{23}) and hence eliminated from the Table 5. 4; 2) a new regression calculation was performed, and a new table was generated; 3) this process was repeated until no factors with significance levels (probabilities) higher than 0.05 were obtained. Table 5. 6 shows the coefficients obtained after each iteration (notice that, between iteration 4 and 5, two factors were eliminated at the same time, because in that case, the factor X_1 was the less significant one and, due to the eq. (65), the factor X_{11} was consequently eliminated as well).

Table 5. 6 Coefficient values conforming the regression model from each simplification step.

Iteration	β_0	β_1	β_2	β_3	β_{12}	β_{13}	β_{23}	β_{11}	β_{22}	β_{33}
1	137.78	0.73	-1.70	4.48	-0.46	0.36	-0.04	1.87	-2.73	-3.73
2	137.78	0.73	-1.70	4.48	-0.46	0.36	-	1.87	-2.73	-3.73
3	137.78	0.73	-1.70	4.48	-0.46	-	-	1.87	-2.73	-3.73
4	137.78	0.73	-1.70	4.48	-	-	-	1.87	-2.73	-3.73
5	137.78	-	-1.70	4.48	-	-	-	-	-2.73	-3.73
6	137.2	-	-1.70	4.48	-	-	-	-	-	-3.73
7	137.2	-	-	4.48	-	-	-	-	-	-3.73

After 7 iterations, it can be observed that the CA variation could be expressed as a function of exclusively the factor X_3, and eq. (64) could be rewritten as:

$$Y = 137.2 + 4.48X_3 - 3.73X_3^2 \quad (67)$$

By obtaining the h from the eq. (68), the CA variation with the pillar height can be obtained:

$$CA = 124.8 + 0.47h - 0.004h^2 \quad (68)$$

This simplified semi-empirical model (denoted from now on as *Regression model*) provided the pillar height, h, as the most significant parameter on the CA performance, as it was also concluded by the author in [151], Zhang et. al in [187] and Ambrosia et. al. in [248], followed by the pillar density. In [187], the authors observed a similar CA trend with the r_f and observed that the pillar height was the most impactful parameter, whereas in [248], the authors developed a MD simulation in which they observed the CA with the pillar height and f_{SL} separately. They concluded that the pillar CA increased with the pillar height upon achieving the CB state, in which the pillar height had little effect on the CA and established the pillar height as the most critical parameter in the CA variation.

Fig. 5. 21 shows a graphical comparison between the experimental results of the CA and the corresponding value obtained by the regression model (see eq. (68)). It can be observed that the CA increases with the pillar height upon reaching a specific value, from which the curve slope achieves the maximum value, showing an indication that the CB state was reached. These results

are in good correlation with the ones provided by Ambrosia et. al [248], as stated in the previous paragraph. The R^2 equals 0.585 due to the dispersion of the values for each height (defined by the corresponding Bell Curve). However, the regression model defines the position of the average value of each Bell Curve. It can be observed that the increase of the CA reaches a maximum at h values of 57 μm. The variances for each h that form each Gaussian Curves exist due the other two factors (a and b), which, even though their significance was lower than h, their contribution should still be considered when designing the textures. As it can be observed in Table 5. 6, the X_2 factor (corresponding to the cavity width) was not removed until the sixth step, indicating its importance on the CA variation, whereas the X_1 factor (corresponding to the pillar width) was removed in the fourth step. Therefore, the cavity width showed more impact on the CA than the pillar width. Overall, even though the pillar height showed the most impactful effect on the CA, the pillar density proved to be an important aspect to be taken into consideration when assessing the results.

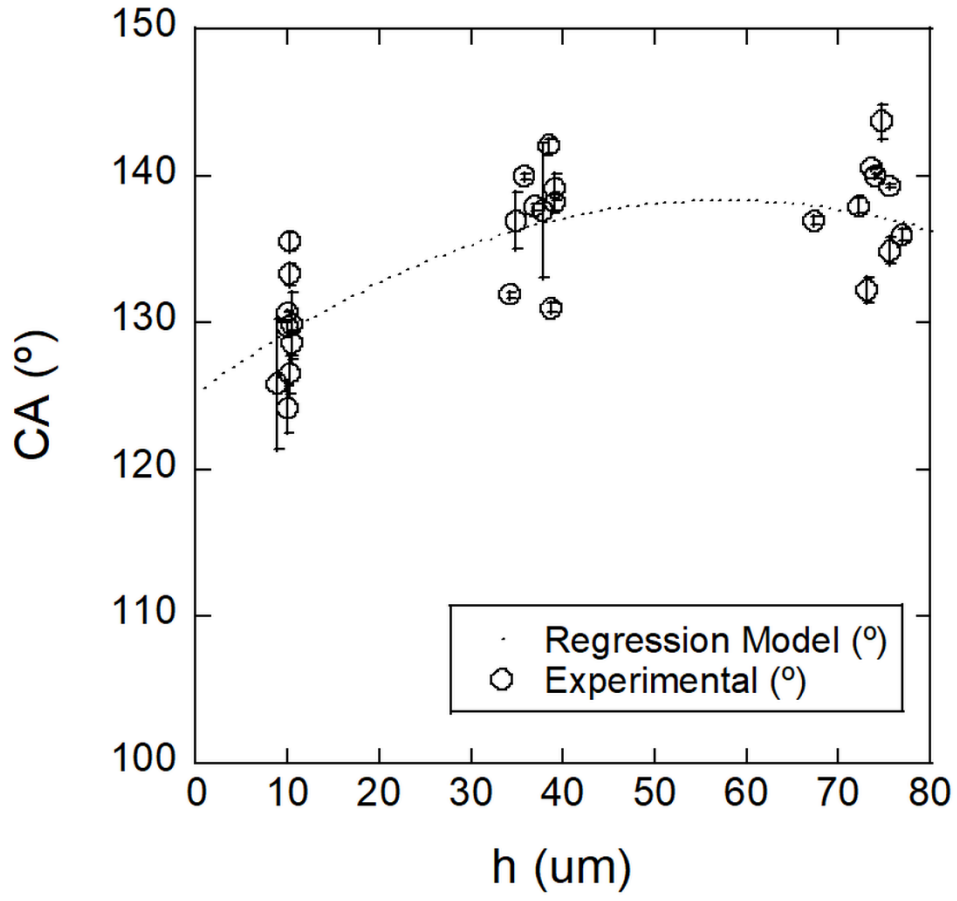

Fig. 5. 21 Simplified regression model CA results comparison with the experimental data, vs the pillar height.

Lastly, it should be clarified that this regression model is valid for the selected PP within the proposed topographic micrometric range. In case other material is considered, or if dimensional values that exceed or do not reach the proposed range, another independent DoE should be performed.

Part III

Computational modelling of the wetting behaviour of a water droplet on laser textured surfaces on polypropylene

5. 3. 1. Introduction

The main goal of the simulations presented in this work is to demonstrate the viability of the CFD model from COMSOL Multiphysics to reproduce the experimentally obtained CA values for the different textures, thus validating this method as a predictive tool. In other words, in this work, the focus is not the dynamics of the wetting phenomenon, but the static apparent CA value adopted by each different texture.

In this work, the objective of the simulations does not revolve around the comprehension of the complex physics behind the effect of topographical and/or chemical modifications on the wettability but providing a step-by-step procedure to develop a model that can fulfil the objective of predicting the CA of a textured surface, or that can help observe similar trends to the CA variation from the experimental results. As it was previously defined, the computational modelling of this phenomenon implies the careful definition of the mobility parameters, the droplet interface thickness, the mesh, the boundary conditions, the initial values and the solver configuration.

In this thesis, a simulation model is proposed, obtained after following a guideline. First, the different domains conforming the model will be defined. Next, a mesh refinement process must be done to ensure the convergence of the simulation and to minimize the computational time. After setting up the initial conditions as defined in section 4. 4, the work will be focused on the selection of the proper inputs, i.e., the selection of the mobility and interface thickness parameters to obtain similar results to the shown in Fig. 5. 19. Each refinement and input selection will be adapted to each texture.

Overall, the objective is to observe if the obtained CA from the surfaces with the textures changes due to solely the topographic variation, by maintaining the same inputs from the flat surface, and the measured CA are going to be compared to those obtained experimentally. Taking into consideration the motivation of the present thesis (to speed up the texture selection process), both accuracy and simulation time are taken into consideration when assessing the computational methods available. In this work, a 2D simulation is performed, taking into consideration the extreme condition of the double depth from the 3D texture, and its ability to capture enough fundamental physical phenomena to provide a feasible result is assessed. The results from this specific case are going to be compared to a 3D simulation, evaluating the effect of the third dimension on the results and assessing the reliability of the equivalent 2D simulation on the accuracy of the measured CA when compared to the experimental results.

5. 3. 2. Input parameter estimation

Considering the small droplet radius of 1.15 mm, which is smaller than the capillary length of water at 20ºC (l_c = 2.71 mm [249]), the droplet shape was considered to be spherical during the simulations, due to the neglectable effect of the gravity. Moreover, the null initial velocity of the droplet at a position close to the wall implies a small Weber number (W_e), defined as eq. (69), which represents the balance between the inertia forces and the surface tension. These small W_e numbers indicate the oscillatory behaviour of the interface during the spreading and receding processes until reaching the equilibrium state [251].

$$W_e = \frac{\rho_L V_L^2 L}{\sigma} \qquad (69)$$

Where ρ_L is the density of the liquid (water, in this work), V_L is the interface velocity, L is the characteristic length (i.e, the diameter of the droplet, D_0) and σ is the surface tension of the considered liquid (0.072 N/m in the case of the water, as measured in the tensiometer).

The Two-Phase flow simulation with Phase Field requires of a careful tuning of the mobility and the meshing for each case considered. In any FEM modelling, selecting the correct mesh size is considered to be of upmost importance, in order to ensure the optimal mesh that maximizes both the speed and the accuracy of the output. In other words, the objective is to identify the particular case scenario from which further increasing the number of elements does not greatly modify the results. In this case, for the proposed 2D system, the mesh elements are bidimensional. Moreover, between the free triangular and free rectangular element types, the former is usually used by default, as they are relatively smaller and may usually reach the solution at a faster rate. Hence, as a first step, a mesh convergence was performed, where a total of 8 different mesh types were used (see Table 5. 7), on both a flat and a textured surface. Afterwards, for the selected mesh size, the influence of both χ and ε on the computational cost and the movement of the contact line was assessed, thus obtaining the combination of parameters that were going to be used afterwards to perform the simulations under the 27 different textures considered.

5. 3. 2. 1. Mesh convergence in flat surfaces

First, the mesh convergence was performed. In any finite element analysis, the **mesh convergence** is one of the most critical aspects affecting its accuracy. This assess the minimum element size needed to ensure that this analysis will not be affected by any changing in the mesh size. In this step, the mesh convergence was evaluated by observing both the droplet mass loss and the contact line movement over the time, in order to identify the optimal parameters from which the solution showed little variation with the element size [250]. In this work, a total of 9 meshes were used, corresponding to the element sizes provided by default by COMSOL, i.e., *Extra Coarse*, *Coarser*, *Coarse*, *Normal*, *Fine*, *Finer*, *Extra Fine* and *Extremely Fine*, labelled in Table 5. 7 with the numbers m1 to m8, respectively. The corresponding size of the elements was varied in each case, in particular the minimum and maximum element size, which values were smaller the finer the mesh.

In each case, the parameter controlling the interface thickness was adapted to the mesh size. Based on the literature, many authors reported that ε should be equal to or greater than half the maximum mesh size, especially near the walls and the interface [200, 232, 252]. In addition, during the Time-dependent period the interface moved inside the mesh, so the diffuse properties of the interface change its position during the movement. This implies that the mesh requirements mentioned before should be applied in the domains contained within the trajectory of the moving interface to avoid computational errors, i.e., the domains defined by 1, 2 and 3 in Fig. 5. 22. The remaining regions (number 4 in Fig. 5. 22) were meshed with the default fine mesh size (i.e., the mesh m6).

Table 5. 7 Definition of each mesh considered in the mesh convergence step

Mesh	Minimum element size (μm)	Maximum element size (μm)	Maximum element growth rate	Curvature factor	Resolution of narrow regions	χ (m·s/kg)	ε (μm)	N elements	Minimum element quality
m1	25	650	1.3	0.8	1	10	650	1294	0.515
m2	20	435	1.25	0.6	1	10	435	1386	0.501
m3	15	335	1.2	0.4	1	10	335	1418	0.492

m4	10	225	1.15	0.3	1	10	225	1690	0.472
m5	5	175	1.13	0.3	1	10	175	1977	0.478
m6	2	140	1.1	0.25	1	10	140	2536	0.541
m7	0.75	65	1.08	0.2	1	10	65	7339	0.603
m8	0.75	33.5	1.05	0.2	1	10	33.5	23106	0.569

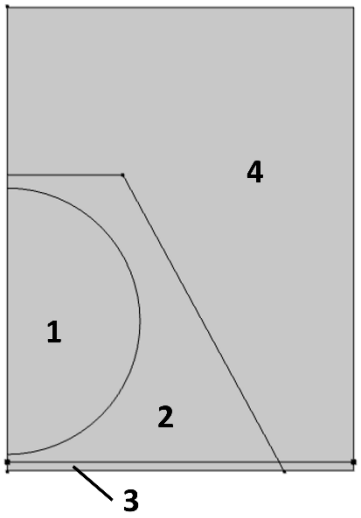

Fig. 5. 22 2D domain identification for the mesh convergence

Once defined the meshes, an initial value of ε was chosen, as previously defined. A first approach could be taken based on the Cahn number (Cn), which is the relationship between ε and a characteristic length scale, L (see eq. (70)), as explained in several publications [232, 252, 253, 254, 255]. Fink et. al. [254] explained that in Phase Field simulations, a good first interface thickness value can be selected according to a more macroscopic length scale, which in this work was stablished as the droplet diameter ($L = D_0$). They indicated that a typical Cn number would revolve around a value of 0.01. In this case, a first ε value would be approximately 30 μm, corresponding to a Cn = 0.015. However, ε should not be much smaller than the minimum element size. Therefore, because very small values of ε lead to numerical instabilities (which can potentially occur from the mesh m5 onward), its value was restricted to the maximum element size.

$$C_n = \frac{\varepsilon}{L}$$

(70)

On the other hand, a constant value of the mobility tuning parameter was used. COMSOL uses a default value of 1 m·s/kg. However, this value could lead to numerical instabilities when ε adopted relatively small values (most likely in the case of m8). Hence, a constant value of 10 m·s/kg was used for this convergence and afterwards, the effect of varying χ was assessed.

Fig. 5. 23 a) shows the droplet mass loss (or loss of the area defined by the water domain), which is a common issue from the Phase Field method. This mass conservation issue occurs especially for coarser meshes, as it can be observed in the figure. The finer the mesh, the lower the mass loss. However, as it can be seen in Fig. 5. 23 b), even though the finest mesh provided a lesser mass loss, the contact line movement was more erratic or more sensitive to the air movement, which led to a permanent oscillatory movement, and could not reach an equilibrium state. Additionally, as the mesh size was decreased, the contact line movement showed an oscillatory damping until the equilibrium state was reached, which is in concordance to the assumption of low Weber number, as in planar surfaces it results on an oscillating behaviour, as explained by Zhang et. al. [251], who observed the bouncing of a water droplet on a flat surface (CA_0=90º) under several Weber and Reynolds number conditions. This behaviour is also in concordance with the report from Lim et. al. [252], who observed that lowering the interface thickness from 3 μm to 0.5 μm led to an overall increase of the maximum spreading of the contact line, which could be translated into a larger time needed for the model to reach the equilibrium state. Eventually, in every case the spreading value obtained at this equilibrium state was the same for the considered ε.

From these results, the mesh m7 was selected as the optimum configuration for the next simulations, corresponding to a Cn number of 0.026, which is near the typical Cn number of 0.01. Not only the results with m7 were similar to the m8, but also the number of elements needed in this case was 3 times lower, which increased the simulation speed to a point where the slightly better mass conservation from the finer mesh could be neglected.

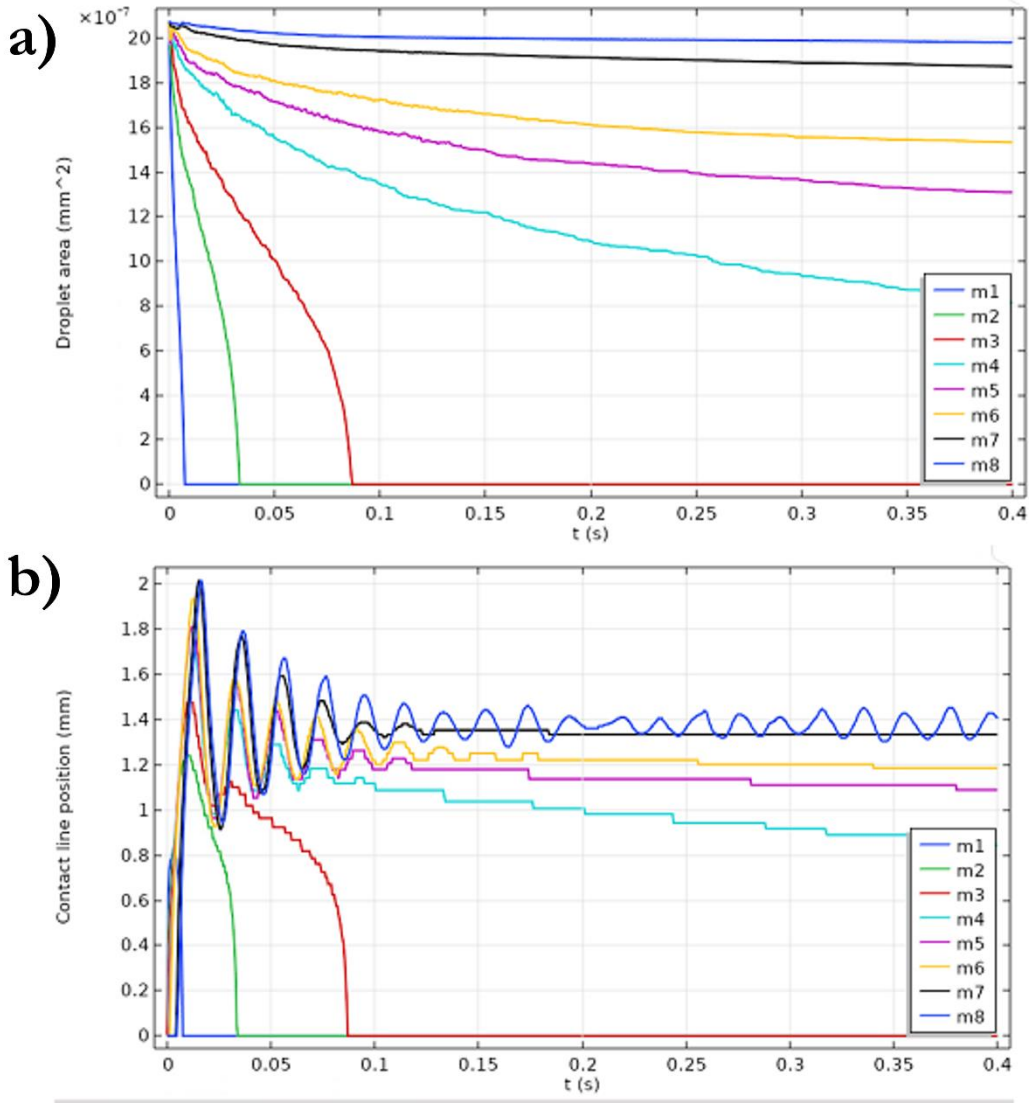

Fig. 5. 23 a) Droplet area loss and b) contact line position on the flat surface (from the droplet centre) over the time for different mesh configurations

5. 3. 2. 2. Effect of χ on the movement on a flat surface

The effect of χ on the resulting interface movement is studied, considering a flat surface. As explained in section 2.6, the conservative form available in COMSOL (the software works with the non-conservative form by default) can minimize the mass loss occurring during the diffuse interface modelling, but it may cause errors in the symmetry axis. This error can be reduced by working on χ. Therefore, the conservative form provides a more precise equation calculation at the expense of more convergence issues than the non-conservative form.

To establish the effect of the χ, a parametric sweep is proposed, in which the value of χ was firstly varied from 1 (the default value) to 1000 m·s/kg. More specifically, the selected values were 1000, 500, 100, 50, 25, 10, 5 and 3 m·s/kg. Mobility tuning parameter values of χ = 1 m·s/kg suffered from convergence issues and the results were not included. The mobility tuning parameter is a difficult to evaluate parameter. Based on the definition of the mobility, and observing the eq. (48), higher χ (which is translated into higher γ, as ε is maintained as a constant) may lead to numerical instabilities, and thereby simulation errors, which can be observed in some cases (especially at 1000 m·s/kg and 500 m·s/kg), observable in Fig. 5. 24. In this figure, the contact line position over time can be seen in a), whereas in b) the maximum horizontal velocity of this same contact line was represented. The lower χ, the more the results converged on an equilibrium state at 1.31 mm from the symmetry axis, as well as the closer the maximum velocity reached a zero value (indicating the complete equilibrium state of the droplet). In general terms, reducing the mobility tuning parameter resulted in a faster damping of the maximum velocity (not considering the higher values due to the erratic results mentioned earlier).

To conclude, the most suitable χ value had to be lower than 10 m·s/kg, which should be further validated by the results obtained in the textured surface and the experimentally measured contact angles. Since values of 10 m·s/kg required less time to finish the simulation, it was this specific χ value the one selected for the next step.

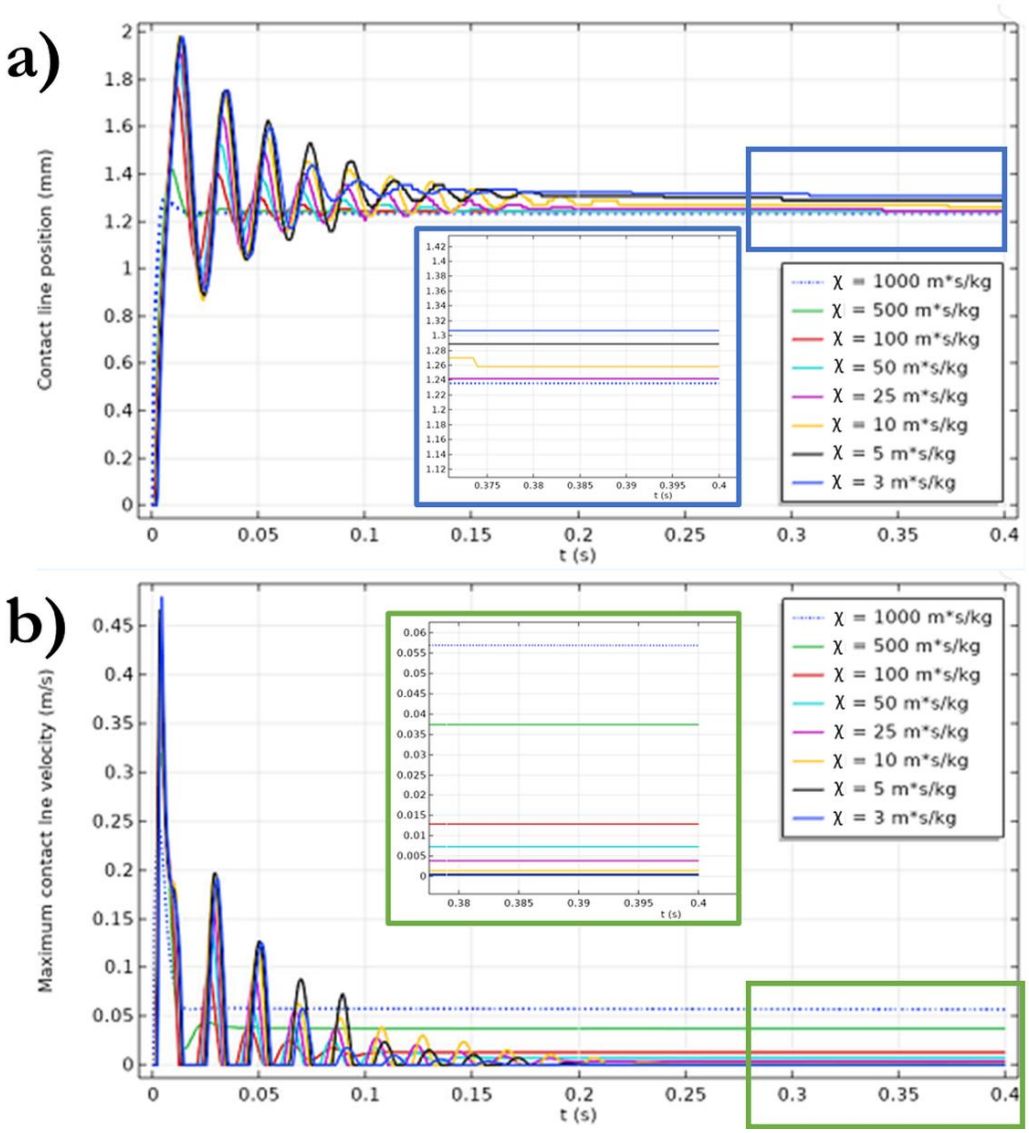

Fig. 5. 24 a) Contact line position and b) maximum contact line velocity over time for different χ values

Fig. 5. 25 shows the droplet evolution over time for the optimal parameters for a flat surface, based on the results shown before, i.e., the mesh configuration m7 (ε = 65 μm) and χ = 10 m·s/kg. The time stamps of 14.5 ms and 24.5 ms represent the exact moment where the droplet reaches its maximum spreading value, both in terms of diameter and height.

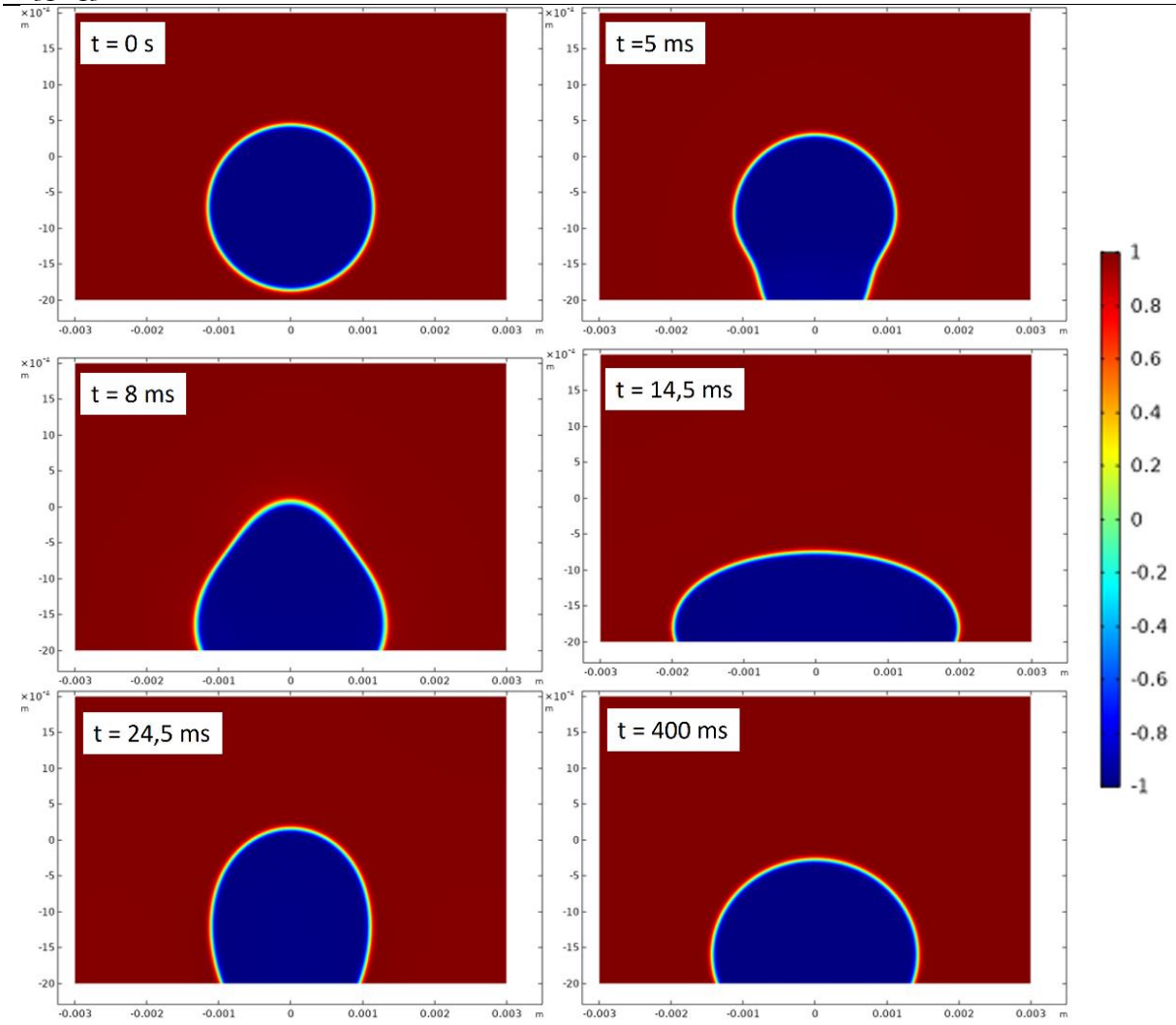

Fig. 5. 25 Droplet evolution at different simulation stages in a flat surface (ε = 33.5 μm and χ = 10 m·s/kg). The time stamps at 14.5 ms and 24.5 ms represent the maximum spreading and the maximum droplet height moments, respectively.

5. 3. 2. 3. Mesh convergence in textured surfaces

As it has been observed throughout this work, modifying the topography of a flat PP surface induce changes in the wettability. In the case of the computational model, the effect of introducing a similar topographic modification on the spreading of a droplet is going to be assessed. One of the 27 developed textures was used as an example texture to study the effect of χ interface mobility and droplet spreading over the textures. More specifically, the texture labelled by the number **2** (a = 75 μm, b = 75 μm and h = 40 μm, which in the 2D simulation is h_{2D} = 80 μm) was selected.

With the introduction of complex geometries due to the textured surfaces, special care must be taken on the meshing process to guarantee the correct geometry shape representation by these mesh elements (see the differences between the mesh sizes in Fig. 5. 26). As it can be observed, the lower the number of elements, i.e., the higher the element size, the triangles forming the mesh described the geometry from the topography more accurately. In the case of m3, the edges were defined only by a single triangular side and could not replicate the curved profile. The m5 and onwards, on the other hand, were able to overcome this negative aspect of coarser meshes.

The same procedure as defined in the previous section was applied to the textured surface scenario. More specifically, the mesh convergence was applied to the texture 2, selected as an example for this step. The same parameters as resumed in Table 5. 7 were applied in this case, but due to the difference in the geometry of the surface topography, the number of elements and minimum quality were different (see Table 5. 8).

Table 5. 8 Mesh number of elements and minimum quality for the mesh convergence of the textured surface

Mesh	N elements	Minimum element quality
m1	5199	0.517
m2	5903	0.533
m3	8303	0.471
m4	14343	0.534
m5	33888	0.5
m6	89076	0.526
m7	111805	0.525
m8	202136	0.539

The results from the simulations can be observed in Fig. 5. 27 and Fig. 5. 28. The former compares the computationally obtained droplet shape on top of the textured surface when compared to the equivalent experimental situation. Fig. 5. 28 a) shows the mass (area) loss from the PF associated to the mesh size, which followed a similar trend as the observed in the flat surface. The best results were obtained for the smallest mesh sizes, observing little difference between the m7 and m8.

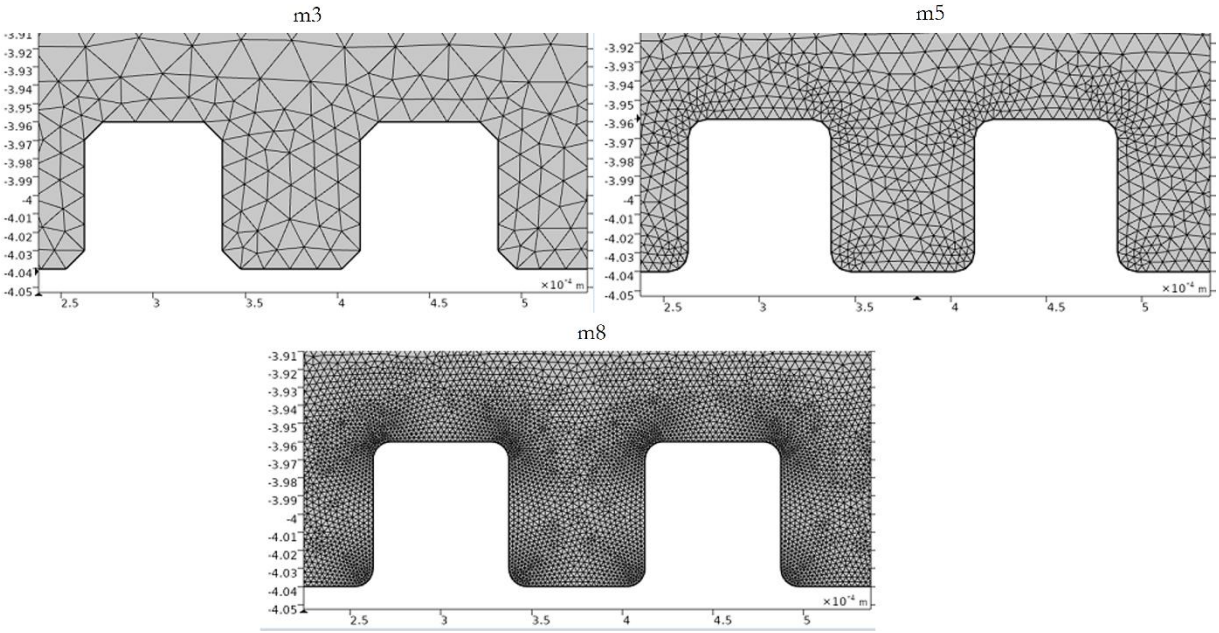

Fig. 5. 26 Meshing of the texture based on three different mesh configurations (m3, m5 and m8)

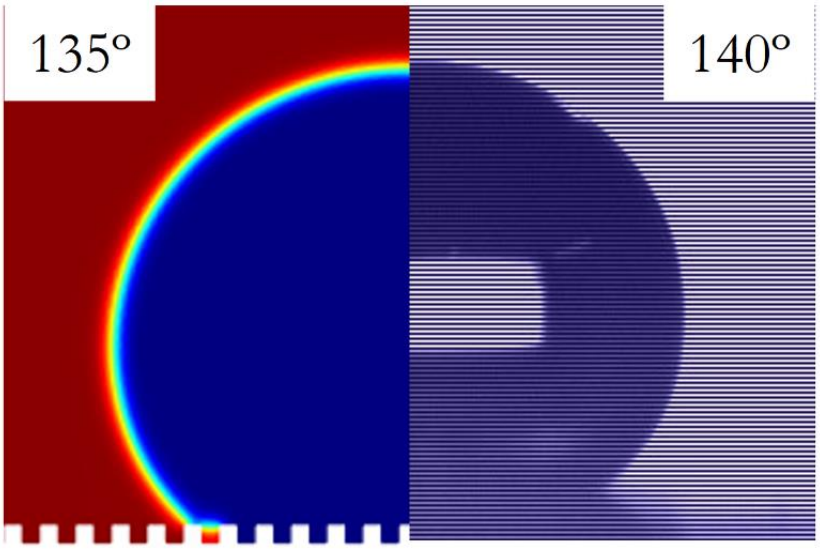

Fig. 5. 27 Result comparison between the simulated (left) and experimental (right) results (for χ = 10 m·s/kg)

Fig. 5. 28 b) shows the contact line movement along the top of the surface pillars. As the mesh size was getting smaller, the spreading value at which the equilibrium state was obtained was converging until the m7 configuration. Finer meshing (m8) resulted in a reduced spreading of the contact line, which could be associated to a more impactful effect of the surface topography on the interface movement. This can also be observed by assessing the results from the droplet bouncing on the perpendicular direction (Fig. 5. 28 c), which showed the poor results obtained when ε was unnecessarily big (more specifically, when $\varepsilon > 65$ μm). This could be related to the high thickness when compared to the relatively small cavity width of 75 μm (in the case of the texture 2).

Contrary to the mesh selection criteria followed in the flat surface, in the textured surface the m8 mesh configuration was selected even though it had almost double the number of elements. However, in this case, the spreading of the droplet in this configuration provided the most accurate CA value when compared to the experimental result (see Fig. 5. 27). Therefore, sacrificing the time reduction from coarser meshes should be required for the sake of promoting more accurate results.

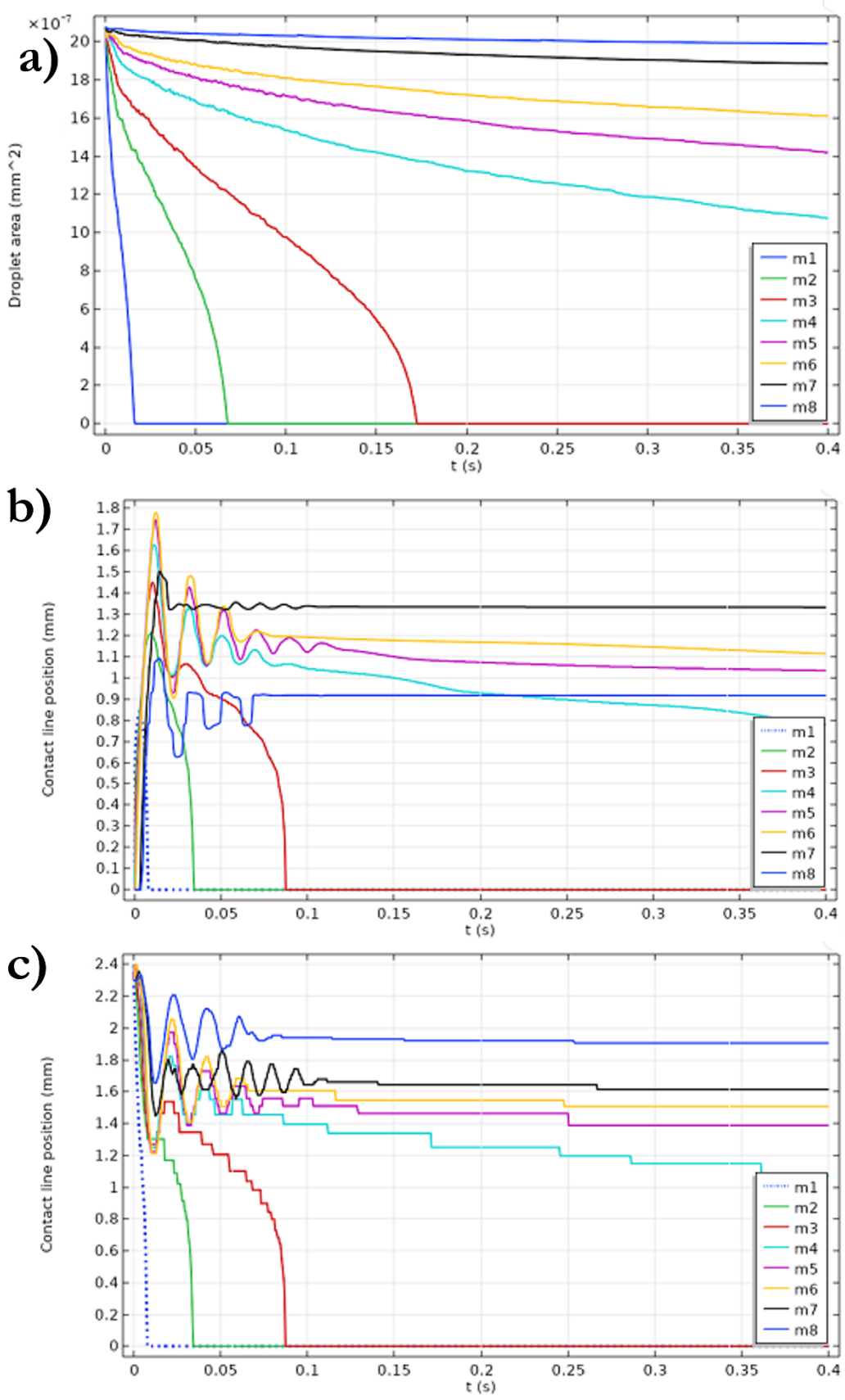

Fig. 5. 28 Mesh size sensitivity results in a) mass loss, and droplet movement in b) x direction, c) y direction

5. 3. 2. 4. Effect of χ on the movement on a textured surface

Based on the results obtained in a flat surface, for the textured surface, only the χ values of 50, 25, 10, 5 and 3 m·s/kg were considered. Moreover, it was observed that, due to the more complex geometry of the surface, χ values of 3 m·s/kg prevented the solver to reach a converging solution.

Fig. 5. 29 shows the contact line movement along two different directions, i.e., a) a horizontal direction (i.e., along the top of the pillars) and b) the perpendicular direction, which would provide information about the bouncing of the droplet. Moreover, based on the results observed in Fig. 5. 29 a), the droplet reached an impinged state at around 0.9 mm from the symmetry axis, which was not observable in the flat surface, demonstrating the effect of the topography modification on the water spreading and, consequently, in the output CA. Therefore, the movement in the vertical direction would provide additional information, especially regarding the sensitivity of the interface to external perturbations or the error associated with the incorrect selection of the input parameters (χ, in this case). In fact, in Fig. 5. 29 b) it can be observed how the movement of the contact line was similar for every χ, up to a time of approximately 0.1 s, from where increasing its value resulted in a faster movement of the water and a faster damping of the oscillatory behaviour. When χ = 50 m·s/kg, the droplet showed an erratic displacement over the time that could not reach the equilibrium state (within the specified time range), due to the continuous oscillating behaviour that could be related to simulation errors that were not as observable in the flat surface. This demonstrates the increased difficulty for the solver to simulate the results when more complex wetted wall surfaces are considered. The lower the χ, the more sensitive to perturbations and, below a certain value, the increased numerical errors (identified as χ = 3 m·s/kg in this case).

On the other hand, the droplet spreading value at the equilibrium was the same in the cases of χ = 50 and 25 m·s/kg, but it was reduced for χ = 10 m·s/kg, which showed a slower evolution until reaching this state. Again, by comparing the CA measured in each case with the obtained experimentally, it could be concluded that χ = 10 m·s/kg offered the most accurate result.

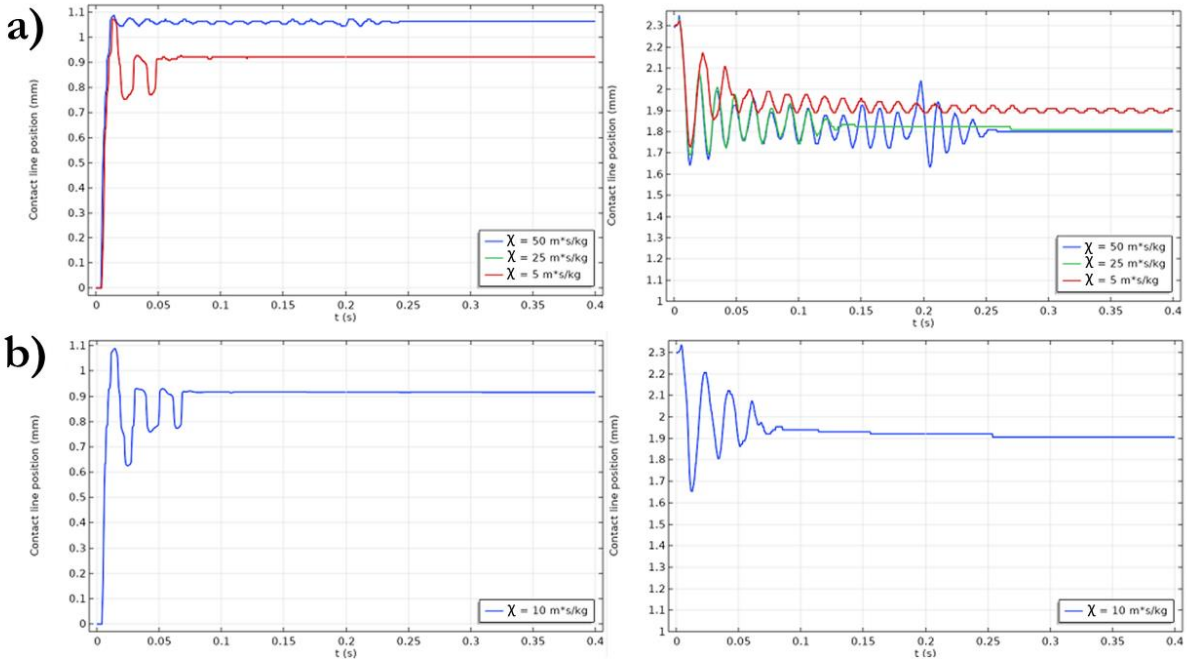

Fig. 5. 29 χ effect on the contact line movement along a) the horizontal direction (i.e., the surface) and b) the perpendicular direction

5. 3. 3. 2D simulation results

After the first estimation of the Cahn-Hilliard input parameters that control the diffusivity of the interface, i.e., χ and ε, the simulation of the remaining textures was performed. When considering the textures with the lowest pillar height of 10 μm (h_{2D} = 20 μm), for the particular example with the Texture 1, an additional simulation was performed, due to the relatively small geometric features. This was performed due to the same explanation given in section 5. 3. 2. 3as in this case, a dimensional parameter smaller than the cavity width was present, i.e., the pillar height, h. Therefore, in order to avoid the possible inaccurate result derived from this situation, two simulations were performed: Sim. 1 used a smaller ε at an expense of reducing the maximum element size and increasing the number of elements if the minimum was kept constant, and Sim. 2 used the previously selected PF mobility parameters for higher depth textures. In the latter, the aim was to demonstrate whether the hypothesis of the existence of this inaccuracy in the results was correct or not.

Table 5. 9 Simulation scenarios for textures of h2D = 20 µm, in which χ and ε are varied

Simulation	ε (µm)	χ (m·s/kg)	γ (m^3·s/kg) Eq. (48)
Sim. 1	10	10	1e-9
Sim. 2	33.5	10	1.12e-8

The simulated results can be observed in Fig. 5. 30. The simulation results that most resembles the experimentally obtained droplet was Sim. 1, i.e., the case where ε = 10 µm. At the cost of increasing the computational effort, the interface movement may have been affected by the small values of the height. The edges of the pillars acted as a stress concentrator where the rounded surface drastically varies the normal vector and thus the interface is not capable of advancing nor receding at low velocities. For ε values higher than 10 µm, the interface thickness, alongside the smaller maximum element sizes, is sufficiently big to neglect the effect of these small features and its movement is less affected than in the former case. Hence, the previously stated hypothesis was demonstrated based on these results.

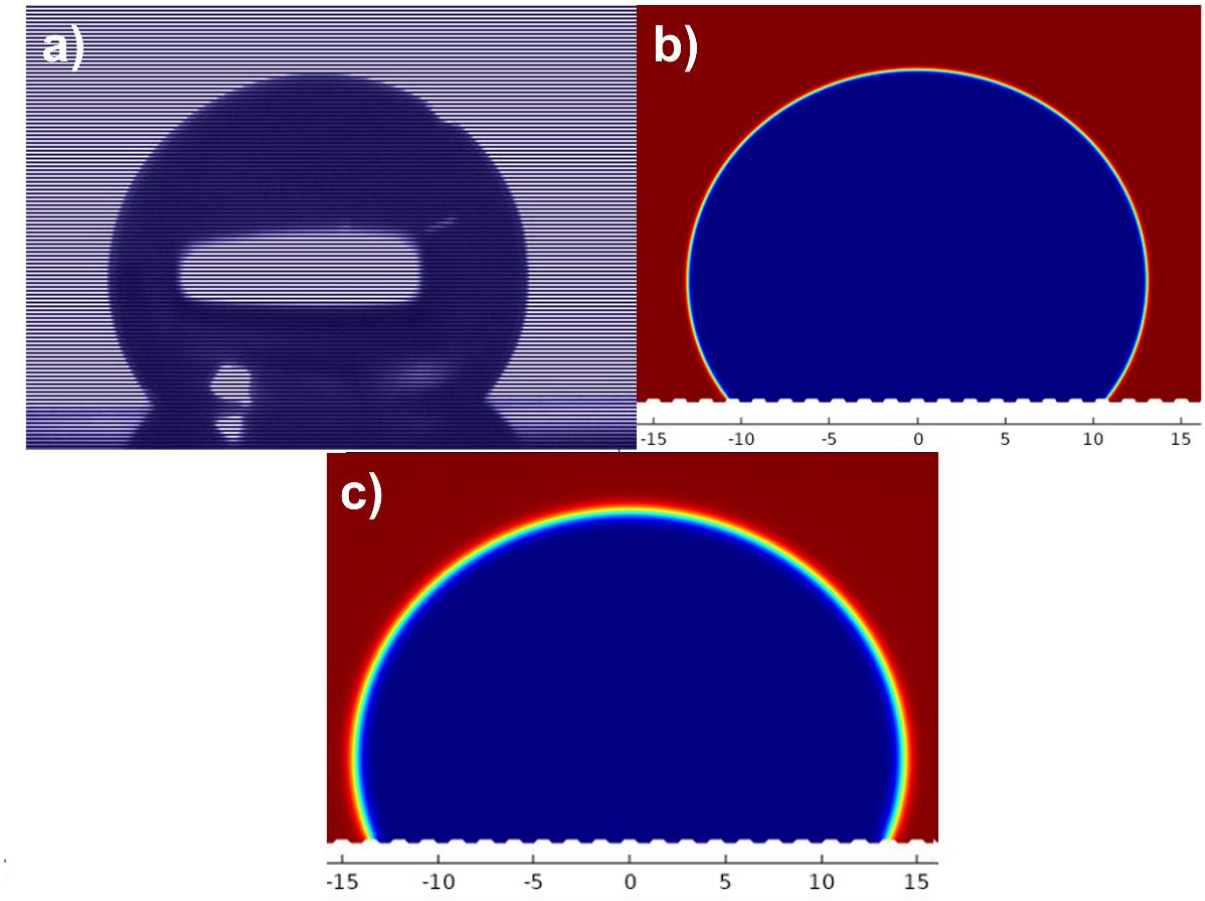

Fig. 5. 30 Droplet images in a) experimentally developed texture, b) Sim. 1 and c) Sim. 2

- First set of simulation with χ = 10 m·s/kg

These results show the importance of the structure depth in the interface movement and the selection of ε when simulating the wetting behavior in the textured surfaces. Hence, for h_{2D} = 20 μm, ε = 10 μm and χ = 10 m·s/kg were used.

In the rest of the cases (i.e., h_{2D} = 80 and 140 μm), ε values of 33.5 μm and χ = 10 m·s/kg were selected. These parameters are not changed between the textures of the same depths in order to assess the effect of the topography on the CA. Table 5. 10 resumes the Phase Field parameter selection for each h considered.

Table 5. 10 Phase Field parameter selection for each height in the first set of simulations

h (μm)	h_{2D} (μm)	ε (μm)	χ (m·s/kg)	γ (m^3·s/kg) Eq. (48)
10	20	10	10	1e-9
40	80	33.5	10	1.1e-8
70	140	33.5	10	1.1e-8

The final simulation results are summarized in the SIMULATION RESULTS (Annex III) chapter (see Fig. AIII. 1, Fig. AIII. 2 and Fig. AIII. 3), in which it can be observed that the contact line is generally pinned on the pillar edges, i.e., the spreading of the droplet is limited by the distribution of these features under the droplet. As it was explained before, these edges are stress concentrators where the contact line suffers a pinning effect that prevents the contact line from further spreading. Fig. 5. 31 shows the simulation results and they are compared with a) the pillar height effect on the experimental results and the regression model and b) the experimental results, represented by the topographic factor. In the former, it can be observed that the results, in particular for h = 40 and 80 μm, show a cloud of points whose best fit approximates to the regression model (and hence to the experimental results). Moreover, in the latter it can be seen that the CA variation with r_f follows a similar trend than the experimental results, which can confirm the null hypothesis (H_0). For lower h values, the simulations were not as accurate due to the need of using very small ε values, which required of a much finer mesh, and it could also lead to higher computational errors if lower mobilities were used. Furthermore, the differences observed at higher pillar heights could be to

several factors such as the location in the texture where the droplet falls on (on top of a cavity instead of the top of a pillar), etc. In Fig. 5. 32, it can be observed how, for a given value of a = b = 75 μm, increasing the pillar height from 80 μm (texture 2) to 140 μm (texture 3) led to a higher CA due to the transition from the Wenzel state in the former to the CB state in the latter. Once reached this air trapping state, further pillar depth increase would not result in a higher CA, and hence the only CA improvement should be achieved by modifying solely the geometry of the structures, the pillar density or the introduction of nanometric features. These results are in concordance with the critical height value proposed by Zhang et. al. [187] (which depends on the f_{SL}) of 70 μm (for f_{SL} values of 0.25, and a=b= 50 μm), so that higher pillar heights would predict that the droplet would settle in the CB state, as it can be observed in the present study, as the droplets on textures with values of h_{2D}>80 μm (h>40 μm) showed this specific wetting state.

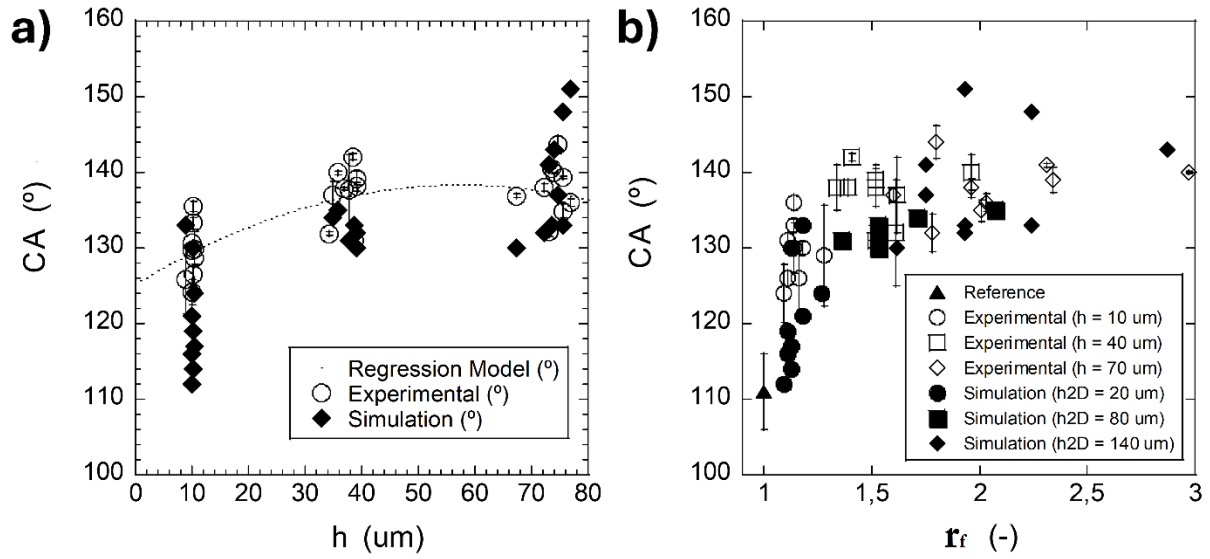

Fig. 5. 31 a) Simulation vs regression model vs experimental results by varying h and b) Simulation result comparison with the experimental CA for different topographic factors. The results are obtained for χ = 10 m·s/kg

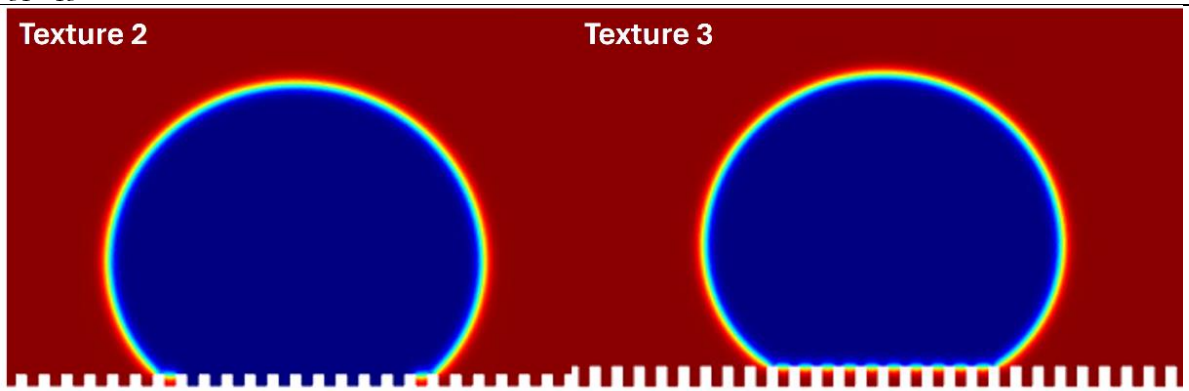

Fig. 5. 32 Pilla height effect on the transition between Wenzel and Cassie Baxter states for a=b= 75 µm for χ = 10 m·s/kg

Based on these results, a second set of simulations were performed, where χ was set to 5 m·s/kg to observe how the output CA varied in relation to the experimental results.

- Second set of simulation with χ = 5 m·s/kg

Due to the relatively good results obtained from Fig. 5. 29, a χ value of 5 m·s/kg was considered. In this case, for h_{2D} = 20 µm, due to the relatively low value of ε, this χ provided a small mobility value enough to result in a simulation problem that the solver could not resolve. Therefore, in this specific case, the mobility was not changed. As seen in Table 5. 11, in this case the mobility was more similar for the considered pillar heights.

Table 5. 11 Phase Field parameter selection for each height in the second set of simulations

h (µm)	h_{2D} (µm)	ε (µm)	χ (m·s/kg)	γ (m^3·s/kg) Eq. (48)
10	20	10	10	1e-9
40	80	33.5	5	5.6e-9
70	140	33.5	5	5.6e-9

Again, the simulation results can be observed in Fig. AIII. 4, Fig. AIII. 5 and Fig. AIII. 6, where it can be observed how, by reducing the mobility tuning parameter, and hence the mobility, the water was not able to fill the cavities for h_{2D} = 80 µm, which was in more agreement with the critical pillar height of 70 µm defined by Zang et. al. [187]. In fact, this mobility modification resulted in an

output variation for h_{2D} = 80 μm, but it did not provide of any differences for h_{2D} = 140 μm, as in this case, the droplet was already in the Cassie Baxter state for higher mobilities.

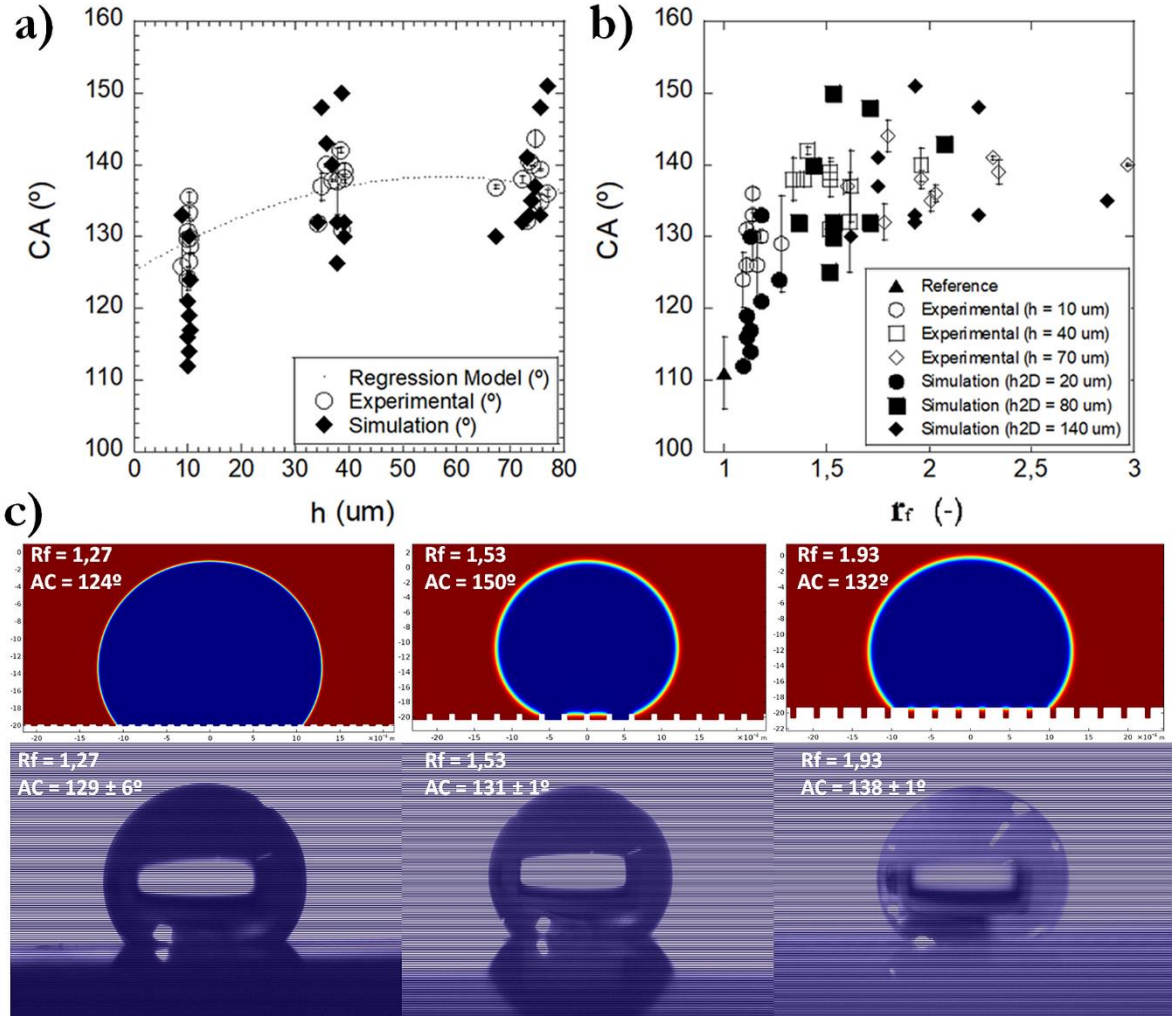

Fig. 5. 33 a) Simulation vs regression model vs experimental results by varying h and b) Simulation result comparison with the experimental CA for different topographic factors. The results are obtained for χ = 5 m·s/kg. In c) a comparative between some of the simulation results and the respective experimental image can be seen.

It can be observed in Fig. 5. 33, due to this air entrapment, the cases of h_{2D} = 80 μm showed an increase in the CA value which resulted in a wetting trend similar to the experimental results. Therefore, it can be concluded that using χ = 5 m·s/kg was more accurate, at an expense of higher simulation times due to the reduced mobility of the system. This can be explained by taking into consideration the theory regarding the mobility, as it defines the motion of the interface, define by the Cahn-Hilliard equations that couple the Laminar Flow and PF physics.

Additionally, the effect of the pillar density (defined by f_{SL}) on the CA was investigated. In the experimental results, it was not possible to gather as much information about this contribution as it could be obtained from the simulations.

Fig. 5. 34 shows the CA variation with f_{SL} (in %) in the case of a) h_{2D}=20 μm, b) h_{2D}=80 μm and c) h_{2D}=140 μm. It can be observed that, depending on the wetting state in which the droplet rest, the increase of the f_{SL} led to higher CA values in the case of the Wenzel state, for h_{2D}=20 μm, or a general lower CA results in the case of the Cassie Baxter state, for h_{2D} = 80 μm and 140 μm. The CA value decrease with higher f_{SL} is in good agreement with the results provided by Wang et. al. [256], who simulated the wettability of a surface with different structure arrangements by a molecular dynamics model. Furthermore, these results are in good agreement with those of Ambrosia et. al. [248], who studied the wetting of a droplet within nano and macro-scales and compared the results with the Wenzel and CB equations. More specifically, they concluded that increasing the f_{SL} in textures where droplets settle in the Wenzel state increased the CA, contrary to what happens in the Cassie Baxter state. From Fig. 5. 34, it can be observed that, for f_{SL} values of 25% (0.25), three different CA values were obtained. This is because each point is located at different r_f locations (see Fig. 5. 31 b) and Fig. 5. 19 a)), due to the variation of the pillar density and therefore different CA can be obtained. More specifically, as it can be seen in Fig. 5. 35 (for f_{SL}=25%), using lower values of a and b showed higher hydrophobicity, as the area under the droplet had more surface to contact with, due to the higher density. It can be concluded that, in order to study the CA variation of a droplet, only considering the surface solid fraction or the topographic factor may lead to incomplete information and may not be enough to completely describe the different texture effects on the wettability behaviour of a surface. Both parameters should be considered for a more complete understanding of the CA variation with different textures. If higher CA are desired, higher r_f, higher h and lower f_{SL} (especially at lower a and b values) provide a narrower dimensional parameter window that may meet these specific requirements.

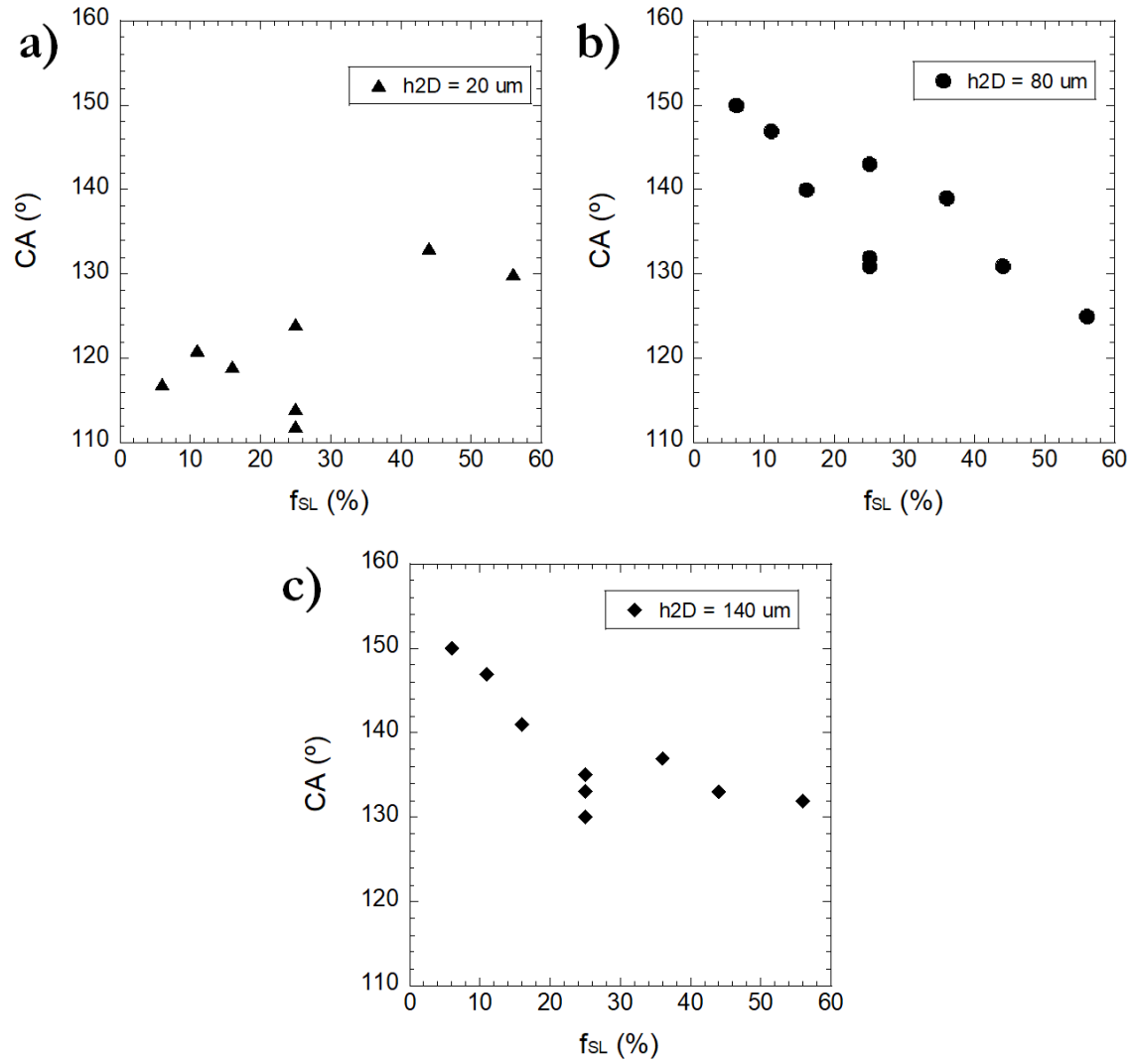

Fig. 5. 34 CA variation with f_{SL} for a) h_{2D} = 20 µm, b) h_{2D} = 80 µm and c) h_{2D} = 140 µm

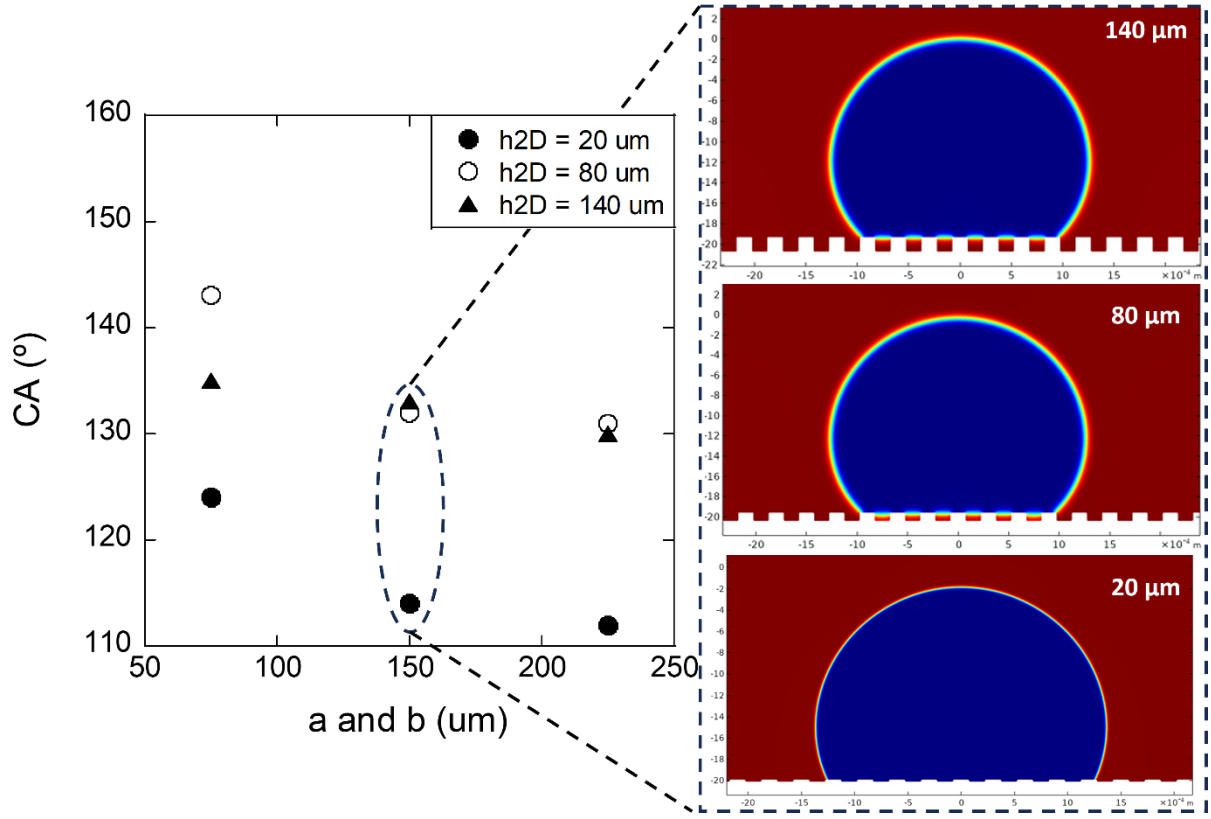

Fig. 5. 35 Pillar and cavity effect on CA for each pillar height value at a f_{SL} of 25%

These results show how the simulation software and the apparently sigmoidal best-fit of the experimental results can be a useful tool for the user to predict or understand the effects of the topography on the CA variation. Even though the measured CA does not exactly correspond to the experimental results, the proposed model can successfully predict its trend with the variation of the topographic factor, which shows its potential as a predictive tool that can be used previously to the experimental development of any texture. Therefore, it has been demonstrated that the 2D successfully captures the fundamental physics governing the wettability of the droplet on a textured polymeric surface. However, a 3D case has been considered as well, with which more information regarding the effect of additional dimensions on the interface movement and CA has been searched. In this 3D model, the effect of the double depth observed in the experimental textures on the CA can be assessed, as well as compared to the 2D equivalent model, at an expense of greatly increasing the computational cost.

5. 3. 4. Adaptation to 3D systems

By introducing a new dimension into the system, an improvement in the simulation is searched. This improvement involves not only the introduction of a double depth, as explained before, which describes more accurately the experimentally obtained texture, but also allowing to capture the interface movement inside the textures. Additionally, due to the good results obtained with an equivalent and simpler 2D models, the need of a third dimension is going to be assessed by comparing it with the 2D result. However, due to the relatively high time-consuming process from the 3D models (even when simulating only an octave of the entire system, due to the symmetries from the pillar-like textures), only an individual texture has been considered in this section.

The simulations performed in this section had their basis on the results observed in the sections 5. 3. 2 and 5. 3. 3 (see Table 5. 10). In this case, the comparison was going to be performed with the texture 21 (see Table 5. 3). After meshing the domain by using the mesh selected in the 2D system, it was observed that the number of elements drastically increased to values where the solver entered the "Out of Core" mode, which indicated the excessive memory usage to perform the simulation. This was an unwanted situation where the computational time increased exponentially. Hence, a minimum element size restriction was included at a value of $\varepsilon/2$. The number of elements was, thereby, reduced, but it was still much higher than in the 2D counterpart.

In Fig. 5. 36 the results for the 3D simulation in the texture 21 are shown. A direct comparison between the computational and experimental results can be observed in Fig. 5. 36 a), but in b) and c), a more detailed representation of the contact line behaviour can be seen. In fact, this simulation captured the wetting of the droplet inside the textures more accurately than in the 2D (Fig. 5. 36 d)), as it can be observed how the water filled the first depth from the texture, but the air was entrapped inside the bottom cavities. However, due to the high number of elements and the need for bigger mesh sizes, the CA obtained from this 3D program deviates more than in the 2D from the experimentally obtained value.

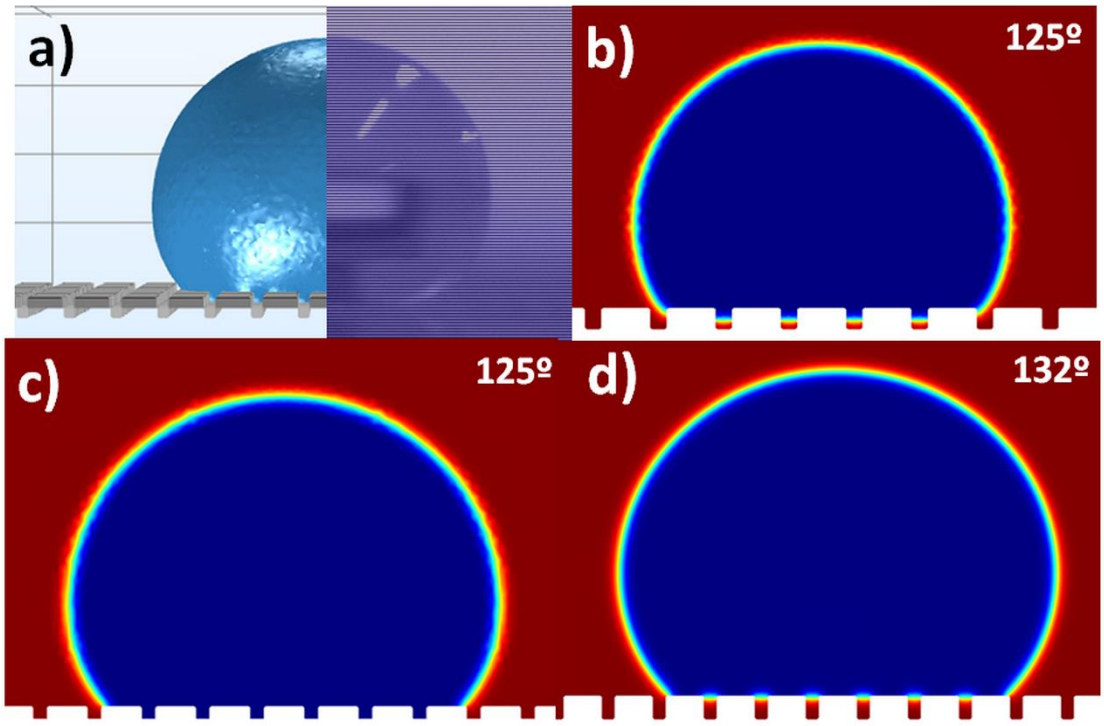

Fig. 5. 36 Simulation results for the 3D domain. a) Simulation vs experimental results, b) droplet shape in a cut plane that includes the double depth, in which the air entrapment can be observed, c) cut plane that only includes the smaller depths, and d) the equivalent 2D texture.

The average time for a 2D simulation (for a time selection of 0.4 seconds) is approximately 1 to 3 hours long, in the particular case of the computer utilized during the thesis, for a strict mesh resolution, whereas in the case of a 3D model, with a lower mesh resolution, the simulation may reach the 30 hours. While it may not seem too excessive, it has to be considered that in this work, a texture with several symmetry planes was selected. In fact, as it can be seen in Fig. 4. 5, the texture presented two symmetry planes at 45 degrees, which promoted the model simplification to one octave, reducing the number of elements by 8. However, in the case where a texture with lesser or no symmetry planes was considered, the simulation time would increase to much higher values. This indicates that the 3D simulations do not fulfil the main objective of the thesis, which is accelerating the texture definition process to ensure a specific CA for a given texture. Therefore, the 3D simulation is a good choice if a more accurate behaviour of the interface inside the cavities is wanted, but it lacks potential regarding its utility as an approach that accelerates the texture selection. In this case, in order to enhance its potential, several approaches can be considered: either a better computer should be used to reduce the simulation time or the 2D model should be used, sacrificing

the additional information missing from the 3D, but ensuring the correct capture of the fundamental physical phenomena.

Chapter 6

CONCLUSIONS

In this thesis, the complete definition of a methodology has been proposed that helps to accelerate the selection procedure of the most suitable texture for tuning the wettability of a surface. This methodology consists of a series of steps that include:

1. Optimisation of the laser ablation process, where a comparison was made between SP and BM. The best laser parameters have been identified, offering an optimal trade-off between quality and productivity.
2. The definition and implementation of a DoE to assess the effect of each topographical factor on the CA. This step involved the development of several textures with different topographic dimensions using an ultrafast laser ablation process.
3. The development of a computational model that is capable of capturing the most fundamental physical phenomena and predicting the CA that can be obtained experimentally.

Each step contributes valuable results, but it is only by using them together that a conclusive and robust result can be obtained. Therefore, this methodology successfully correlates each step by combining their respective optimal inputs and outputs to speed up the surface functionalization process.

6. 1. Laser ablation of Polypropylene: parameter optimization

In this work, maximizing the ablation capabilities provided by a high-repetition rate ultrashort laser system has been searched, by optimizing the laser parameters that provide a fair quality/throughput trade-off. Therefore, the study of the laser-material interaction by means of a comparative procedure between SP and BM has been performed, being the latter the selected to work with the proposed polymer, due to the higher efficiencies offered by the third pulse, as well as the better quality (in terms of material splashing and recast material on the edges) and higher throughputs. The nonlinear mechanism governing the interaction of the laser with the PP is shown based on the observed results in terms of structure depth, removed volume and pulse efficiency. These results also provide information regarding the pulse interaction due to the relatively small temporal distance between the pulses, especially in the BM, which is translated into a reduction of the efficiency of the following pulse, as a consequence of the lower energy that reaches the surface (as some energy is reflected or absorbed by the particle plume, the ionization of the air due to the high pulse intensities and the plasma plume). This may help reducing the heat accumulation of the surface and improving the surface quality by decreasing the accumulated material on the structure edge.

The laser parameter optimization process has been performed in both crater-like structures, which can be considered the most basic structure obtainable with a Gaussian pulse, and cavity-like features, where processing parameters related the pulse overlapping (i.e., a combination of the repetition rate and scanning speed) were considered.

The main partial conclusions obtained from this study are the following:

- The temporal distance between the pulses has shown a high impact on the efficiency of the ablation process of the consecutive pulses.
- From the study performed with crater-like structures, it has been demonstrated that the BM has shown better results regarding the trade-off between quality and throughput than the SP. In fact, working with 3 pulses per burst was offered the most optimal results.
- The study performed on grooves showed that the most appropriate pulse overlap was between 60% and 75%.
- Lastly, for the selected pulse overlap of 70%, the optimal pulse energies for the ablation of a square cavity structure were concluded to be of 2 μJ.

Additionally, it has been observed that these results could be extrapolated to other laser systems, where different wavelengths, BM characteristics and pulse energies were utilized. As it can be in EXTRAPOLATION TO SIMILAR LASER REGIME BY OTHER LASER SOURCES (Annex IV), similar conclusions could be obtained by dividing the energy of an individual pulse into n pulses inside a burst, instead of maintaining the pulse energy in each one. As part of the PhD studies, a short stay of one week in the Laser Centre of the UPM (from the Spanish name, Universidad Politécnica de Madrid) was spent, in which a set of experiments was performed with an ultrashort laser system that emits femtosecond pulses in the infrared wavelengths of 1030 nm (at SP and BM), at maximum pulse energies of approximately 95 μJ (for further details, see the section AIV. 2). It was observed that, following the conclusions with the Monaco laser, by increasing the number of pulses inside a burst, the ablation pulse energy threshold could be lowered, and the efficiency could be enhanced.

6. 2. Semi-empirical predictive model of laser textured surfaces

A semi-empirical model has been developed, in which a DoE has been presented with a total of 27 textures with different combinations of pillar width, cavity width and pillar heights. The

combination of these parameters has been defined by a topographic factor which has shown great impact on the CA variation. By taking the laser parameters selected from the previous section, a final refinement has been performed for the development of the pillar-like structures to ensure that the accumulated material in the edges was minimized. It allows to ensure a good quality texture, so that it could be more easily simulated in the next section and so that this recast material would not affect the measured CA.

Afterwards, a regression procedure has been presented, from which the following conclusions could be obtained:

- The most impactful factor in the wettability alteration of the PP surface was the pillar height.
- However, other factors such as the pillar or cavity widths cannot be neglected.
- A trend can be observed between the CA and the r_f, contrary to the f_{SL}.
- A regression model has been developed, which depends solely on the most impactful factor (h), which can help accelerating the selection of a texture geometry to achieve a certain CA but centred on the PP and within the range of dimensions considered.

Therefore, the methodology followed in this work can be implemented as a guiding tool for future semi-empirical prediction of the CA variation for other materials and/or geometries. It opens the way to implement the developed semi-empirical model for a wider range of materials and microstructures.

6. 3. Computational modelling of the wettability of polypropylene

The experimentally observed results have been employed as a validation tool for the development of a CFD model able to predict the CA performance of a droplet as function of a topographic modification of the surface. An especial care has been taken with the parameters that define the interface and its behaviour throughout the Time-Dependent step from the Solver, i.e., the parameter controlling the diffuse thickness, the mesh resolution, and the mobility tuning parameter optimization. An indirect mesh sensitivity process has been performed by relating it with the ε selection procedure, both in a flat and in a textured surface.

The CFD model of the 27 different textures from the experimental DoE have been implemented. The CA values were obtained with the post-processing software (ImageJ) and compared to the experimental values.

The main partial conclusions obtained are as follows:

- The 2D symmetric model is capable of correctly capturing the most fundamental physical phenomena.
- The correct meshing of the domain, χ and ε are the most critical input parameters that affect the convergence of the solution. ε values of 10 and 33.5 μm, and χ values of 5 and 10 m·s/kg have been used, depending on the texture.
- The computational modelling gives further information regarding the influence of r_f and f_{SL} (more specifically, of each factor, a, b and h) on the CA. It shows trends that could not be identified in the experimental results.
- The CA vs r_f results show a similar trend than in the experimental results.
- Even though the 3D provided of a more accurate representation of the droplet penetration inside the cavities and the air entrapment, the 2D model provided a CA measurement closer to the experimental result. This, together with the better performance in terms of computational time when compared to the equivalent 3D model, and taking into consideration the motivation of this thesis, makes the 2D model a reliable option.

Therefore, even though the CA values were not equal (especially at the lowest pillar heights considered), a similar trend was identified, which proves the potential utility of this approach for the considered hydrophobic material. Moreover, the results help identifying the pillar height at which no CA improvement is achievable, and also understanding the contribution of each factor on the air entrapment phenomenon among the cavities or in the contact line position over the surface.

6. 4. Overall conclusion

As a final remark, it can be concluded that the present methodology has the potential to reduce the time needed to select the texture dimensions to ensure a specific CA. This thesis may serve as a guided step by step procedure to develop a predictive model with future polymeric materials and topographic features. Moreover, the implemented procedure may provide valuable understanding about the liquid-solid interface performance when different topographical modifications are introduced. Therefore, it is possible to properly narrow the dimensional values of the different topographic factors reducing both the time and economical cost that arise from this process. Even though these results are specific to the considered polymer, in future works using a different

polymeric material, the same procedure can be followed in order to further validate the results observed in this work, both experimental and computational models. This methodology could be implemented at laboratory and as an envisaged concept for the future digital and autonomous high precision manufacturing process by laser technology. It could also be implemented in different fields/application sectors that require the knowledge of the surface wetting behaviour (where the chemical factor is not imposed over the topographic effect on the CA results), such as the self-cleaning surfaces (automotive, packaging, etc.), anti-icing surfaces (aeronautic, etc.) or antimicrobial surfaces (naval industries, etc.), among others.

Chapter 7

FUTURE WORK LINES

In this last chapter, the next steps regarding the unanswered questions arise during the consecution of this work, as well as the possible applications and scenarios where these tools and results could be implemented with.

- **Semi-empirical modelling of the wettability**

The results shown in this work are specific to the selected material and to the proposed cavity geometries and dimensional parameters. As a next step, a similar procedure should be followed with different materials, liquids and/or feature geometries. Previously, a similar LST was performed by the author of this thesis in another material (ABS [151]) under a different context, but from which experimental results were obtained. Therefore, based on the results obtained from the PP [211] and the ABS [151] samples, it can be observed that the CA variation with r_f could follow a sigmoidal function, as it presents a plateau region upon reaching a certain value of this factor. This function can be expressed based on different parameters that can be obtained experimentally (see (71)).

$$\theta = \theta_0 + \frac{\theta_m - \theta_0}{1 + e^{-\left(\frac{(r_f - q)}{k}\right)}} \quad (71)$$

In this equation, θ is the predicted CA, θ_0 is the reference CA value, θ_m is the expected maximum value obtainable in the plateau region (and obtainable by either applying the Cassie Baxter equation, i.e., eq. (12), or by experimentally obtained CA value from a texture that is expected to give this value due to its high r_f), r_f is the topographic value and q and k are correction factors that may depend on the material of the surface. As an example, the corresponding function of the PP results is obtained and presented in Fig. 7. 1 a), from which the values of q (always greater than 1, as it can be related to the topographic factor) and k are obtained and used afterwards to draw the function of the ABS (see Fig. 7. 1 b)). θ_m is selected as 142º, based on the approximate value at which the best-fit may reach the plateau, q can represent the value at which the CA variation slope suffers a quick variation, which is chosen as 1.1, and k is chosen depending on the r_f region, and adapted to the experimental results, i.e.:

$$k(x) = \begin{cases} 0.3, & x \leq q \\ 0.05, & x > q \end{cases} \quad (72)$$

Afterwards, the same q and k values are adopted for the results from the ABS, but in the latter, a θ_m of 145º is selected, based on the experimental results, and θ_0 equals 91º.

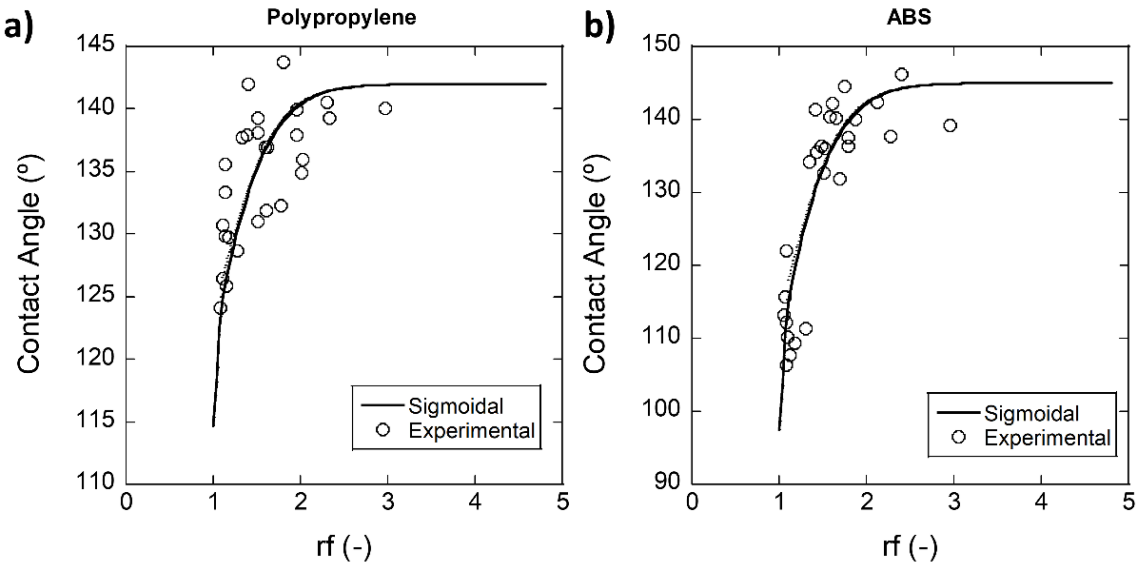

Fig. 7. 1 Experimental fitting with the sigmoidal function proposed in eq.(71) for a) PP and b) ABS [151]

In Fig. 7. 1, it can be seen that, despite being different materials, the results can approximately describe the experimental results, which can be a potential predictive tool for future works. Therefore, as a next step, not only using the described steps on a new material, but also observing if the sigmoidal fitting proves the CA dependence on the r_f is searched.

- **<u>Computational modelling of the wettability</u>**

The computational model can be applied into a wide variety of applications and studies, such as the assessment of the impact of different inputs on the results. Some examples are: the droplet initial velocity, the liquid considered, the reference CA, the pressure generation during the spreading and recoiling, the introduction of a dynamic CA as a wetted wall input, the inclination of the surface to observe the rolling of the droplet and the effect of the texture on its behavior, the definition of different textures, the diameter of the droplet, the modelling of the deposition with a syringe (and its corresponding optimization to eliminate the singularities), the obtention of the surface energy by using diiodomethane in the model, and much more. Fig. 7. 2 shows the simulation results of three different textures on an inclined surface (with an inclination of 10º). It can be observed how, depending on the topography, the bouncing of the droplets was different. From worse to better results, regarding the hydrophobicity of the surface, three different textures were included. Fig. 7. 2

a) (texture 20) shows how the droplet was rapidly stuck on the surface due to the high surface it could be adhered onto, as the value of the pillar width and the f_{SL} were high. As these values were smaller (for mid to high pillar heights), the droplet was able to fall farther before getting stuck (Fig. 7. 2 b), i.e., the texture 2) or even falling off completely from the surface (Fig. 7. 2 c), i.e., the texture 9). Therefore, with these simulations, the importance of the f_{SL} on other factors that define the hydrophobicity of the surface can be established.

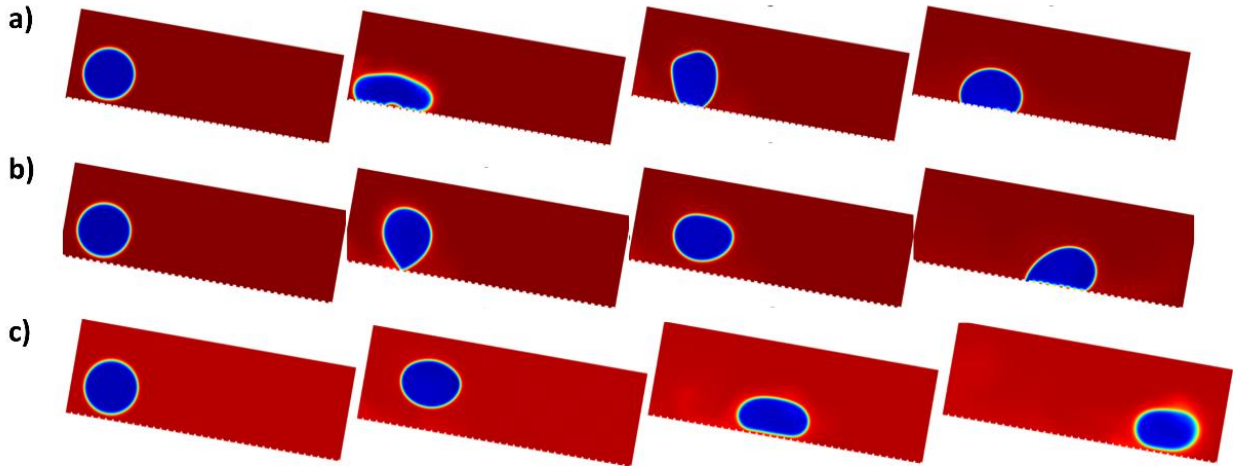

Fig. 7. 2 Evolution of the droplet bouncing on inclined surfaces. a) Texture 20, b) Texture 2 and c) Texture 9

If a more hydrophilic material is considered, the necessary changes on the initial and boundary conditions should be considered in order to ensure the possible high CA values that can be observed. Therefore, as a next step, following the proposed steps and adapting the inputs to the results is proposed, and hence observing the potential utility or the limitations of this Two-Phase Flow model (which uses a diffuse interface instead of a sharp one) to replicate the structure effect on the interface movement.

REFERENCES

[1] L. Jianxin, L. Zonggi, Z. Xiaolei, H. Gulizhaina, C. Xuedi, Wettability and wettability modification methods of porous transport layer in polymer electrolyte membrane electrolysis cells (PEMEC): A review, *International Journal of Hydrogen Energy* 48 (69), 26629 – 26651 (2023), https://doi.org/10.1016/j.ijhydene.2023.03.409

[2] C. G. Jothi Prakash, R. Prasanth, Approaches to design a surface with tunable wettability: a review on surface properties, *Journal of Materials Science* 56, 108-135 (2021), https://doi.org/10.1007/s10853-020-05116-1

[3] Y. Noruzi, M- Sharifi, J. Fahimpour, M. Sabet, M. Akbari, S. Hosseini, The state-of-the-art of wettability alteration in sandstones and Carbonates: A mechanistic review, *Fuel* 356, 129570 (2024), https://doi.org/10.1016/j.fuel.2023.129570

[4] X. Wang, C. Fu, C. Zhang, Z. Qiu, B. Wang, A comprehensive review of wetting transition mechanism on the surface of microstructures from theory and testing methods, *Materials* 15 (14), 4747 (2022), https://doi.org/10.3390/ma15144747

[5] Y. Wang, W. Sun, Y. Xue, X. Sui, B. Yuan, Y. Wang et. al., Functional surfaces with reversibly switchable wettability: Fundamentals, progresses, applications and challenges, *Progress in Organic Coatings* 188, 108167 (2024), https://doi.org/10.1016/j.porgcoat.2023.108167

[6] J. Liu, Y. Yao, X. Li, Z. Zhang, Fabrication of advanced polydimethylsiloxane-based functional materials: Bulk modifications and surface functionalizations, *Chemical Engineering Journal* 408, 127262 (2021), https://doi.org/10.1016/j.cej.2020.127262

[7] Q. Zaman, K. M. Zia, M. Zuber, Y. N. Mabkhot, F. Almaki, T. B. Hadda, A comprehensive review on synthesis, characterization, and applications of polydimethylsiloxane and copolymers, *International Journal of Plastics Technology* 23, 3+2 – 282 (2019), https://doi.org/10.1007/s12588-019-09259-y

[8] J. Salguero, J. M. Vazquez, M. Batista, I. del Sol, Recent Advances in Surface Functionalisation, *Coatings* 13 (3), 530, https://doi.org/10.3390/coatings13030530

[9] S. K. Nemani, R. K. Annavarapu, et. al., Surface modification of polymers: Methods and applications, *Advanced Materials Interfaces* 5 (24), 1801247 (2018), https://doi.org/10.1002/admi.201801247

[10] W. Li, E. S. Thian, M. Wang, Z. Wang, L. Ren, Surface Design for Antibacterial Materials: From Fundamentals to Advanced Strategies, *Advance Science* 8 (19), 2100368 (2021), https://doi.org/10.1002/advs.202100368

[11] P. C. Uzoma, et. al., Recent design approaches, adhesion mechanisms, and applications of antibacterial surfaces, *Chemical Engineering Journal Advances* 16, 100563 (2023), https://doi.org/10.1016/j.ceja.2023.100563

[12] M. Ferrari, F. Cirisano, Superhydrophobic coating solutions for deicing control in aircraft, *Applied Sciences* 13 (21), 11684 (2023), https://doi.org/10.3390/app132111684

[13] J. W. Gose, K. Golovin, et. al., Characterization of superhydrophobic surfaces for drag reduction in turbulent flow, *Journal of Fluid Mechanics* 845, 560 – 580 (2018), https://doi.org/10.1017/jfm.2018.210

[14] Y. Cheng, X. Jiao, et. al., Wetting transition in nanochannels for biomimetic free-blocking on-demand drug transport, *Journal of materials chemistry B* 6 (39), 6269 – 6277 (2018), DOI: 10.1039/c8tb01838c

[15] Scopus, https://www.scopus.com/search/form.uri?display=basic#basic

[16] A. Wang, A. Das, D. Grojo, Ultrafast Laser Writing Deep inside Silicon with THz-Repetition-Rate Trains of Pulses, *Research* 2020 , 8149764 (2020), DOI: 10.34133/2020/814976

[17] U. Loeschner, J. Schille, A. Streek, et. al., High-rate laser microprocessing using a polygon scanner system, *Journal of Laser Applications* 27, S29303 (2015), https://doi.org/10.2351/1.4906473

[18] A. Zemaitis, P. Gecys, G. Raciukaitis, M. Gedvilas, Efficient ablation by ultra-short pulsed lasers, *Procedia CIRP* 94, 962 – 965 (2020), https://doi.org/10.1016/j.procir.2020.09.083

[19] J. Zhang, Y. Meng, A study of surface texturing of carbon steel by photochemical machining, *Journal of Materials Processing Technology* 212 (10), 2133 – 2140 (2012), https://doi.org/10.1016/j.jmatprotec.2012.05.018

[20] H. C. Barshilia, Surface Modification Technologies for Aerospace and Engineering Applications: Current Trends, Challenges and Future Prospects, *Transactions of the Indian National Academy of Engineering* 6, 173 – 188 (2021), https://doi.org/10.1007/s41403-021-00208-z

[21] K. Bobzin, N. Bagcivan, A. Gillner, C. Hartmann, J. Holtkamp, W. Michaeli, et. al., Injection molding of products with functional surfaces by micro-structured, PVD coated injection molds, *Prod. Eng. Res. Devel.* 5, 415-422 (2011), https://doi.org/10.1007/s11740-011-0319-9

[22] P. Hernández, A. Murawko, J. Martínez, G. Peláez, E. Ares, Replication of Micro Laser Textures by Injection Molding, *Procedia Engineering* 63, 885 – 894 (2013), https://doi.org/10.1016/j.proeng.2013.08.201

[23] W. Tong, D. Xiong, Direct laser texturing technique for metal surfaces to achieve superhydrophobicity, *Materials Today Physics* 23, 100651 (2022), https://doi.org/10.1016/j.mtphys.2022.100651

[24] J. Bonse, S. V. Kirner, and J. Krüger, Laser-Induced Periodic Surface Structures (LIPSS), In *Handbook of Laser Micro- and Nano-Engineering, K. Sugioka, Ed. Cham: Springer International Publishing*, 879–936, (2021), https://doi.org/10.1007/978-3-030-63647-0_17

[25] S. Milles, V. Vercillo, S. Alamri, A. I. Aguilar-Morales, T. Kunze, E. Bonaccurso et. al., Icephobic Performance of Multi-Scale Laser-Textured Aluminum Surfaces for Aeronautic Applications, *Nanomaterials* 11, 135 (2021), https://doi.org/10.3390/nano11010135

[26] J. M. Vazquez-Martínez, I. D. S. Illana, E. U. Arrien, M. Batista, J. Salguero, Laser surface texturing as a finishing process for aerospace alloys, In*: Advanced Machining and Finishing. 1st ed. BH Amsterdam: Elsevier Inc*, 643 – 666 (2021), https://doi.org/10.1016/B978-0-12-817452-4.00010-5

[27] J. Schille, L. Schneider, S. Mauersberger, S. Szokup, S. Höhn, J. Pötschke et. al., High-Rate Laser Surface Texturing for Advanced Tribological Functionality, *Lubricants* 8 (3), 33 (2020), https://doi.org/10.3390/lubricants8030033

[28] B. Mao, A. Siddaiah, Y. Liao, P. L. Menezes, Laser surface texturing and related techniques for enhancing tribological performance of engineering materials: A review, *Journal of Manufacturing Processes* 53, 153 – 173 (2020), https://doi.org/10.1016/j.jmapro.2020.02.009

[29] G. Sundararajan, S. V. Joshi, L. R. Krishna, Engineered surfaces for automotive engine and power train components, *Current Opinion in Chemical Engineering* 11, 1 – 6 (2016), https://doi.org/10.1016/j.coche.2015.10.001

[30] J. H. Abboud, K. Y. Benyounis, A. G. Olabi, M. S. J. Hashmi, Laser surface treatments of iron-based substrates for automotive application, *Journal of Materials Processing Technology* 182, 427 – 431 (2007), https://doi.org/10.1016/j.jmatprotec.2006.08.026

[31] What Are The Advantageous Properties Of Polymers Over Metals?, *Piedmon Plastics* (2022), https://www.piedmontplastics.com/blog/polymer-vs-metal

[32] Changing old polymers for use in new applications, *Phys Org* (2021), https://phys.org/news/2021-12-polymers-applications.html

[33] J. Baranwal, B. Barse, A. Faism G. L. Delogu, A. Kumar, Biopolymer: A Sustainable Material for Food and Medical Applications, *Polymers* 14 (5), 983 (2022), https://doi.org/10.3390/polym14050983

[34] V. Busico, R. Cipullo, Microstructure of polypropylene, *Progress in Polymer Science* 26 (3), 443-533 (2001), https://doi.org/10.1016/S0079-6700(00)00046-0

[35] O. Vogl, Polypropylene: An introduction, *Journal of Macromolecular Science Part A Pure and Applied Chemistry* 36 (11), 1547-1559 (2007), 10.1081/MA-100101614

[36] M. Gahleitner, C. Paulik, Polypropylene, in *Ullmann's Encyclopedia of Industrial Chemistry* (2014), https://doi.org/10.1002/14356007.o21_o04.pub2

[37] C. Cathelin, M. Dorini, G. Mei, J. Pater, R. Rinaldi, Polypropylene, in *Kirk-Othmer Encyclopedia of Chemical Technology* (2018), https://doi.org/10.1002/0471238961.1615122512090502.a01.pub3

[38] A. Z. Batyrshin, G. D. Bukatov, I. I. Salakhov, S. A. Sergeev, M. A. Mats'ko, A. A. Barabanov, A. G. Sakhabutdinov, Effect of Polymerization Conditions on Polypropylene Synthesis in Liquid Monomer, *Petroleum Chemistry* 59, 167-173 (2019), https://doi.org/10.1134/S0965544119020038

[39] *PCC Group Manufacturer of specialty chemicals,* Polypropylene – properties, application and everything you need to know about it (29/07/2021), https://www.products.pcc.eu/en/blog/polypropylene-properties-application-and-everything-you-need-to-know-about-it/

[40] *Kimia Forooz Inc. Co. Manufacturer of Engineering Plastics*, Forolen (Polypropylene compounds), http://en.kimiaforooz.com/product-category/forolen-polypropylene-compounds

[41] *Dongguan JinJun Machinery Co.*, Advantage and application of multilayer co-extrusion blow molding on plastic bottles packaging (12/12/2019), https://www.blowmoldingsuper.com/advantage-and-application-of-multilayer-co-extrusion-blow-molding-on-plastic-bottles-packaging.html

[42] *IQS Directory*, Poly Tubing, https://www.iqsdirectory.com/articles/plastic-tubing/poly-tubing.html#what-is-poly-tubing

[43] M. S. Brown, C. B. Arnold, Fundamentals of Laser-Material interaction and application to multiscale surface modification, in *Laser Precision Microfabrication* 135 (2010), https://doi.org/10.1007/978-3-642-10523-4_4

[44] S. R- Kumar, B. Lies, H. Lyu, H. Qin, Laser ablation of polymers: a review, *Procedia Manufacturing* 34, 316 – 327 (2019), https://doi.org/10.1016/j.promfg.2019.06.155

[45] L. Urech, T. Lippert, C. R. Phipps, A. Wokaun, Polymer ablation: From fundamentals of polymer design to laser plasma thruster, *Applied Surface Science* 253 (15), 6409 – 6415 (2007), https://doi.org/10.1016/j.apsusc.2007.01.026

[46] I. Mirza, N. M. Bulgakova, et. al., Ultrashort pulse laser ablation of dielectrics: Thresholds, mechanisms role of breakdown, *Scientific Reports* 6, 39133 (2016), https://doi.org/10.1038/srep39133

[47] D. Li, K. Du, Ultrashort Pulse Lasers, In: K. Sugioka (eds) *Handbook of Laser Mocro- and Nano-Engineering*, Springer, Cham, https://doi.org/10.1007/978-3-030-63647-0_58

[48] N. A. Shepelin, Z. P. Tehrani, N. Ohannessian, C. W. Schneider, D. Pergolesi, T. Lippert, A practical guide to pulsed laser deposition, *Chem. Soc. Rev.* 52, 2294-2321 (2023), https://doi.org/10.1039/D2CS00938B

[49] H. Liu, W. Lin, M. Hong, Hybrid laser precision engineering of transparent hard materials: challenges, solutions and applications, *Light Sci Appl* 10, 162 (2021), https://doi.org/10.1038/s41377-021-00596-5

[50] R. R. Gattass, E. Mazur, Femtosecond laser micromachining in transparent materials, *Nature Photonics* 2, 219-225 (2008), https://doi.org/10.1038/nphoton.2008.47

[51] L. J. Jiang, S. Maruo, R. Osellame, W. Xiong, J. H. Campbell, Y. F. Lu, Femtosecond laser direct writing in transparent materials based on nonlinear absorption, *MRS Bulletin* 41, 975-983 (2016), https://doi.org/10.1557/mrs.2016.272

[52] A. Gillner, A Horn, Ablation. In *Tailored Light 2* (2011), https://doi.org/10.1007/978-3-642-01μ-2_15

[53] D. Bäuerle, Thermal, Photophysical, and Photochemical Processes. In *Laser Processing and Chemistry* (2011); https://doi.org/10.1007/978-3-642-17613-5_2

[54] A. F. Obilor, M. Pacella, A. Wilson, V. V. Silberschmidt, Micro-texturing of polymer surfaces using lasers: a review, *The International Journal of Advanced Manufacturing Technology* 120, 103 – 135 (2022), https://doi.org/10.1007/s00170-022-08731-1

[55] R. Suriano, A. Kuznetsov, et. al., Femtosecond laser ablation of polymeric substrates for the fabrication of microfluidic channels, *Applied Surface Science* 257 (14), 6243 – 6250 (2011), https://doi.org/10.1016/j.apsusc.2011.02.053

[56] R. Ortiz, Ultrashort-pulsed laser ablation of Poly-L-Lactide (PLLA) for cell and tissue engineering applications (2017) [PhD Thesis, Universidad del Pais Vasco], from *ADDI: Archive Digital Docencia Investigadora*

[57] S. S. Harilal, J. R. Freeman, P. K. Diwakar, A. Hassanein, Femtosecond laser ablation: fundamentals and applications, In: S. Mussazi, U. Perini (eds) *Laser-induced breakdown spectroscopy*. Springer Series in Optical Sciences 182, Springer, Berlin, Heidelberg (2014), https://doi.org/10.1007/978-3-642-45085-3_6

[58] I. Miraoui, M. Boujelbene, M. Zaied, High-power laser cutting of steel plates: heat affected zone analysis, *Advances in Materials Science and Engineering* 2016, 1 – 8 (2016), https://doi.org/10.1155/2016/1242565

[59] I.-B. Sohn, Y.-C. Noh, S.-C. Choi, D.-K. Ko, J. Lee, Y.-J. Choi, Femtosecond laser ablation of polypropylene for breathable films, *Applied Surface Science* 254 (16), 4919-4924 (2008), https://doi.org/10.1016/j.apsusc.2008.01.166

[60] A. P. Yalin, N. Wilvert, C. Dumitrache, S. Joshi, M. N. Shneider, Laser Plasma formation assisted by ultraviolet pre-ionization, *Physics of Plasma* 21 (10), 103511 (2014), https://doi.org/10.1063/1.4898059

[61] A. Vogel, J. Noack, G. Hüttman, G. Paltauf, Mechanisms of femtosecond laser nanosurgery of cells and tissues, *Applied Physics B* 81, 1015-1047 (2005), https://doi.org/10.1007/s00340-005-2036-6

[62] A. Rahaman, X. Du, B. Zhou, A. Kar, X. Yu, Pulse to pulse evolution of optical properties in ultrafast laser micro-processing of polymers, *Journal of lasrs applications* 33, 012020 (2021), https://doi.org/10.2351/7.0000306

[63] A. Rahaman, A. Kar, Microstructures formed in polypropylene by a single pulse of near-infrared ultrafast laser with nonlinear absorption, *Optics & Laser Technology* 158, 108886 (2023), https://doi.org/10.1016/j.optlastec.2022.108886

[64] A. Rahaman, A. Kar, X. Yu, Time-resolved measurements of optical properties in ultrafast laser interaction with polypropylene, *Optics Express* 28 (2), 2640 – 2648 (2020), https://doi.org/10.1364/oe.384302

[65] H. Mustafa, M. Mezera, D. T. A. Matthews, G. R. B. E. Römer, Effect of surface roughness on the ultrashort pulsed laser ablation fluence threshold of zinc and steel, *Applied Surface Science* 488, 10 – 21 (2019), https://doi.org/10.1016/j.apsusc.2019.05.066

[66] J.-Q. Chen, X.-Z. Xie, Q.-F. Peng, Z.-Y. He, W. Hu, Q.-L. Ren et. al., Effect of surface roughness on femtosecond laser ablation of 4H-SiC substrates, *Journal of Central South University* 29, 3294 – 3303 (2022), https://doi.org/10.1007/s11771-022-5136-0

[67] F. D. Niso, C. Gaudiuso, T. SIbillano, F. P. Mezzapesa, A. Ancona, P. M. Lugarà, Influence of the Repetition Rate and Pulse Duration on the Incubation Effect in Multiple-Shots Ultrafast Laser Ablation of Steel, *Physics Procedia* 41, 698 – 707 (2013), https://doi.org/10.1016/j.phpro.2013.03.136

[68] A. Zemaitis, M. Gaidys, M. Brikas, P. Gecys, G. Raciukaitis, M. Gedvilas, Advanced laser scanning for highly-efficient ablation and ultrafast surface structuring: experiment and model, *Scientific Reports* 8, 17376 (2018), https://doi.org/10.1038/s41598-018-35604-z

[69] L. Pongratz, K. Vannahme, Beam Shaping the Direct Laser Interference Patterning Spot, *Journal of Laser Micro/Nanoengineering* 17, (2022), DOI: 0.2961/jlmn.2022.01.2007

[70] V. Furlan, A. G. Demir, A. Bianco, Direct laser interference patterning via scanning optics using the Michelson-Morley configuration, *Applied Surface Science* 606, 154536 (2022), https://doi.org/10.1016/j.apsusc.2022.154536

[71] M. El-Khoury, B. Voisiat, T. Kunze, A. F. Lasagni, Utilizing fundamental beam-mode shaping technique for top-hat laser intensities in Direct Laser Interference Patterning, *Journal of Laser Micro/Nanoengineering* 13, (2018), DOI: 10.2961/jlmn.2018.03.0021

[72] L. Ackermann, C. Roider, K. Cvecek, M. Schmidt, Methods for uniform beam shaping and their effect on material ablation, *Applied Physics A* 128, 877 (2022), https://doi.org/10.1007/s00339-022-06004-y

[73] R. Weber, T. Graf, P. Berger, V. Onuseit, M. Wiedenmann, C. Freitag et. al., Heat accumulation during pulsed laser materials processing, *Optics Express* 22 (23), 28232 (2014), DOI: 10.1364/OE.22.011312

[74] R. Weber, T. Graf, C. Freitag, A. Feuer, T. Kononenko, V. I. Konov, Processing constraints resulting from heat accumulation during pulsed and repetitive laser materials processing, *Optics Express* 25 (4), 3966 – 3979 (2017), https://doi.org/10.1364/OE.25.003966

[75] J. Martan, L. Prokesová, D. Moskal, B.C. Ferreira de Faria, M. Honner, V. Lang, Heat accumulation temperature measurement in ultrashort pulse laser micromachining, *International Journal of Heat and Mass Transfer* 168, 120866 (2021), https://doi.org/10.1016/j.ijheatmasstransfer.2020.120866

[76] F. Bauer, A. Michalowski, T. Kiedrowski, S. Nolte, Heat accumulation in ultra-short pulsed scanning laser ablation of metals, *Optics Express* 23 (2), 1035-43 (2015), DOI: 10.1364/OE.23.001035

[77] T. V. Kononenko, C. Freitag, M. S. Komlenok, V. Onuseit, R. Weber, T. Graf, V. I. Konov, Heat accumulation effects in short-pulse multi-pass cutting of carbon fiber reinforced plastics, *Journal of Applied Physics* 118, 103105 (2015), https://doi.org/10.1063/1.4930059

[78] K. Jindal, *Plastic Ranger*, Polypropylene Melting Point, the definitive guide (14/09/2023), https://plasticranger.com/polypropylene-melting-point/#:~:text=Polypropylene%20exhibits%20a%20melting%20point%20range%20of%20160%C2%B0C,for%20deployment%20in%20settings%20that%20experience%20high%20temperatures.

[79] *The Engineering Toolbox* (2005), Metals and Alloys - Melting Temperatures (online), https://www.engineeringtoolbox.com/melting-temperature-metals-d_860.html

[80] M. Domke, V. Matylitsky, S. Stroj, Surface ablation efficiency and quality of fs lasers in single-pulse mode, fs lasers in burst mode and ns lasers, *Applied Surface Science* 505, 144594 (2020), https://doi.org/10.1016/j.apsusc.2019.144594

[81] D. Metzner, P. Lickschat, S. Weiβmantel, Influence of heat accumulation during laser micromachining of CoCrMo alloy with ultrashort pulses in burst mode, *Applied Physics A.* 126, 84 (2020), https://doi.org/10.1007/s00339-019-3203-7

[82] D. Metzner, P. Lickschat, S. Weiβmantel, Investigations of qualitative aspects with burst mode ablation of silicon and cemented tungsten carbide, *Applied Physics A.* 125, 411 (2019), https://doi.org/10.1007/s00339-019-2696-4

[83] V. N. Lednev, M. N. Filippov, A .F. Bunkin, S. M. Pershin, Laser ablation comparison by picosecond pulses train and nanosecond pulse, *Laser Physics Letters* 12, 126001 (2015), https://doi.org/10.1088/1612-2011/12/12/126001

[84] B. Neuenschwander, T. Kramer, B. Lauer, B. Jaeggi, Burst mode with ps- and fs-pulses: Influence on the removal rate, surface quality, and heat accumulation, *Laser Applications in Microelectronic and Optoelectronic Manufacturing* 9350, (2015); https://doi.org/10.1117/12.2076455

[85] T. Kramer, B. Neuenschwander, B. Jäggi, S. Remund, U. Hunziker, J. Zürcher, Influence of pulse bursts on the specific removal rate for ultra-fast pulsed laser micromachining of copper, *Physics Procedia* 83, 123 – 134 (2016), https://doi.org/10.1016/j.phpro.2016.08.024

[86] T. Kramer, W. Zhang, S. Remund, B. Jaeggi, A. Michalowski, L. Grad et. al., Increasing the Specific Removal Rate for Ultra Short Pulsed Laser-Micromachining by Using Pulse Bursts, *Journal of Laser Micro/Nanoengineering* 12, (2017), DOI: 10.2961/jlmn.2017.02.0011

[87] B. Neuenschwander, B. Jaeggi, D. J. Foerster, T. Kramer, S. Remund, Influence of the burst mode onto the specific removal rate for metals and semiconductors, *Journal of Laser Applications* 31, 022203 (2019); https://doi.org/10.2351/1.5096083

[88] B. Neuenschwander, B. Jaeggi, E. V. Zavedeev, N. R. Arutyunyan, S. M. Pimenov, Heat accumulation effects in laser processing of diamond-like nanocomposite films with bursts of femtosecond pulses, *Journal of Applied Physics* 126, 115301 (2019), https://doi.org/10.1063/1.5121424

[89] S. M. Remund, M. Gafner, M. V. Chaja, A. Urniezius, S. Butkus, B. Neuenschwander, Milling applications with GHz bursts: Investigations concerning the removal rate and machining quality, *Procedia CIRP* 94, 850 – 855 (2020), https://doi.org/10.1016/j.procir.2020.09.111

[90] A. Zemaitis, P. Gecys, M. Barkauskas, G. Raciukaitis, M. Gedvilas, Highly efficient laser ablation of copper by bursts of ultrashort tuneable (fs-ps) pulses, *Scientific Reports* 9, 12280 (2019), https://doi.org/10.1038/s41598-019-48779-w

[91] R. F. Gattas, L. R. Ceramo, E. Mazur, Micromachining of bulk glass with bursts of femtosecond laser pulses at variable repetition rates, *Optics Express* 14, 5279-84 (2006), https://doi.org/10.1364/OE.14.005279

[92] R. Knappe, H. Haloui, A. Seifert, A. Weis, A. Nebel, Scaling ablation rates for picosecond lasers using burst micromachining, *Proceedings of SPIE* 7585, (2010), DOI: 10.1117/12.842318

[93] E. Kazukauskas, S. Butkus, P. Tokarski, V. Jukna, M. Barkauskas, V. Sirutkaitis, Micromachining of Transparent Biocompatible Polymers Applied in Medicine Using Bursts of Femtosecond Laser Pulses, *Micromachines* 11, 1093 (2020), DOI: doi:10.3390/mi11121093

[94] D. J. Förster, B. Jäggi, A. Michalowski, B. Neuenschwander, Review on Experimental and Theoretical Investigations of Ultra-Short Pulsed Laser Ablation of Metals with Burst Pulses, *Materials* 14 (12), 3331 (2021); https://doi.org/10.3390/ma14123331

[95] C. Gaudiuso, P. N. Terekhin, A. Volpe, S. Nolte, B. Rethfeld, A. Acona, Laser ablation of silicon with THz bursts of femtosecond pulses, *Scientific reports* 11, 13321 (2021), https://doi.org/10.1038/s41598-021-92645-7

[96] G. Boanmis, K. Mishchick, E. Audouard, C. Hönninger, E. Mottay, J. Lopez et. al., High efficiency femtosecond laser ablation with gigahertz level bursts, *Journal of Laser Applications* 31, 022205 (2019), https://doi.org/10.2351/1.5096087

[97] H. Le, T. Karkantonis, V. Nasrollahi, P. Penchev, S. Dimov, MHz burst mode processing as a tool for achieving removal rates scalability in ultrashort laser micro-machining, *Applied Physics A* 128, 711 (2022), https://doi.org/10.1007/s00339-022-05864-8

[98] E. Kazukauskas, S. Butkus, P. Tokarski, V. Jukna, M. Barkauskas, V. Sirutkaitis, Micromachining of transparent biocompatible polymers applied in medicine using bursts of femtosecond laser pulses, *Micromachines* 11 (12), 1093 (2020), https://doi.org/10.3390/mi11121093

[99] S. A. Ahmed, M. Mohsin, S. M. Z. Ali, Survey and technological analysis of laser and its defense applications, *Defence Technology* 17 (2), 583 – 592 (2021), https://doi.org/10.1016/j.dt.2020.02.012

[100] A. Samanta, Q. Wang, S. K. Shaw, H. Ding, Roles of chemistry modification for laser textured metal alloys to achieve extreme surface wetting behaviors, *Materials* & *Design* 192, 108744 (2020), https://doi.org/10.1016/j.matdes.2020.108744

[101] S. Jiang, Y. Diao, H. Yang, Recent advances of bio-inspired anti-icing surfaces, *Advances in Colloid and Interface Science* 308, 102756 (2022), https://doi.org/10.1016/j.cis.2022.102756

[102] V. Vercillo, S. Tonnicchia, J.-M. Romano, A. García-Girón, A. I. Aguilar-Morales, S. Alamri et. al., Design Rules for Laser-Treated Icephobic Metallic Surfaces for Aeronautic Applications, *Advanced Functional Materials* 30 (16), 1910268, https://doi.org/10.1002/adfm.201910268

[103] A. Peter, A. H. A. Lutey, S. Faas, L. Romoli, V. Onuseit, T. Graf, Direct laser interference patterning of stainless steel by ultrashort pulses for antibacterial surfaces, *Optics* & *Laser Technology* 123, 105954 (2020), https://doi.org/10.1016/j.optlastec.2019.105954

[104] V. Furlan, A. G. Demir, A. Bianco, Direct laser interference patterning via scanning optics using the Michelson-Morley configuration, *Applied Surface Science* 606, 154536 (2022), https://doi.org/10.1016/j.apsusc.2022.154536

[105] A. Madelung, S. Alamri, T. Steege, B. Krupop, A. F. Lasagni, T. Kunze, Scanner-Based Direct Laser Interference Patterning on Stainless Steel, *Advanced Engineering Materials* 23 (6), 2001414 (2021), https://doi.org/10.1002/adem.202001414

[106] A. Volpe, C. Gaudiuso, L. D. Venere, F. Licciulli, F. Giordano, A. Ancona, Direct Femtosecond Laser Fabrication of Superhydrophobic Aluminum Alloy Surfaces with Anti-icing Properties, *Coatings* 10 (6), 587 (2020), https://doi.org/10.3390/coatings10060587

[107] H. Prime, S. Lowrey, R. Blaikie, A. Sommers, Z. Sun, J. Juras, Micro-fabricated aluminium surfaces for reduced ice adhesion, *Experimental Thermal and Fluid Science* 136, 110646 (2022), https://doi.org/10.1016/j.expthermflusci.2022.110646

[108] Y. Yusuf, M. J. Ghazali, Y. Otsuka, K. Ohnuma, S. Morakul, S. Nakamura et. al., Antibacterial properties of laser surface-textured TiO2/ZnO ceramic coatings, *Ceramics International* 46 (3), 3949 – 3959 (2020), https://doi.org/10.1016/j.ceramint.2019.10.124

[109] F. H. Rajab, C. M. Liauw, P. S. Benson, L. Li, K. A. Whitehead, Production of hybrid macro/micro/nano surface structures on Ti6Al4V surfaces by picosecond laser surface texturing and their antifouling characteristics, *Colloids and Surfaces B: Biointerfaces* 160, 688 – 696, https://doi.org/10.1016/j.colsurfb.2017.10.008

[110] A. H. A. Lutey, L. Gemini, L. Romoli, G. Lazzini, F. Fuso, M. Faucon et. al., Towards Laser-Textured Antibacterial Surfaces, *Scientific Reports* 8, 10112 (2018), https://doi.org/10.1038/s41598-018-28454-2

[111] E. Stratakis, J. Bonse, J. Heitz, J. Siegel, G. D. Tsibidis, E. Skoulas et. al, Laser engineering of biomimetic surfaces, *Materials Science and Engineering: R: Reports* 141, 100562 (2020), https://doi.org/10.1016/j.mser.2020.100562

[112] S. Pogodin, J. Hasan, V. A. Baulin, H. K. Webb, V. K. Truong, T. H. P. Nguyen et. al., Biophysical model of bacterial cell interactions with nanopatterned cicada wing surfaces, *Biophysics Journal* 104 (4), 835 - 840 (2013), DOI: 10.1016/j.bpj.2012.12.046

[113] T. Stark, S. Alamri, A. I. Aguilar-Morales, T. Kiedrowski, A. F. Lasagni, Positive Effect of Laser Structured Surfaces on Tribological Performance, *Journal of Laser Micro/Nanoengineering* 14, (2019), DOI: 10.2961/jlmn.2019.01.0003

[114] V. Ezhilmaran, N. J. Vasa, S. Krishnan, L. Vijayaraghavan, Femtosecond Pulsed Ti:Sapphire Laser-Assisted Surface Texturing on Piston Ring and Its Tribology Characterization, *Journal of Tribology* 143 (4), 041801 (2021), https://doi.org/10.1115/1.4048385

[115] X. Li, Y. Li, Z. Tong, Q. Ma, Y. Ni, G. Dong, Enhanced lubrication effect of gallium-based liquid metal with laser textured Surface, *Tribology International* 129, 407 – 415 (2019), https://doi.org/10.1016/j.triboint.2018.08.037

[116] D. Chen, Y. Liu, H. Chen, D. Zhang, Bio-inspired drag reduction surface from sharkskin, *Biosurface and Biotribology* 4 (2), 39 – 45 (2018), https://doi.org/10.1049/bsbt.2018.0006

[117] D. W. Bechert, M. Bruse, W. Hage, Experiments with three-dimensional riblets as an idealized model of shark skin, *Experiments in Fluids* 28, 403 – 412 (2000), https://doi.org/10.1007/s003480050400

[118] D. W. Bechert, M. Bruse, W. Hage, J. V. D. Hoeven, Experiments on drag-reducing surfaces and their optimization with an adjustable geometry, *Journal of Fluid Mechanics* 338, 59 – 87 (1997), DOI: 10.1017/S0022112096004673

[119] K. M. T. Ahmmed, J. Montagut, A.-M. Kietzig, Drag on superhydrophobic sharkskin inspired surface in a closed channel turbulent flow, *The Canadian Journal of Chemical Engineering* 95 (10), 1934 – 1942 (2017), https://doi.org/10.1002/cjce.22850

[120] S. Martin, B. Bhushan, Modeling and optimization of shark-inspired riblet geometries for low drag applications, *Journal of Colloid and Interface Science* 474, 206 – 215 (2016), https://doi.org/10.1016/j.jcis.2016.04.019

[121] J. J. J. Kaakkunen, J. Tiainen, A. Jaatinen-Värri, A. Grönman, M. Lohtander, Nanosecond laser ablation of the trapezoidal structures for turbomachinery applications, *Procedia Manufacturing* 25, 435 – 442 (2018), https://doi.org/10.1016/j.promfg.2018.06.114

[122] W. Rong, H. Zhang, Z. Mao, L. Chen, X. Liu, Improved Stable Drag Reduction of Controllable Laser-Patterned Superwetting Surfaces Containing Bioinspired Micro/Nanostructured Arrays, *ACS Omega* 7 (2), 2049 – 2063 (2022), https://doi.org/10.1021/acsomega.1c05507

[123] G. D. Bixler, B. Bhushan, Fluid Drag Reduction with Shark-Skin Riblet Inspired Microstructured Surfaces, *Advanced Functional Materials* 23 (36), 4507 – 4528 (2013), https://doi.org/10.1002/adfm.201203683

[124] J. Bonse, S. V. Krimer, S. Höhm, N. Epperlein, D. Spaltman, A. Rosenfeld, J. Krüger, Applications of laser-induced periodic surface structures (LIPSS), *Proceedings SPIE* 10092 (2017), https://doi.org/10.1117/12.2250919

[125] T. D. Blake, The physics of moving wetting lines, *Journal of Colloid and Interface Science* 299, 1-13 (2006), https://doi.org/10.1016/j.jcis.2006.03.051

[126] B. Wang, Y. Zhang, J. Song, Z. Wang, Investigation and Prediction on Regulation of Hydrophobicity of Polymethyl Methacrylate (PMMA) Surface by Femtosecond Laser Irradiation, *Coatings* 10 (4), 386 (2020), https://doi.org/10.3390/coatings10040386

[127] C. Yao, S. Xu, X. Jiang, J. Chen, X. Yuan, A Simple Way to Achieve Self-Cleaning Surfaces with Unique Antifouling Property, *Journal of Chemistry* 2020, 9072432 (2020), https://doi.org/10.1155/2020/9072432

[128] T. Young, An essay on the cohesion of fluids, *Proceedings of the Royal Society of London* 1, 171 – 172 (1832), https://doi.org/10.1098/rspl.1800.0095

[129] D. Wang, Q. Sun, M. J. Hokkanen, C. Zhang, F.-Y. Lin, Q. Liu et. al., Design of robust superhydrophobic surfaces, *Nature* 582, 55 – 59 (2020), https://doi.org/10.1038/s41586-020-2331-8

[130] *Krüss*, Surface free energy (SFE), surface energy, https://www.kruss-scientific.com/en/know-how/glossary/surface-free-energy

[131] T. Huhtamäki, X. Tian, J. T. Korhonen, R. H. A. Ras, Surface-wetting characterization using contact-angle measurements, *Nature Protocols* 13, 1521 – 1538 (2018), https://doi.org/10.1038/s41596-018-0003-z

[132] J. Yong, Q. Yang, C. Guo, F. Chen, X. Hou, A review of femtosecond laser-structured superhydrophobic or underwater superoleophobic porous surfaces/materials for efficient oil/water separation, *RSC Advances* 9 (22), 12470 – 12495 (2019), https://doi.org/10.1039/C8RA10673H

[133] V. D. Ta, A. Dunn, T. J. Wasley, J. Li, R. W. Kay, J. Stringen, et. al., Laser textured superhydrophobic surfaces and their applications for homogeneous spot deposition, *Applied Surface Science* 365, 153 – 159, (2016), https://doi.org/10.1016/j.apsusc.2016.01.019

[134] K. Ding, C. Wang, Y. Zheng, Z. Xie, Z. Luo, S. Man, et al., One-step fabrication of multifunctional fusiform hierarchical micro/nanostructures on copper by femtosecond laser, *Surface and Coatings Technology* 367, 244 – 251 (2019), https://doi.org/10.1016/j.surfcoat.2019.04.005

[135] A. O. Ijaola, E. A. Bamidele, C. J. Akisin, I. T. Bello, A. T. Oyaboto, A. Abdulkareem et. al., Wettability Transition for Laser Textured Surfaces: A Comprehensive Review, *Surfaces and Interfaces* 21, 100802 (2020), https://doi.org/10.1016/j.surfin.2020.100802

[136] M. Callies, Y. Chen, F. Marty, A. Pépin, D. Quéré, Microfabricated textured surfaces for super-hydrophobicity investigations, *Microelectronic Engineering* 78 – 79, 100 – 105 (2005). https://doi.org/10.1016/j.mee.2004.12.093

[137] D. Patel, V. Jain, J. Ramkumar, Surface Texturing for Inducing Hydrophobicity, *Directions* 15, 46 – 53 (2016), DOI: 10.13140/RG.2.1.4165.6401

[138] B. J. Li, H. Li, L. J. Huang, N. F. Ren, X. Kong, Femtosecond pulsed laser textured titanium surfaces with stable superhydrophilicity and superhydrophobicity, *Applied Surface Science* 389, 585 – 593 (2016), https://doi.org/10.1016/j.apsusc.2016.07.137

[139] C. Ma, S. Bai, X. Peng, Y. Meng, Improving hydrophobicity of laser textured SiC surface with micro-square convexes, *Applied Surface Science* 266, 51 – 56 (2013), https://doi.org/10.1016/j.apsusc.2012.11.068

[140] J. Qiao, L. N. Zhu, W. Yue, Z. Q. Fu, J. J. Kang, C. B. Wang, The effect of attributes of micro-shapes of laser surface texture on the wettability of WC-CrCo metal ceramic coatings, *Surface and Coatings Technology* 334, 429 – 437 (2018), https://doi.org/10.1016/j.surfcoat.2017.12.001

[141] H.-J. Butt, J. Liu, K. Koynov, B. Straub, C. Hinduja, I. Roismann, Contact angle hysteresis, *Current Opinion in Colloid & Interface Science* 59, 101574 (2022), https://doi.org/10.1016/j.cocis.2022.101574

[142] D. Murakami, H. Jinnai, A. Takahara, Wetting transition from the cassie-baxter state to the wenzel state on textured polymer surfaces, *Langmuir* 30 (8), 2061 – 2067 (2014), https://doi.org/10.1021/la4049067

[143] D. Kim, N. M. Pugno, S. Ryu, Wetting theory for small droplets on textured solid surfaces, *Scientific Reports* 6, 37813 (2016), https://doi.org/10.1038/srep37813

[144] V. Belaud, S. Valette, G. Stremsdoerfer, M. Bigerelle, S. Benayoun, Wettability versus roughness: Multi-scales approach, *Tribology International* 82, 343 – 349 (2015), https://doi.org/10.1016/j.triboint.2014.07.002

[145] R. N. Wenzel, Resistance of solid surfaces to wetting by water, *Industrial and Engineering Chemistry* 28 (8), 988 – 994 (1936), https://doi.org/10.1021/ie50320a024

[146] A. B. D. Cassie, S. Baxter, Wettability of porous surfaces*, Transactions of the Faraday Society* 40, 546 – 551 (1944), https://doi.org/10.1039/TF9444000546

[147] B. K. Cheng, B. Naccarato, K. J. Kim, A. Kumar, Theoretical consideration of contact angle hysteresis using surface-energy-minimization methods, *International Journal of Heat and Mass Transfer* 102, 154 – 161 (2016), https://doi.org/10.1016/j.ijheatmasstransfer.2016.06.014

[148] F. J. Montes Ruiz-Cabello, M. A. Cabrerizo-Vílchez, M. A. Rodríguez-Valverde, Evaluation of the solid-liquid contact area fraction of drops deposited on rough surfaces beyond the Wenzel regime, *Colloids and Surfaces A: Physicochemical and Engineering Aspects* 568, 455 – 460 (2019), https://doi.org/10.1016/j.colsurfa.2019.02.047

[149] A. Fernández, A. Francone, L. H. Thamdrup, A. Johansson, B. Bilenberg, T. Nielsen, et. al., Hierarchical surfaces for enhanced self-cleaning applications, *Journal of Micromechanics and Microengineering* 27, 045020 (2017), DOI: 10.1088/1361-6439/aa62bb

[150] B. Yin, X. Xie, S. Xu, H. Jia, S. Yang, F. Dong, Effect of pillared surfaces with different shape parameters on droplet wettability via Lattice Boltzmann method, *Colloids and Surfaces A: Physicochemical and Engineering Aspects* 615, 126259 (2021), https://doi.org/10.1016/j.colsurfa.2021.126259

[151] J. Molinuevo, I. Quintana, E. Rodríguez-Vidal, R. Díez-Ahedo, A. Retolaza, C. Molpeceres, Role of roughness levels induced by the laser texturing on the wettability behaviour of ABS, *Procedia CIRP* 94, 885 – 890 (2020). https://doi.org/10.1016/j.procir.2020.09.066

[152] P. Fan, R. Pan, M. Zhong, Ultrafast Laser Enabling Hierarchical Structures for Versatile Superhydrophobicity with Enhanced Cassie-Baxter Stability and Durability, *Langmuir* 35 (51), 16693 – 16711 (2019), DOI: 10.1021/acs.langmuir.9b02986

[153] I. P. D. S. Ramos, C. Gavazzoni, D. Lazzari, C. Brito, Hierarchical structured surfaces enhance the contact angle of the hydrophobic (meta-stable) state, *The Journal of Chemical Physics* 158, 154703 (2023), https://doi.org/10.1063/5.0146948

[154] J. Bonse, S. Höhm, S. V. Kirner, A. Rosenfeld, J. Krüger, Laser-Induced periodic surface structures – A scientific evergreen, *IEEE Journal of selected topics in quantum electronics* 23, 9000615 (2017), DOI: 10.1109/JSTQE.2016.2614183

[155] H. M. van Driel, J. E. Sipe, J. F. Young, Laser-Induced periodic surface structure on solids; a universal phenomenon, *Physical Review Letters* 49, 1955 (1982), https://doi.org/10.1103/PhysRevLett.49.1955

[156] R. J. Nemanich, D. K. Biegelsen, W. G. Hawkins, Aligned, coexisting liquid and solid regions in pulsed and CW laser annealing of Si, *MRS Online Proceedings Library* 13, 211 – 216 (1982), https://doi.org/10.1557/PROC-13-211

[157] R. Liu, D. Zhang, Z. Li, Femtosecond laser induced simultaneous functional nanomaterial synthesis, in situ deposition and hierarchical LIPSS nanostructuring for tunable antireflectance and iridescence applications, *Journal of Materials Science & Technology* 89, 179 – 185 (2021), https://doi.org/10.1016/j.jmst.2021.02.024

[158] D. Banerjee, M. Akkanaboina, R. K. Kanaka, V. R. Soma, Femtosecond Bessel beam induced ladder-like LIPSS on trimetallic surface for SERS-based sensing of Tetryl and PETN, *Applied Surface Science* 616, 156561 (2023), https://doi.org/10.1016/j.apsusc.2023.156561

[159] D. Zhang, R. Liu, Z. Li, Irregular LIPSS produced on metals by single linearly polarized femtosecond laser, *International Journal of Extreme Manufacturing* 4, 015102 (2022), DOI: 10.1088/2631-7990/ac376c

[160] Y.-F. Gao, C.-Y. Yu, B. Han, M. Ehrhardt, P. Lorenz, L.-F. Xu et. Al., Picosecond laser-induced periodic Surface structures (LIPSS) on crystalline silicon, *Surfaces and Interfaces* 19, 100538 (2020), https://doi.org/10.1016/j.surfin.2020.100538

[161] S. Höhm, M. Herzlieb, A. Rosenfeld, J. Krüger, J. Bonse, Dynamics of the formation of laser-induced periodic surface structures (LIPSS) upon femtosecond two-color double-pulse irradiation of metals, semiconductors, and dielectrics, *Applied Surface Science* 374, 331 – 338 (2016), https://doi.org/10.1016/j.apsusc.2015.12.129

[162] M. Ehrhardt, S. Lai, P. Lorenz, K. Zimmer, Guiding of LIPSS formation by excimer laser irradiation of pre-patterned polymer films for tailored hierarchical structures, *Applied Surface Science* 506, 144785 (2020), https://doi.org/10.1016/j.apsusc.2019.144785

[163] H. Vaghasiya, P.-T. Miclea, Investigating Laser-Induced Periodic Surface Structures (LIPSS) Formation in Silicon and Their Impact on Surface-Enhanced Raman Spectroscopy (SERS), *Optics* 4 (4), 538 – 550 (2023), https://doi.org/10.3390/opt4040039

[164] E. L. Gurevich, Mechanisms of femtosecond LIPSS formation induced by periodic surface temperature modulation, *Applied Surface Science* 374, 56 – 60 (2016), https://doi.org/10.1016/j.apsusc.2015.09.091

[165] A. V. Dostovalov, T. J.-Y. Derrien, S. A. Lizunov, F. Preucil, K. A. Okotrub, T. Mocek et. al., LIPSS on thin metallic films: New insights from multiplicity of laser-excited electromagnetic modes and efficiency of metal oxidation, *Applied Surface Science* 491, 650 – 658 (2019), https://doi.org/10.1016/j.apsusc.2019.05.171

[166] J. Bonse, S. V. Kirner, M. Griepentrog, D. Spaltmann, J. Krüger, Femtosecond Laser Texturing of Surfaces for Tribological Applications, *Materials* 11 (5), 801 (2018), https://doi.org/10.3390/ma11050801

[167] H. Wan, S. Li, J. Li, T. Liu, J. Lin, J. Min, Wettability transition of metallic surfaces from laser-generated superhydrophilicity to water-induced superhydrophobicity via a facile and eco-friendly strategy, *Materials & Design* 226, 111691 (2023), https://doi.org/10.1016/j.matdes.2023.111691

[168] L. Bonova, A. Zahoranova, D. Kovacik, M. Zahoran, M. Micusik, M. Cernak, Atmospheric pressure plasma treatment of flat aluminum surface, *Applied Surface Science* 331, 79 – 86 (2015), https://doi.org/10.1016/j.apsusc.2015.01.030

[169] T. S. M. Mui, L. L. G. Silva, V. Prysiazhnyi, K. G. Kostov, Surface modification of aluminium alloys by atmospheric pressure plasma treatments for enhancement of their adhesion properties, *Surface and Coatings Technology* 312, 32 – 36 (2017), https://doi.org/10.1016/j.surfcoat.2016.08.024

[170] A. Samanta, Q. Wang, S. K. Shaw, H. Ding, Roles of chemistry modification for laser textured metal alloys to achieve extreme surface wetting behaviors, *Materials & Design* 192, 108744 (2020), https://doi.org/10.1016/j.matdes.2020.108744

[171] J. Long, M. Zhong, H. Zhang, P. Fan, Superhydrophilicity to superhydrophobicity transition of picosecond laser microstructured aluminum in ambient air, *Journal of Colloid and Interface Science* 441, 1 – 9 (2015), https://doi.org/10.1016/j.jcis.2014.11.015

[172] J. Hu, R. Jia, K.-T. Wan, X. Xiong, Simulation of Droplet Impingement on a Solid Surface by the Level Set Method, *2014 COMSOL Boston Conference*, (2014).

[173] J. Venkatesan, S. Ganesan, On the Navier-slip boundary condition for computations of impinging droplets, *IEEE, International Conference on High PERFORMANCE Computing Workshops, IEEE Computer Society* 2 – 11 (2015), https://doi.org/10.1109/HiPCW.2015.10

[174] P. R. Jelia, A. Agrawal, R. K. Singh, S. S. Joshi, Design of textured surfaces for super-hydrophobicity, *Sadhana - Academy Proceedings in Engineering Sciences* 42, 1915 – 1927 (2017), https://doi.org/10.1007/s12046-017-0736-3

[175] L. Wang, R. Zhang, X. Zhang, P. Hao, Numerical simulation of droplet impact on textured surfaces in a hybrid state, *Microfluid Nanofluidics* 21, 61 (2017), https://doi.org/10.1007/s10404-017-1900-0

[176] S. Chen, J. Wang, T. Ma, D. Chen, Molecular dynamics simulations of wetting behavior of water droplets on polytetrafluorethylene surfaces, *Journal of Chemical Physics* 140, 114704 (2014), https://doi.org/10.1063/1.4868641

[177] T. Werder, J. Walther, R. Jaffe, T. Halicioglu, P. Koumoutsakos, On the Water-Carbon Interaction for Use in Molecular Dynamics Simulations of Graphite and Carbon Nanotubes, *The Journal of Physical Chemistry B* 107 (6), 1345 – 1352 (2003), https://doi.org/10.1021/jp0268112

[178] J. A. Ko, T. W. Kwon, M. Ambrosia, M. Y. Ha, Study of the wetting characteristics of water droplet on a heterogeneous pillared surface, *Journal of Mechanical Science and Technology* 29, 1243 – 1256 (2015), https://doi.org/10.1007/s12206-015-0238-3

[179] J. Chai, S. Liu, X. Yang, Molecular dynamics simulation of wetting on modified amorphous silica surface, *Applied Surface Science* 255 (22), 9078 – 9084 (2009), https://doi.org/10.1016/j.apsusc.2009.06.109

[180] Z. Wang, L. Li, M. Yang, Molecular dynamics simulation of the wetting characteristics of a nanofluid droplet on rough substrate, *Journal of Molecular Liquids* 319, 114204 (2020), https://doi.org/10.1016/j.molliq.2020.114204

[181] S. Khan, J. K. Singh, Wetting transition of nanodroplets of water on textured surfaces: a molecular dynamics study, *Molecular simulation* 40 (6), 458 – 468 (2014), https://doi.org/10.1080/08927022.2013.819578

[182] V. Kumar, S. Sridhar, J. R. Errington, Monte Carlo simulation strategies for computing the wetting properties of fluids at geometrically rough surfaces, *The Journal of Chemical physics* 135 (18), 184702 (2011), DOI: 10.1063/1.3655817

[183] P. Sulc, J. Doye, A. Louis, Introduction to molecular simulation, *Computer Science* (2016),

[184] R. T. Eiswirth, H. J. Bart, T. Atmakidis, E. Y. Kenig, Experimental and numerical investigation of a free rising droplet, *Chemical Engineering and Processing: Process Intensification* 50 (7), 718 – 727 (2011), https://doi.org/10.1016/j.cep.2011.04.008

[185] Y. Q. Zu, Y. Y. Yan, Single Droplet on Micro Square-Post Patterned Surfaces-Theoretical Model and Numerical Simulation, *Scientific Reports* 6, 19281 (2016), https://doi.org/10.1038/srep19281

[186] I. Malgarinos, N. Nikolopoulos, M. Marengo, C. Antonini, M. Gavaises, VOF simulations of the contact angle dynamics during the drop spreading: Standard models and a new wetting force model, *Advances in Colloid and Interface Science* 212, 1 – 20 (2014), https://doi.org/10.1016/j.cis.2014.07.004

[187] W. Zhang, R. R. Zhang, C. G. Jiang, C. W. Wu, Effect of pillar height on the wettability of micro-textured surface: Volume-of-fluid simulations, *International Journal of Adhesion and Adhesives* 74, 64 – 69 (2017), https://doi.org/10.1016/j.ijadhadh.2016.12.011

[188] C. S. Zhu, F. I. Ma, P. Lei, D. Han, L. Feng, Comparison between level set and phase field method for simulating bubble movement behavior under electric field, *Chinese Journal of Physics* 71, 385 – 396 (2021), https://doi.org/10.1016/j.cjph.2021.02.012

[189] X. Duan, L. Qin, J. Lu, A novel moving mesh method for solving fluid dynamic equations, *AIP Advances* 10, 085120 (2020), https://doi.org/10.1063/5.0014413

[190] R. Li, T. Tang, P. Zhang, Moving Mesh Methods in Multiple Dimensions Based on Harmonic Maps, *Journal of Computational Physics* 170 (2), 562 – 588 (2001), https://doi.org/10.1006/jcph.2001.6749

[191] R. Li, T. Tang, P. Zhang, A Moving Mesh Finite Element Algorithm for Singular Problems in Two and Three Space Dimensions, *Journal of Computational Physics* 177 (2), 365 – 393 (2002), https://doi.org/10.1006/jcph.2002.7002

[192] E. Fontes, Modeling Free Surfaces in COMSOL Multiphysics® with Moving Mesh, *COMSOL Blog* (31/05/2018), https://www.comsol.com/blogs/modeling-free-surfaces-in-comsol-multiphysics-with-moving-mesh/

[193] J. J. Moreno, Parametrization and simulation of blister-actuated laser-induced forward transfer (BA-LIFT) and LIFT for high viscosity pastes (2021) [PhD Thesis, Universidad Politécnica de Madrid), from *Archivo Digital UPM*

[194] V. Slavov, S. Dimova, Phase-Field Versus Level Set Method for 2D Dendritic Growth, In: *Boyanov, T., Dimova, S., Georgiev, K., Nikolov, G. (eds) Numerical Methods and Applications. NMA 2006. Lecture Notes in Computer Science* 4310. Springer, Berlin, Heidelberg, https://doi.org/10.1007/978-3-540-70942-8_87

[195] H. Hua, J. Shin, J. Kim, Level Set, Phase-Field, and Immersed Boundary Methods for Two-Phase Fluid Flows, *Journal of Fluids Engineering* 136 (2), 201301 (2014), DOI: 10.1115/1.4025658

[196] M. Grave, A. L. G. A. Coutinho, Comparing the convected level-set and the Allen–Cahn phase-field methods in AMR/C simulations of two-phase flows, *Computers & Fluids* 244, 105569 (2022), https://doi.org/10.1016/j.compfluid.2022.105569

[197] H. A. A. Amiri, A. A. Hamouda, Evaluation of level set and phase field methods in modeling two phase flow with viscosity contrast through dual-permeability porous medium, *International Journal of Multiphase Flow* 52, 22 – 34 (2013), https://doi.org/10.1016/j.ijmultiphaseflow.2012.12.006

[198] M. Provenzano, F. M. Bellusi, M. Morciano, E. Rossi, M. Schleyer, P. Asinari, et. al., Experimentally validated phase-field model to design the wettability of micro-structured surfaces, *Materials & Design* 231, 112042 (2023), https://doi.org/10.1016/j.matdes.2023.112042

[199] COMSOL Multiphysics, 5.4®. https://www.comsol.com/

[200] I. S. Omeje, T. E. Itina, Numerical study of the wetting dynamics of droplet on laser textured surfaces: Beyond classical Wenzel and Cassie-Baxter model, *Applied Surface Science Advances* 9, 100250 (2022), https://doi.org/10.1016/j.apsadv.2022.100250

[201] T. K. Phung, T. L. M. Pham, K. B. Vu. G. Busca, (Bio)Propylene production processes: A critical review, *Journal of environmental chemical engineering* 9 (4), 105673 (2021), https://doi.org/10.1016/j.jece.2021.105673

[202] P. Govindaswamy, E. Wada, H. Kono, T. Uozumi, H. Funabashi, Propylene Polymerization Performance with Ziegler-Natta Catalysts Combined with U-Donor and T01 Donor as External Donor, *Catalysts* 12 (8), 864 (2022), https://doi.org/10.3390/catal12080864

[203] A. Cicolella, E. Romano, V. Barone, C. De Rosa, Metallocenes and Beyond for Propene Polymerization: Energy Decomposition of Density Functional Computations Unravels the Different Interplay of Stereoelectronic Effects, *Organometalics* 41 (24), 3872-3883 (2022), https://doi.org/10.1021/acs.organomet.2c00534

[204] H. Katogi, K. Takemura, The effect of crystallinity on the mechanical properties of plain woven carbon reinforced composites using polypropylene, *WIT Transactions on the Built Environment* 137, 301–310 (2014), https://doi.org/10.2495/HPSM140281

[205] J. Vallejo, J.A. Gonzalez-Calderon, D. Contreras-Lopez, Main Features of Propylene and crystallization aspects, *Modification of Polypropylene by additives* (pp. 3 – 12), LAMBERT Academic Publishing (2018), ISBN: 978-613-8-17490-5

[206] G. R. Koerner, R. Koerner, Polymeric geomembrane components in landfill liners, *Solid Waste Landfilling* (pp. 313 – 341), Elsevier BV (2018), https://doi.org/10.1016/b978-0-12-407721-8.00017-6

[207] A. Calhoun, Polypropylene, *Multilayer flexible Packaging* (pp. 35 – 45), William Andrew Publishing (2016), https://doi.org/10.1016/B978-0-323-37100-1.00003-X

[208] V. P- Ranjan, S. Goel, Recyclability of polypropylene after exposure to four different environmental conditions, *Resources, Conservation and Recycling* 169, 105494 (2021), https://doi.org/10.1016/j.resconrec.2021.105494

[209] A. Alsabri, F. Tahir, S. G. Al-Ghamdi, Environmental impacts of polypropylene (PP) production and prospects of its recycling in the GCC region, *Materials today: proceedings* 56, 2245-2251 (2022), https://doi.org/10.1016/j.matpr.2021.11.574

[210] GoodFellow. https://www.goodfellow.com/

[211] J. Molinuevo, E. Rodríguez-Vidal, I. Quintana, M. Morales, and C. Molpeceres, Semi-Empirical and computational modelling of the laser structuring effect on wettability performance of polypropylene. *Optics* & *Laser Technology*. Under review (expected approval and publication in 2024)

[212] MONACO User's manual

[213] A. Volpe, G. Trotta, U. Krishnan, A. Ancona, Prediction model of the depth of the femtosecond laser micro-milling of PMMA, *Optics* & *Laser Technology* 120, 105713 (2019), https://doi.org/10.1016/j.optlastec.2019.105713

[214] G. D. Bowden, B. J. Pichler, A. Maurer, A Design of Experiments (DoE) Approach Accelerates the Optimization of Copper-Mediated ^{18}F-Fluorination Reactions of Arylstannanes, *Scientific Reports* 9, 11370 (2019), https://doi.org/10.1038/s41598-019-47846-6

[215] R. P. Niedz, T. J. Evens, Design of experiments (DOE)-history, concepts, and relevance to in vitro culture, *In vitro cellular & Developmental Biology – Plant* 52, 547 – 562 (2016), https://doi.org/10.1007/s11627-016-9786-1

[216] E. Rodríguez-Vidal, C. Sanz, J. Etxarri, A. Bejarano, Y. Lebour, R. Malet, Modification of ABS wetting properties by ultrashort and short pulse lasers, *Procedia CIRP* 74, 568 – 572 (2018), https://doi.org/10.1016/j.procir.2018.08.085

[217] D. Huerta-Murillo, A. García-Girón, J. M. Romano, J. T. Cardoso, F. Cordovilla, M. Walker, et. al., Wettability modification of laser-fabricated hierarchical surface structures in Ti-6Al-4V titanium alloy, *Applied Surface Science* 463, 838 – 846 (2019), https://doi.org/10.1016/j.apsusc.2018.09.012

[218] M. Li, Q. Dai, W. Huang, X. Wang, Pillar versus dimple patterned surfaces for wettability and adhesion with varying scales, *Journal of the Royal Society Interface* 15 (148), 20180681 (2018), https://doi.org/10.1098/rsif.2018.0681

[219] A. Hongru, L. Xiangqin, S. Shuyan, Z. Ying, L. Tianqing, Measurement of Wenzel roughness factor by laser scanning confocal microscopy, *RSC Advances* 7, 7052 – 7059 (2012), https://doi.org/10.1039/C6RA26897H

[220] A. Jankovic, G. Chaudhary, F. Goia, Designing the design of experiments (DOE) – An investigation on the influence of different factorial designs on the characterization of complex systems, *Energy and Buildings* 250, 111298 (2021), https://doi.org/10.1016/j.enbuild.2021.111298

[221] Sensofar Metrology, Sensofar. https://www.sensofar.com/metrology/

[222] Digital Surf, https://www.digitalsurf.com/

[223] D. Metzner, P. Lickschat, S. Weiβmantel, Influence of heat accumulation during laser micromachining of CoCrMo alloy with ultrashort pulses in burst mode, *Applied Physics A.* 126, 84 (2020), https://doi.org/10.1007/s00339-019-3203-7

[224] ZEISS Group, https://www.zeiss.com/corporate/en/home.html

[225] OEG, Products ⋮ OEG Optical Metrology, Image processing, Software development GmbH (oeggmbh.com)

[226] W. S. Rasband, ImageJ, *U. S. National Institutes of Health*, Bethesda, Maryland, USA, https://imagej.nih.gov/ij/, 1997-2018

[227] The Finite Element Method, *Multiphysics Cyclopedia*, https://www.comsol.com/multiphysics/finite-element-method

[228] J. H. Ferziger, M. Peric, R. L. Street, Introduction to numerical methods, In *Computational Methods for Fluid Dynamics*, (2020) https://doi.org/10.1007/978-3-319-99693-6

[229] B. Koncar, J. Sotosek, I. Bajsic, Experimental verification and numerical simulation of a vortex flowmeter at low Reynolds numbers, *Flow Measurement and Instrumentation* 88, 102278 (2022), https://doi.org/10.1016/j.flowmeasinst.2022.102278

[230] Two-Phase Flow Modeling Guidelines, *COMSOL*, https://www.comsol.com/support/learning-center/article/Two-Phase-Flow-Modeling-Guidelines-46471

[231] Z. Mao, M. J. Demkowicz, Mobility inference of the Cahn–Hilliard equation from a model experiment, *Journal of Materials Research* 36, 2830 – 2842 (2021), https://doi.org/10.1557/s43578-021-00266-7

[232] F. Bai, X. He, X. Yang, R. Zhou, C. Wang, Three dimensional phase-field investigation of droplet formation in microfluidic flow focusing devices with experimental validation, *International Journal of Multiphase Flow* 93, 130 – 141 (2017), https://doi.org/10.1016/j.ijmultiphaseflow.2017.04.008

[233] X. Wang, H. Yu, P. Li et. Al., Femtosecond laser-based processing methods and their applications in optical device manufacturing: A review, *Optics & Laser Technology* 135, 106687 (2021), https://doi.org/10.1016/j.optlastec.2020.106687

[234] R. Ortiz, I. Quintana, J. Etxarri, A. Lejardi, J. R. Sarasua, Picosecond laser ablation of Poly-L-Lactide: Effect of crystallinity on the material response, *Journal of Applied Physics* 110, 094902 (2011), https://doi.org/10.1063/1.3653964

[235] V. Belaud, S. Valette, G. Stremsdoerfer, B. Beaugiraud, E. Audouard, S. Benayoun, Femtosecond laser ablation of polypropylene: A statistical approach of morphological data, *Scanning* 36 (2), 209 – 217, DOI: 10.1002/sca.21090

[236] J.M. Liu, Simple technique for measurements of pulsed Gaussian-beam spot sizes, *Optics Letters* 7(5), 196 – 198 (1982), DOI: 10.1364/ol.7.000196

[237] G. H. Pettit, R. Sauerbrey, Pulsed ultraviolet laser ablation, *Applied Physics A* 56, 51 – 63 (1993), https://doi.org/10.1007/BF00351903

[238] A. Zemaitis, M. Gaidys, P. Gecys, M. Gedvilas, Bi-stability in femtosecond laser ablation by MHz bursts, *Scientific Reports* 14, 5614 (2024), Žemaitis, A., Gaidys, M., Gečys, P. et al. Bi-stability in femtosecond laser ablation by MHz bursts. Sci Rep 14, 5614 (2024). https://doi.org/10.1038/s41598-024-54928-7

[239] M. Lu, M. Zhang, K. Zhang, Q. Meng, X. Zhang, Femtosecond UV Laser Ablation Characteristics of Polymers Used as the Matrix of Astronautic Composite Material, *Materials* 15 (19), 6771 (2022), https://doi.org/10.3390/ma15196771

[240] I. B. Sohn. Y. C. Noh, Y. S. Kim, D. K ko, J. Lee, Laser Ablation of Polypropylene Films using Nanosecond, Picosecond and Femtosecond Laser, *Journal of the Optical Society of Korea* 12, 38 – 41 (2008), DOI: 10.3807/JOSK.2008.12.1.038

[241] C. Chen, F. Zhang, Y. Zhang, X. Xiong, B.-F. Ju, H. Cui, et. al., Single-pulse femtosecond laser ablation of monocrystalline silicon: A modeling and experimental study, *Applied Surface Science* 576, 151722 (2022), https://doi.org/10.1016/j.apsusc.2021.151722

[242] D. Gómez, I. Goenaga, On the incubation effect on two thermoplastics when irradiated with ultrashort laser pulses: Broadening effects when machining microchannels, *Applied Surface Science* 253 (4), 2230 – 2236 (2006), https://doi.org/10.1016/j.apsusc.2006.04.036

[243] E. Rebollar, G. Bounos, M. Oujja, S. Georgiou, M. Castillejo, Effect of Molecular Weight on the Morphological Modifications Induced by UV Laser Ablation of Doped Polymers, *The Journal of Physical Chemistry B* 110 (33), 16452 – 16458 (2006), https://doi.org/10.1021/jp062060i

[244] E. Rebollar, G. Bounos, A. Selimis, M. Castillejo, S. Georgiou, Examination of the influence of molecular weight on polymer laser ablation: polystyrene at 248 nm, *Applied Physics A* 92, 1043 – 1046 (2008), https://doi.org/10.1007/s00339-008-4590-3

[245] J. Molinuevo, E. Rodríguez-Vidal, I. Quintana, M. Morales, C. Molpeceres, Experimental investigation into ultrafast laser ablation of polypropylene by burst and single pulse modes, *Optics & Laser Technology* 152, 108098 (2022), https://doi.org/10.1016/j.optlastec.2022.108098

[246] S. Lee, D. Yang, S. Nikumb, Femtosecond laser micromilling of Si wafers, *Applied Surface Science* 254 (10), 2996 – 3005 (2008), https://doi.org/10.1016/j.apsusc.2007.10.063

[247] J.-M. Romano, M. Gulcur, A. Garcia-Giron, E. Martinez-Solanas, B. R. Whiteside, S. S. Dimov, Mechanical durability of hydrophobic surfaces fabricated by injection moulding of laser-induced textures, *Applied Surface Science* 476, 850 – 860 (2019), https://doi.org/10.1016/j.apsusc.2019.01.162

[248] M. S. Ambrosia, M. Y. Ha, S. Balachandar, The effect of pillar surface fraction and pillar height on contact angles using molecular dynamics, *Applied Surface Science* 282, 211 – 216 (2013), https://doi.org/10.1016/j.apsusc.2013.05.104

[249] S. D. N. Lourenço, Y. Saulick, S. Zheng, H. Kang, D. Liu, H. Lin, et. al., Soil wettability in ground engineering: fundamentals, methods, and applications, *Acta Geotechnica* 13, 1 – 14 (2018), https://doi.org/10.1007/s11440-017-0570-0

[250] A. Harish, What is Convergence in Finite Element Analysis?, https://www.simscale.com/blog/convergence-finite-element-analysis/

[251] Q. Zhang, T. Z. Qian, and X. P. Wang, Phase field simulation of a droplet impacting a solid surface, *Physics of Fluids* 28 (2), 022103 (2016), https://doi.org/10.1063/1.4940995

[252] C. Y. Lim, Y. C. Lam, Phase-field simulation of impingement and spreading of micro-sized droplet on heterogeneous surface, *Microfluidics and Nanofluidics* 17, 131 – 148 (2014), https://doi.org/10.1007/s10404-013-1284-8

[253] M. Shen, B. Q. Li, Modeling Air Entrapment in the Impact-Freezing of YSZ Drops Using a Cahn–Hilliard Phase Field Model, *Journal of Thermal Spray Technology* 32, 2014 – 2027 (2023), https://doi.org/10.1007/s11666-023-01591-5

[254] V. Fink, X. Cai, A. Stroh, R. Bernard, J. Kriegseis, B. Frohnapfel, et. al., Drop bouncing by micro-grooves, *International Journal of Heat and Fluid Flow* 70, 271 – 278, (2018), https://doi.org/10.1016/j.ijheatfluidflow.2018.02.014

[255] A. Dadvand, M. Bagheri, N. Samkhaniani, H. Marschall, M. Wörner, Advected phase-field method for bounded solution of the Cahn-Hilliard Navier-Stokes equations, *Physics of Fluids* 33, 053311 (2021), https://doi.org/10.1063/5.0048614

[256] P. Wang, L. He, Z. Wang, The effect of surface structure and arrangement on wettability of substrate surface, *Colloids and Surfaces A: Physicochemical and Engineering Aspects* 614, 126165 (2021), https://doi.org/10.1016/j.colsurfa.2021.126165

[257] J. Jonkman, C. M. Brown, G. D. Wright, K. I. Anderson, A. J. North, Tutorial: guidance for quantitative confocal microscopy, *Nature Protocols* 15, 1585 – 1611 (2020), https://doi.org/10.1038/s41596-020-0313-9

[258] K. Akhtar, S. A. Khan, S. B. Khan, A. M. Asiri, Scanning Electron Microscopy: Principle and Applications in Nanomaterials Characterization, In: *Handbook of materials Characterization*, 113 – 145 (2018), https://doi.org/10.1007/978-3-319-92955-2_4

[259] EasyDyne Force Tensiometer K20, Krüss GmbH, https://www.kruss-scientific.com/en/products-services/products/k20

[260] Solutions to Linear Systems of Equations: Direct and Iterative Solvers | COMSOL Blog, https://www.comsol.com/blogs/solutions-linear-systems-equations-direct-iterative-solvers

[261] FemtoLux Series femtosecond fiber laser, Technical Description User's Manual

[262] X. Wolters, G. Bonamis, K. Mishchick, E. Audouard, C. Hönninger, E. Mottay, High power GHz femtosecond laser for ablation efficiency increase, *Procedia Manufacturing* 36, 200 – 207 (2019), https://doi.org/10.1016/j.promfg.2019.08.026

Annex I

SCIENTIFIC OUTPUT

AI. 1. Papers in JCR Journals

J. Molinuevo, E. Rodríguez-Vidal, I. Quintana, M. Morales, C. Molpeceres, Experimental investigation into ultrafast laser ablation of polypropylene by burst and single pulse modes, Optics & Laser Technology 152, 108098, (2022), https://doi.org/10.1016/j.optlastec.2022.108098 (Q1)

J. Molinuevo, E. Rodríguez-Vidal, I. Quintana, M. Morales, C. Molpeceres, Semi-Empirical and computational modelling of the laser structuring effect on wettability performance of polypropylene. Under submission.

AI. 2. Congress Contributions

J. Molinuevo, I. Quintana, E. Rodríguez-Vidal, R. Díez-Ahedo, A. Retolaza, C. Molpeceres, Role of roughness levels induced by the laser texturing on the wettability behaviour of ABS, Procedia CIRP 94, 885–890 (2020). https://doi.org/10.1016/j.procir.2020.09.066

J. Molinuevo, E. Rodríguez-Vidal, I. Quintana, M. Morales, C. Molpeceres, Effect of temporal distance in the ultrashort pulse range on the ablation of polypropylene with single pulses and burst pulses, Procedia CIRP 111, 634–637, (2022), https://doi.org/10.1016/j.procir.2022.08.002

J. Molinuevo, E. Rodríguez-Vidal, S. Vela, M. Morales, C. Molpeceres. Increased efficiency of ultrafast laser ablation Polypropylene surfaces using burst pulses, LPM June 2024.

J. Molinuevo. XVIII edición de las Jornadas de Procesado de Materiales con Tecnología Láser. October 2024

Annex II

EXPERIMENTAL INSTRUMENTATION

AII. 1. Confocal microscopy

The image acquisition uses the light reflected on the sample collected by a photodetector [257]. The confocal microscopy contains a light source that emits a light beam that illuminates the sample and is reflected towards the photodetector. This light passes through a pinhole that ensures that only the light coming from the focal plane of the optical system on the sample passes through. Changing the focal plane allows a 3D reconstruction of the sample with extreme accuracy in the direction of the incident light. The schematic representation of this process can be observed in Fig. AII. 1. The microscope allows the measurement by different magnification values, i.e., 5x, 20x, 50x and 150x. Moreover, several light sources can be selected, regarding the available wavelengths (white, red, blue and green).

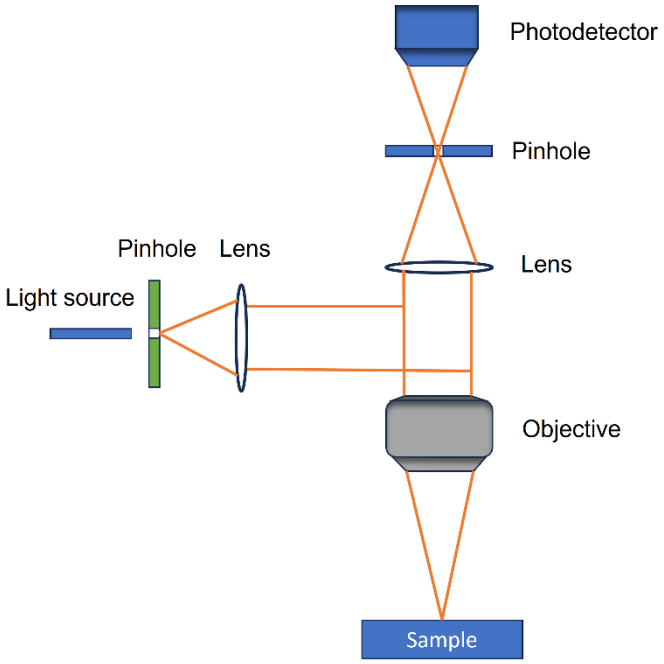

Fig. AII. 1 Schematic representation of the image acquisition of the confocal microscopy

The image acquisition of a crater-like structure can be observed in Fig. AII. 2, regarding the a) 3D, b) 2D top-view and c) 2D profile imagery, as an example. In this work, the confocal microscopy was used to evaluate the topographic results obtained from the laser parameter optimization process (in terms of structure depth and recast material height, among others), and to assess the correct results from the final textured surfaces (in terms of structure depth and width).

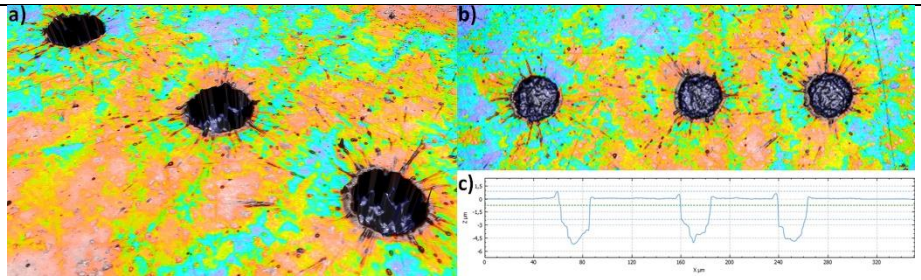

Fig. AII. 2 a) 3D confocal image, b) 2D top view and c) 2D profile view

AII. 2. Scanning Electron Microscope

Scanning Electron Microscopy is an advanced instruments that provide quantitative information regarding the morphology, topography, composition, etc. of a surface. The system is equipped with an electron gun that generates focused electron beam onto the sample, which provide energy to the atomic electrons from the surface, releasing secondary electrons from each point that are collected afterwards by a detector [258]. This recollection forms the image, hence the importance of avoiding the interactions between the electrons and the gas molecules, which is why it is necessary to work under vacuum conditions [258].

AII. 3. Goniometer

The wettability performance of a material is determined by the CA and the CAH measurement of a liquid droplet carefully deposited on top of a surface. A goniometer is a device designed to measure the CA between a liquid and a solid surface, as well as the CAH. Moreover, it also offers the capability of using different liquids besides water, and hence it has proven to be a useful tool to determine the surface energy of a sample. In this case, both deionized water and diiodomethane can be used, as the combination of polar and dispersive components from the former and latter, respectively, can provide of useful information regarding the possible behaviour of different liquids on a surface. In this work, a Surftens Universal goniometer (OEG) [225] was used (see Fig. AII. 3).

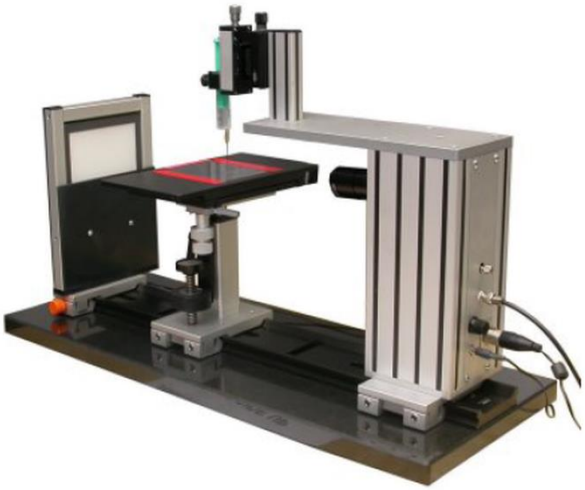

Fig. AII. 3 Goniometer from Surftens Universal (OEG)

The experimental setup (see Fig. AII. 4) involved the positioning of the sample on the stage and a syringe dispensed a controlled volume of a liquid. A high-resolution camera was positioned in order to capture a well-defined droplet boundary for accurate CA measurements. A light source is positioned on the opposite in order to easily identify the droplet shape.

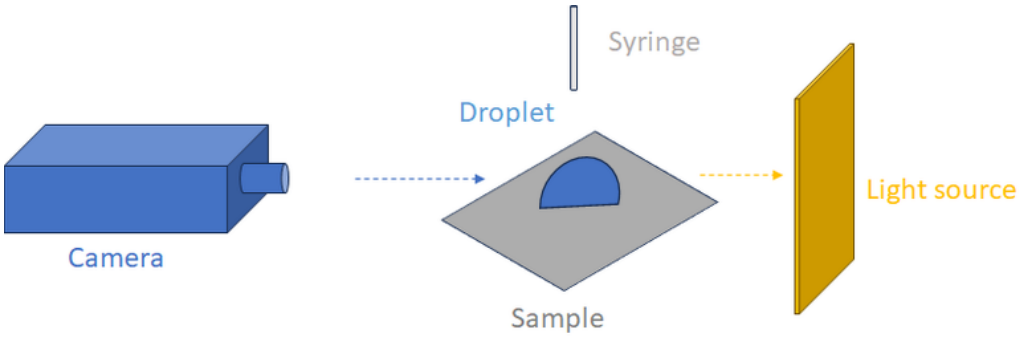

Fig. AII. 4 Schematic representation of the goniometer setup

The static CA measurements (were carried out using 5 μL of deionized water, fitting each droplet shape with the tangent searching method (see Fig. AII. 5). A postprocessing software, i.e., ImageJ [226], was also used for CA measurements (see Fig. AII. 5 b). In order to ensure the repeatability of the measurements and to identify and avoid any possible anomaly, the CA measurement on each surface were performed three times.

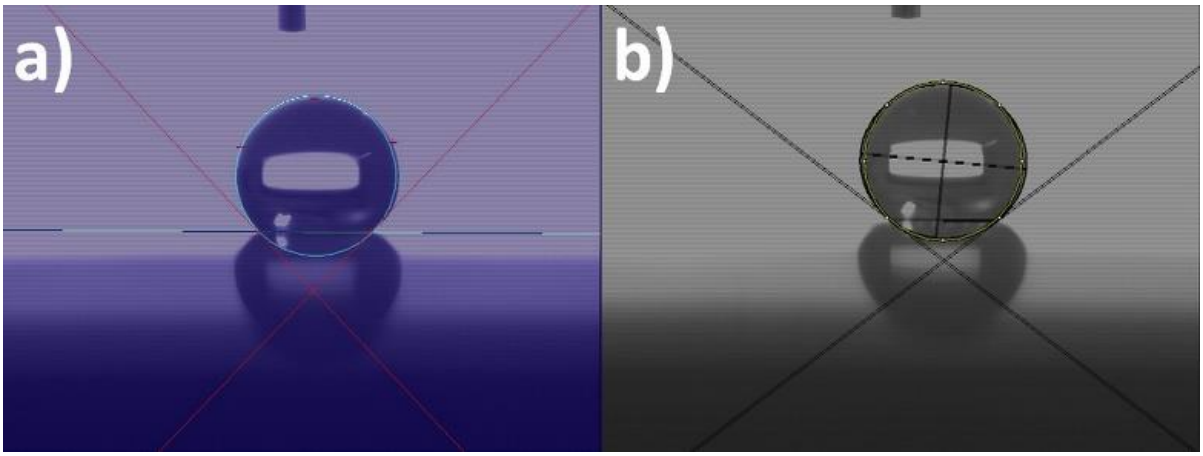

Fig. AII. 5 a) CA measurement with the goniometer and b) CA measurement with the postprocessing software ImageJ

The goniometer can also be used as a CAH measurement tool by the sessile droplet method. This method consists of slowly increasing the liquid volume from 5 μL to 10 μL and constantly measuring the CA value as the volume increases (providing an advancing CA, determined by the maximum value), and repeating the process for the obtention of the receding CA (by decreasing the volume back to 5 μL (see Fig. AII. 6)).

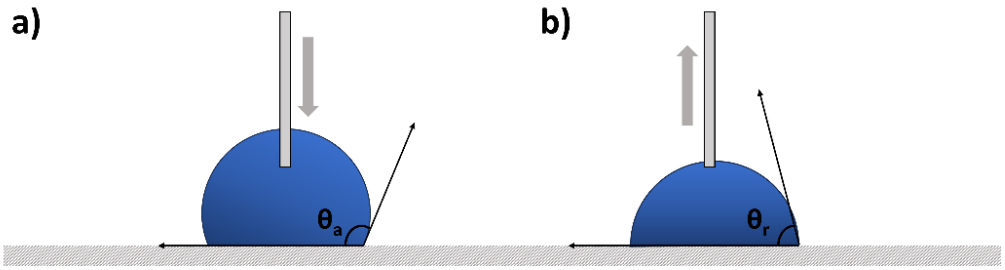

Fig. AII. 6 Sessile droplet method for the measurement of a) advancing CA and b) receding CA

Lastly, the goniometer allows the calculation of the surface energy of a solid through the equations of Owens, Wendt, Rabel and Kaeb (OWRK) (see eq. (73)) or the algorithm of Souheng Wu (see eq. (74)), depending on the value of surface energy (whether it is higher or lower than 20 mN/m, it is used one or the another). In order to do that, the contact angle of two opposite liquids, i.e., water (a polar liquid) and diiodomethane (a dispersive liquid) is obtained, and their respective surface tensions are calculated with the surface tensiometer (σ_i), as it is going to be briefly described in the

next section. After resolving the system of equations, both the polar (γ^p) and dispersive (γ^d) components of the solid surface are obtained, and their summation equals the total surface energy.

$$(1 + cos\theta_0)\sigma_i = 2\left(\sqrt{\sigma_i^d \gamma^d} + \sqrt{\sigma_i^p \gamma^p}\right) \quad (73)$$

$$(1 + cos\theta_0)\sigma_i = 4\left(\frac{\sigma_i^d \gamma^d}{\sigma_i^d + \gamma^d} + \frac{\sigma_i^p \gamma^p}{\sigma_i^p + \gamma^p}\right) \quad (74)$$

AII. 4. Surface tensiometer

The surface tension of a liquid can be measured with a tensiometer (EasyDyne, from KRUSS [259], see Fig. AII. 7), which can be obtained through two methods, i.e., the Wilhelmy Plate or the Du Noüy Ring method. The latter is one of the most used methods, which uses an aluminium ring situated inside the liquid and measures the additional force (ΔF) needed to overcome the resistance of the liquid in the exact moment where it breaks and separates from the ring (Fig. AII. 8). This force is used to calculate the surface tension with the equation:

$$\sigma = \frac{\Delta F}{4\pi R_r} f_c \quad (75)$$

In eq. (75), R_r is the radius of the aluminium ring and f_c is a correction factor.

Fig. AII. 7 Surface tensiometer EasyDyne (from KRUSS) [259]

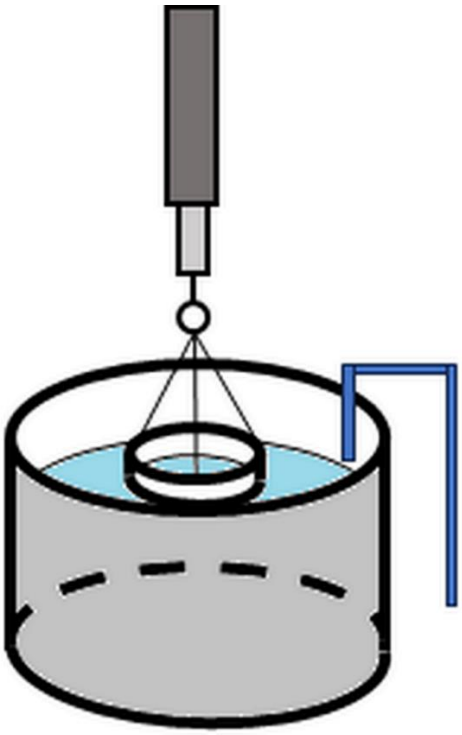

Fig. AII. 8 Du Noüy Ring method for the surface tension measurement of a liquid

Annex III

SIMULATION RESULTS

AIII. 1. Setting up the solver conditions

After the proper model and mesh definition, the last step revolves around the correct setup of the solver in order to optimize the simulation process. The nature of the process being simulated with the combination of Laminar Flow and PF branches require of a two-step solution model:

- First, COMSOL must identify the initial conditions of the model, in terms of phase definition of each domain. In other words, for a two-phase flow a first step would calculate the distance to the phase interface. Therefore, a **stationary phase initialization** step must be included, in which the initial equations are generated, the initial conditions are set-up and where the time variable is not a part of the equation.
  This step obtains the auxiliary variable of the interface tracking parameter and then it is transferred to the value of ϕ in the next step, i.e., the time-dependent step.
- Afterwards, a **time-dependent** solver is included, which uses the solutions from the first step and calculates the Laminar Flow and PF equations over time. Therefore, in this step the time is a variable, contrary to the stationary step.

Inside each step, several extensions can be found, in the form of the Solver and Job configurations, and the utility, operation and attribute nodes. The *Solver configuration* node contains all the configurations defined in the study. The *Job configurations* can be used to store solutions from cluster computing, such as parametric sweeps (a special type of study in which several consecutive simulations can be run, so that in each one of them one or several parameters are varied), optimization, etc. Therefore, this configuration prevents the enlargement of the simulation result files by storing the model and associated data and plots in an individual save file. The *utility nodes* handle special types of study extensions such as the solution store, the adaptive mesh refinement, the parametric sweep or the combine solutions, among others. These are mainly used for specific problems. The *operation nodes* are responsible for producing the result outputs. These results can be visualized and analysed. The *attribute nodes* can control the operation behaviour by using them as an input. This node is arguably the most important one among the three defined nodes, as it provides the possibility of selecting the linear solver to perform the simulation. These linear solvers solve a system in the form of eq. (76):

$$\boldsymbol{Ax = b} \tag{76}$$

In this equation, **A** is the Jacobian matrix that contains the coefficients of the variables from the linearized model, **x** is a vector of unknown variables that give the expected solution in **b**. If the problem is non-linear, the equation system and the vector **b** become non-linear as well, and the convergence (the error between the obtained and expected solutions) of the solution is slower and the results take longer to reach. In fact, when a simulation is converging, the solver tries to increase the time step to reduce the computational time. However, if it increases the step to excessively high values, the error may increase and the tolerance may fail again, in which case the solution would not converge. This can be reduced or avoided by manually setting time steps constraints.

The nonlinear problem is controlled by either the *Fully coupled* or *Segregated* solver. The former resolves every unknown variable and all the couplings between the Laminar Flow and the PF with a single large system of equations, whereas the latter subdivides this system into several smaller steps, each usually grouped into the same physics, thus lesser memory usage is needed. Regardless of the selected method, both revolve around an iterative process in which several parameters can be modified, such as the **tolerance** (the error value with which a solution can be considered as acceptable, hence controlling it modifies how strict the solver is regarding the validity of the obtained solution).

The solver provides information about the errors with two different categories, i.e., the nonlinear failure (in case of the nonlinear systems, as it is this case) denoted as NLFAIL, and the tolerance failure, denoted as TFAIL. As it was described before, each time the solver is not capable of solving the complexity of the algebraic problem, the Jacobian matrix must be reevaluated, which is relatively expensive to compute. Hence, the NLFAIL counter is increased a number of times equal to the number of failures after each try, and the timestep is reduced to repeat the evaluation of the algebraic problem. These errors can be avoided by increasing the number of iterations allowed for the solver to try solving the problem. Another error is related to not meeting the tolerance requirements, which implies a time step reduction to ensure a smaller error. Each time it happens, the TFAIL counter is increased by 1. This can be reduced or avoided by adjusting the tolerances and by the scaling of the variables (i.e., the pressure, the velocity or the phase field variables). In order to scale these variables, a first simulation may be performed from which an estimation of the values of each one of them may be identified and later included manually within the solver. In the present work, the tolerance error may occur due to the periodic (oscillating) movement of the interface, which produces a constant change in the gradient direction and go through a zero-crossing.

Taking into consideration that in this thesis, a Direct solver has been used, in order to perform the simulation, COMSOL provides different Direct solver options: PARDISO, MUMPS and

SPOOLES. All the solvers are based on the LU factorization on the matrix A to compute the solution x [260]. They use a preordering algorithm in the matrix A that minimizes the number of non-zeros in the L and U factors, as well as shared memory parallelism in order to prevent excessive memory usage. Among the different options, both MUMPS and PARDISO have an option of reusing the preordering, which accelerates the simulation, at a cost of higher memory usage. Moreover, in case the memory usage reached an excessively high peak (to values where the RAM could not, both can work under the "out of core" mode, where they could work with part of the hard disk of the computer. In this work, the Fully coupled method was chosen, and the PARDISO solver was preferred over MUMPS, as the former improves the parallel and sequential performance, which in this work was observed that could increase the simulation speed.

In the case where the solver would run out of memory, the PARDISO can automatically switch to MUMPS, or a manual change into the latter must be done to prevent it, at the expense of making the simulation process slower. Additionally, if the MUMPS solver would face memory problems as well, other solvers are available, such as the iterative solvers (GMRES, FGMRES, GMG, SOR or AMG), which could be beneficial when working with large 3D problems, or the SPOOLES solver, which even though it uses even less memory, it is numerically more instable than the first two options.

To conclude, a careful solver definition is mandatory in order to ensure an optimized computational modelling in terms of convergence and simulation time. The influence of other modelling aspects like the mobility, boundary and initial conditions, and the mesh setting in the solver definition makes this computational model a challenge regarding the study of generic wetting situations, which involve the use of different materials, fluids, etc.

In the next pages, the simulation results from the section 5. 3. 3 can be seen.

AIII. 2. Simulation results

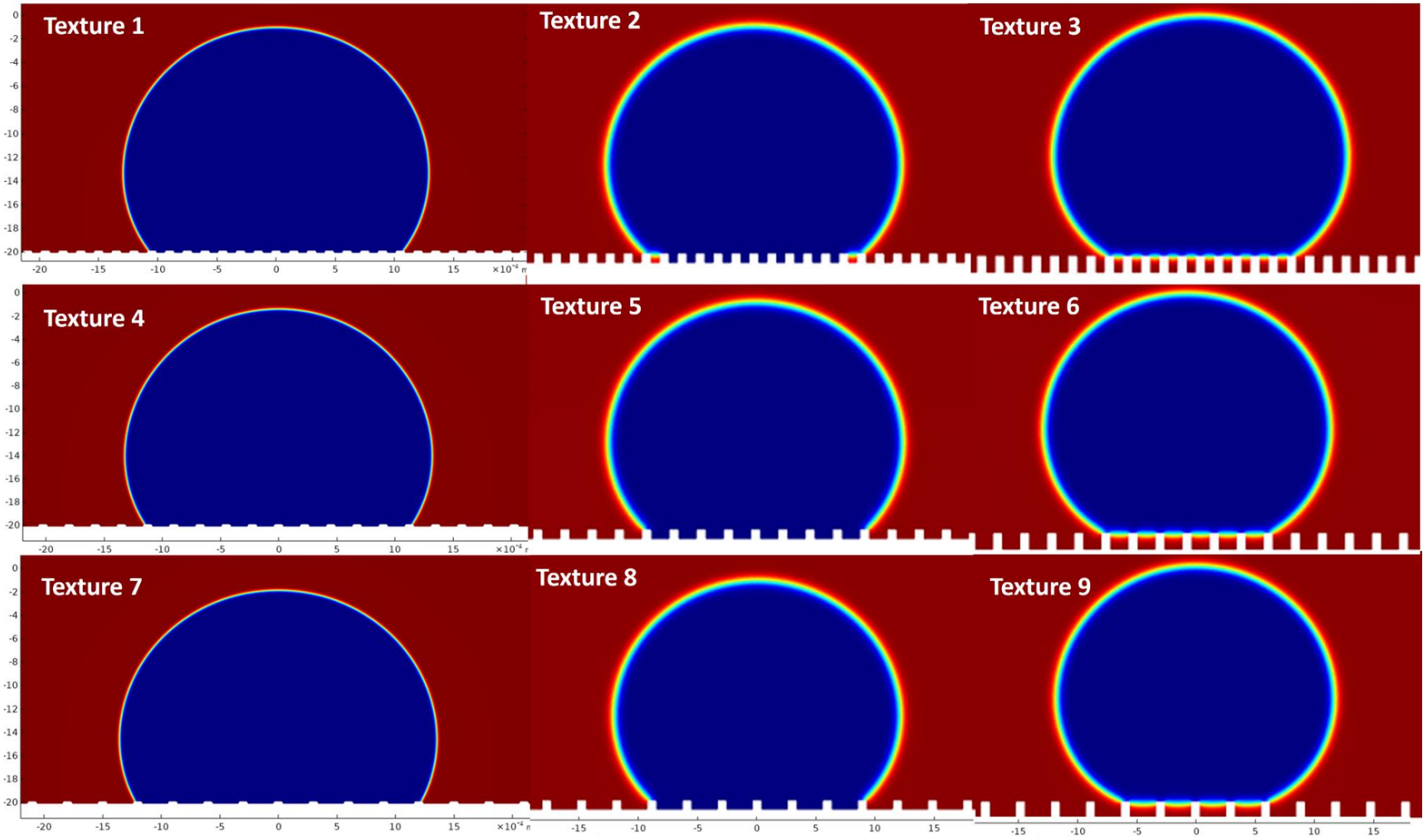

Fig. AIII. 1 Simulation results from textures 1 to 9 in 2D for χ = 10 m·s/kg

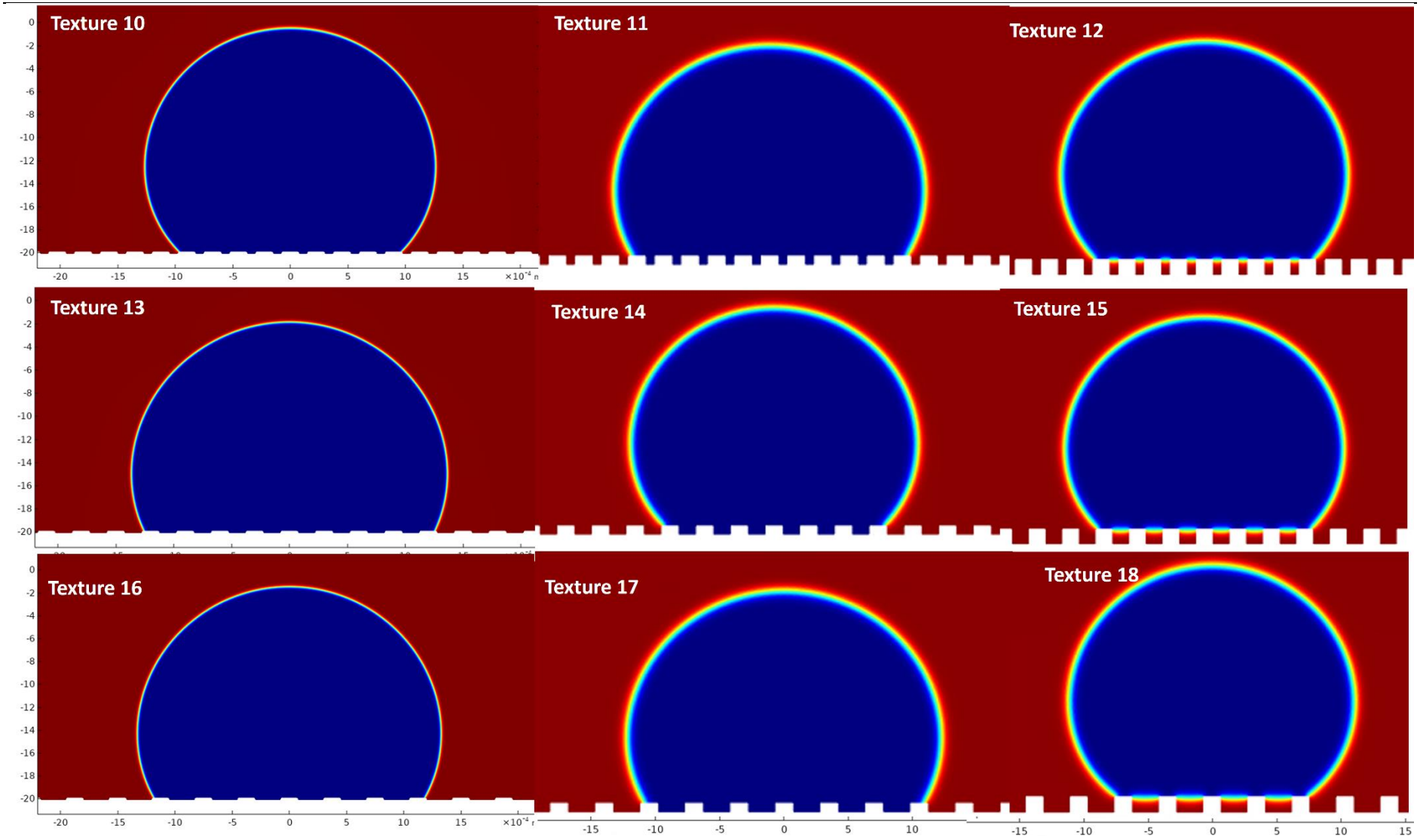

Fig. AIII. 2 Simulation results from textures 10 to 18 in 2D for χ = 10 m·s/kg

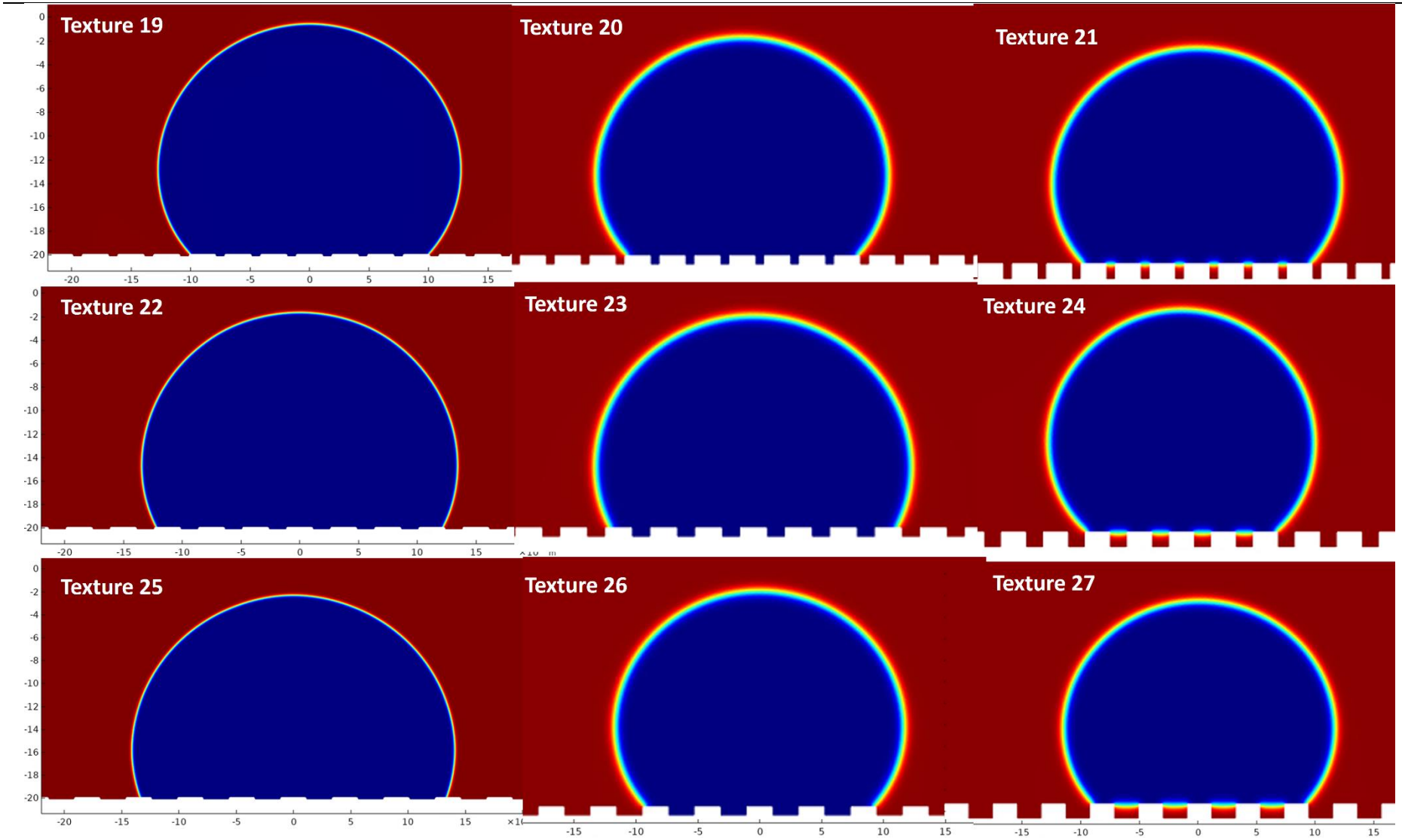

Fig. AIII. 3 Simulation results from textures 19 to 27 in 2D for χ = 10 m·s/kg

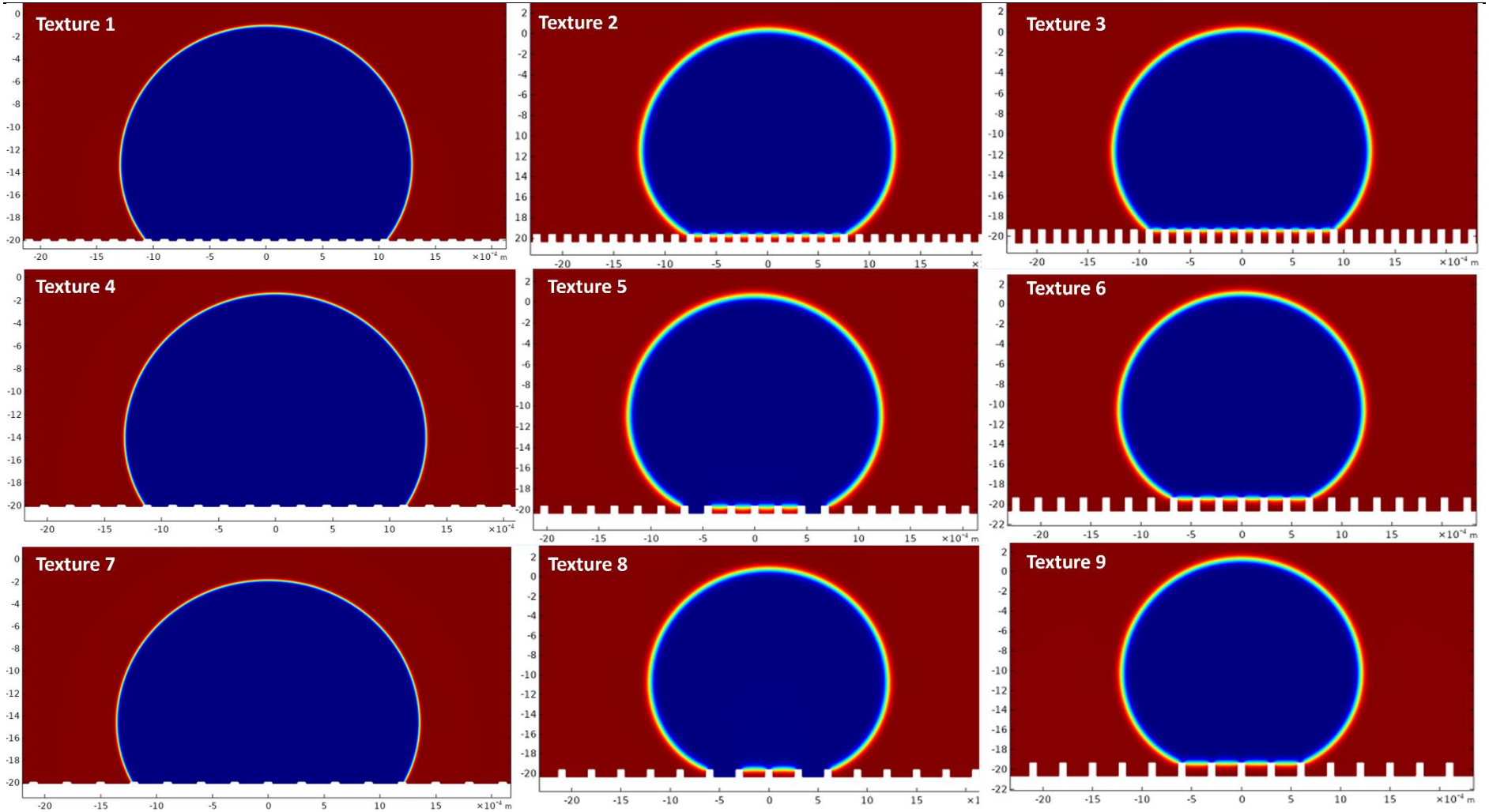

Fig. AIII. 4 Simulation results from textures 1 to 9 in 2D for χ = 5 m·s/kg

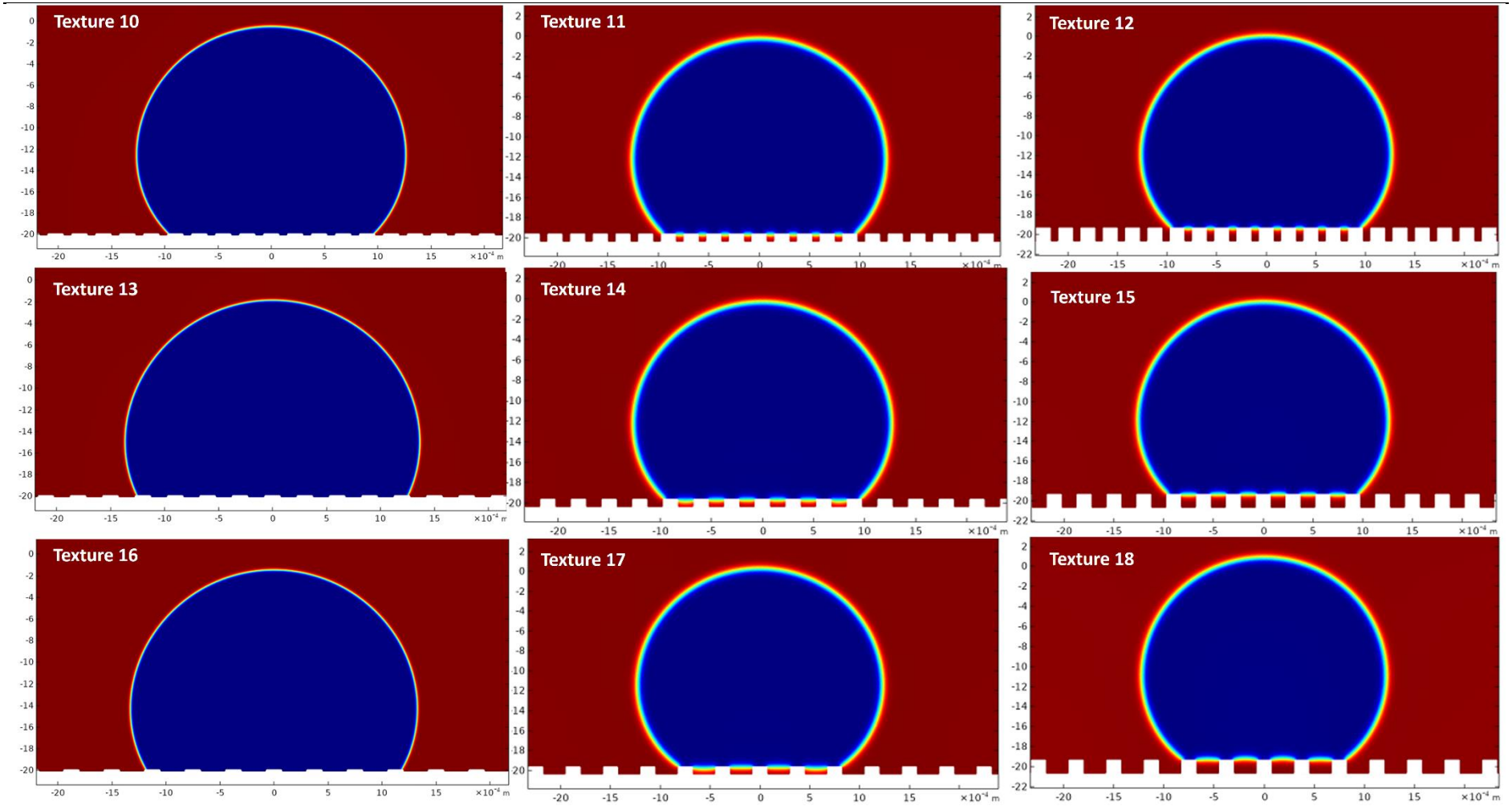

Fig. AIII. 5 Simulation results from textures 10 to 18 in 2D for χ = 5 m·s/kg

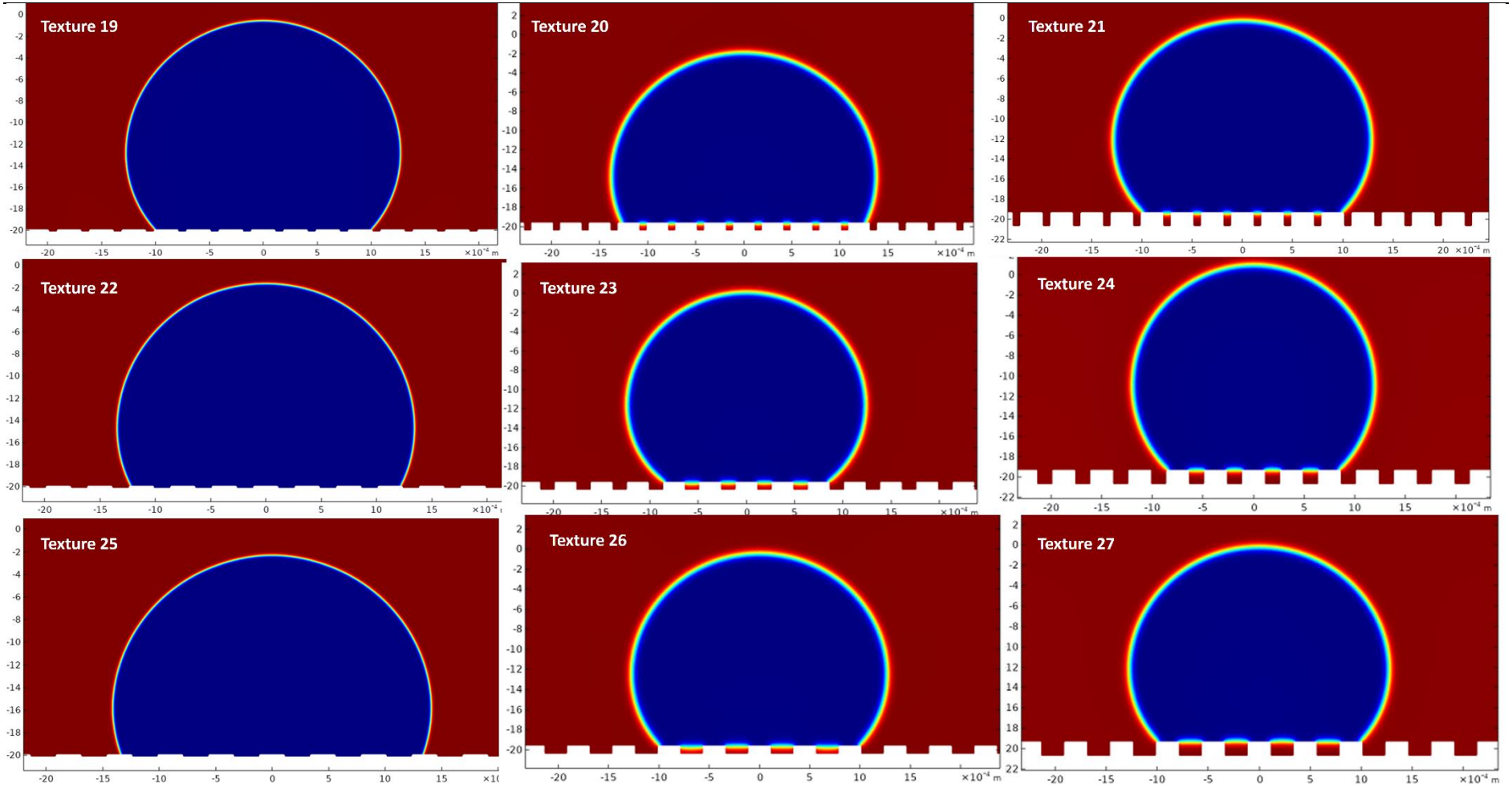

Fig. AIII. 6 Simulation results from textures 19 to 27 in 2D for χ = 5 m·s/kg

Annex IV

EXTRAPOLATION TO SIMILAR LASER REGIME BY OTHER LASER SOURCES

AIV. 1. Motivation

During the present work, regarding the study of laser-material interaction, the results were obtained with a specific laser system, as defined in section 3.3. However, to assess if the results observed in this thesis could be extrapolated to other laser systems with different specifications, a short experimentation was performed with a laser system from the Laser Centre from the UPM. During this experimentation procedure, the same material was used. The results from this work were presented in the international Symposium on Laser Precision Microfabrication 2024 (LPM 2024) by the author of this thesis.

AIV. 2. Experimental setup

A FemtoLux 30 from EKSPLA [261] was used, which emitted pulses at nominal wavelengths of 1030nm. The main specifications of the laser system are summarized in Table AIV. 1. The laser was guided by a Raylase SS-III scanner with a f-theta focusing lens of 163 mm focal length, providing a spot diameter of 24 μm at the focal plane, and a depth of focus of 400 μm.

Table AIV. 1 General specifications of the FemtoLux 30 laser system

Technical characteristics (wavelength of 1030 nm)	
Pulse repetition rate (MHz)	0.2 – 4
Output power	> 27 W
Pulse energy	90 μJ (at lowest pulse repetition rate)
Maximal total energy in a burst	>250 μJ (for 10 pulses per burst at the lowest pulse repetition rate)
Pulse width (FWHM)	<350 fs – 10 ps
Seed repetition rate	50 MHz
Pulse repetition rate (output)	1 – 750 KHz – 50 MHz
Laser beam characteristics	
Spatial Mode	TEM_{00}
Beam quality	M^2<1.2
Beam divergence	<1 mrad

Beam Diameter	2.5 ± 0.3 (mm, at 50 cm distance from laser aoerture)
Beam circularity	>0.85

The laser system can work both in SP and BM. In the latter, a number of pulses inside a burst between 2 and 10 can be selected, in which case the E_p of each pulse inside (Ep_n) varied accordingly to the eq. (77):

$$E_{p_n} = \frac{E_p}{n} \quad (77)$$

Where E_p was the pulse energy of the SP mode. In other words, the same total energy was applied to the crater development in every case. Therefore, with this laser system, not only the wavelength and pulse repetition rate were varied, but also the energy distribution along the different pulses inside a burst. The main objective of this work was to assess how the same energy, delivered in several different pulse emitting characteristics, affected the ablation efficiency of the polypropylene.

AIV. 3. Results and discussion

The experimental procedure was performed with the lowest pulse repetition rate of 200 KHz available in the laser system, and a series of crater-like structures were performed by a single shot (either in SP and BM) and varying the number of pulses inside a burst from 2 to 10. A single shot with the SP mode produced the same swelling effect observed in the Monaco laser system and introducing a burst with only two pulses showed material accumulated inside the crater, which resulted in a negligible measurement of the removed volume when compared to higher pulses per burst. It was with 3 pulses per burst when a defined volume could be measured with Mountainmaps, following the methodology from section 3.5.

The results can be seen in Fig. AIV. 1. The results of the SRR for each pulse number inside a burst was divided into several figures in Fig. AIV. 1 (from 2 to 4 in a), from 5 to 7 in b) and from 8 to 10 in c). In Fig. AIV. 1 d), a direct comparison between a selected number of pulses can be seen (i.e., 3, 6, 7 and 10 ppb). From the latter, it can be observed how distributing the energy of a SP into several pulses per burst increased the efficiency of the ablation process, which, alongside the findings from the section 5. 1. 2, demonstrates the feasibility of this pulse mode to enhance the

ablation process. In fact, a similar trend as reported in other materials, laser systems and/or laser parameters [90, 262]. This trend revolved around the identification of an optimum E_p value at which the SRR was maximum, which it was closer to the E_p ablation threshold as the number of ppb increased. As it can be seen in Fig. AIV. 1 d), the optimum E_p varied from 16 µJ with 2 ppb to 6 µJ with 10 ppb, and the efficiency increased from 0.82 $\mu m^3/\mu J$ to 25 $\mu m^3/\mu J$, respectively. The optimum E_{tot} was, therefore, 32 µJ and 60 µJ, respectively. Nevertheless, as the number of ppb increased, the curve followed by SRR was stretching until the peak was reached at E_p values the same E_{tot} of 60 µJ, i.e., at 12 µJ for 5 ppb, 10 µJ for 6 ppb, etc. This showed that there could exist an optimum E_p value regardless of how it was distributed. Only the SRR value varied and increased with the ppb.

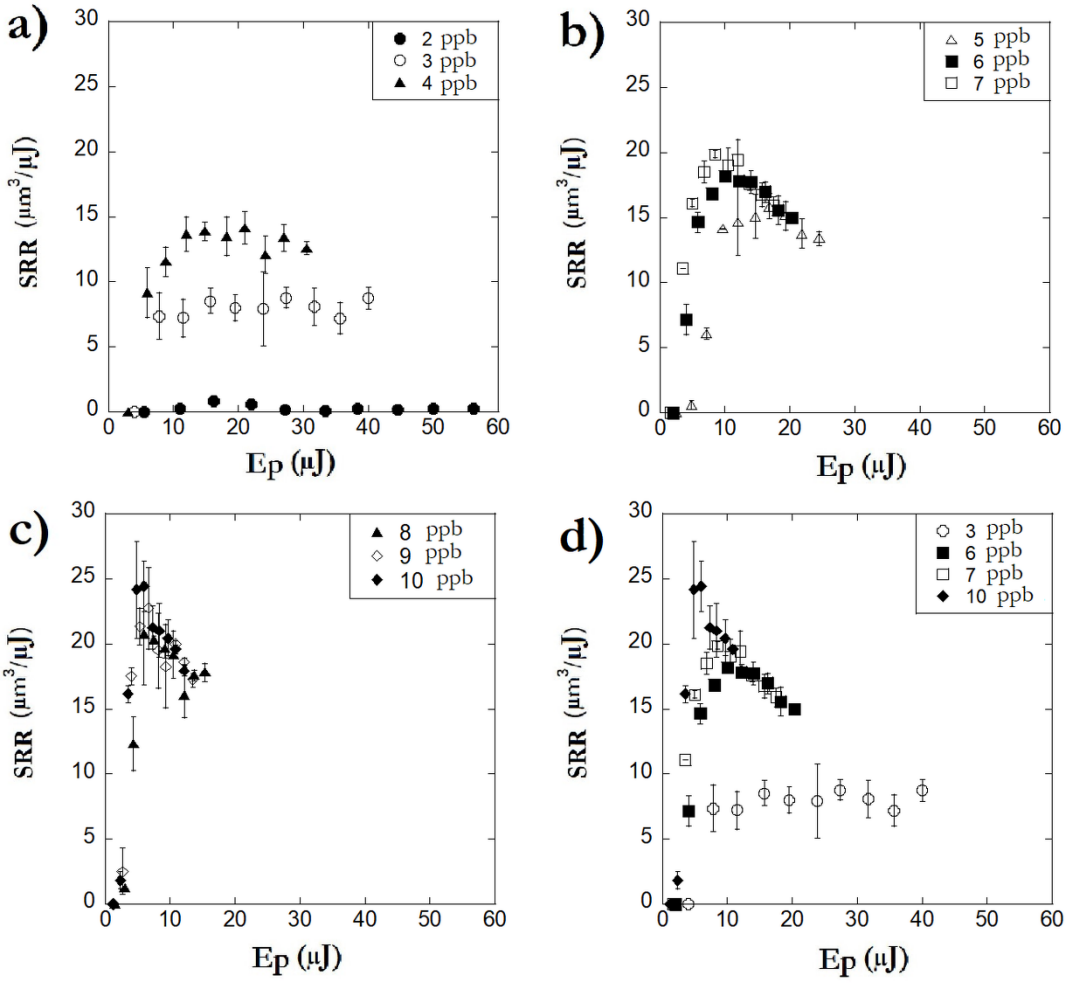

Fig. AIV. 1 Laser ablation efficiency of the BM, for a) 3 to 5, b) 6 to 8, c) 9 and 10 pulses per burst, and d) a visual comparison between 3, 6, 7 and 10 pulses per burst

In Fig. AIV. 2 a), it can be observed how, for the same total energy delivered onto the surface, increasing the number of pulses inside a burst resulted in an overall raise of the SRR. This is because the higher the number of ppb, the lower the E_p and the more efficient the process. However, it can

be observed how upon reaching bursts of seven pulses, a saturation effect can be seen in the ablation efficiency for the three different E_{tot} showed (i.e., 28.5 µJ, 60 µJ and 100 µJ). Additionally, the results from E_{tot} = 60 µJ showed the highest of the three selected values for practically all the number of ppb considered. In fact, this value corresponded to the E_p of 6 µJ that provided the maximum SRR in every case, and therefore it can be concluded that the best-case scenario involved the use of E_p values of 6 µJ. At the lowest E_{tot}, two anomalous results could be identified with 5 and 8 ppb.

By observing the equation (77), it can be deduced that, for a maximum total energy of 100 µJ, the maximum E_p that can be reached with 10 pulses per burst under the conditions used in this work was 10 µJ. Therefore, the SRR results were plotted against the number of pulses inside the burst, considering the pulse energies of 10 µJ in every case, as it can be observed in Fig. AIV. 2 b). For the same pulse energy, as the number of ppb increased, the maximum efficiency was observed with 7 ppb. This shows how, due to the high efficiency of the seventh pulse, based on the experimental results discussed in this work (see section 5. 1. 2), it could generate a plume (plasma and/or particle) that could shield the next pulse, hence the high SRR reduction for the eighth pulse. After the seventh pulse, the SRR showed an oscillating behaviour that was previously identified in the Monaco laser, and which correlates to the conclusions provided by other authors [81], and could be related to the recently mentioned interaction between pulses, thoroughly explained in section 5. 1. 2.

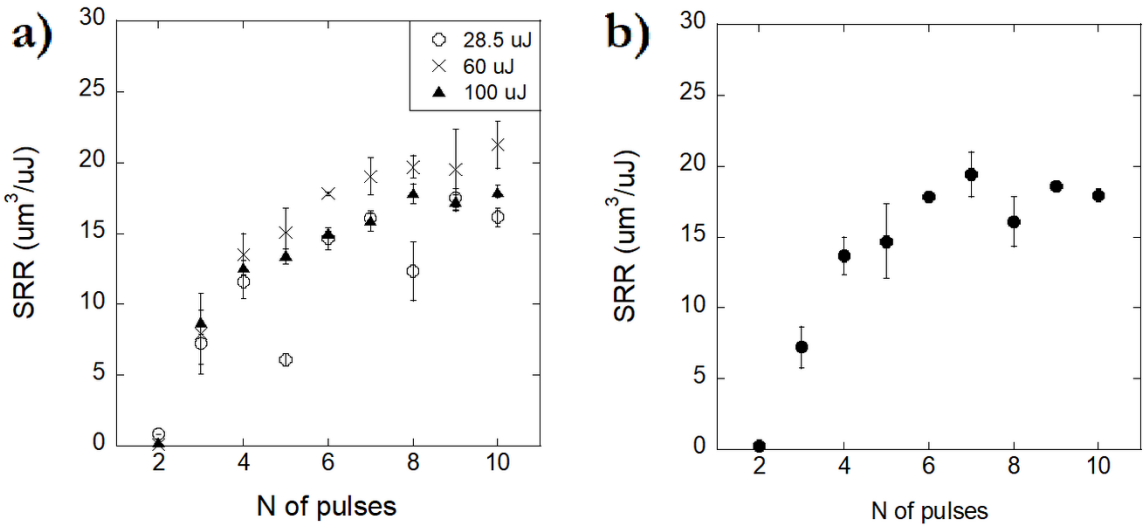

Fig. AIV. 2 a) Effect of the number of pulses on the SRR when the same total energy is compared and, b) effect of increasing the number of pulses of the same pulse energy of 10 µJ on the SRR

To conclude, it was demonstrated how the results observed in the Monaco laser system can be extrapolated to other ultrashort laser systems, where the laser parameters were different than in the

former. This proves that the same methodology can be applied to other laser systems to identify the most fitting parameters in terms of efficiency.